Reynolds Number Effects on an Adverse Pressure Gradient Turbulent Boundary Layer

A DISSERTATION
SUBMITTED TO THE DEPARTMENT OF MECHANICAL ENGINEERING
AND THE COMMITTEE ON GRADUATE STUDIES
OF STANFORD UNIVERSITY
IN PARTIAL FULFILLMENT OF THE REQUIREMENTS
FOR THE DEGREE OF
DOCTOR OF PHILOSOPHY

Carolyn D. Aubertine
June 2005

I certify that I have read this dissertation and that in my opinion it is fully adequate, in scope and in quality, as a dissertation for the degree of Doctor of Philosophy.

John K. Eaton
(Principal Adviser)

I certify that I have read this dissertation and that in my opinion it is fully adequate, in scope and in quality, as a dissertation for the degree of Doctor of Philosophy.

James P. Johnston

I certify that I have read this dissertation and that in my opinion it is fully adequate, in scope and in quality, as a dissertation for the degree of Doctor of Philosophy.

Juan G. Santiago

Approved for the University Committee
on Graduate Studies.

Abstract

While much recent work has focused on equilibrium turbulent boundary layers, those which are out of equilibrium have been examined much less frequently. Typically they have been examined far from equilibrium, making it difficult to draw general conclusions regarding the changes in the turbulence and mean velocity profiles. When the turbulence is out of equilibrium with the mean flow the standard inner and outer layer velocity and length scales are no longer the only relevant scales in the flow and additional scales become necessary to characterize the flow.

This thesis examines an adverse pressure gradient boundary layer developing along a 4° ramp. A moderate range of Reynolds numbers, factor of 7, is achieved using a wind tunnel located inside a pressure vessel by varying the freestream velocity and the ambient pressure, and thus the air density. A custom made high resolution 2-component laser Doppler anemometer with a 40 μm by 80 μm measurement volume allows for measurement of the mean and turbulence over the range of Reynolds numbers examined.

Experimentally the mean velocity profiles are observed to be weak functions of Reynolds number, while the turbulence quantities are more affected by the changing Reynolds number. The mean velocity profiles are only moderately affected by the adverse pressure gradient, with no measurable inflection point developing in the flow along the ramp. The turbulence quantities are observed to change greatly along the adverse pressure gradient ramp when scaled in traditional flat plate coordinates. The overall turbulence structure as indicated by the single-point structure parameters is not strongly affected by this adverse pressure gradient. The mean velocity profiles are observed to collapse in standard inner layer coordinates over the Reynolds number range. In addition, the mean flow at various locations along the ramp also collapses using previously developed empirical scalings. The traditional flat plate normal stress scalings do not collapse the adverse pressure gradient profiles over this Reynolds number range onto the flat plate profiles; therefore, new empirical scalings were determined for this flow. These empirical scalings for the normal stresses collapse the flat plate stress profiles along with the adverse pressure gradient profiles for this range of Reynolds numbers. These scalings are mostly based on flat plate reference profile parameters, implying that the normal stresses are determined almost entirely by the upstream flow. The small angle that the flow must turn and the resulting pressure gradient

only weakly affect the normal stresses. The streamwise normal stress collapses in the inner layer using local values implying that for the inner layer the pressure gradient does play a role in this region of the streamwise stress profile unlike in the outer layer.

Acknowledgements

First, I would like to thank my advisor, John Eaton, for all his support throughout this experience. He allowed me the freedom and flexibility necessary to finish this project. I know that without his support I would not have made it to the end of this journey.

I would like to thank my reading committee James Johnston and Juan Santiago for their valuable insight, comments and discussions. In addition, I would like to thank them for their support and encouragement at the end of this experience. I would also like to thank Juan Alonso for serving as the chair of my defense committee and providing additional insight into the computational aspects of this work.

I am indebted to Dr. Simon Song for his help in teaching me how to operate this facility at the start of my time at Stanford. I am also indebted to Lakhbir Johal for his technical assistance in fabricating many of the necessary components for this experiment.

The members of the Eaton group both past and present have provided an invaluable set of resources both inside and outside the lab. I am particularly grateful to Chuck Booten, Paul Kodzwa and Claude Matalanis for their support and assistance over the last year of this project both in and out of the lab. My friends, both at Stanford and afar, have provided me with an incredible amount of encouragement during this time and I thank them for this and more importantly for their friendship.

I want to thank my family for their love and support throughout my entire educational experience and for their reminders that I could do it. Finally, I want to thank my husband, Dan, who has supported me through this entire ordeal. I could not have done it without your support and love.

Funding for this work was provided by the Office of Naval Research under contract N00014-00-10078. In addition, I gratefully acknowledge the financial support of the Stanford Graduate Fellowship Program and the National Science Foundation Graduate Fellowship Program, which provided me with funding for the first three years of my graduate education.

Contents

List of Tables

List of Figures

Nomenclature

Roman Symbols

a_1	Townsend structure parameter, $\overline{u'v'}/q^2$.
B	Additive constant in the log law.
	Integral layer thickness.
B_o	Bond number.
c_f	Coefficient of friction: $\tau_w/(0.5\rho U_e^2)$.
C_p	Coefficient of wall-static pressure, $(P_s - P_{s,ref})/(0.5\rho U_{e,ref}^2)$.
D	LDA beam diameter.
d	LDA measurement volume diameter.
d_f	Fringe spacing in the LDA measurement volume.
d_p	Particle diameter.
f	Lens focal length.
F	Normal stress correction for a_1 structure function.
G	Clauser shape factor.
h	Ramp height (21 mm),
H	Shape factor, δ^*/θ.
	Hyperbolic hole size for quadrant analysis.
I_Q	Indicator function for quadrant analysis.
L	Ramp length in the streamwise direction (300 mm).
	Height above wall of maximum value of shear stress.
n_{oil}	Index of refraction of oil.
P	Pressure,
	TKE production rate.
P_s	Static pressure at the wall.
Q	Quadrant.
q^2	Twice the turbulent kinetic energy, $\overline{u'u'} + \overline{v'v'} + \overline{w'w'}$.
R_{uv}	Correlation coefficient.
Re_θ	Momentum thickness Reynolds number, $U_e\theta/\nu$.
ΔS_f	Oil fringe spacing.

u	Instantaneous streamwise velocity.
u'	Instantaneous, streamwise fluctuation velocity.
U	Streamwise mean velocity.
U_e	Freestream velocity evaluated at $y = \delta_{99}$.
U_m	Base velocity scale from work of Perry and Schofield (1973).
U_p	Pressure gradient velocity scale.
U_s	Velocity scale from work of Perry and Schofield (1973).
U_τ	Friction velocity, $\sqrt{\frac{\tau_w}{\rho}}$.
$\overline{u'u'}$	Streamwise Reynolds normal stress (divided by fluid density).
$-\overline{u'v'}$	Reynolds shear stress (divided by fluid density).
v	Instantaneous wall-normal velocity.
v'	Instantaneous, wall-normal fluctuation velocity.
V	Wall-normal mean velocity.
$\overline{v'v'}$	Wall-normal Reynolds normal stress (divided by fluid density).
w	Beam waist.
	Transfer function for LDA.
$\overline{w'w'}$	Spanwise Reynolds normal stress (divided by fluid density).
x	Streamwise coordinate. (The origin is the beginning of the ramp.)
x'	Streamwise coordinate normalized by the ramp length (L). (The beginning of the ramp is x$'$ = 0.00, and the ramp trailing edge x$'$ = 1.00.)
y	Wall-normal coordinate direction (always vertical).

Greek Symbols

β	Clauser's pressure gradient parameter.
δ_{99}	Boundary layer thickness (distance from the wall to where the mean velocity is 99% of the maximum velocity in the profile).
δ^*	Boundary layer displacement thickness.
Δ	Clauser defect thickness.
ϵ	Turbulent kinetic energy dissipation rate.
θ	Momentum thickness.
θ_c	Angle between LDA laser beams.

κ	Karman Constant.
λ	Laser light wavelength.
Λ	Similarity parameter from analysis of Castillo and George (2001).
μ	Dynamic viscosity coefficient.
ν	Kinematic viscosity, μ/ρ.
Π	Coles wake parameter function.
ρ	Fluid density.
ρ_p	Particle density.
σ	Surface tension.
τ	Shear stress.
τ_p	Relaxation time of flow tracer.
τ_f	Kolmogorov time scale for flow.
τ_o	Wall shear stress.

Subscripts/Superscripts

$-$	Averaged quantity over time.
$+$	Normalized by inner scales: ν/U_τ or U_τ.
e	Quantity evaluated in the freestream.
max	Maximum.
o	Quantity evaluated at the wall.
ref	Quantity evaluated at the reference station, x$'$ = -0.33.

Abbreviations

CFD	Computational Fluid Dynamics.
DES	Detached Eddy Simulation.
DNS	Direct Numerical Simulation.
DR	Normalized data rate.
FFT	Fast Fourier Transformation.
LDA	Laser Doppler Anemometer.

LES	Large Eddy Simulation.
PIV	Particle Image Velocimeter.
RANS	Reynolds Averaged Navier-Stoke equation.
STD	Standard Deviation.
TKE	Turbulent Kinetic Energy.

Chapter 1

Introduction and Objectives

1.1 Introduction and Motivation

Adverse pressure gradient boundary layers occur in many practical applications, for example diffusers, the trailing edge of airfoils and the aft section of ship hulls, and they often play a critical role in determining the performance of engineering devices. In many cases, accurate knowledge of the adverse pressure gradient boundary layer development is the most critical factor in predicting the overall device performance. For example, the design objective in diffusers and aircraft high lift systems often is to obtain the maximum pressure recovery, while avoiding separation. Unfortunately, as discussed below, the adverse pressure gradient boundary layer is usually the most difficult aspect of these flow systems to predict using computational fluid dynamics (CFD). Many of these applications are at Reynolds numbers significantly higher than can be examined even in large scale laboratory experiments. Therefore, it is necessary to understand how to extrapolate results from experiments or numerical simulations to much higher Reynolds numbers, particulary the scaling of the various mean velocity and turbulence quantities. While much prior research has been done on specific types of adverse pressure gradient flows, very little has been focused on the effects of Reynolds number on non-equilibrium adverse pressure gradient boundary layers. A non-equilibrium boundary layer can be described as one which is subjected to perturbations such that the turbulence structure changes in the streamwise direction. Most practical flows include non-equilibrium boundary layers. From an experimental point of view, an equilibrium flow, while more difficult to initially setup is simpler to examine since the turbulence properties do not change with downstream distance and thus measurements at only one location are sufficient to understand the behavior of the entire boundary layer. Therefore, equilibrium boundary layers are examined frequently.

Recently, a few high Reynolds number experiments have been performed which have shown that extrapolating from low and moderate Reynolds number data to high Reynolds numbers is difficult or impossible. This is particularly true in non-equilibrium boundary layers where very complex scaling behavior has been found. Therefore, it is necessary to

measure flow properties at high Reynolds numbers for use in modifying the predictive models to account for the effects now being observed at these high Reynolds numbers. Unfortunately, from both an experimental and computational perspective, detailed examination of complex high Reynolds number flows is not practical. Experimentally, the methods of producing high Reynolds number flows are either to build a very large facility or to use very high resolution measurement techniques, because of the decrease in the size of the viscous length scale with increasing Reynolds number. McDonald et al. (2004) discussed the difficulties associated with extrapolating experimental wind tunnel data to flight conditions. Wind tunnel testing still plays a critical role in the design of aircraft. While computational fluid dynamics is becoming accurate enough to compute many of the necessary flow parameters at cruise conditions, it is still too time consuming and not reliable enough to test certain off design conditions. With wind tunnel testing, it is necessary to correct the wind tunnel results for any differences which exist between the wind tunnel test and the flight environment. This includes well known issues such as the effects of mounting fixtures and wind tunnel walls, but also more subtle effects including, the incomplete modeling of the airplane details and material property differences. In addition, corrections must be made for the non-linear effects of Reynolds number differences. This is particularly important when trying to predict the separation location or complex shock boundary layer interactions as well as the lift characteristics. While much work has been started on Reynolds number extrapolation and reducing its uncertainty, it is difficult to separate the Reynolds number effects from the model deformation effects.

Computationally, there are a variety of possible approaches to high Reynolds number flows. Direct numerical simulation (DNS) is limited to very low Reynolds number and simple geometries due to the computational costs. Other computational models, such as Reynolds stress transport and two equation models require fine meshes in the near wall region to properly resolve the flow, leading to very expensive computations for complex flows. Additionally, these models are calibrated using low and moderate Reynolds number data for specific types of flows. When these models are used for flows outside the flow types and Reynolds numbers for which they were calibrated, the results are often incorrect. Large eddy simulation (LES) is a possible alternative for high Reynolds numbers, however to resolve the near wall flow accurately the mesh used in the inner region of the boundary layer must be very fine, making this method computationally expensive as well. A recent computational effort involving a large number of researchers at a variety of institutions was

summarized by Mellen et al. (2003). This study attempted to use large eddy simulation (LES) on the flow around an airfoil at typical flight Reynolds numbers. The results showed that while success was possible using LES, very high grid resolution was required in order to sufficiently predict the location of separation on the airfoil, as well as the rest of the flow field. The results of this study show that adverse pressure gradient boundary layers are still often a very significant challenge to advanced computational schemes.

Another method of predicting how a flow will act at high Reynolds number is to compare data from a variety of experiments over a wide range of Reynolds numbers from different flow facilities. This method is not without its own difficulties since the use of different measurement techniques and facilities leads to questions about the uncertainties and resolution of the data being compared.

Recently, the need for experiments and computational modeling to work together in order to improve the current models and develop new ones has been pointed out. Marvin (1995) noted that there has been a lot of forward progress on combining experiments and computations to validate each other. More work of this type is needed as there are many practical flows which can neither be tested fully in experiments nor calculated using turbulence models or simulations. He also noted that for experiments, it is necessary to measure all the commonly reported data with high accuracy and realistic uncertainties. The uncertainty analysis is very important for the use of the data to tune and test CFD models. As CFD models are tested against new data and modified to better predict basic flows, their applicability to more complex flows will improve.

The use of high resolution laser Doppler anemometry (LDA) by a few groups to make flow measurements over a wide range of Reynolds numbers in a single flow facility has produced results, which, though measured in very different geometries, show some strikingly similar results. DeGraaff (1999) examined the turbulent boundary layer on a flat plate and over swept and unswept bumps for a Reynolds number range of $Re_\theta = 1400 - 24,000$. Song (2002) examined the turbulent boundary layer on a ramp with separation, reattachment and redevelopment for a Reynolds number range of $Re_\theta = 1100 - 20,100$. Olcmen et al. (2001) studied the two and three dimensional boundary layers outside of a wing, body junction for a Reynolds number range of $Re_\theta = 5940 - 23,200$. For all of these experiments the mean flow was found to be a weak function of the Reynolds number, while the turbulence stresses and other turbulent quantities were observed to be very sensitive to Reynolds number.

Of particular interest is the scaling of both the mean and turbulence quantities over a

wide range of Reynolds numbers, including moderately high Reynolds numbers. Previously, the work of DeGraaff (1999) verified the typical flat plate mean velocity scaling and produced a new robust mixed scaling, which collapsed the Reynolds stresses over a wide range of Reynolds numbers. This scaling has been shown by Metzger et al. (2001) to hold over a much larger range of Reynolds numbers than originally tested. The works of DeGraaff (1999) and Song (2002) examined complex boundary layers including regions of strong adverse pressure gradient and separation in an attempt to find similarly useful scaling laws. They found complex scaling laws that seemed applicable only to the particular flow studied. However, it was observed that when the pressure gradient was removed and the flow was allowed to redevelop on a flat plate, the flat plate mixed scaling proposed by DeGraaff and Eaton (2000) once again held.

The empirical scalings for the flat plate boundary layer discovered by DeGraaff and Eaton (2000) are very useful for extrapolating experimental and simulation results to high Reynolds numbers. Unfortunately for highly non-equilibrium turbulent boundary layers, such as those involving separation, the turbulent stresses collapse in much more complicated and geometry dependent scalings. Using a mild adverse pressure gradient, which is perturbed only a small amount from the zero pressure gradient case, it is hoped that a better understanding of adverse pressure gradient boundary layers can be obtained. The goal of this project is to extend the empirical scalings of DeGraaff and Eaton to include both the flat plate and mild adverse pressure gradient boundary layer turbulent stress data. The next sections will discuss general adverse pressure gradient flows, mean flow and turbulent stress scalings for adverse pressure gradient flows, and the specific goals of this thesis.

1.2 Experimentally studied adverse pressure gradient boundary layers

Much work has been done over the years on adverse pressure gradient flows. Experimental work has examined equilibrium flows, flows over airfoils and similar practical geometries, and flows near separation.

1.2.1 Equilibrium boundary layers

Equilibrium turbulent boundary layers are very commonly examined when studying adverse pressure gradient flows. This is because they are simple to describe analytically,

the pressure distribution is easy to define, and measurements are required at only a single position once equilibrium conditions are established.

The idea behind the equilibrium turbulent boundary layer was laid out by Clauser (1954), who set out to examine a turbulent boundary layer with a well defined, and simple pressure history. Defining an equilibrium profile as one of a set of profiles in which a constant force history was obtained, the non-dimensional parameter β was introduced, as the ratio of the pressure force to the shear force:

$$\beta = \frac{\delta^*}{\tau_o}\frac{dP}{dx} \tag{1.1}$$

Clauser defined a new thickness, Δ, and a new integral parameter, G, which were related to the universal velocity profile plot and thus did not change for a given set of equilibrium profiles:

$$\Delta = \int_0^\infty \frac{U-u}{u_\tau}dy = -\delta_{99}\int_0^\infty f(\eta)d\eta \tag{1.2}$$

where for constant pressure profiles the integral has a value of 3.6 and:

$$G = \frac{\int_0^\infty \left(\frac{U-u}{u_\tau}\right)^2 dy}{\int_0^\infty \left(\frac{U-u}{u_\tau}\right) dy} \tag{1.3}$$

These parameters were related to the more commonly used integral parameters by:

$$\delta^* = \sqrt{c_f/2}\Delta \tag{1.4}$$

$$\theta = \sqrt{c_f/2}\left(1 - G\sqrt{c_f/2}\right)\Delta \tag{1.5}$$

$$H = 1/\left(1 - G\sqrt{c_f/2}\right) \tag{1.6}$$

Since this original work on equilibrium turbulent boundary layers, many others have proposed new requirements for equilibrium and described methods of producing boundary layers near enough to equilibrium to reproduce the general profiles of an equilibrium boundary layer, while avoiding some of the major difficulties with producing an equilibrium flow experimentally.

Townsend (1961) defined an exactly self preserving flow as one in which the mean velocity distribution was given by:

$$U = U_1 - u_o f(y/l_o) \tag{1.7}$$

and the Reynolds stress was defined as:

$$\overline{u'v'} = u_o^2 g(y/l_o) \tag{1.8}$$

where $u_o = (\tau/\rho)_o^{1/2}$ and $l_o = \tau/\alpha$ were velocity and length scales, which varied only with downstream distance and the functions f and g characterize the entire flow. Here α comes from approximating the shear stress as $\tau = \tau_o + \alpha y$ for an impermeable boundary. Applying these distributions to the typical boundary layer equation for the mean flow in two dimensions led to:

$$-\frac{d(u_o U_1)}{dx} f + \frac{u_o}{l_o}\frac{d(U_1 l_o)}{dx}\eta f' + u_o \frac{du_o}{dx} f^2 - \frac{u_o}{l_o}\frac{d(u_o l_o)}{dx} f' \int_o f d\eta + \frac{u_o^2}{l_o} g' = 0 \tag{1.9}$$

an ordinary differential equation, as was expected for a truly self preserving flow. The only ways for this equation to be compatible with the equilibrium layer scales were for the flow to either be defined as:

$$U_1 \propto (x_o - x)^{-1} \propto \tau_o^{1/2}, l_o \propto (x_o - x) \tag{1.10}$$

an accelerating flow in a converging wedge, or:

$$\tau_o = 0, U_1 \propto (x - x_o)^{-0.23}, l_o \propto (x - x_o) \tag{1.11}$$

a zero stress flow in an adverse pressure gradient.

Skote et al. (1998) summarized the typical analysis necessary to produce approximately self similar adverse pressure gradient boundary layers. The basic equations of a two dimensional turbulent boundary layer with a pressure gradient were written as:

$$\frac{\partial u}{\partial x} + \frac{\partial v}{\partial y} = 0 \tag{1.12}$$

$$u\frac{\partial u}{\partial x} + v\frac{\partial u}{\partial y} = -\frac{1}{\rho}\frac{dP}{dx} + \nu\frac{\partial^2 u}{\partial y^2} - \frac{\partial}{\partial y}\langle u'v'\rangle \tag{1.13}$$

where u was the mean streamwise velocity, v was the mean wall normal velocity, dP/dx was the streamwise pressure gradient and $\langle u'v'\rangle$ was the Reynolds shear stress. For moderate pressure gradients, the inner layer of the boundary layer was the same as for a zero pressure gradient case. However, the outer portion required modification even in a very mild pressure gradient. To obtain a self similar solution there must be no x dependence and thus solutions of the following form were sought:

$$\frac{u - U}{u_\tau} = F(\eta) \tag{1.14}$$

$$\frac{\langle u'v' \rangle}{{u_\tau}^2} = R\eta \tag{1.15}$$

where:

$$\eta = \frac{y}{\Delta}, \Delta = \frac{U\delta^*}{u_\tau} \tag{1.16}$$

When substituted into the mean streamwise momentum equation, these equations led to a condition on self similarity, namely that the Clauser pressure gradient parameter, β, should be constant. The mean streamwise velocity must change with downstream distance and thus it was necessary to determine the relationship between β and m, where:

$$U \sim x^m \tag{1.17}$$

This relationship could be derived starting with the integrated momentum equation:

$$\frac{U'\delta^*}{U\delta^{*\prime}} = -\frac{\beta}{H\left(1+\beta\right) + 2\beta + \left(H-1\right)\beta\left(1 - \frac{u'_\tau U}{u_\tau U'}\right)} \tag{1.18}$$

This used the relationships:

$$H = \frac{1}{1 - \frac{u_\tau}{U}G} \tag{1.19}$$

and:

$$G = \int_0^\infty F^2 d\eta \tag{1.20}$$

To remain consistent with experiments and prior computations u_τ/U was held constant which led to the simplification that:

$$\frac{U'\delta^*}{U\delta^{*\prime}} = -\frac{\beta}{H(1+\beta) + 2\beta} = m \tag{1.21}$$

This could be integrated and combined with the definition of the Clauser pressure gradient parameter and through the introduction of a virtual location x_o, where $\delta^* = 0$, led to:

$$\frac{U}{U_o} = \left(1 - \frac{x}{x_o}\right)^m \tag{1.22}$$

and:

$$\frac{\delta^*}{{\delta_o}^*} = 1 - \frac{x}{x_o} \tag{1.23}$$

Note that x_o has a negative value. The above implied that:

$$\delta^* \sim x \tag{1.24}$$

where:

$$m = -\frac{\beta}{H(1-\beta)+2\beta} \tag{1.25}$$

The use of power law freestream velocity profiles to produce equilibrium adverse pressure gradient boundary layers is a commonly used experimental technique, based on this and other similar analyses.

Townsend (1961) developed more qualitative and practical definitions of equilibrium boundary layers. His working definition of an equilibrium layer was one in which the local rates of energy production and dissipation were so large that the shear stress distribution in a region completely determined the turbulent motions, independent of the conditions outside the region. He assumed that equilibrium layers possessed a universal structure, leading to a simple relationship between the mean velocity gradient, the Reynolds stresses and the height above the solid surface. Similarity arguments could be extended considerably if an equilibrium layer was defined locally, requiring only absolute equilibrium between energy production and dissipation, and not the requirement of stress equilibrium. This definition of equilibrium allows a zero pressure gradient boundary layer to be considered in equilibrium boundary, since the skin friction and shape factor change very slowly with downstream distance. The method described in this paper to solve the mean flow problem for different equilibrium layers stemmed from Clauser's work where the outer layer of the mean velocity profile for self preserving boundary layers was closely reproduced by an eddy viscosity, which was held in a constant ratio with the integral of the velocity defect. The eddy viscosity changed linearly with the integral of the velocity defect and the product of the two was held constant. Comparison with experiments showed that this was a good description of the mean distribution, and the constant ratio appeared to depend not on the pressure gradient, but on the conformation of flow to the non-moving boundary. The turbulence in an equilibrium layer was not shown to be in a universal state. This led to the idea that the motion at any location had two components, the active component which transferred momentum and determined the stress distribution and the inactive component which did not transfer momentum or interact with the universal component. It was hypothesized that these inactive motions were made of attached eddies of large size that contributed to the Reynolds stresses far away from the wall. This would have led to the ratio of turbulent intensity to Reynolds stress increasing with total thickness of the constant stress layer, a phenomena later verified by DeGraaff and Eaton (2000)

The limits of existence of equilibrium boundary layers has been a widely discussed topic.

Taking Clauser's work for equilibrium turbulent boundary layers as a basis, Mellor and Gibson (1966) developed a model to calculate velocity profiles that showed good agreement with experimental profiles. Following the work of Clauser, an effective viscosity, ν_e, was defined as $\nu_e = KU\delta^*$, where K was an inverse turbulent Reynolds number that had to be determined empirically. For the outer 80% of the boundary layer this value could be assumed to be constant as discovered by Clauser. For the overlap layer Prandtl's mixing length theory was used to define the effective viscosity, $\nu_e = \kappa^2 y^2 \mid \frac{\partial u}{\partial y} \mid$. A method of calculating the velocity defect was determined and from this the range of possible equilibrium turbulent boundary layer solutions was also determined. The limits were found to be $-0.5 \leq \beta \leq \infty$. For the constant pressure case, $\beta = 0.0$, the computation gave good agreement with a wide range of prior experiments. The model was used to calculate a few of Clauser's adverse pressure gradient flows with good agreement for the mean velocity defect profile. Even for the Stratford data near separation the model worked very well for the velocity defect profile. The model made it possible to determine the skin friction by matching the defect profiles, the logarithmic law of the wall and the shape factor for the flow, assuming that the viscous sublayer was not affected by the pressure gradient. A family of solutions was defined to determine where equilibrium flows could exist and how the power-law for the mean velocity must be defined. The authors felt that the Coles' wake parameter, Π, may have simply been related to β based on a comparison of their work and the work of Coles. For cases of small Clauser parameter the Coles solution worked well, but in the large Clauser parameter limit the correlation did not agree with Stratford's data or Mellor and Gibson's model.

Mellor (1966) expanded the previous model to include the near wall layer. Different from previous effective viscosity models, the one developed here worked for a wide range of pressure gradients and the entire boundary layer. The near wall velocity was found to be a function of y^+, and $\alpha = \frac{\nu \frac{dp}{dx}}{\rho u_\tau^3}$. Using this extension of the previous model for a given value of β, the defect profile overlapped the wall profile and matched well with previous data. In addition, unlike previous work by Townsend and others, only one value of skin friction was found near separation and it was not necessary to explain why one solution was more likely to occur than the other, thus only one equilibrium boundary layer was possible near separation for each value of β.

Head (1976) used an integral method to examine how the shape parameter, G, varied with the initial condition of the boundary layer for a given freestream velocity variation. For an equilibrium boundary layer, G must remain constant with downstream distance,

which required the pressure force and the skin friction force to remain in a constant ratio, β held constant. This required the freestream velocity to be of the form $U_e = cx^n$, where the appropriate value of n for a particular value of G or β was not determined. The results of this computational work showed that for certain values of the exponent, n, a wide range of equilibrium boundary layers was possible depending on the momentum thickness at the initial reference location. However, for certain values of n a unique equilibrium profile developed, and for others the boundary layer separated regardless of the starting conditions.

Schofield (1981) set up an analytical model of the equilibrium boundary layer, which attempted to address many of the disagreements between various groups, including the limits of existence for an equilibrium layer and the appropriate parameters for defining an equilibrium layer. Clauser's use of u_τ and δ^* led to a number of difficulties near separation, particularly where u_τ approached zero. Schofield followed the analysis of Perry and Schofield (1973) to determine the appropriate velocity scale for this model. The base velocity scale used was:

$$U_m = \sqrt{\frac{\tau_{max}}{\rho}} \tag{1.26}$$

This velocity scale was chosen for a number of reasons, particularly that it maintained the half power law description of the mean velocity profile and had an invariant analytical form for all adverse pressure gradients, as long as the maximum value of the shear stress was at least 1.5 times larger than the wall shear stress. The limits for equilibrium layers based on this analysis were that the flow must be an adverse pressure gradient flow, the skin friction coefficient must remain positive (attached flow), and the shear stress must be 1.5 times as large as the wall shear at its maximum location. Therefore, this scaling was only valid for a moderate to strong adverse pressure gradient flow. Schofield defined the mean velocity profile as:

$$\frac{u}{U_e} = 0.47\left(\frac{U_s}{U_e}\right)^{3/2}\left(\frac{y}{\delta^*}\right)^{1/2} + 1 - \frac{U_s}{U_e} \tag{1.27}$$

which modeled the flow as a small logarithmic layer tangentially joined to a half power law region. In this model, U_s was a velocity scale, proposed by Perry and Schofield (1973), determined by plotting the velocity profile as a scaled velocity versus a half power scaled length scale and extrapolating the linear region of the plot back toward the wall. The velocity scale U_s was related to the base velocity scale by the relationship, $U_s = 8\sqrt{(B/L)}U_m$, where L was the height of the maximum shear stress away from the solid wall and B was

an integral layer thickness. Schofield compared this model with previously published experimental data for a large number of moderate and strong attached equilibrium adverse pressure gradients. For each experiment, he calculated the velocity scale U_s and used this scale to plot the mean velocity profiles produced by this model against the experimental data, finding good agreement.

Schofield expanded the analysis of Perry and Schofield (1973) to determine the range of equilibrium profiles that were possible for a specific pressure gradient or value of m. Because this analysis gave a general analytical expression for the mean flow, the shear stress gradient could be determined as well. Fixing the wall value at the measured wall shear stress value, the complete shear stress profile could be calculated. The results were in good agreement with the experimental data and showed that the position of maximum shear stress moved away from the wall as the ratio of maximum shear stress to wall shear stress increased. Two solutions, a high skin friction branch and a low skin friction branch were observed when using this model to predict the flow. The choice of solution was based entirely on the initial conditions of the velocity ratio, U_e/U_s.

Numerous experiments have been performed on equilibrium boundary layers. These boundary layers are difficult to setup experimentally, but once developed only one set of experimental data is necessary to capture the entire flow.

Clauser (1954) used a flexible top surface wind tunnel to develop an equilibrium adverse pressure gradient boundary layer on the wind tunnel floor. For a mild pressure gradient, he obtained a set of self-similar velocity profiles with a shape factor of between 1.4 and 1.5.

Bradshaw (1967a) examined three boundary layers, one with a constant free stream velocity and two with different power-law variations of freestream velocity, producing zero, moderate and strong adverse pressure gradients. The mean velocity profile shape factors were $H = 1.34$, 1.4 and 1.54 for the three cases. The pressure gradient cases exhibited a strong peak in the shear stress away from the wall. As the pressure gradient increased, the maximum value of the shear stress increased, while the wall shear stress decreased.

Skåre and Krogstad (1994) examined a turbulent boundary layer near separation, imposed by an adjustable top wall. The flow developed with a constant skin friction coefficient at a reasonably large Reynolds number. The flow was held in equilibrium for a reasonable length, which allowed for the examination of this equilibrium flow at a number of locations. The wake parameter for this strong adverse pressure gradient case grew to a maximum value of 7. The mean velocity profiles agreed well in both defect coordinates and in logarithmic

coordinates, where the wake was shown to be a dominant part of the flow. The turbulent stresses were in equilibrium in both the inner and outer layers. As the flow developed in the adverse pressure gradient, the stress profiles scaled in inner variables exhibited a shift away from the wall in the outer layer. The turbulent production term exhibited two peaks, the inner one was caused by the high velocity gradient near the wall and the outer peak was caused by the peak in the turbulent stresses, due to the strong adverse pressure gradient. The mixing length near the wall exhibited a slope of 0.41, the typical value for zero pressure gradient; however this value increased rapidly through the log layer to a value of 0.78, indicating a strong dependence on the pressure gradient. Further away from the wall the mixing length took on a constant value slightly below the typical value for zero pressure gradient. The von Karman constant in the logarithmic region of the mean flow was the same as for a zero pressure gradient flow. This agreed with the findings of Perry et al. (1966) that the pressure gradient only defined the region of applicability of the logarithmic profile for a flow, but did not distort it. The ratios of different normal stresses were shown to produce good similarity implying that the mean flow pressure gradient did not affect the mechanism for redistribution of turbulent energy between the various normal stress components. For the main portion of the boundary layer, $v'v'/u'u'$, was constant at about 0.45. The correlation coefficient was nearly constant, $0.4 < R_{uv} < 0.46$, for $0.2 < y/\delta < 0.7$. There was no systematic x dependence on the variation and the value was taken to be 0.42. The structure parameter, a_1, was slightly lower than the value of 0.15 found in zero pressure gradient flows.

An equilibrium adverse pressure gradient boundary layer was studied by Krogstad and Kaspersen (2002). The value of β was fixed at a value of 20 using an adjustable top surface in the wind tunnel. The turbulent production was observed to have two peaks. The outer peak moved away from the wall with increasing pressure gradient and had a significant impact on the turbulent field. They concluded that the adverse pressure gradient caused the outer layer of turbulence to interact more efficiently with the inner flow than in the case of zero pressure gradient. The shear stress distribution for the adverse pressure gradient had a large peak compared with that in a zero pressure gradient, which significantly changed the turbulent kinetic energy budget. Through the use of two point space-time correlations, the authors demonstrated that strong adverse pressure gradients reduced the anisotropy in a turbulent boundary layer due to the stretching of the coherent structures by the streamwise gradient of the mean velocity. This was more pronounced near the surface. The dominant

length scales in the streamwise direction were reduced in size, which tilted the correlations for any scale towards the wall normal.

Additional equilibrium turbulent boundary layer experiments have examined how boundary layers recover in an equilibrium flow downstream of separation and reattachment. Cutler and Johnston (1989) studied the relaxation of a turbulent boundary layer in an equilibrium adverse pressure gradient downstream of separation. The boundary layer was separated using a wall fence and the adverse pressure gradient was obtained using a flexible top wall and suction. The Clauser parameter, G, was held constant. This alone was not enough to ensure an equilibrium boundary layer. The freestream velocity also had to vary as a power of the streamwise distance, or equivalently the Clauser pressure gradient parameter, β, had to be maintained at a constant value. The mean velocity profiles obtained for this flow agreed with both the law of the wall and the law of the wake. The Reynolds stresses were seen to peak near the center of the boundary layer. As the flow developed downstream, the peak values fell, but the shapes remained similar. Here streamline coordinates were examined and some parameters such as the structure parameter, a_1, were found to be more representative of the data when evaluated in streamline coordinates. The turbulent kinetic energy was estimated using the common practice of assuming $w'w' = \frac{1}{2}(u'u' + v'v')$. The use of this estimate in the structure parameter may have explained the low values (0.12) for the downstream locations. The eddy viscosity profiles did not agree well with the equilibrium model of Cebeci and Smith; however, the eddy viscosity was nearly self-similar in this region over a number of profiles. The value of the eddy viscosity was twice as large as expected for an equilibrium flow, and this may have been due to the separation upstream and its long range effects on the history of the flow. The mixing length model showed that the experimental data had a steeper slope in the near wall region than the typical value of 0.41 and plateaued at a much higher value than the common zero pressure gradient result. The value of G was much lower than previously examined for the given value of β, possibly due to the upstream history of the flow.

Finally, some computational modeling of equilibrium turbulent boundary layers has been performed. Skote et al. (1998) performed a direct numerical simulation (DNS) on self-similar or equilibrium turbulent boundary layers in adverse pressure gradients. As with all DNS the momentum thickness Reynolds numbers were relatively small, in this case on the order of 500. The authors performed two separate adverse pressure gradient simulations, one with $\beta = 0.24$, which was near the value for laminar boundary layer separation, and the

other with $\beta = 0.65$, the value from the experiment of Bradshaw. The mean profiles showed self similarity, particularly in the inner region for each case of equilibrium. An outer peak was observed in both the turbulent production and the streamwise normal stress profiles, in agreement with the experimental work done near separation. Peaks were not observed in the other turbulent stresses. However, low Reynolds number effects led to the Reynolds shear stress never achieving self similarity, which may have explained the differences between the simulation and experimental results.

The study of equilibrium boundary layers has led to a greater understanding of some of the basic changes which occur to boundary layers in adverse pressure gradient. However, equilibrium boundary layers are not representative of practical engineering flows and thus their results can only be used to extrapolate general behavior of adverse pressure gradient boundary layers. Equilibrium adverse pressure gradient boundary layers follow the logarithmic law of the wall, although a large wake region develops, which has been observed to shorten the region over which the logarithmic law of the wall is applicable. The mean velocity profiles are self-similar when equilibrium is achieved. The turbulent stresses however change greatly when exposed to an adverse pressure gradient. The stresses and the turbulent production develop a peak which moves away from the wall. The Reynolds stresses develop peaks in the outer layer with the maximum value of the peak depending on the strength of the pressure gradient.

1.2.2 Flows near separation

The prediction of when separation will occur is a very important practical issue. Because of the interest in this problem a great deal of research has been performed on flows both in the vicinity of separation and downstream of separation. This goes back at least as far as the work of Schubauer and Klebanoff (1950). Only flows which separate due to the application of an adverse pressure gradient are discussed here, much other work has been performed on flows which separate due to a step change or other obstruction in the flow.

A turbulent boundary layer near separation subjected to an increasingly adverse pressure gradient was examined by Simpson et al. (1977). The experiment produced an airfoil type pressure distribution using an adjustable top wall wind tunnel with suction. They concluded that while the logarithmic law of the wall held for all adverse pressure gradient flows until the point of separation, the convective and normal stress terms of the momentum equation became significant near the wall. Using the Perry and Schofield (1973) mean velocity

correlation for the two measurement locations with increasingly adverse pressure gradients, they found that the results fell within the range of accepted results for the correlation. A modification to the Perry and Schofield correlation to account for the normal stress term in the momentum equation was described. This provided a slight improvement to the fit of the experimental results.

Simpson et al. (1981) studied the structure of a separating boundary layer using a similar experimental setup as in the prior experiment, except for a longer test section. They noted that prior to the point of separation, the mean flow obeyed the logarithmic law of the wall. The Perry and Schofield correlations for the outer region were also obeyed. Upstream of separation, the mixing length and eddy viscosity models were shown to be adequate to predict the flow. The mixing length and eddy viscosity models were also shown to hold in the outer region of the flow above the separation bubble.

The flow along a flat plate subjected to a strong enough adverse pressure gradient to cause separation was investigated by Dianat and Castro (1991). Similar to prior work in adverse pressure gradient flows, especially near separation, the normal stresses near the wall were found to be much larger than in zero pressure gradient flows. These stresses were shown to be important contributors to the production of turbulent energy in the boundary layer.

More recently Elsberry et al. (2000) maintained a boundary layer on the verge of separation through the use of a wind tunnel with an adjustable top wall. The shape factor was maintained at a value of 2.5, which is indicative of a flow on the verge of separation. The mean velocity profile developed a very large wake, which was adequately represented by Coles' law. The mean velocity profile also followed the logarithmic law of the wall, although only for a very short region. The turbulent stresses developed peaks, which moved away from the wall as the flow continued to develop. These peaks were located at the same height as the inflection point in the mean flow. The results of their work led to a new set of turbulent stress scalings along the flow, which are discussed later.

Bernard et al. (2003) examined a two-dimensional bump, in the shape of a half airfoil, designed to develop the same adverse pressure gradient observed on the suction side of an airfoil on the verge of separation at a high angle of attack. Their results showed that the boundary layer did not separate, but grew rapidly in thickness. This flow was a mild adverse pressure gradient since the shape factor, H, reached a maximum value of 1.7 at the end of the bump. The design of the experiment was based on a k-ε model of the flow, which was

in good agreement with the experimental results for mean flow properties. An inflection point developed in the flow downstream of the start of the adverse pressure gradient region. As compared to an equilibrium adverse pressure gradient flow, this flow was much different since linear growth rates for δ and θ were not observed. Other than the logarithmic law of the wall, a universal representation was not seen. No turbulence quantities were shown in this work.

Song and Eaton (2004) examined the Reynolds number effects on a flow which separated, reattached and finally redeveloped in a zero pressure gradient boundary layer. The boundary layer was examined at five separate Reynolds numbers in a range of $Re_\theta = 1100 - 20,100$. The separation and reattachment locations were found to be only very weak functions of the Reynolds number, except for the lowest Reynolds number, where low Reynolds number effects were most likely present. Downstream of the reattachment point, the mean velocity profile showed evidence of the development of a stress equilibrium layer. The logarithmic law of the wall was seen to once again be valid in the near wall region at a distance six ramp lengths downstream of the ramp. For the upstream flat plate location the DeGraaff and Eaton (2000) mixed scaling held. Empirical scalings were found to collapse the turbulent stresses at specific regions along the flow including separation, the ramp edge, reattachment and downstream in the recovery region. While these scalings may have only applied to this flow, they may be useful in other separating and reattaching flows as a starting point for examination. Many of these scalings were related to the mean velocity at the inflection point, which was a good indicator of the scale of the streamwise velocity fluctuations. It was also the location where the maximum production of turbulent kinetic energy production occurred. As had been noted by other groups, the Reynolds number effects on the mean flow were small, while the effects on the turbulent stresses were large over the entire range of Reynolds numbers examined.

Axisymmetric boundary layers are another common flow for separation studies due to the absolute two-dimensionality of these flows. While two dimensional cartesian boundary layers can be very closely approximated as two dimensional, there are in fact three dimensional effects present, which are absent in axisymmetric flows. This is particularly important in separating flows where three dimensional affects may trigger separation at a different location than in a two dimensional flow.

An axisymmetric flow with the Stratford-Smith pressure recovery was examined by Hammache et al. (2002). The Stratford ramp was the shortest surface over which the

maximum recoverable pressure rise could occur without separation, and was developed for planar surfaces. Smith (1977) expanded this concept to axisymmetric surfaces, where it was most commonly studied. In order to obtain the maximum recoverable pressure rise without separation, the flow must be maintained on the verge of separation, with a skin friction coefficient of zero. Two experiments were performed, one with a slightly less steep recovery and one with a slightly more steep recovery. The mean velocity profiles here did not display a logarithmic region. The streamwise normal stresses exhibited a peak which appeared to have moved away from the wall. This was more observable for the steeper pressure recovery case.

An axisymmetric boundary layer in the vicinity of separation was examined by Dengel and Fernholz (1990). They examined three cases with the skin friction held constant very near zero, one case with the skin friction slightly larger than zero, one case with the skin friction slightly lower than zero and one case with the skin friction equal to zero. The shape factor values were seen to increase slightly with downstream distance and were all in the vicinity of the typical values given for separation. The mean velocity profile was found to not agree well with the Coles' law of the wake in the region near separation. When the Perry and Schofield defect law for adverse pressure gradients near separation was used, the agreement with the experimental measurements was much better. Near separation the Perry and Schofield coordinates showed that the mean velocity profiles had reached an asymptotic profile. The mean velocity profiles were also observed to have a universal profile near separation, this however was not observed in the turbulent stress profiles. Instead the turbulent stresses showed a rise in stress level as the flow developed downstream. In the near wall region, the Reynolds stresses and turbulent production exhibited a decrease due to the decrease in the mean velocity gradient caused by the pressure gradient. As had been noted by other groups, the peak value of the Reynolds stresses and the turbulent production moved away from the wall due to the pressure gradient, which led to the production peak being located near the center of the boundary layer. Of the turbulent stresses, the streamwise normal stress was found to be more strongly affected by the adverse pressure gradient and was also more sensitive to the differences between the three skin friction cases. The Reynolds shear stress peak value was observed to be reasonably constant over much of the flow, although by the final measurement station, the value had increased significantly, with most of the increase occurring in close proximity to the final measurement station.

Another experimental study of an axisymmetric flow subjected to a strong adverse pressure gradient which led to separation was examined by Alving and Fernholz (1996). In this flow a small separation bubble developed and the flow was examined around the separation bubble as well as downstream of reattachment. The flow reattachment was in a region of mild adverse pressure gradient that then relaxed back to zero pressure gradient. The separation bubble examined here was shallow, corresponding to less than 5% of the boundary layer thickness. The boundary layer thickness and momentum thickness increased monotonically through the region of separation, reattachment and recovery, while the displacement thickness fell after reattachment. Three bubble lengths after reattachment, the log law became valid again, while the wake region remained distorted at the end of the measurement section. After reattachment the stress behavior in the outer part of the boundary layer showed the stresses relaxing, with the stress peaks dropping and the stress levels near the edge of the boundary layer growing. The peak in production continued to follow the peaks in the stress profiles, but also decreased in magnitude through the region of relaxation. The streamwise normal stress in the near wall region showed a decay in the peak value, so that the profile was mostly flat by the last measuring station. In addition a small near wall peak was evident, characteristic of the inner layer in a zero pressure gradient case. The wall normal and Reynolds shear stress never reached a plateau in the inner region of the boundary layer. They in fact did not change much in the relaxation region, except for the decaying of the peak values. The slow response of the Reynolds shear stress near the wall was unusual. For this flow the outer layer relaxed back to a typical unperturbed boundary layer, while the inner layer remained perturbed even at the final measurement location.

Finally, direct numerical simulations of two boundary layers subjected to strong adverse pressure gradient were performed by Skote and Henningson (2002). One of the boundary layers remained attached for all locations, while the other separated. The data gathered from this DNS were compared with a set of scalings developed analytically in the paper. For the adverse pressure gradient without separation, scaling by the friction velocity worked as did the scaling by a pressure gradient based velocity scale, $u_p = (\nu \frac{1}{\rho} \frac{dP}{dx})^{1/3}$. For the flow which separated, the only scaling that worked was the pressure gradient based scaling. The theoretical work showed that a universal self-similar velocity profile was possible only in two cases, zero pressure gradient and zero wall shear stress. Two velocity scales yielded two different velocity profiles, valid at the two limits of separation and zero pressure gradient, in between these two cases, the velocity profiles depended on the Reynolds number and the

pressure gradient in both the sub-layer and the overlap region. The scalings were as follows, for the friction velocity scaling in the sub layer:

$$u^+ = y^+ \tag{1.28}$$

and for the pressure velocity scale in the sublayer:

$$u_p = 1/2(y_p)^2 + \left(\frac{u_\tau}{u_p}\right)^2 y_p \tag{1.29}$$

For the adverse pressure gradient boundary layer, the logarithmic law of the wall held in the overlap region, while for the separated flow the velocity scale in the overlap region was:

$$u_p = \frac{1}{\kappa} 2\sqrt{y_p} + Constant \tag{1.30}$$

the half power law, where the constant was found to be -7. These equations, which were developed for the overlap region, were in qualitative agreement with the DNS data and were more consistent than any zero pressure gradient laws for describing the flow field.

For flows exposed to strong enough adverse pressure gradients to cause separation, a number of generalities can be made. For the mean flow, the logarithmic law of the wall was observed to be applicable upstream of separation for two dimensional flows, but not in the case of axisymmetric flow. The correlation of Perry and Schofield has been observed to hold in a wide range of flows near separation. The turbulent normal stresses in the near wall region are much larger than in a zero pressure gradient flow and develop large peaks away from the wall up until the point of separation. After separation, the flow field is generally very different from an attached boundary layer due to the large perturbations.

1.2.3 Complex and practical geometry flows

Adverse pressure gradient flows in practical geometries, which are often much more complex than those discussed above, have been studied by a few research groups as a method of answering questions about adverse pressure gradients in a practical engineering applications.

Tsuji and Morikawa (1976) examined a turbulent boundary layer subjected to a pressure gradient alternating in sign. The alternating pressure gradient varied twice between an adverse and favorable pressure gradient. The flow was examined in a zero pressure gradient region before being subjected to an adverse pressure gradient, a favorable pressure gradient,

another adverse pressure gradient and a final favorable pressure gradient. Even in the presence of the varying pressure gradient, the shape factor and wall shear stress continued to exhibit the behavior of a fully developed boundary layer for the first three regions of the flow. The mean velocity profile followed the logarithmic law of the wall for the first three regions of the flow, before the history of the flow started to have a large impact on the mean flow. The first adverse pressure gradient region showed the typical features of the turbulent stresses in an adverse pressure gradient flow. However, downstream the history of the flow had a large impact on the stresses, as the stresses did not match prior favorable pressure gradient stress data. In the second adverse pressure gradient region a knee point appeared between the maximum value of the Reynolds shear stress and the outer edge of the boundary layer. New Reynolds stresses were observed to develop inside the knee point due to the abrupt pressure gradient change. The alternating sign of the pressure gradient led the flow to depart from the equilibrium turbulent boundary layer and this departure became more pronounced farther downstream. In regions of adverse pressure gradient following a favorable pressure gradient, an internal boundary layer developed due to the sudden change in the shear stress gradient at the wall. The rapid changes of the pressure gradient in this flow led to very complicated structures downstream, however for the initial adverse pressure gradient flow, the results were very similar to those observed by other research groups in flows subjected to adverse pressure gradients prior to separation.

Webster et al. (1996a) examined the turbulent boundary layer developing over a two dimensional bump. The flow was subjected to a mild adverse pressure gradient and then accelerated up the bump under a strong favorable pressure gradient. On the other side of the bump the flow encountered a strong adverse pressure gradient. The mean velocity profiles did not follow the logarithmic law of the wall once the flow reached the top of the bump, most likely due to the strong favorable pressure gradient, which may have started to cause relaminarization. A large velocity deficit developed in the adverse pressure gradient. The turbulent stresses developed an internal layer in the favorable pressure gradient and this layer grew in the adverse pressure gradient. The knee point moved away from the wall in the adverse pressure gradient, much like the stress peaks in other adverse pressure gradient flows. The flow then recovered quickly on a flat plate downstream of the bump.

Webster et al. (1996b) examined a turbulent boundary layer developing over a swept bump. The flow was subjected to the same pressure gradients as in the previous experiment, along with cross flow. Again the mean velocity deviated from the log law for the region of

the adverse pressure gradient, most likely due to the upstream favorable pressure gradient. The turbulent stresses developed internal layers, which moved away from the wall in the adverse pressure gradient.

An increasingly adverse pressure gradient without separation was examined by Samuel and Joubert (1974). In this flow both $\partial P/\partial x$ and $\partial^2 P/\partial x^2$ were greater than zero. They found that for this type of flow the only model of the boundary layer that remained valid was the logarithmic law of the wall. The results were compared with the model of Perry et al. (1966) which includes a 'wall region' and a 'historical region'. This model led to three regions: a sublayer, a logarithmic layer and a half-power layer. Townsend's model based on a linear stress layer was also compared with the mean flow results. Since the shear stress did not exhibit a region of linearity, the model's failure was not surprising. Neither of these models adequately predicted the mean flow for the increasingly adverse pressure gradient. The Perry and Schofield model worked well once $\partial^2 P/\partial x^2$ became negative, such that the pressure gradient was no longer increasingly adverse. The streamwise normal stress in an increasingly adverse pressure gradient did not have the same large outer layer increase in turbulent intensity here. The mean velocity profiles showed excellent agreement with the logarithmic law of the wall. The shear stress distributions near the wall agreed reasonably with the values calculated using the method of Coles.

Complex engineering flows in axisymmetric geometries were summarized by Azad (1996), whose research in conical diffuser flows has continued for almost three decades. The experiments were performed in two conical diffusers, each with a divergence angle of 8°. The pressure distribution was initially favorable, then increasingly adverse and finally decreasingly adverse. The velocity defect profiles deviated significantly from Perry and Schofield's model even where the required condition on the shear stress was satisfied. The velocity defect was also found to differ from the results of Dengel and Fernholz, which were performed in an axisymmetric adverse pressure gradient boundary layer near separation. The stress peak, which developed near the wall at the diffuser inlet, was found to move outward as the flow progressed in the streamwise direction, in agreement with observations from two dimensional flows. The turbulence production at the inlet was maximum at the wall but as the flow developed, the peak shifted away from the wall into the core region of the flow where its value decreased before asymptoting to an constant value near the outlet.

The interaction of the wake of an airfoil with a boundary layer subjected to both curvature and adverse pressure gradient was studied by Tulapurkara et al. (2001). The results

presented examined the effects of pressure gradient and curvature on the flow, both together and individually. The Clauser pressure gradient parameter, β, was 0.62 for the adverse pressure gradient examined here. Both the curvature and pressure gradient were selected to be mild so as to avoid separation. The convex curvature was seen to suppress the boundary layer growth, while the adverse pressure gradient and the concave curvature each enhanced the boundary layer growth. The concave curvature was seen to enhance the boundary layer growth more than the adverse pressure gradient. Individually, the effects of curvature and pressure gradient were seen to be the same as observed by previous groups. The turbulent kinetic energy and shear stress increased with adverse pressure gradient. The magnitude of the change due to the convex curvature was more than that due to the adverse pressure gradient. The effects of concave curvature and adverse pressure gradient were nearly the same. Although the curvature parameters were nearly the same, the effect due to convex curvature was much larger than that due to concave curvature. When the pressure gradient and convex curvature were combined the result on the turbulent kinetic energy and the shear stress was greater than the sum of the two effects acting independently. The same was seen for the concave curvature and pressure gradient.

Olcmen et al. (2001) examined the flow outside of a wing/body junction. The boundary layer they examined was three dimensional, with a two dimensional boundary layer in the region approaching the wing/body junction. This flow was examined at two different momentum thickness Reynolds numbers, $Re_\theta = 5940$ and $23,200$. The mean velocity deficit profiles did not collapse in the outer region of the profiles in any coordinate system, which may have been due to the complexity of the flow. For the higher Reynolds number case, the Townsend structure parameter was shown to not correlate between any stations, while the parameter S:

$$\frac{1}{S} = \frac{\tau}{\overline{v'v'}} = \frac{\sqrt{\overline{u'v'}^2 + \overline{v'w'}^2}}{\overline{v'v'}} \tag{1.31}$$

was seen to correlate well for the outer region of the boundary layer even though the stress profiles varied along the direction of the flow. They noted that the streamwise normal stress, normalized by the friction velocity squared, for the higher Reynolds number was equal to or larger than for the lower Reynolds number case. Near the wall, the values were not very different for most of the stations and the differences may have been due to greater inactive motions for the high Reynolds number case. The wall normal stress profiles were very similar for $y^+ < 1000$. The shear stress increased in the outer layers and the maximum

stress locations moved away from the wall as the flow progressed. They noted that if the vorticity flux at the wall was similar for different Reynolds numbers, then the mean and Reynolds stress profiles would be the same for the inner layer. For this experiment, the non-dimensional pressure gradient and streamwise vorticity flux were equal for the two Reynolds numbers.

A combined experimental and numerical study of a turbulent boundary in an adverse pressure gradient was performed by Spalart and Watmuff (1993). The parameter β increased from 0 to 2 along the length of the flow. The experiments were run at low Reynolds numbers ($Re_\theta < 1600$) to allow for direct comparison between the direct numerical simulation (DNS) results and those of the experiment. The pressure coefficient distribution agreed very well between the experiment and the DNS and the integral parameters agreed reasonably well, although towards the end of the domain the DNS values dropped below the experimental values for both θ and δ^*, which led to the shape factor, H, falling well below the experimental values. For the shear stress the DNS was consistently higher than for the experiment. The structure parameter, a_1, agreed well between the experiment and DNS once the flow was firmly located in the adverse pressure gradient, however the authors noted that this agreement was slightly misleading since both the numerators and denominators in the equation for a_1 were off by approximately 15% between the experiment and DNS. The differences between the experiment and simulation may have been due to the very low Reynolds number. The flow was probably much more sensitive to initial condition effects at such low Reynolds numbers as compared to a fully turbulent case.

For complex engineering flows in adverse pressure gradients, the logarithmic law of the wall is once again observed to be valid. The Perry and Schofield correlation held for these flows as long as the pressure gradient was not increasingly adverse. The stresses once again developed a peak, which moved away from the wall as the flow developed.

1.2.4 Turbulence structure in adverse pressure gradient flows

The structure of the flow in adverse pressure gradient boundary layers has been examined by a number of groups through the use of a variety of techniques. There are a variety of parameters which are used to quantify the structure of a turbulent flow and the changes of these parameters in adverse pressure gradient flows, as well as the changes in the structure this implies, are described in this section.

Quadrant Analysis for Adverse Pressure Gradient Flows

The idea of using quadrant analysis of the u and v velocity fluctuations to examine the structure of the turbulence and the relative contributions of sweeps and ejections was introduced by Wallace et al. (1972). The four quadrants produce the following contributions to the flow: in quadrant 2, bursts or ejections; in quadrant 4, sweeps; in quadrant 1, outward interactions, where high speed fluid from the sweep is reflected back toward the central region; and in quadrant 3, inward interactions, where low speed fluid from the decelerated region is pushed back toward the wall. The ejections and sweeps were approximately equally probable at $y^+ = 15$, the location of maximum production, and each accounted for 70% of the total Reynolds shear stress in a zero pressure gradient boundary layer. The inward and outward interactions, each produced a negative contribution of 20%, which resulted in the net Reynolds shear stress. The two negative contributions were approximately equal over the region and by reexamining the films of Corino and Brodkey (1969), they were found to correspond to interactions between the sweeps and ejections.

Lu and Willmarth (1973) examined the structure of the Reynolds stress in a flat plate boundary layer. They reviewed a large number of previous data sets and concluded that the correlation coefficient $R_{uv} = \overline{u'v'}/\overline{u''v''}$ is near 0.45 for all zero pressure gradient boundary layers. Here the double prime is used to indicate the rms value of a fluctuating velocity component. They developed the concept of a hyperbolic hole of size H and then defined the contribution to the Reynolds shear stress of each quadrant (Q) as:

$$\left(u'v'\right)_Q = \frac{1}{N}\sum u'v'I_Q \tag{1.32}$$

where N is the number of samples acquired by the LDA and I_Q is an indicator function defined as:

$$I_Q = \begin{cases} 1, & |u'v'|_Q \geq Hu''v'' \\ 0, & otherwise \end{cases} \tag{1.33}$$

This concept allows one to ignore the contributions of small velocity fluctuations and consider only the contributions of structures, which produce large positive or negative values of the shear stress. As the hole size was increased, the contributions of quadrant 2 (bursts) became relatively more important. This showed that bursts were very important to the turbulent boundary layer. When H = 0, all events, both quadrant 2 and quadrant 4 (bursts and sweeps) were nearly constant across the boundary layer except near the wall and the

edge of the boundary layer. For most of the boundary layer the ratio of bursts to sweeps was constant, only near the wall was there a sharp rise, implying that near the wall, bursts were more dominant than throughout the rest of the boundary layer.

The turbulent structure of shear flows using quadrant analysis was examined by Brodkey et al. (1974). They also attempted to show that the structures observed by various groups, although called different names by each research group, were in fact the same flow structures. Brodkey et al. (1974) measured the contributions to the Reynolds stresses for the four different types of motion, as well as visually observing the events associated with these four motions. They noted that ejections and sweeps were more intense and of a larger scale than the interaction type motions. Outside the near wall region ($y^+ > 10$) the frequency of occurrence was the same. The ejections were 1/3 more intense than sweeps near the region of maximum Reynolds stress even though they lasted for 20% less time due to the larger average stresses. They also observed, using probability density distributions, that a decelerating flow led to more ejection motions and wallward interactions.

The turbulent structure in a boundary layer subjected to a strong adverse pressure gradient was examined by Krogstad and Skåre (1995). This study was a continuation of the work of Skåre and Krogstad (1994), where the pressure gradient was observed to effect the kinetic energy and shear stress, thus suggesting changes in the turbulence structure. The diffusion rate from the kinetic energy equation was much larger in a strong adverse pressure gradient and negative diffusion was observed in the inner layer, below the outer peak in the turbulent production. The authors performed quadrant decomposition to examine the importance of ejections and sweeps throughout the flow field, finding many differences between zero and adverse pressure gradient flows. Near the wall for all events, quadrant 2 events are comparable, while quadrant 4 events follow a similar trend but differences are noted. For strong events, ($H = 4$), very few quadrant 2 events were found near the wall for the adverse pressure gradient boundary layer and strong quadrant 4 events dominated the flow. In the presence of an adverse pressure gradient, turbulent motions directed towards the wall were much more frequent. Weak quadrant 4 events in an adverse pressure gradient boundary layer were dominated by short duration intense activity, while quadrant 2 events were slower and longer lasting. For a zero pressure gradient boundary layer, quadrant 2 and quadrant 4 events were similar for the inner half of the boundary layer, except very close to the wall, while for an adverse pressure gradient quadrant 4 motions were dominant. Adverse pressure gradient flows have more quadrant 1 and 3 contributions than zero pressure gradient

boundary layers, with quadrant 1 contributions dominating. For the outer region, quadrant 2 contributions were dominant for both flows. In zero pressure gradients, quadrants 2 and 4 were approximately equal in the inner part of the layer and quadrants 1 and 3 were negligible, while for an adverse pressure gradient, quadrants 1 and 4 contributed to the inner part of the layer and quadrants 2 and 3 were negligible. The turbulent motion in the outer part of the boundary layer for an adverse pressure gradient flow was more isotropic than the flow near the wall.

Nagano et al. (1998) studied a boundary layer subjected to a sustained adverse pressure gradient to examine the structure of the turbulence. Using quadrant analysis they showed that quadrant 2 and quadrant 4 events became equal and increased toward the wall and therefore the quadrant 1 and quadrant 3 events increased near the wall as well. This indicated that in an adverse pressure gradient, the transfers of energy through turbulent diffusion toward the wall became more dominant than in a zero pressure gradient flow.

Houra et al. (2000) examined the effect of an adverse pressure gradient on quasi-coherent structures in the turbulent boundary layer. Using the quadrant decomposition for H=0, they found that the frequencies of each motion were basically the same for zero and adverse pressure gradients. As H was increased, quadrant 2 and quadrant 4 motions exceeded quadrant 1 and quadrant 3 motions for zero pressure gradient flow while for adverse pressure gradients, quadrant 4 was dominant and quadrant 1 events occurred more frequently then quadrant 3 events. The contributions of coherent motions, especially from quadrant 2 decreased significantly in adverse pressure gradient flows.

Changes in structural parameters for Adverse Pressure Gradient Flows

The behavior of a turbulent boundary layer when subjected to sudden perturbations was reviewed by Smits and Wood (1985). They found that the logarithmic law of the wall applied for a wide range of adverse pressure gradients, up to those strong enough to cause separation. However, the structure parameter, a_1, and the mixing length were observed to change strongly in an adverse pressure gradient. The values were seen to decrease in adverse pressure gradients, with the amount of decrease dependent on the strength of the pressure gradient.

Bradshaw (1967a), in the three boundary layers in equilibrium discussed earlier, showed that the eddy viscosity was not constant in the outer portion of the boundary layer. In addition, he emphasized that in non-equilibrium boundary layers the eddy viscosity and mixing

length should not be assumed to be universal. The structure parameter, a_1, peaked about 80% of the way through the boundary layer, before decreasing near the outer edge. The importance of active and inactive motions was also examined. In the inner layer, the active universal motion produced the shear stress. In the outer layer, the inactive component, which produces velocity and pressure fluctuations, but not shear stress, was important. As the boundary layer developed in an adverse pressure gradient the inactive motions' intensity increased, which led to the decrease in a_1. The streamwise normal turbulent intensity was significantly larger than either the wall normal or the spanwise intensities and the peak value of the intensity increased as the pressure gradient was increased.

In the previously discussed equilibrium boundary layer near separation examined by Skåre and Krogstad (1994), the Townsend structure parameter, a_1, was observed to maintain a constant value, which was slightly lower for an adverse pressure gradient flow than for a zero pressure gradient flow. They also observed a dip in the outer region of the boundary layer. For the Reynolds stress correlation, $\overline{u'v'}/\overline{u''v''}$, they observed that the value was approximately the same for their flow near separation as it was for a zero pressure gradient case. In the mixing length model, they found that the slope near the wall started at the typical value of 0.41 at the beginning of the logarithmic layer, but rapidly increased to a value of 0.78. This was taken to imply a dependence on the pressure gradient.

Simpson et al. (1977) found the turbulent structure of their increasingly adverse pressure gradient flow to be similar to previously reported results. Upstream of separation, the Townsend structure parameter, a_1, was found to take on a value of 0.13 for the outer portion of the boundary layer, with smaller values in the near wall region. They added the effect of the normal-stress terms to the structure parameter by introducing a parameter, F, which was defined as:

$$F = 1 - \frac{\left(\overline{u'u'} - \overline{v'v'}\right)\frac{\partial U}{\partial x}}{-\overline{u'v'}\frac{\partial U}{\partial y}} \tag{1.34}$$

This factor compared the ratio of total production to shear production. According to their results the product, a_1F led to a value closer to 0.15, the value typical of zero pressure gradient flows. The new parameter, a_1F represented the ratio of the total turbulence that was produced by production mechanisms to the amount of turbulent energy that was actually produced.

In the axisymmetric flow of Alving and Fernholz (1996) in which a small region of separation developed, the structure parameter, a_1, as the flow approached separation was seen

to drop across the boundary layer. After reattachment a_1 rose rapidly to the characteristic zero pressure gradient level in the outer layer. However, in the inner layer the structure parameter remained small throughout the region of relaxation.

Elsberry et al. (2000) noted that the Reynolds stress correlation was not constant for an adverse pressure gradient flow and varied as the downstream distance increased, for their flow maintained on the verge of separation. The flow field was also anisotropic with the longitudinal stress component being 3 times that of the transverse component.

For a turbulent boundary layer in an adverse pressure gradient examined both experimentally and using DNS, Spalart and Watmuff (1993) noted that the streamwise normal intensity peak rose only slightly in the adverse pressure gradient, while the other components rose rapidly. The structure parameter, a_1, similar to earlier findings was seen to dip in the outer part of the boundary layer in the adverse pressure gradient.

1.2.5 Summary of experimental observations in adverse pressure gradient flows

Experimental investigations of adverse pressure gradient boundary layers have shown that the mean velocity profile develops a large wake region once the flow is subjected to an adverse pressure gradient, but the logarithmic law of the wall has been seen to remain applicable over a wide range of pressure gradients. The turbulent stresses have been seen to develop peaks, which move away from the wall as the flow progresses. These peaks are also seen in the turbulent kinetic energy production development. The structure parameter, a_1, dips in the outer part of the boundary layer for adverse pressure gradient flows. Quadrant analysis has shown that bursts and sweeps, quadrant 2 and 4 events, increase in the near wall region for adverse pressure gradient flows.

1.3 Computational work

Computational work in adverse pressure gradient boundary layers spans a wide range of methods and applications. While direct numerical simulation (DNS) will provide very well resolved results at low Reynolds numbers, it is not possible to run a DNS simulation on a practical high Reynolds number flow due to computational constraints. The work of Spalart and Watmuff (1993) shows the potential pitfalls of studies at such low Reynolds numbers. Other methods of closure have been developed for application in adverse pressure

gradient flows and their ability to provide accurate predictions will be discussed below.

1.3.1 Integral/Algebraic Techniques

The simplest techniques for closure are the integral boundary layer methods and algebraic eddy viscosity or mixing length techniques. However these techniques have not provided a lot of agreement between the modeled and experimental results. The difficulties associated with various forms of these models were well known even many years ago as described by Bradshaw (1967b). Integral methods use empirical fits to profile data, usually from low Reynolds number experiments, leading to problems at high Reynolds numbers. Mixing-length and prescribed eddy-viscosity methods in rapidly changing boundary layers have not been shown to work or produce accurate results in adverse pressure gradients.

Bradshaw et al. (1967) converted the turbulent energy equation into a differential equation for the shear stress using three empirical functions, which led to a refinement of the mixing length equation to account for diffusion and advection. The three empirical functions, assumed to change slowly in the streamwise direction, were: the structure parameter $a_1 = \tau/\overline{\rho q^2}$, taken to be constant with a value of 0.15; a length parameter, similar to the dissipation length, $L = (\tau/\rho)^{2/3}/\epsilon$; and a parameter $G = (\overline{pv}/\rho + 1/2\overline{q^2 v})/(\tau/\rho)(\tau_{max}/\rho)^{1/2}$ which was a diffusion function. Near the surface, the equation reduced to production balanced dissipation, so L became equal to the mixing length. Near the outer edge of the boundary layer, diffusion balanced advection and the equations defined the entrainment rate based on a_1 and G. The three empirical parameters were determined from Klebanoff's zero pressure gradient boundary layer and the model was applied to several equilibrium boundary layers, including a variety of favorable and adverse pressure gradients. The agreement with the mean flow and the shear stress profiles was very reasonable.

A variety of eddy viscosity and mixing length models were compared with experimental data from a number of sources by Galbraith and Head (1975). The models included the model developed by Thompson. Mean velocity profiles were fit using the profile family developed by Thompson:

$$\frac{u}{U_e} = \gamma_s \left(\frac{u}{U_e}\right)_{inner} + (1 - \gamma_s) \tag{1.35}$$

where γ_s was Sarnecki's intermittency function. These analytic functions were then used to determine the shear stress distribution and the mixing length. The Thompson profile included a number of regions to represent $(u/U_e)_{inner}$: the viscous layer, a blending region

and the log law region and thus failed when the pressure gradient was large, such as near separation, where the log law region was poorly captured. This model compared very well with the experimental data shown over a wide range of pressure gradients. Galbraith and Head (1975) then compared their model with a large number of other eddy viscosity and mixing length models. None of the models examined reflected the experimentally noted trends of an increase in the value of κ with increasingly adverse pressure gradient, and an increase in the maximum value of $\nu_T/U\delta^*$ for the outer region of equilibrium boundary layers in increasingly adverse pressure gradients. Of the models examined, the model of Cebeci and Smith (1974), accounting for pressure gradients, was the most realistic but still did not accurately portray the flow.

A new turbulence model for two dimensional turbulent boundary layers in strong adverse pressure gradient boundary layers based on a modification of a mixing length model was developed by Hytopoulos et al. (1997). The new model used the integrated turbulent kinetic energy equation to take into account the past history of the flow; the peak shear stress as a scaling factor, including the contribution due to the normal stresses; an empirical function to account for structural changes to the turbulence near separation, using a_1; and a shear stress profile model in the near wall region, since the shear stress does not equal the wall stress for strong pressure gradients. The shear stress distribution across the boundary layer was predicted using a mixing length formula, which contained an inner and outer portion along with a blending region. The agreement with experiments was at least as good, if not better than the previous models.

1.3.2 Two Equation Models

The most widely used differential eddy viscosity model is the k-ϵ model. This model has been modified in a number of ways to attempt to adequately predict experimental adverse pressure gradient data, however it is well known that the k-ϵ model has difficulties in predicting these flows correctly.

A number of k-ϵ and k-ω models for pressure gradient flows were compared by Wilcox (1993). The k-ϵ model was inaccurate in adverse pressure gradient flows due to its defect layer structure only being consistent with measurements in constant pressure layers. Low Reynolds number modifications to the k-ϵ model did not improve the model predictions in adverse pressure gradient flows. The k-ω model was shown to produce a defect layer

structure, which was consistent with the experimental measurements for all pressure gradients. For skin friction prediction, the k-ω model did an overall better job for favorable and adverse pressure gradients of all strengths.

Menter (1994) presented a new two-equation eddy viscosity turbulence model which combined aspects of both a k-ϵ and a k-ω model. This new model blended the k-ω model near the wall with the k-ϵ model in the outer layer to get the best parts of each model, avoiding some of the difficulties associated with each of them. A shear stress transport model was also developed from a modification to the eddy viscosity. The shear stress transport model was able to predict the reduction of the eddy viscosity due to the adverse pressure gradient better than any of the other models. While this new model showed small improvements over the k-ω model, the shear stress transport model showed large improvements to the predictive abilities of the model to match the experimental data of Driver (1991).

A modified k-ϵ model for complex adverse pressure gradient flows, eliminating the eddy viscosity through the use of three structural parameters, was developed by Chukkapalli and Turan (1995). They concluded that two equation models typically have trouble predicting turbulence fields in arbitrary adverse pressure gradient flows for a number of reasons: the normal stresses were neglected or poorly modeled in complex flows; the diffusion was inaccurately modeled as isotropic when large eddies were present in the flow; and the dissipation was improperly modeled as isotropic. Their modified model used three structure parameters, including a_1 that were determined empirically. Despite the empirical input, the new model did not improve the predictions substantially.

Some of the problems associated with the performance of the k-ϵ model in adverse pressure gradients were investigated by Rodi and Scheuerer (1986). Comparing the results of the k-ϵ model with a one-equation model showed that the one-equation model yielded better overall agreement with experimental results than the k-ϵ model. The poor performance of the k-ϵ model was found to be due to the ϵ equation and the empirical coefficients used in this model were found to be incompatible with the experimental observations of adverse pressure gradient flows. By changing these coefficients to better match the experimental results the overall prediction of the model was greatly improved.

Huang and Bradshaw (1995) developed a model for pressure gradient flow using the mixing length formula where the turbulent length scale was taken as proportional to the distance from the wall, and the velocity scale was derived from the local shear stress not the wall shear. For both two equation and Reynolds stress transport models the success in

predicting boundary layer flows with pressure gradients depended largely on the variable used for the length scale. The dissipation length led to incorrect velocity slopes in the log law region for pressure gradient flows. The variable $\omega = \epsilon/k$ seemed to be the best choice, although no physical reason was known.

1.3.3 Reynolds Stress Transport Models

Launder et al. (1975) developed the first Reynolds stress transport model in an attempt to remedy the poor performance of effective viscosity models in complex flows. The Launder et al. (1975) model and many subsequent second moment closure models solve transport equations for the Reynolds stress components, eliminating the need for an eddy viscosity. However modeling of many terms in the transport equations are required and empirical input is needed from either experiments or direct numerical simulations. A concern is that most of the data used are from low to moderate Reynolds number simulations and experiments. The models have not been well tested over a wide range of Reynolds numbers. Many variants of the original model have been proposed, some of them designed especially for adverse pressure gradient flows.

A second moment closure scheme with low Reynolds numbers and wall vicinity modifications was tested by Hanjalic et al. (1999). For a boundary layer flow in an adverse pressure gradient this scheme produced results that agreed well with those from two different experiments, Nagano et al. (1998) and Samuel and Joubert (1974). In particular, good agreement was observed in the regions where prior models had failed. The model reproduced the departure from the logarithmic law of the wall and the variation in the slope of the normalized turbulent stresses near the wall. Other complex flows in pressure gradients, including separation, were accurately predicted using this model as well.

1.3.4 LES and DES

Large eddy simulation is a method that attempts to reproduce the dominant large scale three dimensional, time dependent structure of the turbulence while modeling smaller scale motions. It was developed to alleviate the enormous computational resource requirements of direct numerical simulation while allowing computations at higher Reynolds numbers. However, high Reynolds number computations of wall bounded flows are complicated by the very small scales of the dominant eddies near the wall.

Mellen et al. (2003) summarized a large scale research effort to examine the use of large eddy simulation (LES) on the flow around an airfoil at relatively large Reynolds numbers. The airfoil configuration chosen had detailed experimental and direct numerical simulation results available and only slight trailing edge separation. Successful simulations using LES were possible but required well resolved near wall regions, which in turn required large numbers of grid cells. They concluded that RANS may still produce superior results. Coarse near wall grids with wall functions produced disappointing results. With highly resolved LES, the simulation results were in reasonable agreement with the experimental results including those in the region of separation.

Detached eddy simulation (DES) is a hybrid RANS-LES technique where RANS is used in attached boundary layers where it is well behaved and LES is used in detached flows to capture large scale instability vortices. The technique was introduced by Spalart et al. (1997) and is still under active development, with the major issue being how the two methods should be blended.

Nikitin et al. (2000) described the use of DES for a channel flow. Their results show that DES of non-separating flows leads to difficulties, which must still be addressed. The solution was stable over a large range of Reynolds numbers using a coarse grid, and the results showed that the turbulence was maintained in the channel and the results were reasonably accurate. The method produced an increase in the mean velocity above the expected values in the region where the near wall and outer layer models were blended. In particular, the constants in the logarithmic law of the wall were far different for this simulation than the traditionally accepted values. The stresses also behaved as expected from this model. DES showed promise here, although more needs to be addressed in the region where the LES and DES are blended.

Breuer et al. (2003) compared LES, DES and RANS for a separated flow around a flat plate at high incidence. The simulations were performed on the same grid using the same code to ensure an accurate comparison. RANS did not capture the unsteady shedding behavior of the plate. DES and LES both produced the asymmetric vortex shedding motion expected for this flow, with the DES results matching the LES results quite well. The DES results did not accurately capture the Kelvin-Helmholtz instability, while the LES results did. The DES results also did not accurately represent the free shear layer, due to the choice of sub-grid scale model. A modified sub-grid scale model was applied and the LES and DES results were much closer.

1.3.5 Comparisons of various types of models

Four popular eddy viscosity turbulence models for adverse pressure gradient flows, both separated and attached flows, were compared by Menter (1992). The models included the Baldwin-Lomax zero equation model, the Johnson-King half equation model, the Baldwin-Barth one equation model and the Wilcox (k-ω) two equation model. All four models did a reasonable job at computing the skin friction for the increasingly adverse pressure gradient flow by Samuel and Joubert (1974). The prediction of separation for the flows of Driver (1991) led to more difficulties for all the models as the prediction of the location of separation and the length of the separation region predicted varied between the models. The algebraic method led to the least accurate results. The Johnson-King model gave the best overall agreement with the experimental results, but led to high peak shear stress values, while predicting the shear stress and velocity profile shape well. The k-ω model overpredicted the turbulent shear stress, while predicting the mean velocity profiles well. This overprediction appeared related to the relationship for the eddy viscosity, which failed to account for advection of the shear stress. The model was significantly improved by fixing this deficiency.

A comparison of four common turbulence models for an equilibrium turbulent boundary layer was performed by Henkes (1998). The four computational models examined were the algebraic model of Cebeci and Smith, the two equation k-ϵ model of Launder and Sharma, the two equation k-ω model of Wilcox and the differential Reynolds stress model of Hanjalic et al. (1999). The turbulent boundary layer scalings for each model were compared. All four models asymptoted to the same classical scalings for the inner and outer layers of the turbulent boundary layer with an adverse pressure gradient. The shape of the logarithmic law of the wall in the inner layer was found to be independent of the value of β at large Reynolds number. The outer layer asymptoted to the defect layer equation of Tennekes and Lumley and not the defect layer equation of Wilcox, which was only valid for $\beta = 0$. Comparisons of the models with the data of Skåre and Krogstad (1994) showed that the differential Reynolds stress model was superior, but the algebraic and k-ω models were reasonably accurate for this flow. Only the k-ϵ model examined here led to large deviations, due to overprediction of the wall shear stress.

Very recently Yorke and Coleman (2004) compared some common turbulence models for adverse pressure gradient flows. A recent DNS of an idealized adverse pressure gradient boundary layer was used as the data for comparison for four common turbulence models.

The DNS was performed in an uncomplicated parallel-flow geometry where the spatial development due to an adverse pressure gradient was added using a temporally developing straining of the channel. This model duplicated a number of adverse pressure gradient flow characteristics, including the outer layer increase in turbulence intensity and the near wall reduction in these same parameters. The four models which were tested were the Baldwin-Lomax algebraic model, the Spalart-Allmaras one-equation eddy-viscosity transport model, the Launder-Sharma low-Reynolds-number k-ϵ model and the Menter Shear Stress Transport (SST) model. The Baldwin-Lomax model was generalized with the Cebeci-Smith two-layer mixing length closure. First the models were run with no channel strain to observe how they performed on two dimensional plane channel flow. All four models performed reasonably in this case, although all but the algebraic model were tuned for external boundary layers and thus had some difficulties with the channel. The algebraic model exaggerated the wake, leading to a slightly too large shape factor for this flow. The eddy viscosity model gave the best overall agreement. The Reynolds shear stress results for this case were all in fairly good agreement. The k-ϵ model shear stress peak was least accurate. The strained channel was then examined. The algebraic model underpredicted the separation time, while the k-ϵ model delayed separation, as was expected based on its well known tendencies to delay or even miss separation. The eddy viscosity model and the SST model were the best at predicting the separation time. The best prediction of the Reynolds shear stress profile was given by the eddy viscosity model and SST model, but both left much room for improvement.

Overall, algebraic models do not predict adverse pressure gradient data well, except when the constants are tuned to the particular flow being studied. The k-ϵ model is not a good predictor in these flows as well, due to its difficulties dealing with the adverse pressure gradient in the ϵ equation. LES is becoming more useful in its ability to predict these types of flows, but still requires too many grid points in the near wall region to make it practical. For now, the Reynolds Stress Transport models give the best results, but even these models are not yet capable to matching the flow field in even very basic adverse pressure gradient flows.

1.3.6 The Attached Eddy Model

In a different approach to modeling adverse pressure gradient flows, Perry's group and successors have worked for quite a few years on using an attached eddy model, based on the

original idea of Townsend, of attached eddies. The original work used the attached eddy hypothesis to model zero pressure gradient flows.

Perry and Marusic (1995) extended the attached eddy hypothesis originally developed for zero pressure gradients to flows with arbitrary pressure gradients, both favorable and adverse. Two types of attached eddies were responsible for the prediction of the turbulent kinetic energy and the Reynolds shear stresses. Type A eddies are horseshoe type vortex lines that extend to the wall. These were used in the original studies to model zero pressure gradient flows and capture the universal wall structure of the mean flow in the log law. Type B eddies, were added to represent the wake component of the mean flow and the non universal turbulence intensities in the region near the wall. For type B eddies, the vortex lines do not reach the wall and undulate in the spanwise direction. Although the legs of the type B eddies do not extend to the wall, they are still attached eddies, in terms of Townsend's work, since their length scales were related to the height above the wall. Perry and Marusic (1995) found that using only type A eddies it was not possible to accurately match the various Reynolds stress profiles in equilibrium adverse pressure gradient flows. They found that type B eddies were necessary to properly predict the flow. The choice of shapes for the types of eddies was based on trial and error. This model could calculate the streamwise normal stresses and the spectra once the development of the mean velocity field and Reynolds shear stress field were known. Agreement with adverse pressure gradient data was improved by the addition of type B eddies, but left room for improvement.

In an extension of the previous work, the modified attached eddy work was tested on flows in non-equilibrium pressure gradients by Marusic and Perry (1995). They measured the mean flow, turbulent stresses and spectra for a non-equilibrium mild adverse pressure gradient turbulent boundary layer to produce the data necessary to test the attached eddy model. The attached eddy model using both type A and type B eddies agreed quite well with the new experimental data. For completeness it was necessary to include fine scale dissipating motions and other detached motions, which at this time was being done empirically for the logarithmic wall region.

Perry et al. (2002) further extended the attached eddy model to compute the entire flow field from a given initial input, rather than requiring the mean velocity and shear stress development to be known. A closure scheme based on the shear stress information for the streamwise evolution of a turbulent boundary layer in equilibrium was expanded to include non-equilibrium flows. The closure scheme developed was based on the log law of the

wall, the law of the wake, continuity and the momentum differential and integral equations. This led to an analysis that showed that the mean velocity profiles and the shear stress profiles were functions of four parameters: $S = \frac{U_e}{U}$, a skin friction parameter; Π; β; and $\zeta = S\delta_{99}\frac{d\Pi}{dx}$, a non equilibrium parameter. The attached eddy hypothesis was used to form a relationship between β and Π for $\zeta = 0$, and the shear stress profiles were assumed to form a two parameter family on which basis shear stress matching was performed. A tentative form of the closure equation was given and used to predict the flows described in Marusic and Perry (1995) with reasonable success.

1.4 Scaling of Mean Velocity and Turbulence

1.4.1 Mean Flow Scaling

The scaling of the mean velocity profile has been examined extensively. Questions continue to arise about the validity of the logarithmic law of the wall for adverse pressure gradient flows and whether a power law velocity profile is more appropriate. New velocity deficit scalings, which collapse the outer region of the flow, have been proposed. In addition, much work has focused on the appropriate mean velocity scale for the wake region of an adverse pressure gradient flow.

Standard Mean Velocity Profiles

The traditional method of describing the flat plate boundary layer was to divide it into two separate layers, the inner layer and the outer layer. The mean velocity in the inner layer depends on the fluid properties (ρ, ν), the distance from the flat plate (y) and the wall shear (τ_{wall}). Non-dimensional inner variables are defined as:

$$U^+ \equiv \frac{U}{u_\tau} \tag{1.36}$$

$$y^+ \equiv \frac{y}{\nu/u_\tau} \tag{1.37}$$

where ν/u_τ is called the viscous length scale and u_τ is the friction velocity, defined as:

$$u_\tau \equiv \sqrt{\frac{\tau_{wall}}{\rho}} \tag{1.38}$$

For the inner layer a universal functional form of the velocity profile should have the form:

$$U^+ = f(y^+) \tag{1.39}$$

Very near the wall the viscous shear stress is dominant and the shear stress is assumed to be uniform and equal to the wall shear stress.

The function f can then be derived by integration of:

$$\mu \frac{dU}{dy} = \tau_{wall} \tag{1.40}$$

yielding:

$$U^+ = y^+ \tag{1.41}$$

This relationship holds in the viscous sublayer of a zero pressure gradient boundary layer, but does not hold further from the wall when the turbulent shear stress is significant.

For the outer region of the boundary layer the flow is more inviscid in character, although the turbulent stresses are still important. The mean velocity is typically expressed as a deficit from the freestream velocity, $(U_e - U)$. This deficit is traditionally assumed to be proportional to the friction velocity, u_τ and the length scale for the outer layer is taken to be the boundary layer thickness, δ_{99}. Under these assumptions, the universal functional form for the outer layer is:

$$\frac{U_e - U}{u_\tau} = g(\eta) \tag{1.42}$$

where $\eta = y/\delta_{99}$. Between the inner and outer layers there must be a region of overlap in which the mean velocity distributions match. The velocity gradients for the inner and outer layer are written:

$$\frac{dU}{dy} = \frac{{u_\tau}^2}{\nu} \frac{df}{dy^+} \tag{1.43}$$

and:

$$\frac{dU}{dy} = \frac{u_\tau}{\delta_{99}} \frac{dg}{d\eta} \tag{1.44}$$

These gradients must be equal in the overlap region. Multiplying them both by y/u_τ and equating them leads to:

$$y^+ \frac{df}{dy^+} = \eta \frac{dg}{d\eta} \tag{1.45}$$

The left hand side is a function of y^+ only and the right hand side is a function of η only, so the two sides must be equal to a constant, which was chosen to be $1/\kappa$, where κ was a universal constant known as the Karman constant. This leads to:

$$y^+ \frac{df}{dy^+} = \eta \frac{dg}{d\eta} = \frac{1}{\kappa} \tag{1.46}$$

Integrating this equation yields two profile descriptions for the overlap region:

$$\frac{U}{u_\tau} = \frac{1}{\kappa} \ln \frac{y u_\tau}{\nu} + B \tag{1.47}$$

the logarithmic law of the wall, with B as a known constant of integration typically taken to be about 5.0 and:

$$\frac{U_e - U}{u_\tau} = \frac{1}{\kappa} \ln \frac{y}{\delta_{99}} + C \tag{1.48}$$

the velocity deficit law for the outer layer where C is another integration constant. Note that this logarithmic velocity profile only occurs in the overlap region, a relatively small fraction of the total boundary layer thickness. The logarithmic law of the wall could also be derived entirely from a dimensional analysis based on the work of Prandtl and von Karman (1921). This analysis showed that in the overlap region the only possible length scale was y, since the location was too far from the wall for a viscous length scale to be appropriate and too far from the outer region of the boundary layer for the boundary layer thickness to be useful either. The velocity scale must be u_τ and therefore the velocity gradient in the overlap region was given as:

$$\frac{dU}{dy} = \frac{u_\tau}{\kappa y} \tag{1.49}$$

based on dimensional arguments. The constant κ was added as a constant of proportionality and from this equation the law of the wall could be computed as before.

Power law profiles have been used as an alternative to the log law. This description came from curve fitting the experimental data to an equation of the form:

$$u^+_{power} = C_{power}(y^+)^\alpha \tag{1.50}$$

where C_{power} and α are Reynolds number dependent (Schlichting (1979)). A discussion below will comment on the validity of these two descriptions of the inner layer.

The outer layer mean velocity profile for a boundary layer subjected to a pressure gradient was expanded by Coles (1956) to include the law of the wake. The mean velocity profile was modified so that the outer layer portion depended not only on the boundary layer thickness, but also on the parameter Π, which will be described further below. This led to:

$$\frac{U}{U_\tau} = f\left(\frac{y u_\tau}{\nu}\right) g\left(\frac{y}{\delta_{99}}, \Pi\right) \tag{1.51}$$

This mean velocity profile could then be rewritten based on the examination of a large amount of experimental data as:

$$\frac{U}{u_\tau} = f\left(\frac{y u_\tau}{\nu}\right) + \frac{\Pi}{\kappa} w\left(\frac{y}{\delta_{99}}\right) \tag{1.52}$$

where Π was a profile parameter, which depended on the strength of the wake in a particular flow and was thus variable. The function $w(\frac{y}{\delta_{99}})$ was called the wake function and it was common to all two dimensional boundary layer flows. The values of the wake function were tabulated in Coles' paper, but it is often approximated using the form:

$$w\left(\frac{y}{\delta_{99}}\right) = 2\sin^2\left(\frac{\pi y}{2\delta_{99}}\right) \tag{1.53}$$

The parameter Π could also be empirically related to the Clauser pressure gradient parameter β (Durbin and Pettersson Reif (2001)):

$$\Pi = 0.8\left(\beta + 0.5\right)^{3/4} \tag{1.54}$$

Mean Flow Inner Layer Description

For many years there has been disagreement over the most appropriate description of the inner layer of the mean flow profile. In addition to the question over whether the logarithmic or power law description was better, the values of the constants chosen for either of these descriptions were also debated.

Huffman and Bradshaw (1972) examined the effect of low Reynolds number on the von Karman constant. Coles and Simpson had both examined the same low Reynolds number data for a turbulent boundary layer and come to contradictory conclusions. Coles' approach led to a constant value of κ, while Simpson found that κ varied with Reynolds number. The optimization used by Huffman and Bradshaw involved the mixing length distribution given by:

$$l^+ = \kappa y^+\left(1 - exp\left[\frac{-\tau^{1/2}y^+}{A^+}\right]\right) \tag{1.55}$$

which for large values of y^+ led to the commonly used mixing length, $l^+ = \kappa y^+$. They found that using a search algorithm, the value of κ had no trends with Reynolds number, although the value of A^+, which led to the constant C did exhibit Reynolds number effects. The optimum value of κ was found to be 0.41 and it was assumed constant for the rest of the analysis. The value of A^+ appeared to be a universal function of the gradient of the shear stress.

A wall boundary layer over a range of Reynolds numbers was examined by Andreopoulos et al. (1984). Small Reynolds number effects were noted for the mean velocity profile in the buffer and log law region. The Karman constant was found to be independent of Reynolds number, while the additive constant B decreased slightly for increasing Reynolds number.

Using the method of incomplete similarity, Barenblatt (1993a) developed a scaling law for the mean velocity distribution in fully developed turbulent shear flows. For the logarithmic law of the wall scaling, the assumption is that at large enough local Reynolds numbers and sufficiently large flow Reynolds numbers the velocity gradient does not depend on the molecular viscosity. The new scaling law assumed instead that the dependence of the velocity gradient on the molecular viscosity is a power law behavior when the flow and local Reynolds numbers are large enough. The resulting law was compared with the traditional logarithmic law of the wall. The new scaling law was assumed to be dependent on the local Reynolds number and for a pipe flow led to:

$$U^+ = \left(\frac{1}{\sqrt{3}} \ln Re_d + \frac{5}{2}\right) \left(y^+\right)^{\frac{3}{2 \ln Re_d}} \tag{1.56}$$

The two mean velocity scaling laws were equally valid for the data examined in this paper.

In a companion paper Barenblatt (1993b) used the above defined scaling law and compared it to the data of Nikuradze to determine the necessary constants and confirm its accuracy. The conclusion was that the scaling law proposed above must be compared with other data to determine if it performed better than the log law or not. Barenblatt et al. (2000) expanded their prior scaling for turbulent pipe flow to turbulent boundary layers with good agreement. They started by defining a new Reynolds number:

$$Re_\Lambda = \frac{U_e \Lambda}{\nu} \tag{1.57}$$

where Λ was a particular length scale that led to the same scaling law they determined for pipe flow with the same values for the constants. This Reynolds number was also defined as:

$$Re_\Lambda = \sqrt{Re_1 Re_2} \tag{1.58}$$

where the two Reynolds numbers, Re_1 and Re_2 should have the same values theoretically, but due to uncertainties in measured quantities were found to be slightly different. To determine the two Reynolds numbers it was necessary to solve the following equations by fitting the data:

$$\frac{1}{\sqrt{3}} \ln Re_1 + \frac{5}{2} = A_1 \tag{1.59}$$

and:

$$\frac{3}{2 \ln Re_2} = \alpha_1 \tag{1.60}$$

which came from the functional forms of the equations given below:

$$U^+ = A_1 \left(y^+\right)^{\alpha_1} \tag{1.61}$$

for the region adjacent to the viscous sublayer and:

$$U^+ = A_2 \left(y^+\right)^{\alpha_2} \tag{1.62}$$

for the region above the previous region. The location where these two regions join was dependent on the Reynolds number of the flow. In these equations the values of A_1, A_2, α_1 and α_2 were all determined from the fitting of experimental data. The new universal scaling law proposed by Barenblatt et al. (2000) was then given as:

$$\psi = \frac{1}{\alpha} \ln \left(\frac{2\alpha U^+}{\sqrt{3} + 5\alpha} \right) = \ln y^+ \tag{1.63}$$

where α was given as:

$$\alpha = \frac{3}{2 \ln Re_\Lambda} \tag{1.64}$$

Plotting experimental data using this scaling produced a bisectrix when plotted as $\ln y^+$ versus ψ. Using a variety of available experimental data, they showed that this scaling law accurately described the mean velocity distribution in the region adjacent to the viscous sublayer. For the region above that region the power law description was not universal, instead depending on freestream turbulence levels.

For turbulent flows subjected to pressure gradients, Huang and Bradshaw (1995) examined the logarithmic law of the wall. The logarithmic law of the wall was found to be accurate for adverse pressure gradients mean velocity profiles almost up to the point of separation.

By examining a large set of experimental data, Buschmann and Gad-el Hak (2003) were able to compare the power law and logarithmic law scaling of the turbulent boundary layer. Using a variety of data sets and the method of fractional difference, they compared the log law and the power law proposed by Barenblatt. They found that the two laws did not cover the same region of the overlap zone. The log law covered an inner region between the buffer zone and a region they called the common region where both the power law and log law appeared to hold. The power law covered this common region and extended up into the wake region as well. They found that in the common region where both laws held, neither could be selected as superior to the other using this method. They also noted that there

was not a second power law zone in the wake region and that data could be fit better in the outer region if a wake function was added to the inner law to complete the profile.

The choice of inner layer model for the mean velocity profile is still open for discussion. From the most recent work, the power law and logarithmic law both appear to hold for slightly different regions of the boundary layer and thus may both be used in scaling and modeling of the flow. In addition, the choice of the most appropriate constants for either model remains open, although standard values for the logarithmic law of the wall appear to be valid over a wide range of flows.

Velocity Deficit/Defect Scaling

Perry and Schofield (1973) found that the mean velocity profiles for an adverse pressure gradient flow collapsed onto a velocity defect profile of the general form of:

$$\frac{(U_1 - U)}{U_s} = f(\eta) \tag{1.65}$$

where U_1 was the local freestream and U_s was a characteristic velocity scale of the outer flow. The parameter $\eta = y/\Delta$ where Δ was a length scale, which could be derived from:

$$\Delta = \left(\frac{U_1}{U_s}\right)\left(\frac{\delta^*}{C}\right) \tag{1.66}$$

using the displacement thickness and a universal constant C:

$$C = \int_0^\infty f(\eta) d\eta \tag{1.67}$$

This set of equations was found to be valid when the maximum shear stress in the flow profile was 1.5 times larger than the wall shear stress. The inner regions of all the velocity profiles collapsed onto a single curve using the relationship:

$$\frac{\partial\left(\frac{U}{u_\tau}\right)}{\partial\left(\frac{y}{e}\right)} = f_1\left(\frac{y}{e}\right) \tag{1.68}$$

Traditional theory calculations of e, a length scale, did not work and the authors found that:

$$e = \frac{L u_\tau^2}{U_{max}^2} \tag{1.69}$$

worked, where L was the height of the maximum value of the shear stress. An overlap region was then defined between the two velocity profiles, this led to:

$$\frac{U_s}{U_{max}} = \left(\frac{J}{2K}\right)\left(\frac{\Delta}{L}\right)^{1/2} \tag{1.70}$$

where K was a universal constant and J was the slope of the straight portion of the mean velocity profile when plotted as U/u_τ versus $(y/e)^{1/2}$. The length scale, Δ, could be expressed as $\Delta = 2.86\delta^* U_1 U_s$. The half power law mean velocity profile could then be written as:

$$\frac{U}{U_1} = 0.47\left(\frac{U_s}{U_1}\right)^{3/2}\left(\frac{y}{\delta^*}\right)^{1/2} - \frac{U_s}{U_1} + 1 \tag{1.71}$$

where U_s could be found from:

$$U_s = 5.68\left(\frac{\delta^*}{L}U_e\right)^{1/3} {U_{max}}^{2/3} \tag{1.72}$$

Mean velocity profiles from a number of experiments were compared to equation 1.73. When the maximum shear stress was less than 1.5 times larger than the wall shear stress, the similarity proposed here failed, and the zero pressure gradient defect law based on u_τ was approached.

The mean flow in a turbulent pipe was examined by Zagarola and Smits (1998) to produce an appropriate mean flow deficit scaling. They found that the log law did not exist for pipe Reynolds numbers less than 400,000. They also noted that a power law was a better fit to the region that was located outside the linear near wall region and before the log region. This power law showed that viscous effects were important out to a y^+ of 500. They observed that as the Reynolds number increased the flow went from power law to log law dependence in the overlap region. There was a region of Reynolds numbers in which both a power and log law existed. Based on the new proposal for the overlap region between the power and log law, a new velocity scale was proposed $(U_{cl} - \overline{U})$ as the outer velocity scale. Using this scaling, they showed that the velocity profiles in the outer layer collapsed much better than using the traditional scale of u_τ for Reynolds numbers greater than 31,000. The collapse was not so good for Reynolds numbers below 13,000 since an overlap/power law region did not exist until this point and therefore similarity would not yet be complete between the profiles. They expanded this analysis to the boundary layer, by replacing $(U_{cl} - \overline{U})$ with $U_e\frac{\delta^*}{\delta}$ based on a mass flux deficit analysis.

An asymptotic analysis of the mean flow of a boundary layer subjected to a strong adverse pressure gradient was performed by Afzal (1983). This asymptotic analysis used two non-dimensional parameters:

$$R_p = \frac{\delta U_p}{\nu} \tag{1.73}$$

and:

$$\Lambda = \frac{\tau_w}{\delta p_x} \tag{1.74}$$

where:

$$U_p = \left(\frac{\nu p_x}{\rho}\right)^{1/3} \tag{1.75}$$

Inner and outer layer equations were developed and matched. The resulting mean flow equation for the velocity profile showed a half power law form. This formulation was then compared with experimental data from a variety of sources and shown to exhibit a substantial half power region when plotted as U/U_p versus $\sqrt{(yU_p/\nu)}$.

Skote and Henningson (2002) examined the use of a pressure gradient velocity scale for a flow near separation. The use of the friction velocity was not appropriate since near separation it approached zero. Therefore a pressure gradient velocity was used:

$$U_p = \left(\nu \frac{1}{\rho}\frac{dP}{dx}\right)^{1/3} \tag{1.76}$$

This was done instead of defining an outer scaling, since the definition of an outer scale must be done a posteriori, while this scaling may be defined based on the flow.

Outer Layer Scaling

In a recent work, Castillo and George (2001) performed a similarity analysis for pressure gradient flows which led to a parameter:

$$\Lambda = \frac{\delta}{\rho U_\infty^2 \frac{d\delta}{dx}}\frac{dP}{dx} = \frac{\delta}{U_\infty \frac{d\delta}{dx}}\frac{dU_\infty}{dx} \tag{1.77}$$

that could be used to describe the outer flow of the turbulent boundary layers. This parameter led to only three separate velocity profiles, one each for favorable, adverse and zero pressure gradients. Starting with the turbulent boundary layer equations given by Townsend for high Reynolds number and pressure gradient, the authors applied a similarity type solution, which showed that the outer equations permitted full similarity and a solution was found for zero pressure gradient. Additional similarity requirements were required for pressure gradients and these led to the relationships $\delta \sim U_\infty^n$ and Λ constant for similarity. These two relationships together led to an explicit relationship for $n = -1/\Lambda$ for equilibrium boundary layers. Based on a wide variety of previous data in pressure gradient boundary layers, the parameter Λ could be seen to take on three distinct values, 0.22 in adverse

pressure gradients, -1.92 in favorable pressure gradients and 0 in zero pressure gradient boundary layers. The mean velocity profiles were then shown to collapse in the outer layer using the Zagarola and Smits scaling.

Wake Region Scaling

Bernard et al. (2003) examined an adverse pressure gradient boundary layer and showed that the logarithmic law of the wall fit the mean velocity data well, although as typical of adverse pressure gradient boundary layers as the wake became more pronounced the region over which the logarithmic law of the wall was applicable decreased. The wake for this flow did not follow any of the typical wake profiles, so a new model was developed. The inner wake developed a linear profile based on a half-power mixing length law and required a new length scale given as:

$$y^* = \left(\frac{y}{\delta^*}\right)\left(\frac{U_e}{u_\tau}\right) \tag{1.78}$$

The velocity profile expression followed the work of Perry and Schofield using a velocity scale U_s calculated in a similar manner to the work of Dengel and Fernholz. The mean velocity scale was still dependent on u_τ but was modified, including the use of a new pressure gradient parameter:

$$\beta' = \beta\frac{u_\tau}{U_e} \tag{1.79}$$

The velocity profile at the last three stations in their experiment tended to a common linear inner wake profile:

$$u^+ = (1/\chi)\left[\sqrt{y^*\left(1+\beta' y^*\right)} + \left(1/\sqrt{\beta'}\right)\ln\mid \beta'\sqrt{y^*} + \sqrt{1+\beta' y^*}\mid\right] + D \tag{1.80}$$

where χ was found to be $1 + 0.9\beta'$ based on a least squares fit of the data.

1.4.2 Turbulent Stress Scaling

Much less work has focused on the scaling of the turbulent stresses when compared with scaling the mean velocity. However due to advances in experimental measurement techniques in the past decades much more turbulent stress data is available, which can be used to develop new turbulent stress scalings. Many of the current turbulent stress scalings for adverse pressure gradient flows are very restrictive or applicable only in very specific flows.

Mixed Scaling for Flat Plate

An investigation by Mochizuki and Nieuwstadt (1996) studied the Reynolds number dependence of the peak in the streamwise normal turbulent intensity using a great deal of previously published boundary layer data from a large number of different research groups. Within the scatter of the data the peak value of the streamwise normal turbulence intensity was found to be constant with a value of $\overline{u_{max}'^2}^+ = 7.34$. Initially a weak Reynolds number dependence was proposed, but the use of a constant value fit the data equally well. Using a least squares fit, the location of the peak value was found to vary as a function of Reynolds number as $y^+|_{peak} = 0.00017Re_\theta + 14.4$. The value of the intensity at the peak location was the same for internal and boundary layer flows, which suggested that the near wall region of fluctuations were locally in equilibrium with the shear stress and the inactive motions which were outer layer in origin were not an influence on the intensity.

The Reynolds number effects for a flat plate boundary layer over a range of momentum thickness Reynolds numbers from $Re_\theta = 1400 - 31,000$ were examined by DeGraaff and Eaton (2000) who reached a different conclusion than Mochizuki and Nieuwstadt (1996). The Reynolds shear stress $\overline{u'v'}$ and the wall normal stress $\overline{v'v'}$ collapsed well in the traditional inner scaling using ${u_\tau}^2$. The streamwise normal stress $\overline{u'u'}$ however did not collapse in the traditional scaling. A new mixed scaling of $U_e u_\tau$ was found empirically to collapse the streamwise normal stress. While it was not possible to support this new scaling using classical arguments, new work by Marusic and Kunkel (2003) led to a possible explanation for its validity. In addition, DeGraaff and Eaton (2000) used the energy balance as a possible explanation, since for a constant density flow the total power dissipation of a boundary layer scales with $U_e {u_\tau}^2$, which depends on both the inner and outer velocity scales.

Metzger et al. (2001) reexamined the results of Klewicki and Falco (1990) and showed that the collapse in this new scaling also held for those experiments, which were run at very high Reynolds numbers, up to $Re_\theta = 5,000,000$.

Attached Eddy Scaling

The streamwise normal stress in a zero pressure gradient boundary layer and how it scales based on the attached eddy hypothesis and Reynolds number similarity was examined by Marusic et al. (1997). The formulation for the streamwise normal stress was extended from the previous work by Perry and colleagues by treating the stress similarly to

the mean flow, which led to two regions of deviation from the straight line portion of the profile, one due to viscous effects and the other due to the wake. The viscous deviation was made up of two parts: the viscous correction, which was isotropic, and of the Kolmogorov eddy-type cut-off and the contribution to the anisotropic behavior as the boundary was approached due to the lack of representative attached eddy scales below the smallest scale. The wake deviation was assumed to be universal as required by Townsend's Reynolds number similarity hypothesis and the self preserving flow assumption for zero pressure gradient boundary layers. A similarity formulation for the entire region of the boundary layer outside the viscous buffer zone was proposed and compared with experimental data over a wide range of Reynolds numbers, showing reasonable agreement for moderate and high Reynolds numbers.

This work was then extended by Marusic and Kunkel (2003) to include the entire boundary layer. As more data has become available in the inner region of the boundary layer it has been noted that the streamwise normal stress peak increased as the Reynolds number increased as: $max(u^+_{rms}) = 1.6 + 0.28log(Re_\theta)$. Based on the assumption that the outer layer turbulence forces the viscous buffer zone and sublayer as a function of Reynolds number, the model was extended to the near wall viscous region. A possible functional form of this extension was proposed and then used to calculate profiles to compare with experimental results. This agreed well with the experimental results for a wide range of Reynolds numbers. The model captured the increase in the streamwise normal stress peak with increasing Reynolds number. This lent support to the ideas that the outer region had a direct effect on the near wall region down to the viscous sublayer. This formulation also provided some explanation as to why the DeGraaff and Eaton mixed scaling worked. In the limit of high Reynolds number it could be shown that the streamwise normal stress scaled on the product of the friction velocity and the freestream velocity would approach a constant, thus leading to the empirical scaling which has been shown to work at moderate Reynolds numbers.

Reynolds Stress Scaling in Adverse Pressure Gradients

A new method of scaling the turbulent stresses in adverse pressure gradient boundary layers was proposed by Elsberry et al. (2000). The method is based on the location of the maximum measured free stream velocity, U_o and the momentum thickness at that location θ_o. The mean velocity profile for the data of Elsberry et al. (2000) was approximately

self-similar and expressed as:

$$\frac{U}{U_e} = f'\left(\frac{y}{\theta}\right) \tag{1.81}$$

To determine the scaling of the turbulent stresses, the mean velocity profile was substituted into the two dimensional mean momentum equation, resulting in the following:

$$U_e\frac{dU_e}{dx}\left(f''^2 - ff'' - 1\right) - \frac{U_e^2}{\theta}\frac{d\theta}{dx}ff'' + \frac{\partial}{\partial x}\left(\overline{u'^2} - \overline{v'^2}\right) + \frac{\partial}{\partial y}\overline{u'v'} = 0 \tag{1.82}$$

The similarity scales for the mean velocity were assumed to be expressible as power laws ($U_e \propto x^{-n}$ and $\theta \propto x^m$), which led to:

$$U_e\frac{dU_e}{dx} \propto \frac{U_e^2}{\theta} \propto x^{-2n-1} \tag{1.83}$$

The maximum value of the freestream velocity U_o was found to collapse the peak value of the normal stresses, however this collapse did not occur at the same height above the wall as for the shear stress and thus a new length scale was also necessary. The new normal stress scales were:

$$\overline{u'u'} = U_o^2 g_{11}\left(\frac{y}{\theta}\right) \tag{1.84}$$

$$\overline{v'v'} = U_o^2 g_{22}\left(\frac{y}{\theta}\right) \tag{1.85}$$

The exponent for the movement of the peak in the stresses away from the wall with increasing downstream distance was found to be 1.2. To obtain this dependence the nondimensional location (y/θ) was multiplied by the Reynolds number based on θ raised to the -0.2 power. This changed the mean velocity profile to:

$$\frac{U}{U_e} = f'\left(\frac{y}{\theta}Re^{-0.2}\right) \tag{1.86}$$

requiring:

$$\frac{\partial}{\partial y}\left(\overline{u'v'}\right) \propto x^{-1.4} \tag{1.87}$$

To satisfy this requirement the velocity scale was the product of the reference velocity and the local external velocity (U_oU_e). A new length scale of $y/(\theta Re_\theta^{0.2})$ collapsed the peaks of the normal stresses when they were nondimensionalized by U_o^2 and the shear stress when nondimensionalized by U_oU_e. The length scale also worked at collapsing the mean velocity profiles and the Reynolds stress correlation. The different scales for similarity of the mean flow and turbulent stresses indicates the flow is not in equilibrium, and that the scales are most likely not unique.

In the separating and reattaching flow of Song and Eaton (2004), the scaling of the turbulent stresses at the separation location was examined. The length scale necessary to collapse the peaks for both the streamwise stresses and the shear stress was found to be $y/y_{inflection}$, where $y_{inflection}$ is the location of the inflection point in the mean flow. For the streamwise normal stress, the stress was found to scale with $U^2_{inflection}$, where $U_{inflection}$ is the velocity in the mean flow at the inflection point. The wall normal stress scaled on the value of $u^2_{\tau,ref}$, the friction velocity in the boundary layer prior to the start of the adverse pressure gradient. Finally, the shear stress scaled on the local freestream velocity. These velocity scales are complex, and most likely depend on the specific geometry. They do however show that for strong adverse pressure gradients, the stresses do not scale in those scales that collapse the flat plate data.

1.5 Summary

For a zero pressure gradient boundary layer, there is still debate over whether the mean flow is best represented by the logarithmic law of the wall or by a power law velocity profile. A very recent study by Buschmann and Gad-el Hak (2003) compared these two models and found that while they apply to slightly different regions of the profile, neither one could be considered to be better than the other. Thus at least for now, the debate over this issue remains open. The scaling of the velocity deficit profile has also been examined in recent years and the recent work of Zagarola and Smits (1998) provides a new velocity scale, $U_e\delta^*/\delta_{99}$, which has been shown to collapse the deficit profiles better than previous velocity scales. For the turbulent stresses, the traditional scale of ${u_\tau}^2$ has been shown to be valid for both the wall normal and Reynolds shear stress. However, for the streamwise normal stress, the mixed scaling of DeGraaff and Eaton (2000), $U_e u_\tau$ is necessary to collapse the stress profiles over a wide range of Reynolds numbers.

In adverse pressure gradient boundary layer flows, the mean profile does not change much and it has been shown that the logarithmic law of the wall still holds, although the region over which it is applicable decreases as the pressure gradient increases. For the mean deficit profile, the new velocity scale proposed by Zagarola and Smits (1998) still holds. In addition, the work of Castillo and George (2001) develops the idea of a specific velocity deficit profile, using the Zagarola and Smits velocity scale which is valid for all adverse pressure gradients regardless of the strength of the pressure gradient. This approach introduces

a non-dimensional parameter, Λ, which they showed has only three values. Recent work by Elsberry et al. (2000) develops a method of scaling the turbulent stresses for adverse pressure gradient flows that depends on the momentum thickness Reynolds number of the flow as well as the maximum free stream velocity the flow experiences during its development.

Downstream, in the redevelopment region, DeGraaff (1999) showed that the flow develops a stress equilibrium layer where the Reynolds stresses are in equilibrium with the local skin friction. In this region the flat plate stress scalings once again hold in the near wall region. This was also shown by Song (2002) in a separating and reattaching flow.

Computational modeling of adverse pressure gradient flows depends strongly on the model chosen. The standard k-ϵ model has been shown repeatedly to fail in regions of pressure gradient. A recent analysis by Yorke and Coleman (2004) compared four of the most common turbulence models used in adverse pressure gradient flows. They showed that particularly for the Shear Stress Transport model and the eddy viscosity the turbulent stresses and general flow were reasonably well predicted, however all current models still leave room for improvement. LES and DES are widely viewed as the methods that will supplant RANS based approaches, largely because of the difficulties RANS methods have in non-equilibrium flows like adverse pressure gradient boundary layers. However, the required near-wall resolution in LES still constrains its application to relatively low Reynolds number flows. A better understanding of scaling in non-equilibrium flows is needed to help development of near-wall models for use with LES and DES codes.

1.6 Objectives

The goal of this thesis is to examine the effect the Reynolds number plays in mild adverse pressure gradient turbulent boundary layers. The new data gathered in this study will be examined using the currently proposed scalings for the mean velocity and turbulent stresses. Additionally, the data will be analyzed with the goal of developing a new set of turbulent stress scalings which will be applicable to general mild adverse pressure gradient flows, and expand the flat plate scalings to include adverse pressure gradient flows which do not approach separation. These scales may lead to a more detailed understanding of the mixed scaling for the flat plate and the physics behind why it holds. The determination of these scales requires analysis of the data to determine length and velocity scales which are

appropriate for a decelerating flow. Experimental measurements were made over a momentum thickness Reynolds number range between 3300 and 20,600 using a high resolution laser Doppler anemometer. Computational modeling of the same flow was then performed using information gathered experimentally whenever possible. The results from this modeling were compared with the experimental data using a typical computational model to examine the ability of this model to accurately represent the flow field. In addition, the results of this set of computations were scaled using the mean velocity and turbulent stress scalings developed for the adverse pressure gradient to examine the ability of the computational models to produce the same scaling as observed experimentally.

In chapter 2, the experimental facility and measurement techniques, including the laser Doppler anemometer and the oil flow interferometry technique used to measure skin friction, are described. Chapter 3 covers development of the adverse pressure gradient flow at $Re_\theta = 3300$. Chapter 4 described the Reynolds number effects on the flow, including the proposed new turbulent stress scaling. The conclusions of this work are presented in chapter 5. The results of the computational effort are presented in Appendix C.

Chapter 2

Experimental Setup and Techniques

2.1 Introduction

The experiments were performed in the Stanford High Reynolds Number Wind Tunnel, which consists of a laboratory scale wind tunnel located inside a large pressure vessel. The vessel can be pressurized up to 8 atmospheres and the wind tunnel speed can be changed by a factor of three, leading to a ratio of 24:1 in the Reynolds number at a single measurement location. At the highest test Reynolds numbers, the viscous length scale in the boundary layer is very small (3.5 μm), requiring the use of high resolution measurement techniques. A custom made high resolution laser Doppler anemometer (LDA) was used to measure the mean and turbulence quantities in the flow. A non-intrusive skin friction measurement technique was adapted to measure the skin friction in the test section without the need to use the conventional log law fit. Additionally, wall pressure measurements were made to quantify the exact pressure distribution through which the flow progressed.

2.2 High Reynolds Number Wind Tunnel

2.2.1 Pressure vessel

The pressure vessel, or tank, is pictured in Figure 2.1. This steel pressure vessel was made by Melco Steel in Asuza, California. The pressure vessel is 8 feet in diameter, 19 feet in length and 1/2 inch thick. The inside of the vessel is accessed using a hydraulically activated door (Harris Quick Opening Door). The tank is rated for a working pressure of 120 psig at 38° Celsius.

To operate the system at 4 or 8 atmospheres of ambient pressure, the tank is pressurized using an Ingersoll Rand compressor (Model SSR-XF-400). The air from the output of the compressor is conditioned using an Ingersoll Rand dryer (Model TM1900-KTE4) to maintain the temperature and humidity at approximately 25° Celsius and 30% respectively. To prevent damage to any of the systems located inside the tank, the pressure change rate

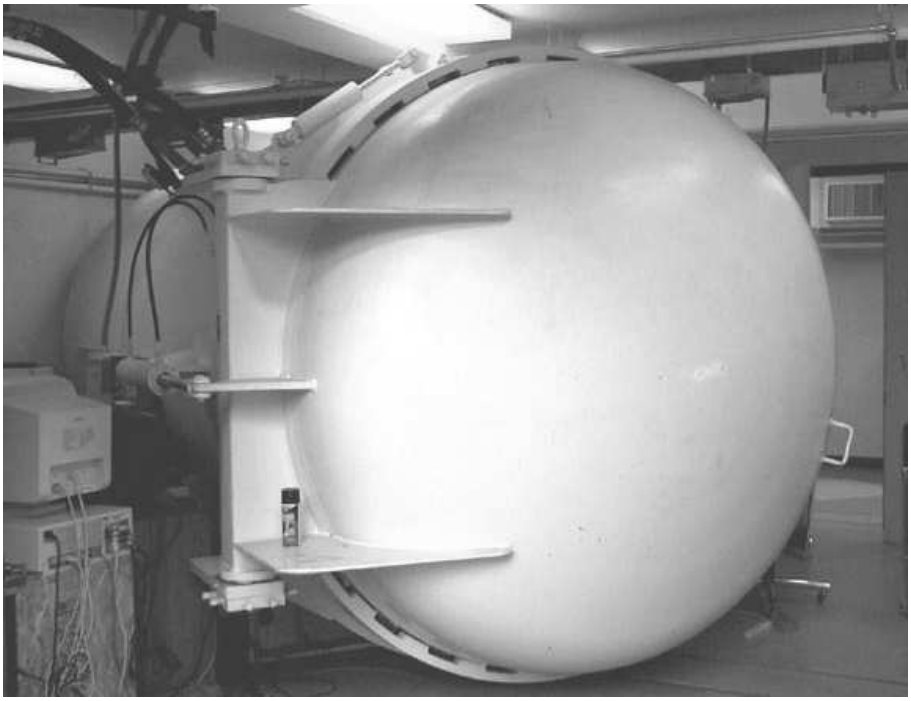

Figure 2.1: Pressure vessel

was kept below 500 Pa/s, during both pressurization and draining.

An air/water heat exchanger (Thermal Transfer Products, Model AB-1002-B4-O) is located between the exit of the dryer and the pressure vessel to reduce the temperature increase caused by pressurizing the vessel. Due to compression work, the typical rise in temperature without the heat exchanger was found to be 1.3^o C/atm (Song (2002)). This leads to high temperatures in the tank at 8 atmospheres of pressure, making it difficult to align the LDA and maintain wind tunnel conditions during measurement. Using the heat exchanger maintains the tank temperature to within $+4^o/-0^o$ C during the filling process for the highest Reynolds number case.

2.2.2 Wind Tunnel

A closed loop laboratory scale wind tunnel, Figure 2.2, is mounted in the pressure vessel. This wind tunnel is made of plexiglass, wood and other common laboratory materials since it is only required to hold the dynamic pressure of the flow, even at high ambient pressures.

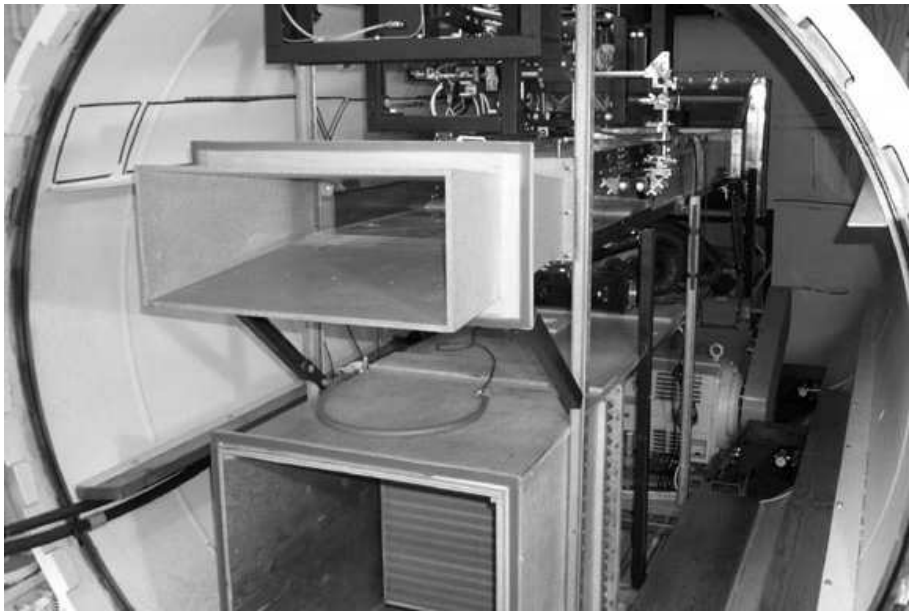

Figure 2.2: Wind tunnel

The wind tunnel is driven by an Eaton Eddy current drive motor (25 HP, model AS-272-504-01, 0-1690 RPM) equipped with an Eaton controller (model 4000), a Furnace motor starter (model ESP100) and a Pacific Fan and Blower centrifugal blower (size 3, class III, 18" diameter wheel).

Inside the pressure vessel the temperature is controlled using an air/water fin-tube heat exchanger (Super Radiator Coils model 30 x 28-4R-58/96-L), located in the return loop of the tunnel. This allows the temperature in the wind tunnel to be maintained to within $\pm 0.1^o$ C through manual adjustment of the flow rate of cold city water through the heat exchanger.

The flow through the wind tunnel is seen in the schematic in Figure 2.3. The flow travels through a rectangular inlet, 762 mm by 711 mm, in the lower half of the vessel door. This inlet is immediately followed by the heat exchanger and then a flow contraction. The flow seeder is mounted at the exit of this contraction. After the flow is seeded, it travels around the motor in a flexible duct before entering the blower through a section of Hexcel honeycomb (3/16 cell size, 75 mm long) used to straighten the flow at the duct exit. Downstream of the blower, the flow turns 180° during which time it is conditioned through three grids (approximately 50% blockage), two Hexcel honeycombs (3/16 size, 75 mm long) and three Howard Wire Cloth screens (34 mesh, 0.165 mm wire). The flow then enters a 5th

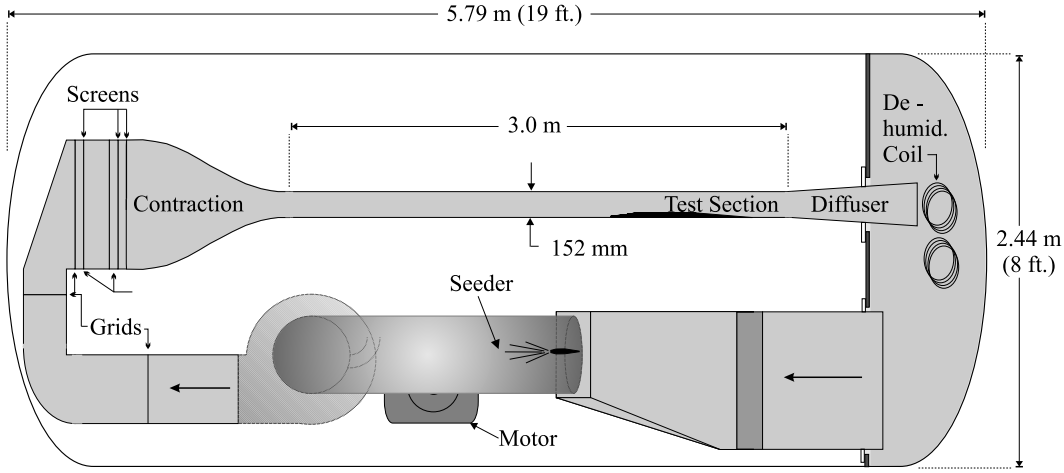

Figure 2.3: Flow diagram (DeGraaff, 1999)

order polynomial contraction, which reduces the height from 762 mm to 152 mm, via a 5:1 contraction, while maintaining a constant width. This results in the test section turbulence intensity being maintained at approximately 0.2% at a freestream velocity of 15 m/s. The flow then enters the development section of the wind tunnel. The boundary layer is tripped 150 mm downstream of the exit of the contraction, using a rectangular strip 1.6 mm height and 6.4 mm long in the streamwise direction. A development length of approximately 920 trip heights exists before the flow is contracted using a special insert to produce the desired flow geometry, which will be discussed later. The side walls and ceiling of the tunnel are tripped using Dymo labeling tape with a line of capital "V's" with a height of 1 mm. The test section is 840 mm long and follows the development section. Two large glass windows are mounted on the top and side walls to allow for clear optical access to the flow. The remainder of the test section is made of 12 mm thick Plexiglass. Finally, a straight walled diffuser is attached at the end of the test section to expand the height from 152 mm to 279 mm over 762 mm of length. The flow then passes through two dehumidifier coils in the tank door before re-entering the inlet.

The motor and blower are isolated from the wind tunnel and pressure vessel by a vibration isolation system, used to minimize the influence of their vibration on the measurements. The motor and blower are attached to a steel frame, which rests on 4 gimbal piston vibration isolators (Technical Manufacturing Corp model 64-25765-01). The pistons are filled with air from a high pressure air cylinder located outside of the pressure vessel. Three of the isolators have height control valves which maintain the pistons at the correct operating

height to minimize vibrations.

2.2.3 Tunnel Condition Monitoring

During experiments the wind tunnel conditions are constantly monitored. These include the tank pressure, the temperature and the freestream velocity. The tank pressure is measured using a Setra pressure transducer (model 207). The freestream velocity is measured using a pitot probe (United Sensor Corp model PDC-8-G-6-KL), located approximately 330 mm upstream of the diffuser inlet and a Setra differential pressure transducer. The temperature in the wind tunnel is measured using a thermistor, located in the development section of the flow and connected to a Fluke multimeter (model 8840A). The temperature information is gathered by one lab computer (Gateway GP6-350) equipped with a National Instruments A/D board (PCI-MIO-16E-4) using LabView (version 6.0) and a National Instruments GPIB board (PCI-GPIB). The temperature information is then passed to another laboratory computer, which also monitors the tank pressure and freestream velocity. This second lab computer (MSE model 486 DX2-66MHz) is equipped with a National Instruments A/D board (model AT-MIO-16) and National Instruments LabView software (version 3.0.1).

2.3 Geometry

The mild adverse pressure gradient geometry is shown in Figure 2.4. The boundary layer develops over a 1.5 meter long flat plate before being mildly contracted, using a 5th order polynomial, over a distance of 169 mm measured along the bottom surface, from a test section height of 152 mm to a height of 131 mm. The boundary layer then relaxes over a 480 mm long flat plate. This length of flat plate is long enough for the boundary layer to relax back to a typical flat plate boundary layer prior to exposure to the adverse pressure gradient. The test section consists of 100 mm of upstream flat plate, a 4° linear expansion, 300 mm in length along the bottom surface, and a downstream redevelopment flat plate of 200 mm length. The 4° linear expansion expands the tunnel height from 131 mm back to 152 mm without separation. The cusp between the upstream flat plate and the linear expansion was smoothed to prevent separation from occurring prior to the application of the adverse pressure gradient. The trailing edge of the expansion produced a small step in height between the end of the expansion and the redevelopment flat plate. This step was

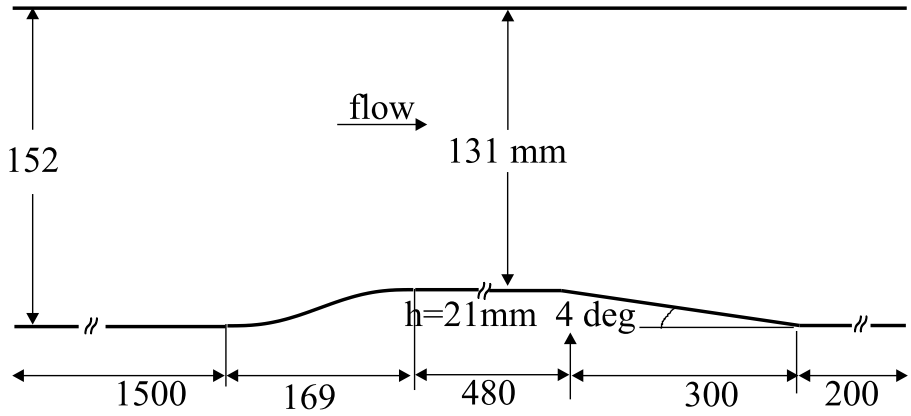

Figure 2.4: Adverse pressure gradient flow geometry

patched using spackling and sanded smooth.

A 4 degree ramp was chosen after using NASA's INS2D RANS code and a modified version of an integral boundary layer code, originally developed by Ashjaee (1980) for the design of diffusers. The integral method code was modified to examine the shape factor and pressure coefficient development for a range of ramp angles from 3° to 6° in 0.5^o increments. From this a 4 degree ramp was chosen. RANS simulations were then performed using INS2D to ensure that the flow would not separate and that it would be moderately perturbed by the adverse pressure gradient. The optimal ramp design was chosen to allow for the test section to include an upstream flat plate region on which to take reference measurements, a short downstream region in which redevelopment of the flow could be examined and the steepest ramp on which a number of separate measurement locations as the flow developed could be examined, without separation. The ramp was then fabricated from aluminum tool plate. The surface was polished with 400 grit sand paper to remove any scratches or other minor imperfections.

2.4 High Resolution LDA

As the Reynolds number increases, the viscous length scale decreases and therefore to accurately measure turbulence quantities at high Reynolds number, high resolution techniques are necessary. DeGraaff (1999) built a two component high resolution laser Doppler anemometer (LDA) with a measurement volume 35 μm in diameter and 60 μm in length for use in this facility. This section describes the general features of the high resolution LDA,

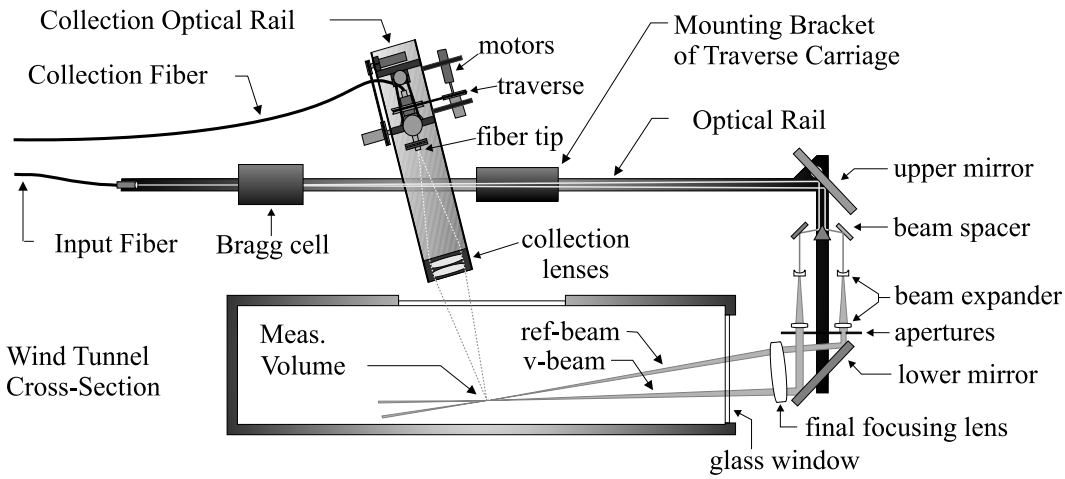

Figure 2.5: LDA (DeGraaff, 1999)

its vibration isolation and height control system, and the seeding system. More detailed information can be found in DeGraaff (1999) and DeGraaff and Eaton (2001).

2.4.1 Optical Design

A schematic of the LDA system is shown in Figure 2.5. A Lexel argon ion laser (model 95), located outside the pressure vessel, produces a green laser beam ($\lambda = 514.5nm$), which is coupled into a single mode polarity maintaining optical fiber (Oz Optics) with a 3.5 μm core at a maximum power of 0.5 W. This fiber delivers the beam into the tank where it is attached to one end of the optical rail and collimated by a 3.5 mm focal length achromatic lens. A two-axis Bragg cell (IntraAction model F2M 40/45) divides the beam into three approximately equal intensity beams: the reference beam, which is frequency unshifted; the u beam, which is 1st order horizontally shifted by 40 MHz; and then v beam, which is 1st order vertically shifted by 42 MHz.

These three beams then pass through individual beam conditioning optics after being reflected down by an upper mirror (50 mm square Melles Griot 02MLE007). The conditioning optics consist of: a planar-concave lens with a focal length of -20 mm (10 mm diameter, Melles Griot 01LLK005); a positive achromatic lens with a focal length of 120 mm (24 mm diameter, Melles Griot 01LAO134); and a set of apertures which are 6.4 mm in diameter for the reference beam, 7.1 mm in diameter for the u beam, and 9.3 mm in diameter for the v beam. The purpose of this set of lenses is to produce a small beam waist in the

measurement volume. The beam waist (w) can be estimated as:

$$w = \frac{\lambda f}{\pi D} \tag{2.1}$$

where λ is the beam wavelength, f is the focal length of a focusing lens, and D is the incoming beam diameter to the focusing lens. The beam apertures are used to determine the beam diameter, with larger beam diameters leading to smaller beam waists.

The three beams are then reflected by a lower mirror (50 mm square, Melles Griot 02MLE007) toward the final focusing lens (TSI model 9167-350), which has a focal length of 350 mm. This lens converges the three beams to the measurement volume near the mid span of the wind tunnel test section. The converging angle between the reference beam and the u beam is 4.99 degrees and the converging angle between the reference beam and the v beam is 3.82 degrees for this set of experiments. The fringe spacing (d_f) at the measurement volume is defined as:

$$d_f = \frac{\lambda}{2 \sin \theta_c / 2} \tag{2.2}$$

where θ_c is the converging angle. The fringe spacings are thus 5.90 μm horizontally and 7.72 μm vertically. The larger the beam spacing, or converging angle, the smaller the fringe spacing and the greater the resolution of the velocity measurements.

The collection optics consist of two achromatic lenses with 200 mm focal length (38.1 mm diameter Newport PAC007) and an optical fiber with a 50 μm core diameter (Realm Communication Group). The collection optics are used in side scatter and are mounted on a rail attached to the main optics rail. The two lenses are used for one to one imaging the measurement volume onto the fiber tip. The optical fiber then transmits the collected light to a photomultiplier tube and to the signal processing devices outside the pressure vessel. The fiber tip has three translational axes relative to the rail on which three DC motors (MicroMo Electronics INC model 1016M006G+10/01, 4096:1) are located with control from outside the tunnel to allow for accurate positioning of the fiber tip from outside the tank.

The use of side scatter to collect the signal leads to a smaller measurement volume length than either forward or backward scatter would. The shallow angle between the converging beams after the final focusing lens leads to an overlap region a few millimeters in length at the measurement volume. For forward and backward scatter collection optics, the measurement volume length depends on the depth of focus of the collection optics, but can be comparable to the length of the overlap region. For side scatter collection optics the

measurement volume length is determined by the smallest aperture in the collection optics system, which in this case is the diameter of the collection fiber.

The actual size of the measurement volume, both diameter and length, was found experimentally since it is dependent on the optical alignment and electronic signal processing. The largest Doppler bursts which passed through the center of the measurement volume were recorded using an oscilloscope (Tektronix, model TSD360). Since the velocity and duration of the burst were known, the measurement volume diameter could be determined to be 35 μm. The measurement volume length was found by monitoring the scattered light intensity while traversing a 5 μm wire along the length of the measurement volume. A conservative estimate for the length is 60 μm, the extra length compared to the 50 μm diameter of the fiber core is caused by lens aberration and diffraction. The actual measured volume using 0.5 μm diameter seed particles is probably somewhat smaller.

The comparative size of the LDA measurement volume and that of a small cross wire hot wire is shown in Figure 2.6. The cross wire hot wire shown has an active length of 600 μm and a spacing between the two wires of 400 μm. This figure includes a scale to indicate the viscous length scale at the lowest Reynolds number examined in these experiments. The LDA measurement volume is approximately 1300 times smaller than that of the cross wire hot wire. At the highest Reynolds number the measurement volume diameter is 10 - 12 viscous lengths.

2.4.2 Signal Processing

The scattered light gathered by the collection optics passes into a TSI photomultiplier tube (model 9162). A TSI frequency shifter (model 9186A) downshifts the signal from the photomultiplier by 35 MHz. This leaves the shift frequencies for the u and v components at 5 and 7 MHz respectively. The signal from the shifter is then bandpass filtered between 1 and 30 MHz using a TSI filter conditioner (model 1984A). The filtered signal enters a Macrodyne processor (model 3102). This processor contains a hardware FFT routine and determines the Doppler burst frequencies for the u and v components. The processor only considers a signal valid if both the velocity components are validated. The validated frequency information is then transferred to a lab computer (Gateway GP6-350) via GPIB. This computer is equipped with a National Instruments A/D board (PCI-MIO-16E-4), a National Instruments GPIB board (PCI-GPIB) and National Instruments Software (version 6.0). The LabView software converts the frequency information into velocity information.

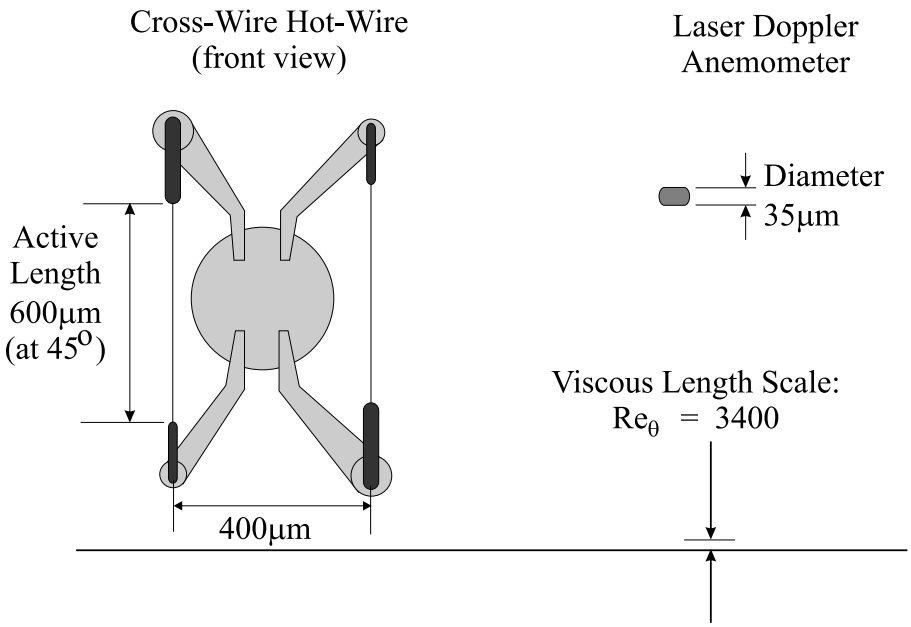

Figure 2.6: Comparison in measurement volume size between the LDA and a cross wire hot wire (DeGraaff, 1999)

A number of biases are commonly associated with LDA systems, although the appropriate corrections are often difficult and still remain a topic of research (McLaughlin and Tiederman (1973) Gould and Loseke (1993), Stevenson et al. (1982), Balakrishnan and Dancey (1998)). Fringe bias occurs when a particle travels through the measurement volume at a large angle and thus does not cross enough fringes to produce a valid measurement. In the present system, this bias is insignificant due to the moving fringes produced by the Bragg cell.

Validation bias is caused by filter bias and processor bias and can be considered to include all deviations from a flat validation response for the entire system over the possible range of velocity measurements. Validation bias is both difficult to estimate and system dependent. For the purpose of analysis of biases and correction performed here, the validation bias and velocity bias are treated together as follows. Velocity bias exists in LDA systems which operate in "burst" mode, where a particle passing through the measurement volume triggers a measurement instead of equal time sampling, which is done in high data density systems. While a number of different correction schemes have been proposed for correcting velocity bias, here the validation bias and velocity bias are combined and a correction is

made to account for both together. The combination of these two biases allows for the formulation of a transfer function for the LDA system, representing the probability the LDA will output a velocity measurement for a given velocity in the measurement volume. The transfer function can be defined as the product of the probabilities of a particle passing through the measurement volume and of the particle being validated by the system. This function is estimated experimentally as the data rate of the system as a function of the velocity with all other variables held constant, including all the processor settings, so as to account for the validation bias. This transfer function can then be used to weight each velocity measurement by the probability of being validated using the following weighted average:

$$U = \frac{\sum_{i=1}^{N} w(u_i u_i)}{\sum_{i=1}^{N} w(u_i)} \tag{2.3}$$

where:

$$w(u_i) = (DR(u_i))^{-1} \tag{2.4}$$

For this system:

$$DR(u_i) = 0.33 - 0.11u_i + 0.049u_i^2 - 0.0059u_i^3 + 0.00031u_i^4 - 0.0000059u_i^5 \tag{2.5}$$

is the measured data rate as a function of the velocity, determined using a fifth order polynomial curve fit.

Finally, velocity gradient bias is caused by the variation in the velocity across the measurement volume. For U, V, $\overline{v'v'}$ and $\overline{u'v'}$ the velocity gradient bias can be neglected since the corrections to these terms are all a function of the diameter of the measurement volume squared times a second derivative, which for this system is very small. The velocity gradient bias for $\overline{u'u'}$ was corrected following the method of Durst et al. (1995) using:

$$\overline{u'u'_{true}} \simeq \overline{u'u'_{measured}} - \frac{d^2}{16}\left(\frac{dU}{dy}\right)^2 \tag{2.6}$$

where d is the $1/e^2$ diameter of the measurement volume.

2.4.3 Vibration Isolation System

Maintaining the position of the measurement volume within a very small tolerance is absolutely critical to avoid affecting the measurements. The motor and blower are already isolated to prevent large scale vibrations from affecting the measurements, but this does

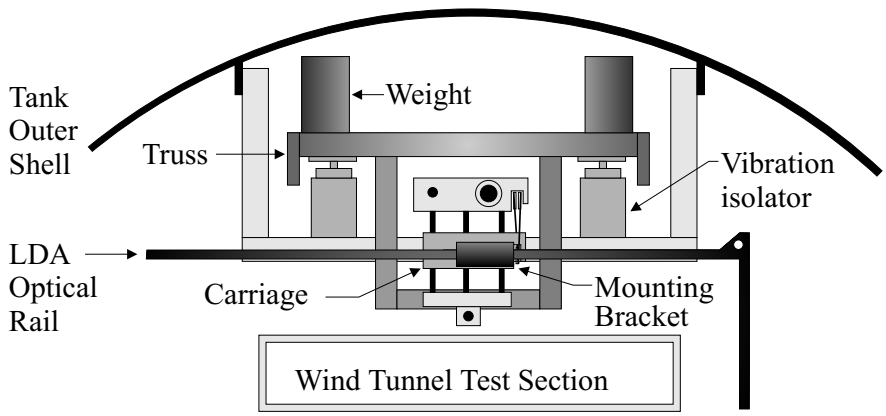

Figure 2.7: LDA vibration isolation (DeGraaff, 1999)

not prevent low frequency vibrations (< 1 Hz) from causing the rest of the wind tunnel to vibrate. Another vibration isolation system is used, along with a precision height control system, to hold the LDA system very accurately in position. This vibration isolation system consists of three gimbal-piston vibration isolators (Technical Manufacturing Corp Model 64-301) along with a custom made active feedback control system to maintain the height. A diagram of the isolation system for the LDA optics rail is shown in Figure 2.7. A more detailed description of the redesigned vibration isolation systems can be found in Appendix A. This system holds the position of the LDA to within ± 3.7 μm for the 1 atmosphere measurements and ± 5 μm for the higher pressure measurements.

2.4.4 Seeding

The seeding system consists of a Paasche air brush (Model VL). Polystyrene spheres with a diameter of 0.49 ± 0.012 μm (Spherotech Inc) are used as the seed. The particles have a specific weight of 1.05 and are added to water with a mass concentration of 14% for the purpose of seeding. The air supply for the air brush is from either a Kaesar compressor (model KK1000) for the 1 atmosphere data, or an Ingersoll Rand compressor (model 2340L5) for the 4 atmosphere data, or a cylinder of breathable air for the 8 atmosphere data. The air brush is mounted in the return loop, as shown in Figure 2.3 and passes through the blower and flow conditioning prior to entering the test section.

A dehumidifying system is located in the door of the tunnel to remove the water added

to the system through seeding. This is done using a set of two dehumidifying coils of 1/2" diameter copper tubing, each 50 feet in length running 5° C chilled water to condense the water vapor on the coils before collecting it in the bottom of the door. The relative humidity can then be maintained at approximately 40% for 1 atmosphere and 70% for 8 atmosphere data.

The seed particles attach themselves to the interior surfaces of the wind tunnel and the screens and mesh of the flow conditioning throughout the experiments and these surfaces are cleaned periodically to prevent the flow conditioning system from becoming too blocked.

The data rate of the LDA system is a function of a number of parameters in this facility: the alignment of the optics, the density of the air and the humidity. At higher pressures, and thus higher air density, the light intensity along the beam path is decreased. The intensity of the scattered light from the seed particles passing through the measurement volume is weaker arriving at the collection optics fiber than for lower air densities. At 1 atmosphere, the data rate is typically 20 Hz and at 8 atmospheres, the data rate is typically less than 1 Hz.

To examine how faithfully the particles follow the flow, the Stokes number of the flow is examined. The relaxation time of a flow tracer to a step change in velocity, using Stokes drag is:

$$\tau_p = d_p^2 \frac{2\left(\frac{\rho_p}{\rho_{fluid}} - 1\right)}{36\nu} \tag{2.7}$$

where d_p is the particle diameter, and ρ_p is the particle density. The relaxation time of the Spherotech polystyrene particles is 0.7 μs at the highest Reynolds number experiments. The Kolmogorov time scale (τ_f), the smallest time scale of the flow is:

$$\tau_f = \left(\frac{\nu}{\epsilon}\right)^{1/2} \tag{2.8}$$

estimated as 12 μs. Therefore, the Stokes number for the worst case is:

$$\frac{\tau_p}{\tau_f} = 0.058 \tag{2.9}$$

which shows that the particles faithfully follow the flow.

2.4.5 LDA Uncertainty

The uncertainty in the LDA measurements is caused by a number of factors, the five most important are: statistical uncertainty, data filtering, estimating the frequency, estimating

the fringe spacing and the correction for velocity bias using a transfer function. These components were all calculated and the sum of the squares was used to determine the total uncertainty.

Statistical uncertainty is the largest contributor to the total uncertainty in the measurements. For the 1 and 4 atmosphere data 5000 samples were gathered at each location, while at 8 atmospheres 3000 samples were taken. The χ^2 distribution can be used to estimate uncertainty in the Reynolds stresses if the samples are independent and normally distributed. For these experiments the peak data rates were approximately 20 Hz, which is considered low and guarantees that the samples were independent. Although the velocities in a boundary layer are not well approximated as being normally distributed, for the purpose of calculating uncertainties this is assumed. For the two lower Reynolds number cases the uncertainty in the mean velocity is $0.028u'$, while for the high Reynolds number case the uncertainty in the mean velocity is $0.036u'$ based on a 95% confidence interval. For the uncertainty calculation in the variance of the velocity, the χ^2 distribution was used. Based on a 95% confidence interval, the uncertainty in the normal stresses at the low Reynolds number was $-3.7\%, +3.9\%$ of the value of the normal stress. For the high Reynolds number the uncertainty was $-4.8\%, +5.2\%$. For the shear stress, the bootstrap technique is used. This technique of resampling, in order to estimate the standard deviation of a quantity with an unknown probability distribution, is very well established (Efron (1982), Efron (1979)). The sample pairs from a data point are made into a new sample set by randomly selecting points from the original set with replacement. The new set has the same number of samples as the original set, but with some samples duplicated and some absent. The shear stress $\overline{u'v'}$ is recomputed for this new sample. This process is repeated many times and a 95% confidence interval from the histogram is computed. This method was also tested on the normal stresses and the uncertainty agrees very well with the χ^2 distribution prediction. This technique resulted in uncertainties of $-3.8\%, +4.0\%$. Overall the statistical uncertainty contributed approximately half of the total uncertainty for the stress components.

Data filtering was performed to remove samples outside three standard deviations from the mean. These samples are removed since some of them are spurious and can distort the statistics greatly, especially the higher order statistics. However, removing these data samples leads to more reliable, but slightly depressed higher order statistics. It is assumed that the correct values lie between the unfiltered and filtered values, so the statistics were calculated with both data sets and the difference between the values was defined as the

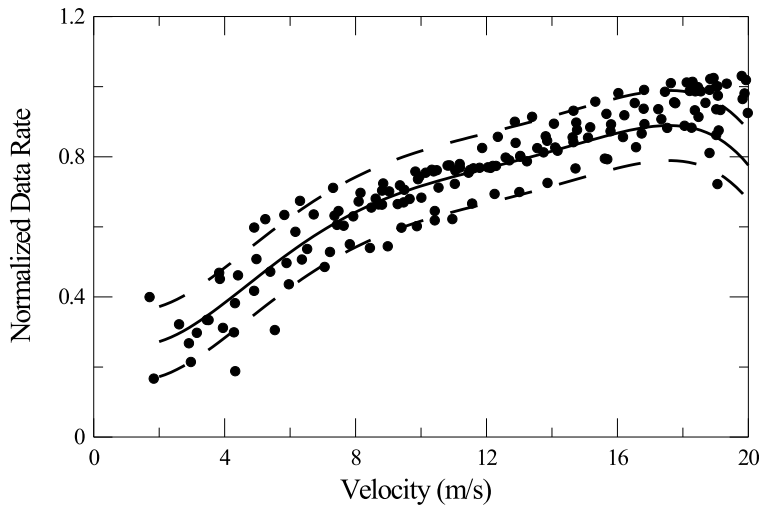

Figure 2.8: Transfer function for current LDA setup

data filtering uncertainty. For the mean, this uncertainty was found to be negligible, while for the stresses the effect varied between one quarter and one half of the total uncertainty.

The uncertainty due to estimating the frequency was analyzed by DeGraaff (1999). He showed that there is a slight augmentation of the turbulence, which is most pronounced in the freestream where the turbulence levels are lowest. This uncertainty is due to uncertainty based on the Macrodyne's resolution in estimating the Doppler frequency. It is only an important contributor in the outer 2 - 3 points in the Reynolds stress profiles, however there it is the main contributor.

Estimating the fringe spacing leads to uncertainty, since it is difficult to measure the crossing angle of the beams with high accuracy. The beam waists are small and the divergence of the beams is large making the angle measurement difficult. The estimated uncertainty in the measuring the crossing angle is 0.07 degrees for both components. This leads to an uncertainty in the u velocity of $\pm 1.5\%$ and in the v component of $\pm 1.9\%$. This uncertainty was found to only be significant for the mean velocity and disappears entirely when the freestream velocity is used to normalize the data.

A transfer function is used to correct for the velocity bias as described previously. This function may not represent the actual performance of the system and thus leads to some uncertainty. A maximum and minimum transfer function were defined encompassing all the data shown in Figure 2.8. These functions were:

$$DR = 0.23 - 0.11U + 0.049U^2 - 0.0059U^3 + 0.00031U^4 - 0.0000059U^5 \tag{2.10}$$

U	$\pm 1.5\%$
$\overline{u'u'}$	$\pm 4\%$
$\overline{v'v'}$	$\pm 8\%$
$\overline{u'v'}$	$\pm 10\%$

Table 2.1: Uncertainty in LDA

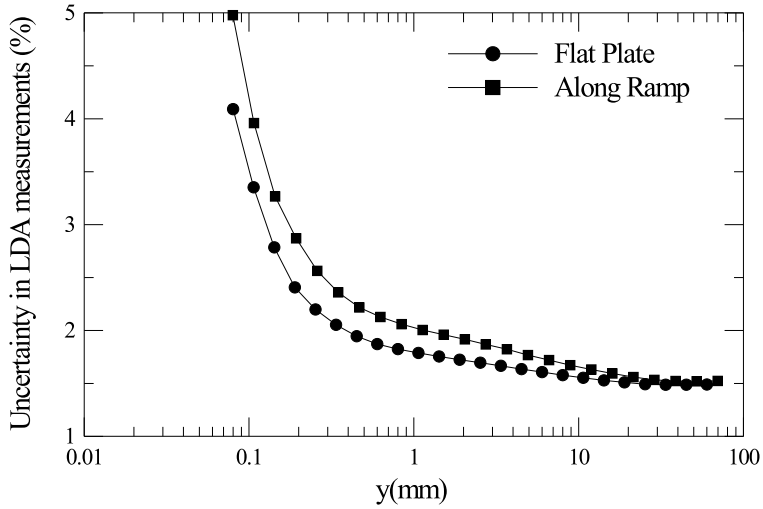

Figure 2.9: Uncertainty in the mean velocity measurements as a function of height above the wall for both locations along the flat plate and along the ramp

and:

$$DR = 0.43 - 0.11U + 0.049U^2 - 0.0059U^3 + 0.00031U^4 - 0.0000059U^5 \tag{2.11}$$

with U in m/s. The difference in the means calculated, using these different transfer functions and the original transfer function determined previously, were considered the uncertainty in the mean streamwise velocity due to this correction. This uncertainty contributed about one quarter of the total in the near wall region.

The total uncertainty in each component measured using the high resolution LDA is shown in Table 2.1. The uncertainty in the mean velocity measurements as a function of height above the wall for both profiles taken along the flat plate regions of the flow and those along the ramp is shown in Figure 2.9.

2.5 Wall Static Pressure Measurements

Wall static pressure data were measured using 0.64 mm diameter surface pressure taps located along the upstream flat plate, the 4° linear expansion, and the downstream redevelopment flat plate. These taps where installed normal to the surface at all locations and the pressure was measured using a Setra pressure transducer (model 264) with a range of 0 to 25 inches of water. Each tap was connected to the transducer using a Scanivalve unit (model SSS 48C MK4). The voltage signal from the transducer was conditioned using a Precision Measurement Engineering Buck and Gain unit (model 107). The zero voltage offset of the transducer was remeasured before every reading of the transducer to avoid voltage drift over time. In addition, the freestream velocity, as measured from a pitot probe (United Sensor Corp model PDC-8-G-6-KL) was compared between the start of the tap scanning and the end. Pressure measurements were retaken if the measured velocity changed by more that 0.1 m/s.

2.5.1 Uncertainty

The uncertainty for both the wall static pressure and the skin friction were determined from the propagation of elemental uncertainties as described by Figliola and Beasley (1995). Thus for a function, f, dependent on parameters, c_i, where $i = 1$ to N, the uncertainty in f is found by:

$$\Delta f_{total} = \sqrt{\sum_i \Delta f_i^2} = \sqrt{\sum_i \left(\left| \frac{\partial f}{\partial c_i} \right| \Delta c_i \right)^2} \tag{2.12}$$

where Δc_i is the uncertainty in c_i. This technique was used to examine the data and calculate the critical uncertainties. It was assumed that the sources of error were statistically independent and that the random errors were Gaussian distributed.

The uncertainty analysis for the wall static pressure data required the inclusion of uncertainty due to transducer resolution, statistical uncertainty in the voltage readings, calibration factor uncertainty and dynamic pressure variation. The wall static pressure data was used both to define the coefficient of pressure, C_p, and Clauser's pressure gradient parameter β. The uncertainty discussed is this section is that in the measurement of $p - p_{ref}$ and in the calculation of C_p, which can be defined as:

$$C_p = \frac{p - p_{ref}}{\frac{1}{2}\rho U_{e,ref}^2} = \frac{Calibration_{transducer}(V_{transducer} - V_{transducer,zero})}{\frac{1}{2}\rho U_{e,ref}^2} \tag{2.13}$$

The uncertainty due to the resolution of the transducer in both the pressure difference and the pressure coefficient has the following forms:

$$\Delta(p - p_{ref})_{transducer} = Calibration_{transducer} \Delta V_{transducer} \tag{2.14}$$

$$\Delta C_{p,transducer} = \frac{Calibration_{tranducer} \Delta V_{transducer}}{\frac{1}{2}\rho U_{e,ref}^2} \tag{2.15}$$

The transducer used in this experiment had a 1% full scale uncertainty over the range of $0 - 25$ inches of water. Based on a typical pressure measurement in this experiment, the uncertainty due to the resolution of the transducer is approximately $\pm 1.7\%$ of the measured value. This uncertainty led to an uncertainty in the value of C_p of $\Delta C_{p,transducer} = \pm 0.0017$ and an uncertainty in the pressure difference of $\Delta(p - p_{ref}) = \pm 0.38 Pa$.

Statistical uncertainty due to noise in the measurement leads to an uncertainty in the voltage given by:

$$\Delta V_{statistical} = t_{\nu,P} s_{statistical} = 1.96 \frac{\sigma}{\sqrt{N-1}} \tag{2.16}$$

where N is the number of samples and σ is the standard deviation. For the calculation of the mean $\nu = N - 1$. The variance in the voltage measurement, $s_{statistical}$, is equal to the standard deviation divided by the square root of ν. The uncertainty in the coefficient of pressure and pressure difference caused by the voltage uncertainty are defined as:

$$\Delta C_{p,statistical} = \frac{Calibration_{tranducer} \Delta V_{statistical}}{\frac{1}{2}\rho U_{e,ref}^2} \tag{2.17}$$

$$\Delta(p - p_{ref})_{statistical} = Calibration_{transducer} \Delta V_{statistical} \tag{2.18}$$

For this experiment the uncertainty in $\Delta C_{p,statistical}$ was ± 0.0011 or 1.1% of the measured value and that of $\Delta(p - p_{ref})_{statistical}$ was $\pm 0.25 Pa$.

The uncertainty in the calibration of the transducer was due to the accuracy of a linear fit to the calibration data. The variance of the slope of the calibration can be calculated using:

$$s_{slope} = s_{xy} \sqrt{\frac{N}{N \sum_{i=1}^{N} {x_i}^2 - \left(\sum_{i=1}^{N} x_i\right)^2}} \tag{2.19}$$

where N is the number of points in the calibration curve, x_i is the value of the independent variable x at the i-th data point and s_{xy} was determined from the linear fit of:

$$s_{xy} = \sqrt{\sum_{i=1}^{N} (y_i - y_{fit,i})^2 \nu} \tag{2.20}$$

where y is the dependent variable and y_{fit} is the value of the dependent variable using the linear fit. This led to an uncertainty in the calibration factor of $\Delta Calibration = t_{\nu,P} s_{slope}$, where $t_{\nu,P}$ is the value of the student t distribution for a system with ν degrees of freedom at a confidence interval of P. The confidence interval of $P = 95\%$ is used and $10,000$ samples were collected so $t = 1.96$. The number of degrees of freedom for a linear fit is $\nu = N - 2$, where N is the number of calibration points. The variation in the calibration factor was $\pm 1.61 Pa/V$. This led to uncertainties in C_p and $p - p_{ref}$ of:

$$\Delta C_{p,calibration} = \frac{\Delta Calibration}{Calibration} C_p \tag{2.21}$$

$$\Delta (p - p_{ref})_{calibration} = \frac{\Delta Calibration}{Calibration} (p - p_{ref}) \tag{2.22}$$

For typical values of the pressure distribution this led to $\Delta C_{p,calibration} = \pm 0.0013$ and $\Delta (p - p_{ref})_{calibration} = \pm 0.29 Pa$.

Therefore the total uncertainty in $\Delta (p - p_{ref})_{calibration}$ can be calculated from:

$$\Delta (p - p_{ref})_{total} = \sqrt{\Delta (p - p_{ref})^2_{resolution} + \Delta (p - p_{ref})^2_{stat} + \Delta (p - p_{ref})^2_{calib}} \tag{2.23}$$

This gives a total uncertainty of $\Delta (p - p_{ref})_{calibration} = \pm 0.54 Pa$.

When calculating the uncertainty in the pressure coefficient distribution C_p, the uncertainty in the dynamic pressure also had to be considered. It was calculated from the same pressure transducer attached to the Scanivalve based on:

$$\frac{1}{2} \rho U^2_{e,ref} = Calibration (V_{transducer} - V_{transducer,zero}) \tag{2.24}$$

The same three separate uncertainties were factored into computing the dynamic pressure uncertainty, as included in the other uncertainties in C_p: resolution in the voltage measurements; statistical uncertainty in the voltage measurements; and uncertainty in the calibration.

The uncertainty due to the resolution of the transducer was again approximately $\pm 1.7\%$ of the measured value, leading to an uncertainty in the dynamic pressure of:

$$\Delta \frac{1}{2} \rho U^2_{e,ref} = Calibration_{transducer} \Delta V_{resolution} \tag{2.25}$$

which for this system is $\pm 0.38 Pa$.

The statistical uncertainty is caused by the noise in the measurements and is again given by:

$$\Delta V_{statistical} = t_{\nu,P} s_{statistical} = 1.96 \frac{\sigma}{\sqrt{N-1}} \tag{2.26}$$

where N is the number of samples and σ is the standard deviation. For the calculation of the mean $\nu = N - 1$. The variance in the voltage measurement, $s_{statistical}$, is equal to the standard deviation divided by the square root of ν. The uncertainty in the dynamic pressure caused by the voltage uncertainty is:

$$\Delta\left(\frac{1}{2}\rho U_{e,ref}^2\right)_{statistical} = Calibration_{transducer}\Delta V_{statistical} \tag{2.27}$$

which for this experiment was $\pm 0.25Pa$.

Finally, the uncertainty due to the accuracy of the fit to the calibration data was calculated as before for the transducer calibration. This results in an uncertainty in the dynamic pressure of:

$$\Delta\left(\frac{1}{2}\rho U_{e,ref}^2\right)_{calibration} = \left(\frac{\Delta Calibration_{transducer}}{Calibration_{transducer}}\right)\left(\frac{1}{2}\rho U_{e,ref}^2\right) \tag{2.28}$$

This gives the uncertainty as a percentage of the measured dynamic pressure of approximately $\pm 2.84Pa$ at a typical velocity of 20 m/s.

The overall uncertainty in $\left(\frac{1}{2}\rho U_{e,ref}^2\right)$ was then computed as:

$$\Delta\left(\frac{1}{2}\rho U_{e,ref}^2\right)_{total} = \sqrt{\Delta\left(\frac{1}{2}\rho U_{e,ref}^2\right)_{res}^2 + \Delta\left(\frac{1}{2}\rho U_{e,ref}^2\right)_{stat}^2 + \Delta\left(\frac{1}{2}\rho U_{e,ref}^2\right)_{calib}^2} \tag{2.29}$$

which gave a value of $\pm 2.88Pa$.

The uncertainty in C_p due to this is given by:

$$\Delta C_{p,\frac{1}{2}\rho U_{e,ref}^2} = \left(\frac{\Delta\left(\frac{1}{2}\rho U_{e,ref}^2\right)}{\frac{1}{2}\rho U_{e,ref}^2}\right) C_p \tag{2.30}$$

This lead to an uncertainty of ± 0.0013 or 1.3%.

The combined effects of these uncertainties led to an overall uncertainty in the pressure coefficient of:

$$\Delta C_{p_{total}} = \sqrt{\Delta C_{p,transducer}^2 + \Delta C_{p,statstical}^2 + \Delta C_{p,calibration}^2 + \Delta C_{p,\frac{1}{2}\rho U_{e,ref}^2}^2} \tag{2.31}$$

where for a 95% confidence the uncertainty was $\pm 2.7\%$ or 0.0027.

2.6 Skin Friction Measurements

Skin friction measurements were made using the oil-fringe imaging technique described by Monson et al. (1993) for all locations, except the two upstream flat plate locations, where the logarithmic law of the wall fit was used instead. This technique has been shown to work in a wide range of conditions to accurately measure the surface skin friction (Driver (2003)). The oil fringe method is non-intrusive and relates the surface skin friction to the thinning rate of a line of oil placed on the surface. The oil is placed on the surface at several locations and the tunnel is started impulsively. Most of the oil quickly flows downstream during a short transient. The remaining oil forms a thin wedge, which when illuminated using monochromatic light produces interference fringes with a uniform spacing near the leading edge of the oil film. The spacing between the fringes can then be measured and compared to that at a reference location to determine the skin friction at the measurement location.

The general configuration for the measurement is shown in Figure 2.10. The surface of the wind tunnel from 1 meter upstream of the mild contraction until the end of the test section was covered with 0.13 mm thick green acetate paper with the back side painted flat black to produce better imaging quality. The green acetate paper was attached to the bottom surface of the tunnel using double sided tape and smoothed out to eliminate any air pockets. For these experiments Dow Corning 200 fluid was applied in a 50 mm oil line using a sharp knife edge at the measurement location and at the upstream reference location. For the 1 atmosphere experiments 50 cs (5x10$^{-5}m^2/s$) Dow Corning 200 fluid was used, for the 4 atmosphere case 200 cs (2x10$^{-4}m^2/s$) fluid was used and for 8 atmospheres 350 cs (3.5x10$^{-4}m^2/s$) Dow Corning 200 fluid was used. The oil line was oriented perpendicular to the flow and the wind tunnel was then run for approximately 10 minutes, until a fringe pattern was visible. For the cases at 4 and 8 atmospheres ambient pressure, the wind tunnel was run at a very low velocity, between 3 and 5 m/s, while the tank filled to prevent the backflow of the Dow Corning fluid. The tunnel was impulsively accelerated to full speed when filling was complete. When a fringe pattern was evident the tunnel was stopped and images were taken at the current measurement location, the upstream reference location and again at the current measurement position. The reason for the two sets of pictures at the measurement location was to allow for more samples with which to estimate the uncertainty. The images were gathered using a Kodak high resolution digital camera (model DC290),

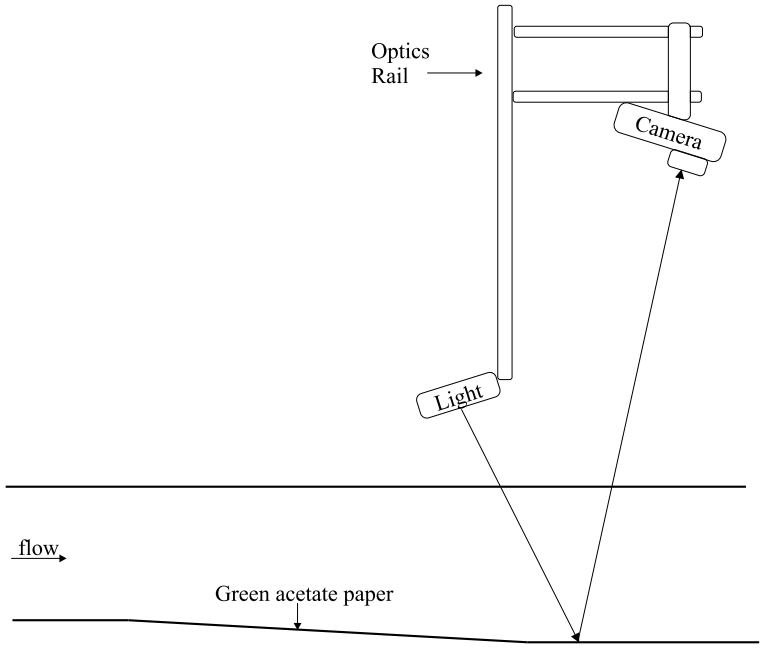

Figure 2.10: Skin friction measurement setup

and a green monochromatic diffuse light source, made of a white fluorescent light, green acetate paper and semi transparent mylar sheet. Five independent runs at each location were performed, with the acetate paper being cleaned between each measurement and a new oil line being applied, with two independent measurements being made at a location during a single run. The fringe spacing was averaged over all ten samples and this value was used to calculate the skin friction. For the ramp, the Bond number was calculated to ensure that the effect of gravity was negligible on the film of oil:

$$Bo = \frac{g(\rho_{oil} - \rho_{air})L^2}{\sigma} \tag{2.32}$$

For the 1 atmosphere case the Bond number is 8.24x10^{-5}, so gravitational effects can be ignored along the ramp. The angle between the camera and the wall normal and the angle between the light source and the wall normal for the flat regions were both 17.4^o. The angles for the ramp locations can then be easily computed.

The fringe spacing depends on the skin friction, but also on the time history of the flow, the properties of the oil, the surface properties and the viewing angle. Because of these limitations, it is very difficult to estimate the absolute value of the skin friction and instead the ratio of the skin friction at the location of interest to the reference location is

used. The time history, oil and surface properties are the same at both locations. For the measurement locations after the trailing edge of the ramp, where both the measurement and reference surface are horizontal, the relationship between the skin friction and fringe spacing (ΔS_f) can be simplified to:

$$\frac{C_{f,local}}{C_{f,ref}} = \frac{\Delta S_{f,localimage}}{\Delta S_{f,refimage}} \tag{2.33}$$

because the viewing angle for both the measurement and reference locations are the same. For the locations along the ramp, the viewing angle for the measurement and reference locations are different and the relationship between the skin friction and fringe spacing can be expressed as:

$$\frac{C_{f,local}}{C_{f,ref}} = \frac{\Delta S_{f,localimage}}{\Delta S_{f,refimage}} \frac{\frac{\cos\left(a \sin\left(\frac{\sin\theta_{light,loc}}{n_{oil}}\right)\right)}{\cos\theta_{camera,loc}}}{\frac{\cos\left(a \sin\left(\frac{\sin\theta_{light,ref}}{n_{oil}}\right)\right)}{\cos\theta_{camera,ref}}} \tag{2.34}$$

where n_{oil} is 1.4022 for 1 atmosphere, 1.4030 for 4 atmospheres and 1.4034 for 8 atmospheres and the angles can be computed based on the 4 degree angle of the ramp, with the light angle increasing by 4° and the camera angle decreasing by 4°.

2.6.1 Uncertainty

The uncertainty in the surface skin friction at a given measurement location is due to statistical uncertainties in both the reference and measurement location fringe spacing, uncertainty in the value of the skin friction at the reference location, and for the measurements along the ramp, the uncertainty in the angle between the camera and the light source.

The uncertainty in the local skin friction due to the uncertainty in the reference skin friction is given by:

$$\Delta\left(C_{f,loc}\right)_{c_f} = \frac{\Delta S_{f,local}}{\Delta S_{f,ref}} \Delta\left(C_{f,ref}\right) \tag{2.35}$$

where the uncertainty in $C_{f,ref}$ is due to the fit of the flat plate data to the law of the wall. The uncertainty in the coefficient of friction due to this is 0.0000811, which is 2.5% of the reference value.

The uncertainty in the measurement of the local fringe spacing is given by:

$$\Delta\left(C_{f,loc}\right)_{statistical,local} = \frac{1}{\Delta S_{f,ref}} C_{f,ref} \Delta\left(\Delta S_{f,local}\right) \tag{2.36}$$

while the uncertainty in the fringe spacing in the reference location it is given by:

$$\Delta\left(C_{f,loc}\right)_{statistical,ref} = -\frac{1}{\left(\Delta S_{f,ref}\right)^2} C_{f,ref} \Delta S_{f,local} \Delta\left(\Delta S_{f,ref}\right) \tag{2.37}$$

The uncertainty in the fringe spacing calculation can be estimated based on:

$$\Delta\left(\Delta S_{f,local_o r_r ef}\right) = t_{\nu,P} s_{statistical,fringe} = 2.571 \frac{\sigma}{\sqrt{N-1}} \tag{2.38}$$

calculated at a 95% confidence interval for 5 samples, giving an estimate of 0.003 as the uncertainty in the calculation of the fringe spacing. This gave an uncertainty in the skin friction due to the fringe spacing at the reference location of 0.000109 and at the local measurement location of 0.000156, which are 3.3% and 4.8% of the reference value respectively.

For the measurements not taken along the ramp, the overall uncertainty in the skin friction was thus:

$$\Delta(C_{f,loc})_{total} = \sqrt{\left(\Delta\left(C_{f,loc}\right)_{c_f}\right)^2 + \left(\Delta\left(C_{f,loc}\right)_{stat,loc}\right)^2 + \left(\Delta\left(C_{f,loc}\right)_{stat,ref}\right)^2} \tag{2.39}$$

which gave an uncertainty of 0.000207, which is an uncertainty of approximately 6.4% of the reference value of the skin friction. This can be used to calculate the uncertainty in the friction velocity based on this method, which gives an uncertainty of ±3% for the calculated value.

The uncertainty due to the measurement of the angle is given by:

$$\begin{aligned}\Delta\left(C_{f,loc}\right)_{angle} = \frac{\Delta S_{f,local}}{\Delta S_{f,ref}} \Delta\left(C_{f,ref}\right) \Bigg(& \frac{cos^2(\theta) sin(\theta)\sqrt{1-\frac{\sin^2(\theta)}{n_{oil}^2}}}{cos(\theta-4) n_{oil}^2 \sqrt{(1-\frac{\sin^2(\theta)}{n_{oil}^2})^3}} \\ & + \frac{cos(\theta) sin(\theta-4)\sqrt{1-\frac{\sin^2(\theta+4)}{n_{oil}^2}}}{\cos^2(\theta-4)\sqrt{1-\frac{\sin^2(\theta)}{n_{oil}^2}}} - \frac{\sin(\theta)\sqrt{1-\frac{\sin^2(\theta+4)}{n_{oil}^2}}}{\cos(\theta-4)\sqrt{1-\frac{\sin^2(\theta)}{n_{oil}^2}}} \\ & - \frac{\cos(\theta)\cos(\theta+4)\sin(\theta+4)}{\cos(\theta-4) n_{oil}^2 \sqrt{1-\frac{\sin^2(\theta+4)}{n_{oil}^2}}\sqrt{1-\frac{\sin^2(\theta)}{n_{oil}^2}}} \Bigg)(\Delta\theta)\end{aligned} \tag{2.40}$$

which is calculated as 0.0000703, or 2.2%, for an uncertainty in θ of 2°.

Therefore the overall uncertainty in the skin friction for measurements along the ramp is:

$$\Delta(C_{f,loc})_{tot} = \sqrt{\left(\Delta(C_{f,loc})_{c_f}\right)^2 + \left(\Delta(C_{f,loc})_{stat,loc}\right)^2 + \left(\Delta(C_{f,loc})_{stat,ref}\right)^2 + \left(\Delta(C_{f,loc})_{angle}\right)^2} \tag{2.41}$$

which gave an uncertainty of 0.000218 or 6.7%, which led to an uncertainty in the friction velocity of ±3.4%.

Chapter 3

Development of Adverse Pressure Gradient Boundary Layer

Adverse pressure gradient boundary layers without separation occur frequently in engineering applications. While much research has been performed in recent years on separating boundary layers and those on the verge of separation, much less has been performed on boundary layers in pressure gradients farther from separation. Simple models of the scaling of the stresses hold in the flat plate boundary layer, but become very complex and difficult to apply to generic flows for stronger pressure gradients. The extent to which the scaling models for the flat plate boundary layer can be applied to weaker pressure gradients has not been explored.

This chapter describes the flow development in the adverse pressure gradient at a Reynolds number of 3300. The flow is measured at 10 streamwise locations. Basic parameters of the flow are given in Table 3.1 for all the streamwise measurement locations. For all the data presented in this thesis the coordinate system is defined with x indicating a location in the streamwise direction and y indicating a location in the wall normal direction. The y location is described as normal to the wall at each location and therefore rotates by four degrees along the adverse pressure gradient ramp. The streamwise location is given normalized by the length of the ramp (300 mm), with x' being used to represent this normalized streamwise location. For the purpose of plotting the data, the beginning of the ramp is set to $x' = 0.0$ and the end of the ramp set to $x' = 1.0$. This sets the reference flat plate location to $x' = -0.33$, or one third of a ramp length upstream of the start of the ramp.

3.1 Wall Pressure Distribution

The wall static pressure coefficient for the bottom and top walls of the wind tunnel is shown in Figure 3.1. The pressure coefficient is defined as:

$$C_p = \frac{P_{local} - P_{ref}}{\frac{1}{2}\rho U_{e,ref}^2} \tag{3.1}$$

x'	$U_e(m/s)$	$\delta_{99}(mm)$	$\theta(mm)$	H	Π	Re_θ	β	$U_\tau(m/s)$	*Symbol*
-0.33	20.48	25.22	2.51	1.34	0.37	3330	-0.17	0.82	●
0	20.62	23.81	2.17	1.29	-0.04	2990	-0.07	0.89	■
0.25	19.87	29.18	3.10	1.39	0.72	3990	2.07	0.73	⊡
0.33	19.60	30.41	3.32	1.39	0.72	4210	1.74	0.72	◊
0.5	19.20	33.77	3.78	1.42	0.87	4700	1.60	0.68	△
0.67	18.80	35.64	4.24	1.46	0.92	5160	2.31	0.66	▽
0.75	18.71	37.53	4.60	1.48	1.29	5570	1.38	0.62	○
1	18.23	41.76	5.66	1.56	1.24	6680	-1.41	0.61	▲
1.33	18.26	39.78	5.37	1.47	0.54	6340	-0.37	0.68	♦
1.67	17.54	38.77	5.26	1.45	0.67	6320	-0.18	0.68	▼

Table 3.1: Flow parameters at $Re_\theta = 3300$

where ρ is the air density and $U_{e,ref}$ is the freestream velocity at the upstream flat plate reference location. It should be noted that the reference static pressure measurement was made at $x' = -0.40$, or slightly upstream of the reference velocity measurement location. The boundary layer of interest develops on the bottom wall of the tunnel so it is subjected to the pressure distribution for the bottom wall. The flow initially develops over a flat plate and then is subjected to an adverse pressure gradient before redeveloping along another flat plate. The pressure distribution shows that the flow encounters a short region of mild favorable pressure gradient at the top of the ramp, before passing into the moderate adverse pressure gradient. At the end of the ramp, the flow starts to recover towards a zero pressure gradient condition, however it is still experiencing a very small favorable pressure gradient at the farthest downstream measurement location. The pressure distribution on the top wall of the wind tunnel shows that no separation occurs along the top surface and a monotonic variation in the streamwise direction is observed.

The pressure data were also used to examine the parameter β, Clauser's pressure gradient parameter as seen in Figure 3.2. This parameter is defined as:

$$\beta = \frac{\delta^*}{\tau_o}\frac{dP}{dx} \tag{3.2}$$

where the pressure gradient is scaled by the wall shear stress, τ_o, and the displacement

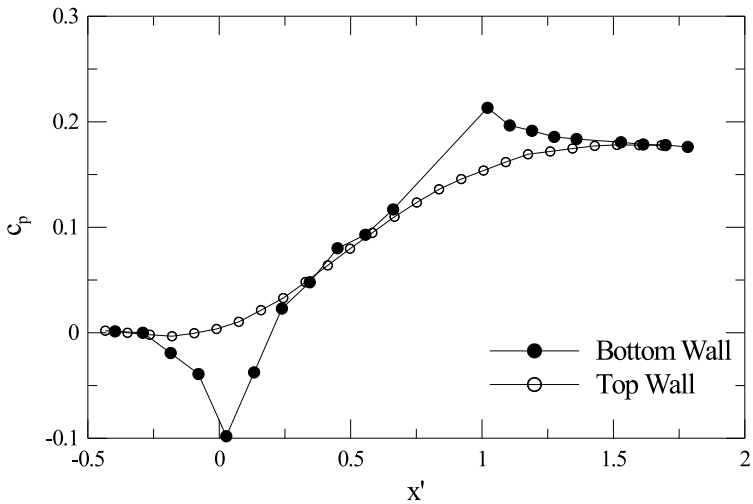

Figure 3.1: Top and bottom wall pressure distribution

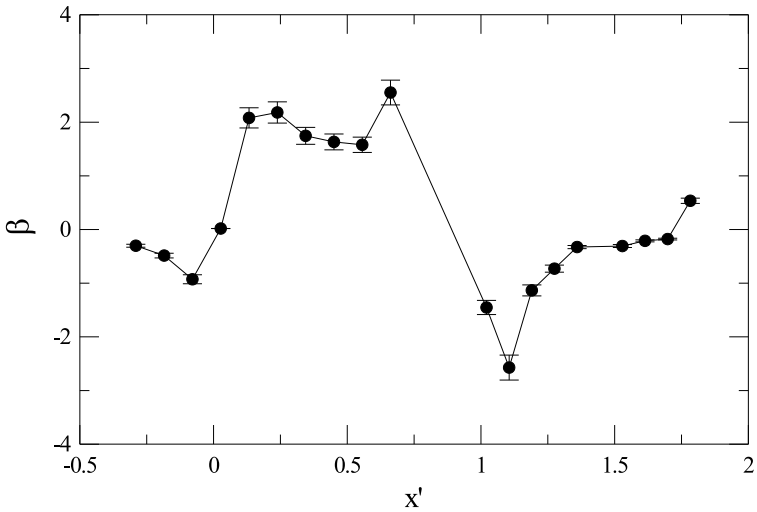

Figure 3.2: β distribution

thickness, δ^*. The complex pressure distribution leads to a varying value of β, which starts at a value of 0 on the flat plate before decreasing to -1 in the mild favorable pressure gradient and then increasing to a maximum value of 2.5 along the ramp. At the end of the ramp, β once again decreases in value, due to the changing pressure gradient, before reapproaching a value of 0, as expected for the redevelopment flat plate. Along the length of the ramp the value of β does not remain constant, but is very small at all locations, indicating that the boundary layer is far from separation. These values of β are similar to those observed

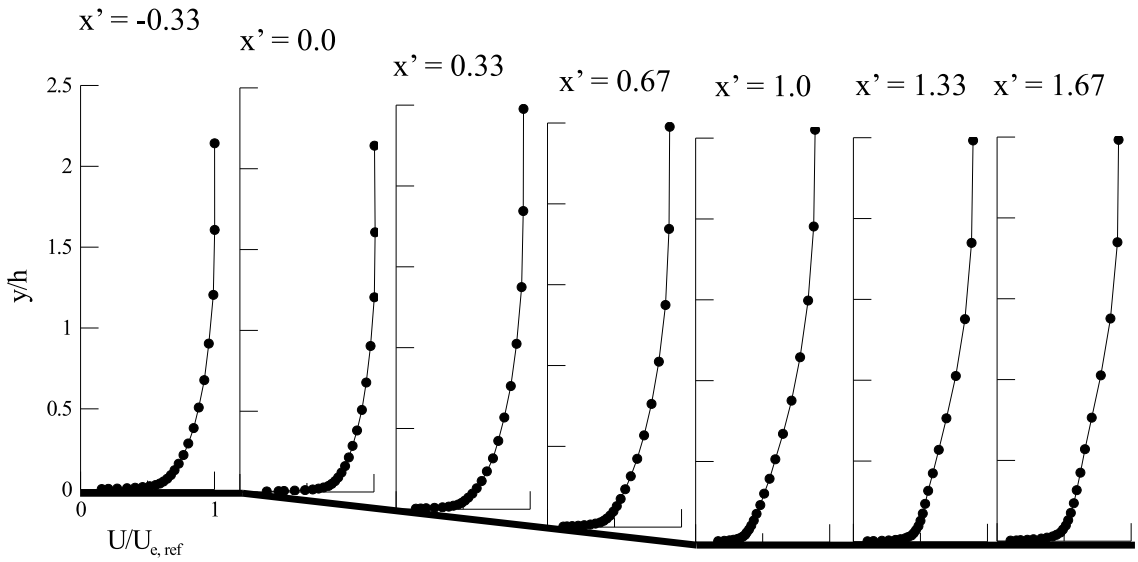

Figure 3.3: Mean flow development

in the mild adverse pressure gradient equilibrium boundary layer flow of Clauser, where the maximum value of β was approximately 2.3 (Coles and Hirst (1969)). For a flow near separation values of β greater that 20 were found by Skåre and Krogstad (1994).

The wall pressure distributions all show that the flow discussed here is subjected to a mild and sustained adverse pressure gradient along a 300 mm long ramp. In addition the flow examined here is not in equilibrium in the sense of the work of Clauser (1954) due to the changing wall pressure distribution.

3.2 Mean Flow Development

Figure 3.3 gives an overall view of the flow development. The ramp shape shown on this figure is drawn to scale with the vertical height expanded by a factor of two relative to the horizontal axis in order to show the flow in the near wall region more clearly. The mean velocity profiles shown are equidistantly separated along the length of the test section with a distance of 100 mm or one third of the ramp length between each sample. Additional data taken along the streamwise direction are not shown here for clarity.

The flow at $x' = -0.33$ is that of a flat plate boundary layer. At the start of the ramp, the flow is seen to accelerate slightly due to the mild favorable pressure gradient caused by the curvature present at the beginning of the ramp. The flow then passes over

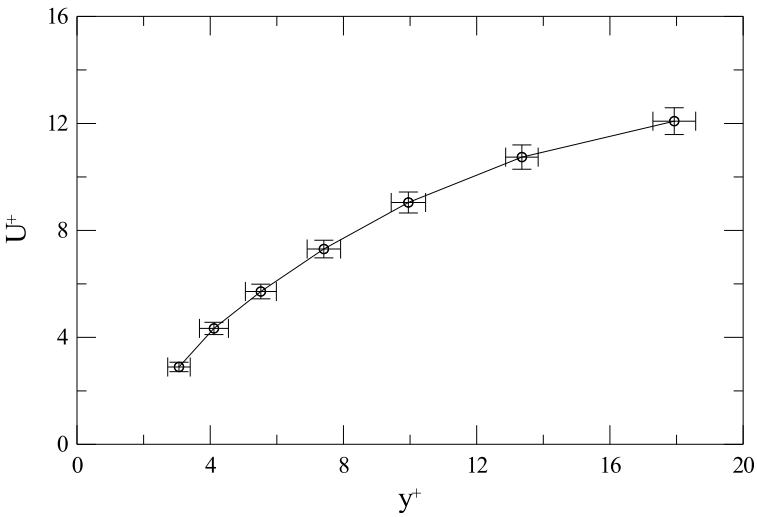

Figure 3.4: Inner region of mean velocity profile at $x' = 0.75$

the ramp where it is subjected to a mild adverse pressure gradient, without separating. The boundary layer thickens rapidly, increasing by 75% along the length of the ramp. No inflection point is observed in the profiles along the ramp, although one is usually expected in adverse pressure gradient flows. Figure 3.4 shows the inner region, ($y^+ < 20$), of the mean velocity profile three quarters of the way down the ramp, where the observation of an inflection point would be most easily noted due to its distance along the adverse pressure gradient. As can be seen in this figure, there is no inflection point observed in this profile. The lack of an inflection point is due to the weak nature of the adverse pressure gradient. For a laminar flow, the necessity of having an inflection point in the mean flow follows from the boundary layer equation. Very near the wall, the inertial terms are negligible so the equation becomes:

$$0 = -\frac{1}{\rho}\frac{\partial P}{\partial x} + \frac{\partial}{\partial y}\left(\nu\frac{\partial U}{\partial y}\right) \tag{3.3}$$

This equation is therefore a balance between the pressure gradient and the curvature of the streamwise mean velocity. For an adverse pressure gradient, the curvature at the wall must have the same sign as the pressure gradient. Therefore, the curvature of the velocity at the wall must be greater than zero. The curvature of the velocity in the outer layer or freestream is negative. Thus there must be an inflection point for a laminar flow in order to match the curvature over the profile. For the turbulent flow an additional term is

included in the Reynolds averaged boundary layer equations so that neglecting the mean inertia terms near the wall:

$$0 = -\frac{1}{\rho}\frac{\partial P}{\partial x} + \nu\frac{\partial^2 U}{\partial y^2} - \frac{\partial}{\partial y}\left(\overline{u'v'}\right) \tag{3.4}$$

In this equation the balance is between the pressure gradient and the sum of a term proportional to the curvature of the mean velocity profile and the Reynolds shear stress gradient. The curvature of the velocity in the freestream is still negative, but now near the wall, the magnitude of the shear stress gradient as compared with the pressure gradient is important. For a turbulent flow to have an inflection point in the mean velocity profile requires:

$$\frac{\partial^2 U}{\partial y^2}\mid_{y=0} = \frac{1}{\mu}\frac{dP}{dx} - \frac{1}{\nu}\frac{\partial}{\partial y}\left(-\overline{u'v'}\right) \geq 0 \tag{3.5}$$

For an inflection point in an adverse pressure gradient flow:

$$\frac{\partial}{\partial y}\left(-\overline{u'v'}\right) \leq \frac{1}{\rho}\frac{dP}{dx}, where \frac{dP}{dx} \geq 0 \tag{3.6}$$

The Reynolds stress gradient in the measurable near-wall region, $(3 < y^+ < 20)$, is around 2 m/s^2, while the pressure gradient term is approximately 0.5 m/s^2. Therefore, we should not expect to find an inflection point in this region. It is possible that the Reynolds stress gradient drops below 0.5 m/s^2 below $y^+ < 3$, but that could not be observed in the present data, as seen in Figure 3.4. We can determine that if an inflection point is present, it must be extremely close to the wall.

Downstream of the ramp, the boundary layer redevelops on another flat plate. The mean velocity profile has still not recovered at the farthest downstream measurement location, although recovery towards a flat plate boundary layer is observed.

The development of the skin friction coefficient, C_f, is shown in Figure 3.5 plotted versus the normalized distance along the test section. The skin friction coefficient increases slightly in the mild favorable pressure gradient before decreasing along the length of the ramp due to the moderate adverse pressure gradient. The boundary layer does not approach separation, but the skin friction still falls by nearly a factor of two relative to the upstream boundary layer. The freestream velocity decreases by only 11% in the same distance. Once the flow starts redeveloping along the flat plate, the skin friction coefficient again rises due to the mild favorable pressure gradient before flattening out at the last measurement location. The Ludweig-Tillmann relation for the skin friction coeffiecient:

$$c_f = 0.246\left(\frac{U_e\theta}{\nu}\right)^{-0.268} 10^{-0.678H} \tag{3.7}$$

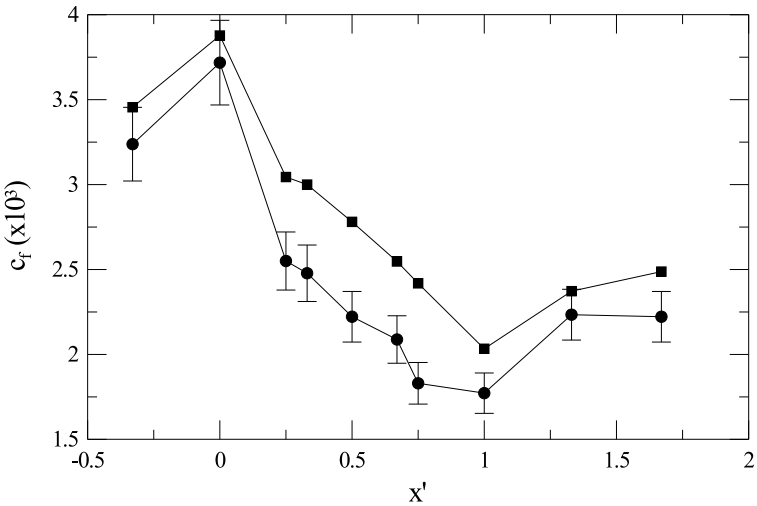

Figure 3.5: Skin friction development (current data •, Ludweig-Tillmann relation ■)

was also plotted using values from the experiments. Overall the relationship overpredicts the skin friction but the trend in skin friction coefficient is well represented by this relationship.

The development of the mean streamwise velocity profile along the flat plate and down the ramp is shown in Figure 3.6a. The velocity is normalized by the local freestream velocity and the y coordinate is scaled by the height of the ramp in order to show the growth of the boundary layer. The mean velocity profile shows that the boundary layer grows rapidly along the ramp. The changing behavior of the shape factor can be observed in the mean velocity profiles. In each successive profile along the ramp, the mean profile becomes less full corresponding to the monotonic increase in shape factor. The shape factor behavior can be observed by examining the values given in Table 3.1. Initially, the shape factor decreases in the region of the flow subjected to the mild favorable pressure gradient. Once the flow reaches the ramp, the shape factor increases in a mostly linear way; however, the shape factor at the start of the ramp does not exhibit this linear trend and is the same for the first two locations.

Figure 3.6b shows the redevelopment of the mean streamwise velocity profile, starting at the end of the ramp where $x' = 1.00$. Again, the velocity is normalized by the local freestream velocity and the y coordinate is scaled by the height of the ramp. The upstream flat plate boundary layer is shown for reference. These velocity profiles exhibit an obvious inflection point in the outer layer and look similar to boundary layers recovering downstream of a separation bubble.

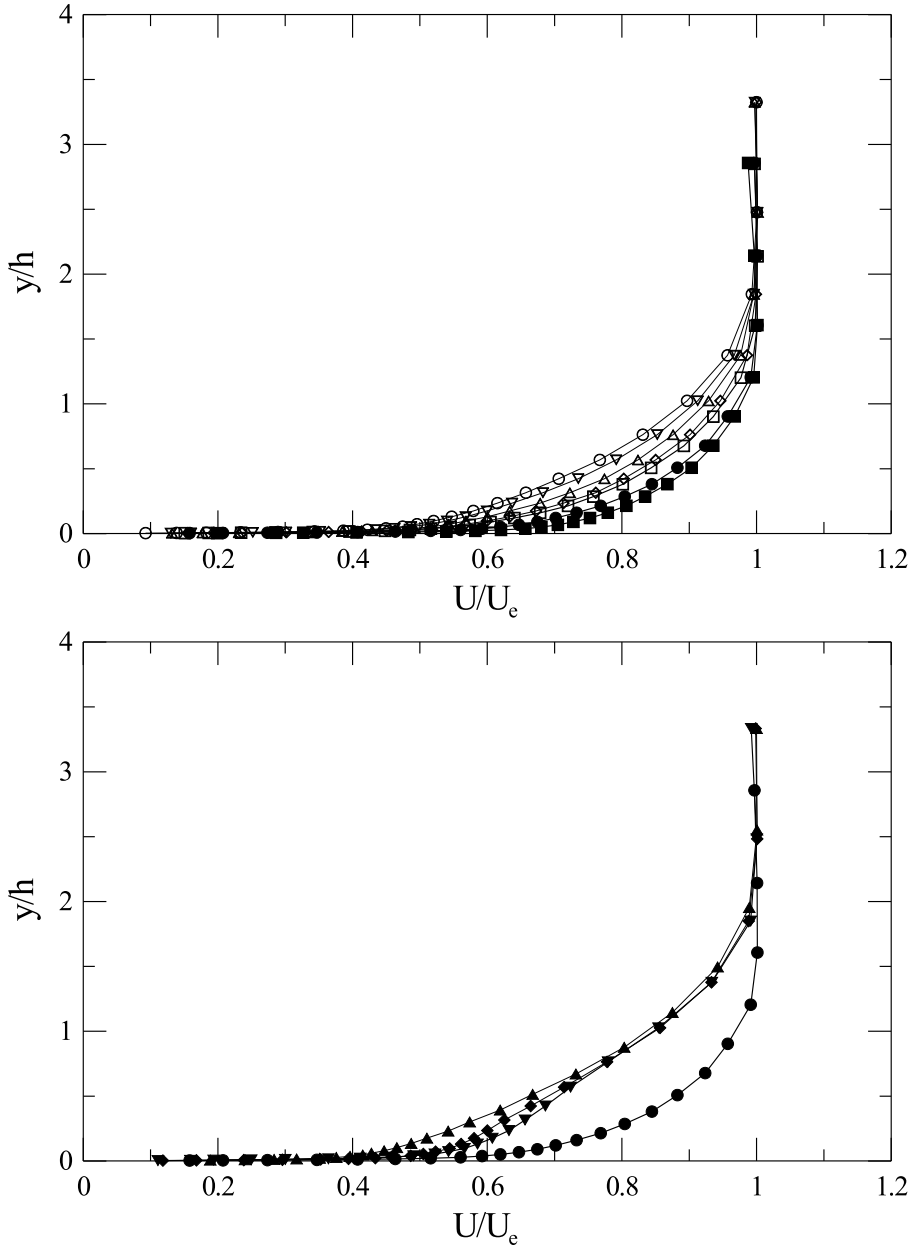

Figure 3.6: Mean velocity profiles in outer coordinates a. along ramp b. in redevelopment region

The mean velocity data are shown in a semi-logarithmic "law of the wall" plot in Figure 3.7a for the upstream flat plate and the ramp. Here the friction velocity calculated from the skin friction measured using oil flow interferometry is used to normalize the profiles, with the exception of the two upstream profile measurements, where the friction velocity

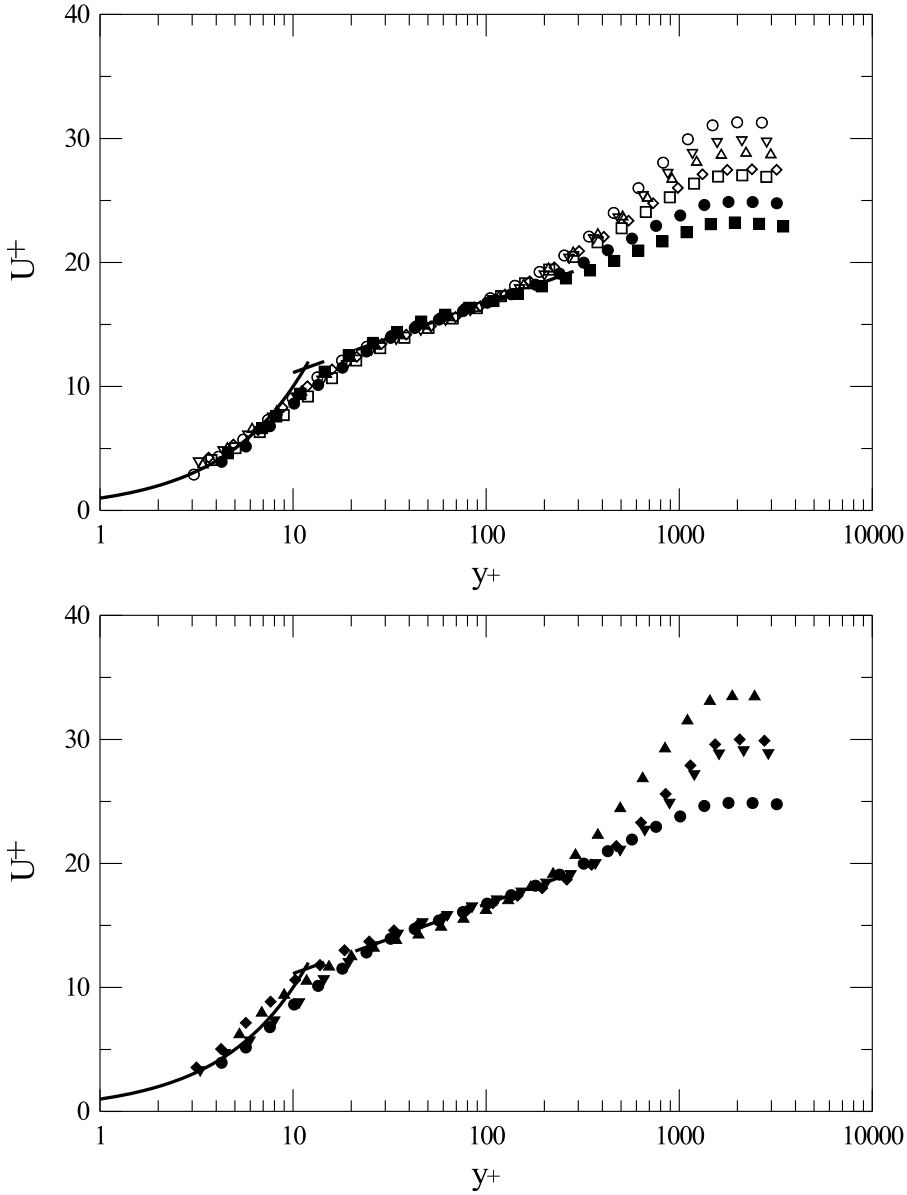

Figure 3.7: Law of the wall plots a. along the ramp b. in redevelopment

was obtained by fitting the mean profile in the logarithmic layer. The profiles exhibit a substantial log region that could be used to estimate the skin friction, however as the flow moves downstream and the wake occupies an increasing fraction of the boundary layer thickness, the outer part of the log region is cut off. In the viscous sublayer, the mean profiles agree well with the line $U^+ = y^+$ for $y^+ = 6.0$ and below. In addition, the profiles

show good agreement in the log layer, between $y^+ = 20$ and 150, using the traditional log law fit with the values of the Karman constant, κ, and the additive constant, B, as 0.41 and 5.5 respectively. The friction velocity values calculated from the oil flow interferometry experiments are accurately estimated based on the agreement between the profiles and the theory. The wake can be observed to grow in strength along the length of the ramp, however for the upstream profile at the start of the ramp, the wake dips below that of the flat plate boundary layer. This is indicative of the acceleration of the flow due to the mild favorable pressure gradient, similar to the results observed by Song (2002).

For the profiles taken downstream of the ramp, the "law of the wall" plot is shown in Figure 3.7b. Again the friction velocity calculated from the skin friction measured using oil flow interferometry is used to normalize the profiles. The profiles exhibit a very large wake profile, which decays as the flow travels downstream in the recovery region. The law of the wall is followed well up to approximately $y^+ = 150$ for the profiles downstream of the end of the ramp, although the wake region has still not recovered back to that of the flat plate boundary layer by the end of the test section.

The recovery profiles shown in Figures 3.6b and 3.7b exhibit some complicated behavior, which is difficult to interpret. The profiles at x' = 1.33 and 1.67 in Figure 3.6b appear similar to inflectional profiles downstream of separation bubbles. However, the boundary layer never separated, and the log law plots do not show the typical dip below the log law commonly observed in such flows. The complex profile shape is probably just caused by the sudden change in pressure gradient near the ramp trailing edge. The mean velocity profile near the wall responds almost immediately to the change in pressure gradient, but the outer layer does not, thus producing an inflectional profile. However, we can not rule out the possibility that the profile shape could have been caused by flow three dimensionality. The boundary layer experiences a small amount of concave streamwise curvature at the ramp trailing edge, which could lead to the formation of roll cells in the boundary layer (Barlow and Johnston (1988)). However, the curvature is quite small, and there was no evidence of spanwise variation in the skin friction near the centerline. Another possibility is secondary flow induced at the endwalls by the vertical pressure gradient. This would cause flow to move down the endwalls and inward toward the center of the channel. Pompeo et al. (1993) showed that converging flow such as this produces mean velocity profiles that are less full than a two-dimensional profile. However, the converging flow would also cause rapid boundary layer growth on the tunnel centerline. As seen in Figure 3.6b, boundary

layer growth was insignificant between x' = 1.00 and 1.67. Therefore, it seems unlikely that three-dimensional effects played a significant role.

Regardless of the reason for its existence, the inflectional mean velocity profile shape in the recovery region makes it difficult to interpret the turbulence data presented below. The primary goal of this thesis is to examine the effects of a sustained mild adverse pressure gradient on the turbulence development. While results in the recovery region are presented below for completeness, the main emphasis will be on the profiles measured over the ramp itself.

The wall-normal component of the mean velocity was also measured, although it is not plotted here for brevity. It remains small throughout the flow field indicating that the boundary layer remains far from separation.

3.3 Reynolds Stress Development

The development of the turbulent stresses, $\overline{u'u'}, \overline{v'v'}$, and $-\overline{u'v'}$ are shown in Figures 3.8, 3.9, and 3.10. To show the change in the peak stress levels as the flow develops, the normalization of the stresses used fixed quantities measured at the reference station. For the streamwise normal stress, $\overline{u'u'}$, the scaling of $u_{\tau,ref}U_{e,ref}$ was used, while for the wall normal, $\overline{v'v'}$, and the Reynolds shear stress, $-\overline{u'v'}$, the normalization of $u^2_{\tau,ref}$ was used, as described by DeGraaff and Eaton (2000). The ramp shape shown on this figure again is drawn to scale with the vertical height expanded by a factor of two relative to the horizontal axis in order to show the flow in the near wall region more clearly. As with the mean velocity development, equally spaced data are shown with additional data profiles removed for clarity.

The development of the streamwise normal stress, $\overline{u'u'}$, shows that as the flow is subjected to the adverse pressure gradient, an outer plateau develops. This outer plateau increases in intensity relative to the inner peak as the flow continues down the ramp. In addition, the maximum value of the inner peak decreases along the adverse pressure gradient. When the adverse pressure gradient is removed, the plateau starts to decay, although by the far downstream measurement location it is still clearly present. The inner peak also starts to increase in value back towards its initial flat plate value. This agrees with the observations of the mean flow redevelopment that the flow has still not redeveloped in the zero pressure gradient by the end of the test section.

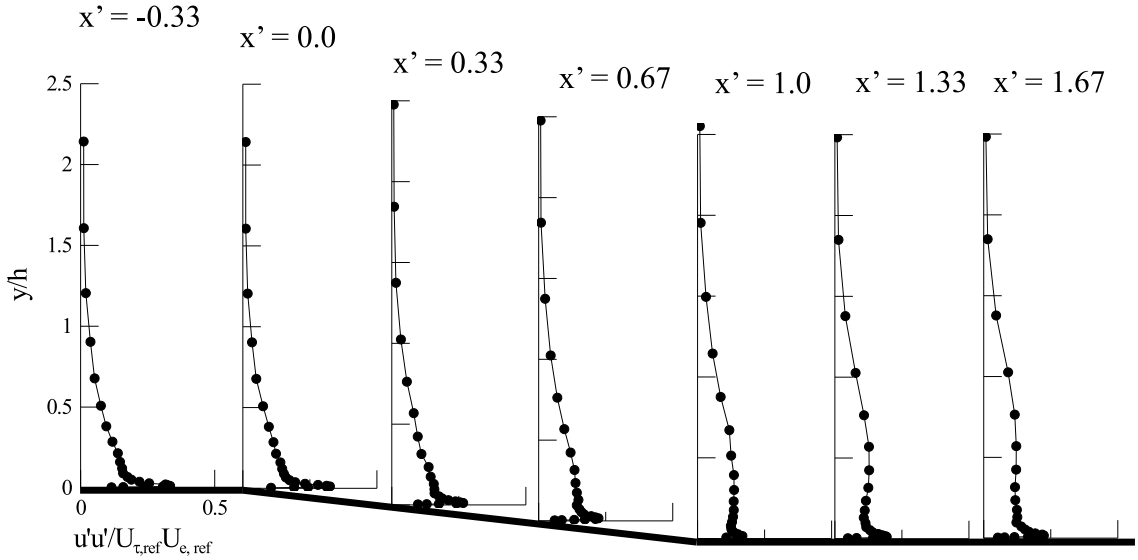

Figure 3.8: Streamwise normal stress development

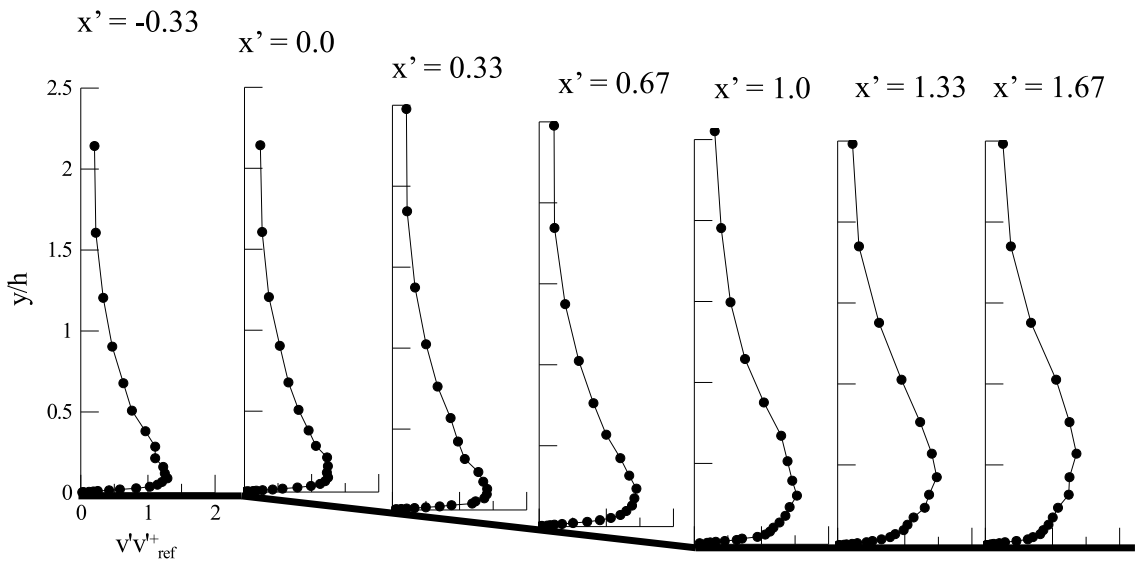

Figure 3.9: Wall normal stress development

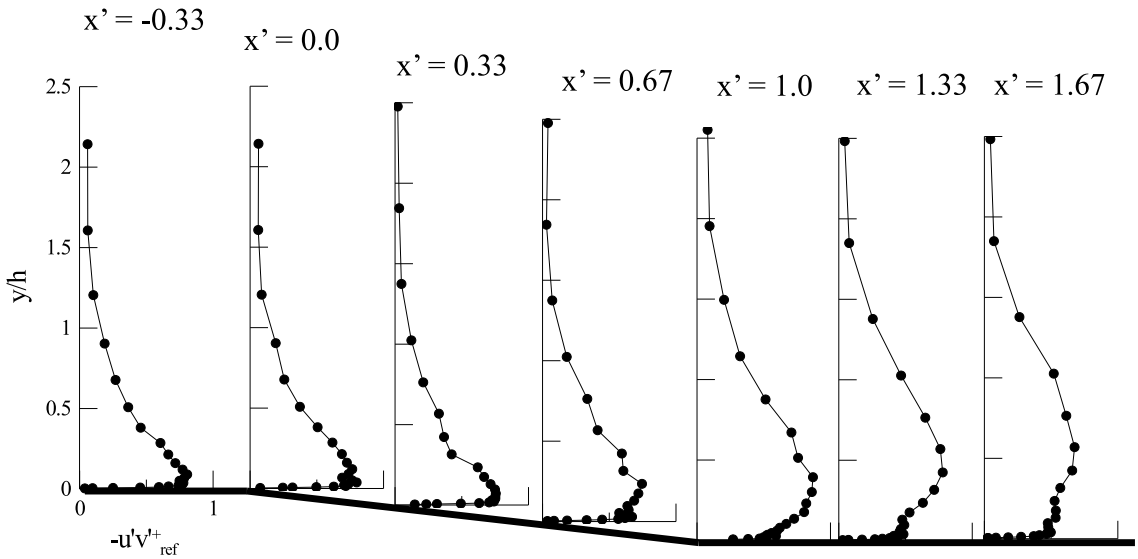

Figure 3.10: Reynolds shear stress development

In the wall normal stress, $\overline{v'v'}$, development, the peak in the stress can be observed to move away from the wall and grow in strength as the flow travels down the ramp. The peak starts to decay over the redevelopment flat plate, although it remains in the outer layer even at the farthest downstream measurement location. In addition, when the flow reaches the flat plate redevelopment region, the peak spreads out becoming wider than along the adverse pressure gradient.

For the Reynolds shear stress, $-\overline{u'v'}$, development, the peak moves away from the wall in the adverse pressure gradient region of the flow, while remaining approximately the same intensity. When the flow again is subjected to a zero pressure gradient, the outer peak can be observed to start to spread out, becoming wider, and to decay away. In addition, an inner peak appears to develop in the near wall region as the flow redevelops.

The streamwise normal stresses profiles are shown in detail in Figure 3.11. Here the profiles are scaled using the scaling proposed by DeGraaff and Eaton (2000), using the local values of the friction velocity and the freestream velocity. The vertical height, in the rotated frame, is normalized by the local viscous length scale and plotted to emphasize the near wall region of the profiles. The first figure shows the development of the stress from the upstream flat plate through the end of the ramp. The second figure shows the redevelopment of the stresses. The inner peak is observed to change very little over the entire test section, while an outer plateau develops as the flow is subjected to the adverse pressure gradient and only

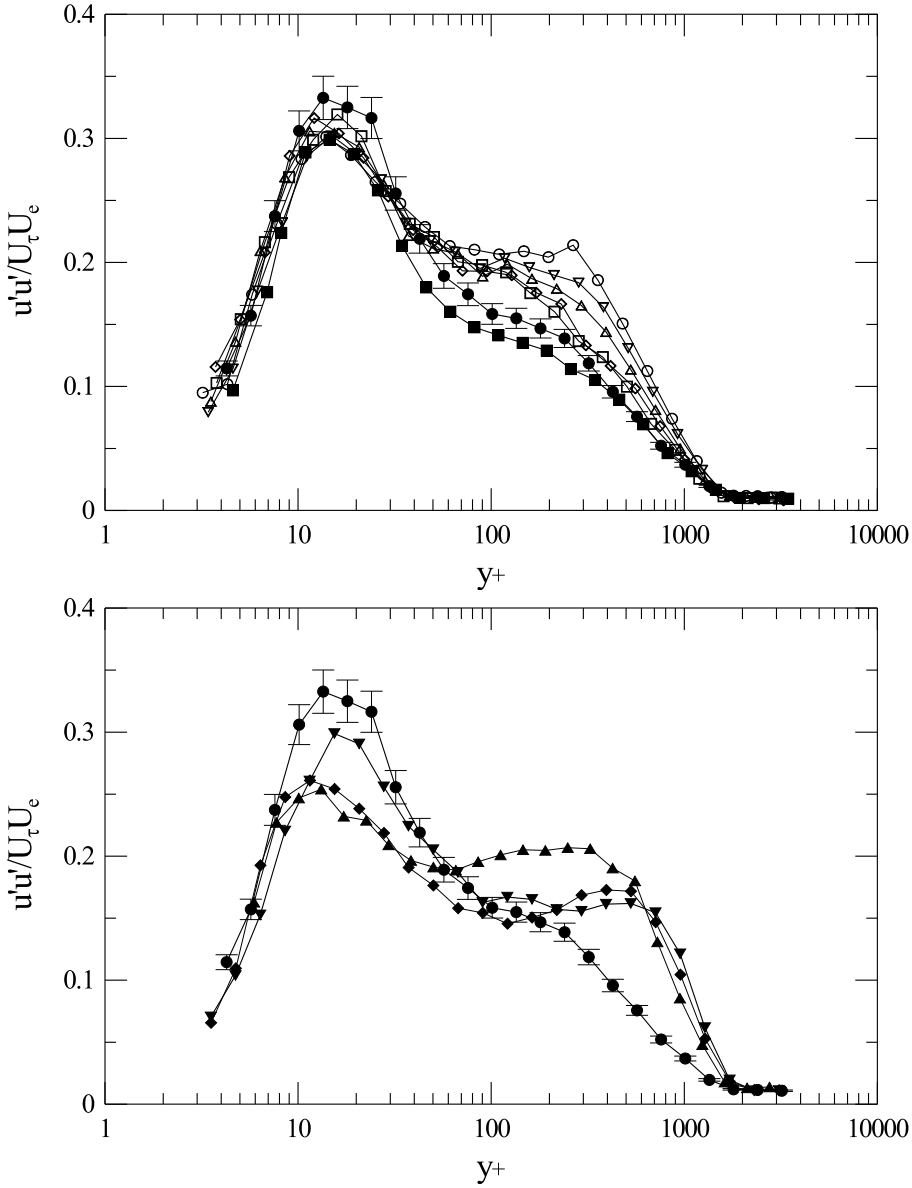

Figure 3.11: Streamwise normal stress profiles in inner coordinates a. along the ramp b. in redevelopment, uncertainty bars indicative of uncertainty in all profiles

slowly decays when the pressure gradient is removed.

The wall normal stress profiles are shown in detail in Figure 3.12. In the inner region, the wall normal stresses collapse well for the adverse pressure gradient, but do not collapse onto the flat plate profile. In addition, in these coordinates the peak of the wall normal stress increases by almost a factor of two along the adverse pressure gradient and also moves

out from the wall. In the redevelopment region, the peak starts to decay and the inner layer recovers back to the flat plate value by the farthest downstream location. Dimensionally, the peak value of the wall normal stress when unscaled remains constant along the flow and the location of the peak moves away from the wall so that it remains at the same relative height within the boundary layer.

The Reynolds shear stresses are shown in detail in Figure 3.13. The Reynolds shear stress scaled in the flat plate scaling shows good collapse for both the adverse pressure gradient data and the upstream flat plate boundary layer data in the inner portion of the boundary layer. However, the Reynolds shear stress does not appear to collapse in the outer layer with a peak forming which then grows along the adverse pressure gradient ramp. This peak in the Reynolds shear stress decays as the flow redevelops, although it too is still present at the farthest downstream measurement location. In the redevelopment profiles, the outer layer shows no collapse due to this peak, while the inner layer shows some collapse.

3.4 Turbulent kinetic energy

The production of turbulent kinetic energy for a two-dimensional boundary layer subjected to an adverse pressure gradient which causes a non-zero wall normal velocity can be written as:

$$Production = -\overline{u'v'}\left(\frac{\partial U}{\partial y} + \frac{\partial V}{\partial x}\right) + \left(\overline{u'u'} - \overline{v'v'}\right)\frac{\partial V}{\partial y} \tag{3.8}$$

where the first term represents shear production and the second term represents the normal stress production. All terms in equation 3.8 were measured, so it can be used to evaluate the turbulent kinetic energy production. The development of the production of turbulent kinetic energy is shown in Figure 3.14, where the production term and the height above the wall are normalized in local inner variables. The peak value is observed to change very slightly in the adverse pressure gradient region, with a slight decrease observed at the start of the ramp. This quickly recovers to a value near that observed in the flat plate boundary layer. The redevelopment profiles show that the production is much lower once the pressure gradient is removed. The value of the slope of the production curve in the log region is -1 for the flat plate case, showing that the flow is in local equilibrium. For the adverse pressure gradient profiles the slope in most of the log region, $40 < y^+ < 100$, is also approximately -1, indicating that the turbulence is in local equilibrium. However, for the mild favorable

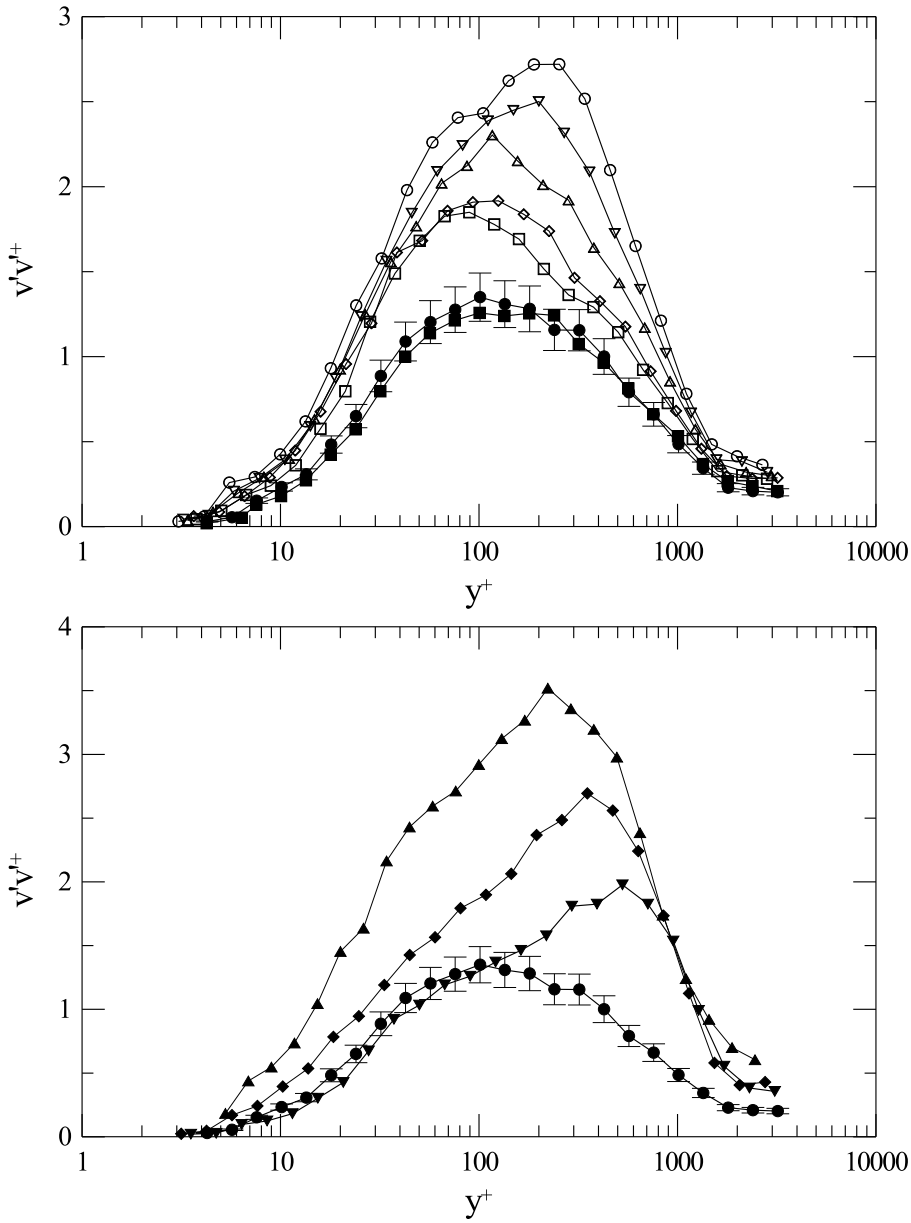

Figure 3.12: Wall normal stress profiles in inner coordinates a. along the ramp b. in redevelopment, uncertainty bars indicative of uncertainty in all profiles

pressure gradient, the slope is distinctly different from -1, showing that the flow at the start of the ramp is out of equilibrium. At the start of the redevelopment region, the slope is again distinct from -1, indicating that the flow is out of local equilibrium. The slope returns to a value of approximately -1 at the farthest downstream measurement location,

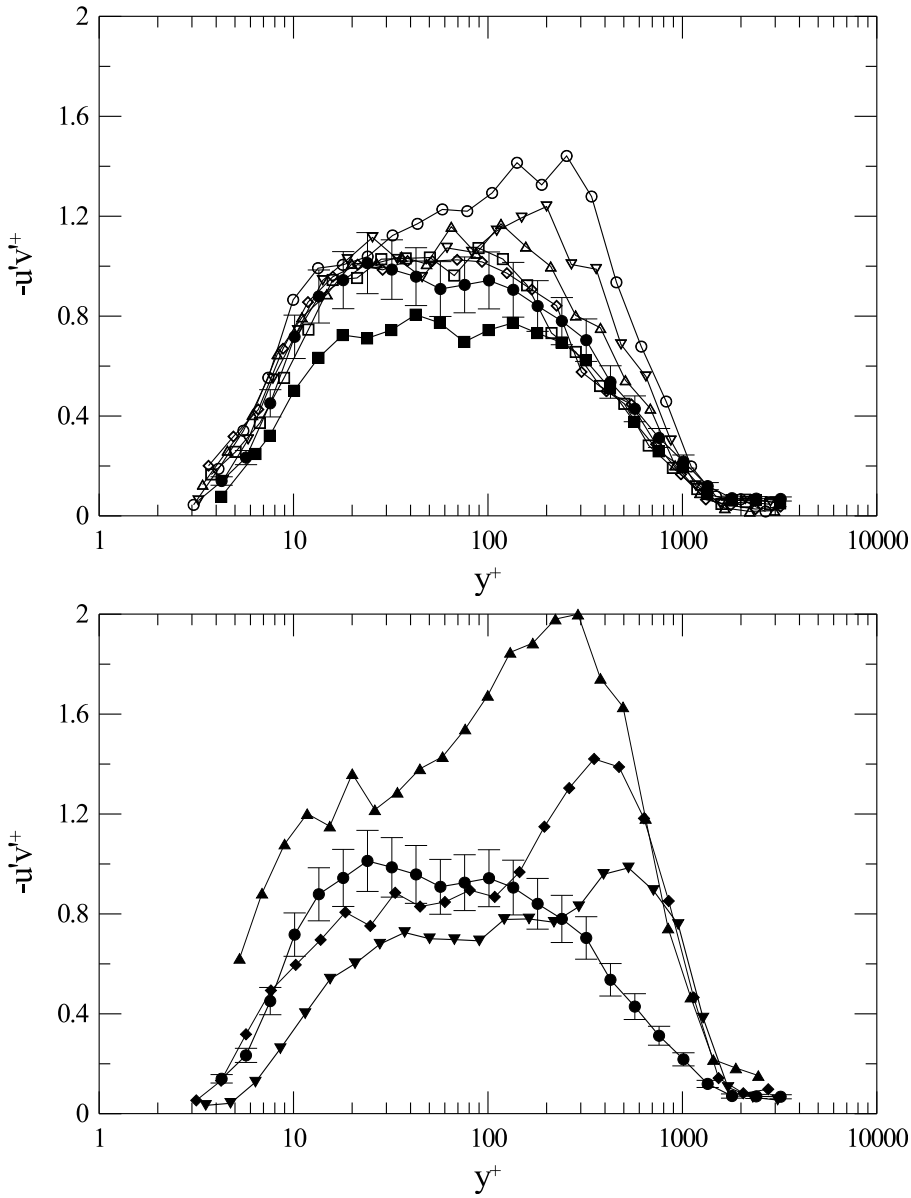

Figure 3.13: Reynolds shear stress profiles in inner coordinates a. along the ramp b. in redevelopment, uncertainty bars indicative of uncertainty in all profiles

implying that the flow is returning to that of an equilibrium flat plate flow. Unlike the work by Skåre and Krogstad (1994), where two peaks were observed in the production term, only one peak is observed in these data. The inner peak, which is observed here, is due to the increase of the mean strain as the wall is approached. The outer peak that was observed by

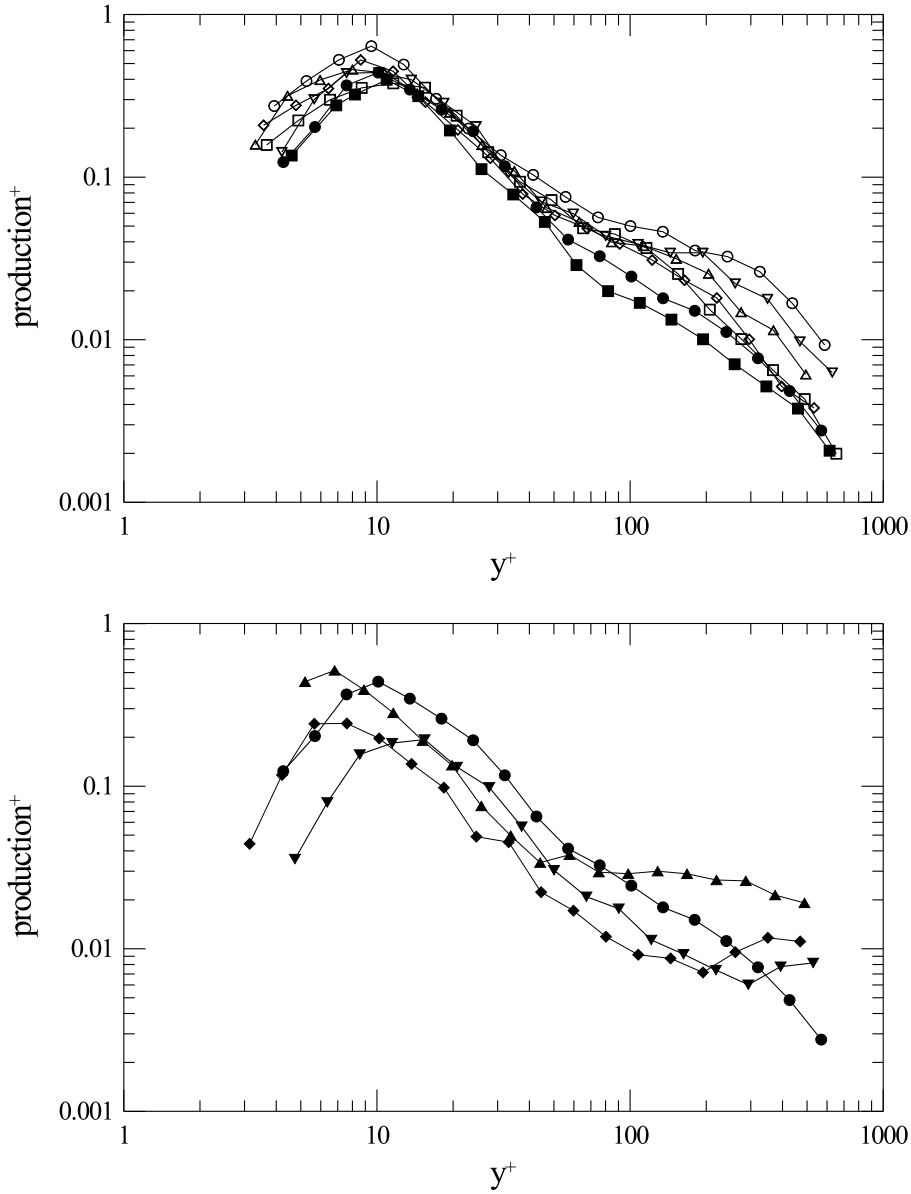

Figure 3.14: Production in inner coordinates a. along the ramp b. in redevelopment

Skåre and Krogstad (1994) is due to the peak in the turbulence stresses, which they noted was caused by the strong adverse pressure gradient in their experiment. In the current case, the outer peak in the Reynolds shear stress produces only a small bump in the outer layer production, which decays away rapidly in the redevelopment region. The weaker pressure gradient in the current case results in a simpler turbulence structure.

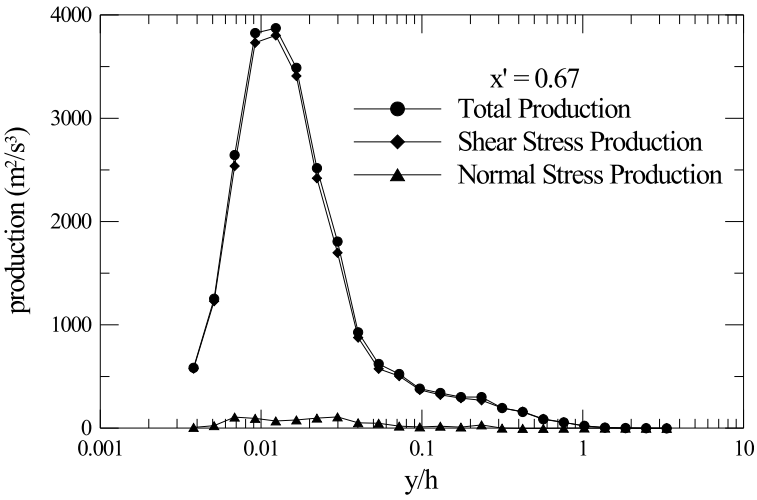

Figure 3.15: Production components at x' = 0.67

The contribution of the normal stresses to the turbulent kinetic energy production is very small in all regions of the flow. Figure 3.15 shows the contributions of the shear and the normal stress components in addition to the total production. In this figure, the production is given dimensionally and is plotted against the height above the wall normalized by the ramp height. This figure is indicative of the entire flow field and shows that the shear stress produces almost all of the production for this flow.

The development of q^2, approximated using $q^2 = \frac{3}{2}(\overline{u'^2} + \overline{v'^2})$ over the ramp is shown in Figure 3.16. The mixed scaling collapses the inner peak well, except for the profile at $x' = 0.0$. This is because q^2 is dominated by the $\overline{u'^2}$ term. In the outer layer, the value of q^2 increases rapidly at the start of the adverse pressure gradient and then increases more slowly as the flow proceeds along the adverse pressure gradient, forming an outer peak similar to those seen in the individual stresses. This peak starts to decay as the flow recovers, but is still present at the last measurement location.

3.5 Structural Parameter Development

The affects of the adverse pressure gradient on the structure of the turbulence is examined through the evaluation of several different dimensionless turbulent structure parameters. The Townsend structure parameter, $a_1 = \overline{u'v'}/q^2$ is shown in Figure 3.17, plotted against the height above the wall scaled by the local momentum thickness. The values of the

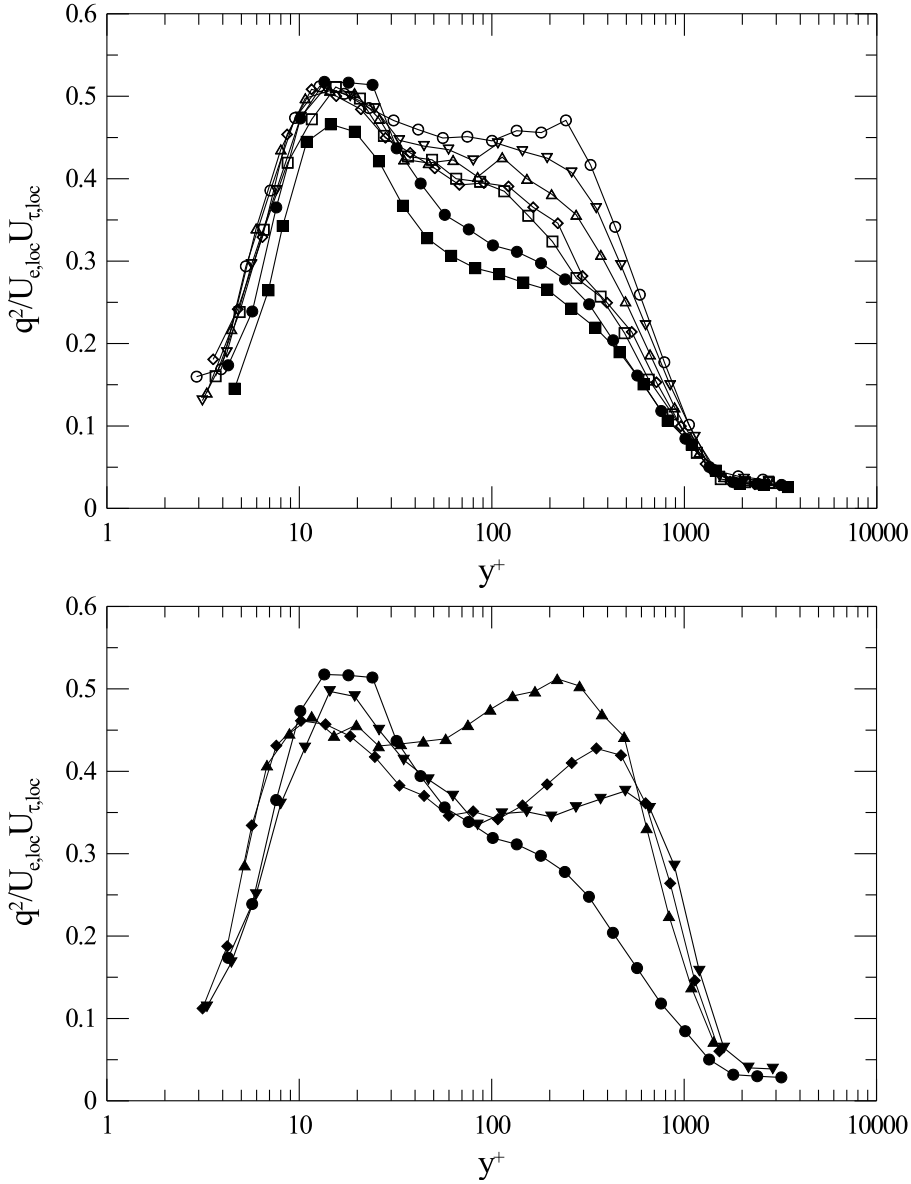

Figure 3.16: Turbulent kinetic energy development a. along ramp b. in redevelopment

structure parameter were smoothed using a weighted average of the point and its nearest neighbors. The Townsend structure parameter for a flat plate boundary layer is generally taken to be constant with a value of 0.15 (Bradshaw (1967a)). As the adverse pressure gradient is imposed, the Townsend structure parameter decreases in value to approximately 0.14 for all the locations in the adverse pressure gradient. The Townsend parameter is seen

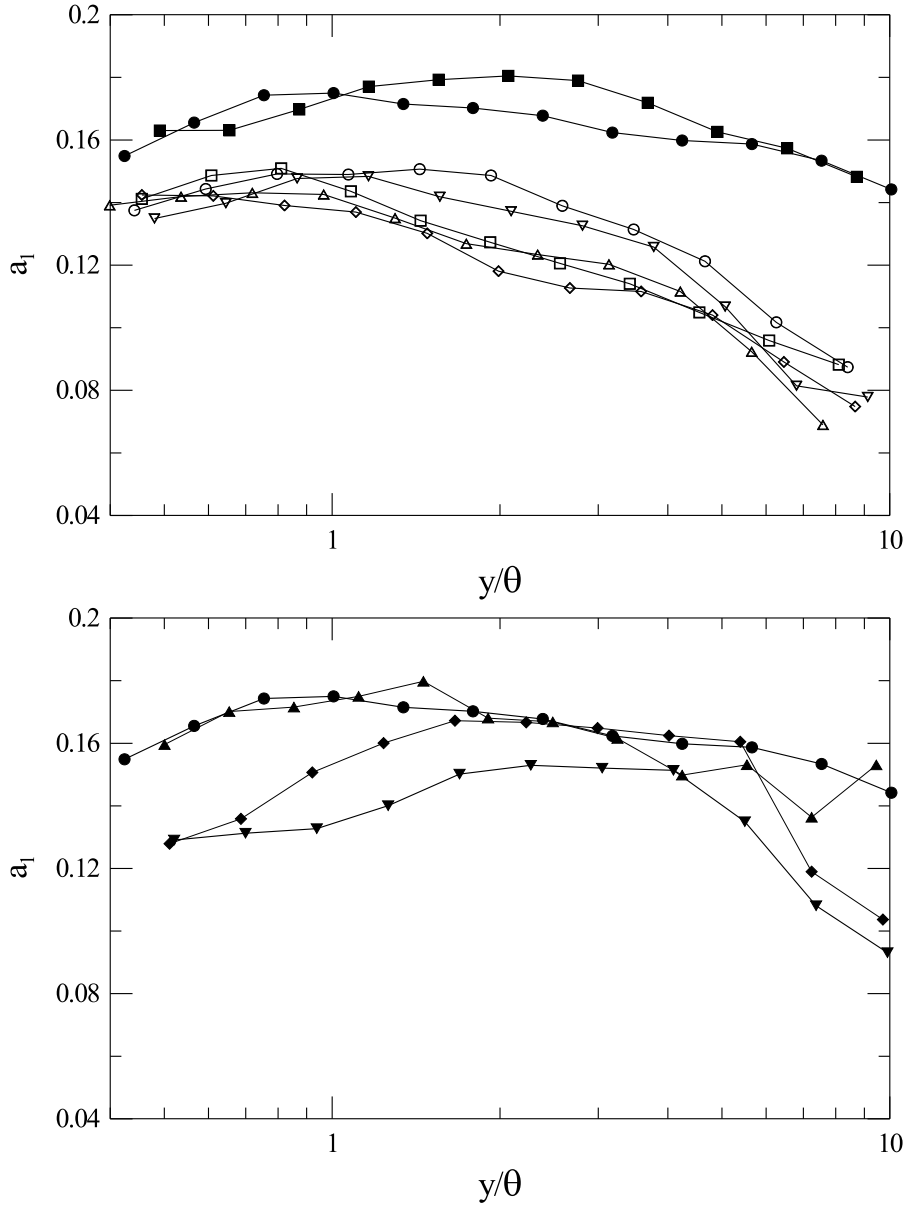

Figure 3.17: Townsend parameter, a_1, development a. along ramp b. in redevelopment

to decrease near the outer edge of the boundary layer as noted by Bradshaw (1967a). Bradshaw attributed this to the irrotational motions becoming comparable in intensity to the turbulence fluctuations. Spalart and Watmuff (1993) also noted this dip in the outer region of the boundary layer in their experimental and computational work. Skåre and Krogstad (1994) found that the structure parameter was constant, but slightly lower for the adverse

pressure gradient case than for the zero pressure gradient case, which is seen in the inner region here. Their plot also shows the same dip in the outer region of the boundary layer as observed by Bradshaw and in the data shown here. As the flow redevelops, the Townsend parameter relaxes back towards its flat plate value, particularly in the outer region where the value increases rapidly back to near the flat plate value, while the inner region increase is much slower. The slow recovery in the inner layer is likely due to the atypical mean velocity profiles discussed previously.

The development of the anisotropy parameter, $\overline{v'v'}/\overline{u'u'}$, plotted against the height above the wall scaled on the momentum thickness, is shown in Figure 3.18. The anisotropy parameter for the flat plate location varies between 0.3 and 0.4 throughout most of the boundary layer. As the adverse pressure gradient is imposed, the anisotropy parameter increases slightly, but this increase is observed to be monotonic. This indicates that the turbulence is becoming slightly more isotropic. After the pressure gradient is removed, the anisotropy parameter does not recover to the zero pressure gradient value over the development length examined. The relatively small changes in the anisotropy parameter indicate that the normal stress components respond almost equally to the imposed adverse pressure gradient. Previous work has shown this parameter to be very sensitive to streamline curvature. The small changes shown here indicate that streamline curvature effects are negligible in the present flow.

Figure 3.19 shows the Reynolds stress correlation plotted against the height above the wall scaled on the momentum thickness. The flat plate profile shows a mostly constant correlation with a value of approximately 0.40. As the flow encounters the adverse pressure gradient, the correlation coefficient decreases to a value of approximately 0.30 and remains at this value until the flow redevelops on the flat plate, at which point the coefficient starts to increase back to a value near that of the initial flat plate profile. This effect due to the adverse pressure gradient is different than what was observed by Skåre and Krogstad (1994). They noted that the value of the Reynolds stress correlation was approximately the same for their flow near separation as it was for the zero pressure gradient case. The difference here may be related to the differences in pressure gradient. The results shown here are also unlike those observed by Elsberry et al. (2000) who noted that the Reynolds stress correlation varied with streamwise position in an adverse pressure gradient flow. The difference in the observations in the current data and in their work may also be due to strength of the adverse pressure gradient.

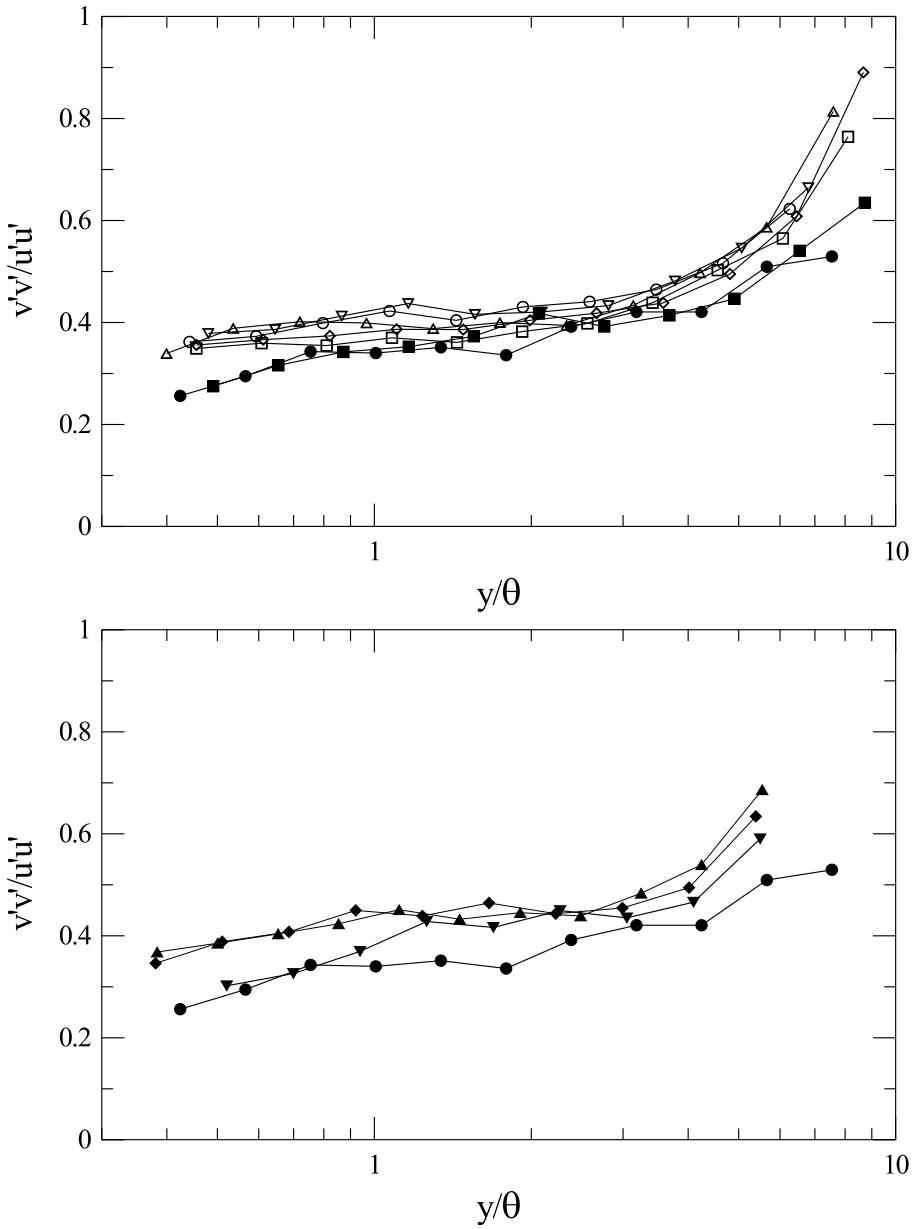

Figure 3.18: Anisotropy parameter development a. along the ramp b. in redevelopment

The overall conclusion that may be reached is that the turbulence structure undergoes relatively mild changes even though it is exposed to the adverse pressure gradient. Thus, we might expect that we will be able to find suitable scalings to collapse the stress data onto the flat plate profiles.

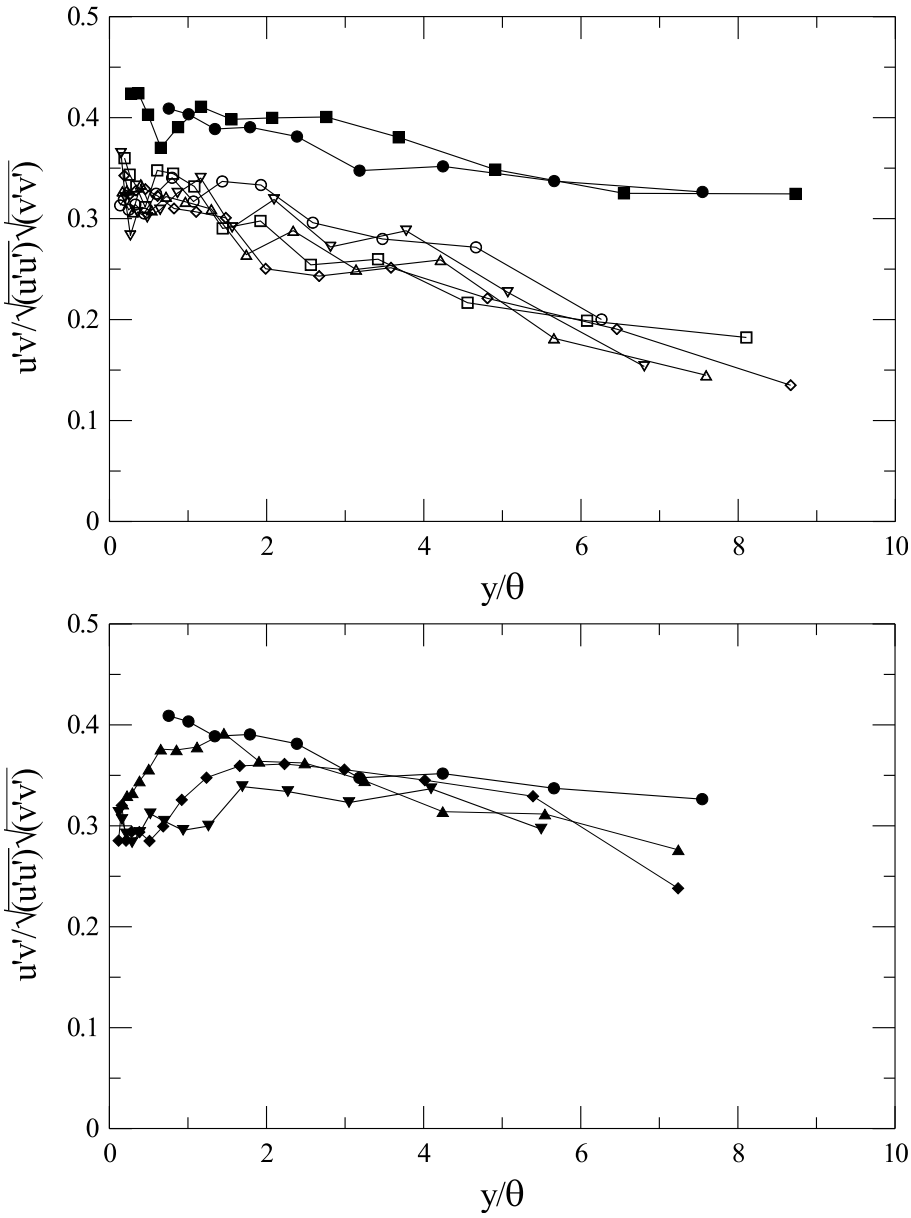

Figure 3.19: Reynolds stress correlation development a. along the ramp b. in redevelopment

3.6 Quadrant Analysis of Adverse Pressure Gradient Flow

Quadrant analysis following the overall approach of Lu and Willmarth (1973) was performed on the current data to examine the contributions of various motions to the overall flow. This analysis shows the structure of turbulence and the relative contribution of sweeps,

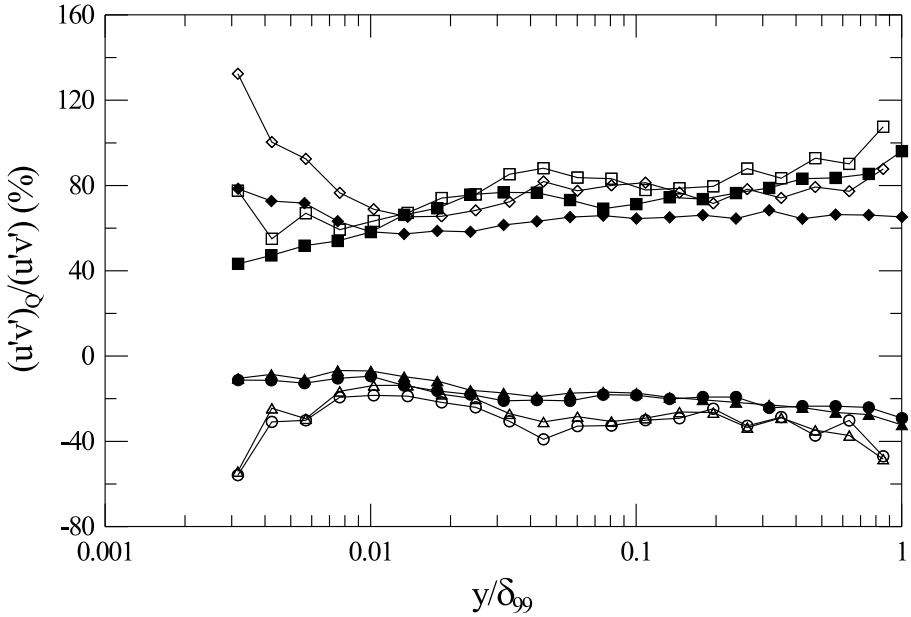

Figure 3.20: Quadrant analysis comparison $H = 0.0$ (closed symbols represent upstream reference location, open symbols represent the adverse pressure gradient location)($Q1\bullet, Q2\blacksquare, Q3\blacktriangle, Q4\blacklozenge$)

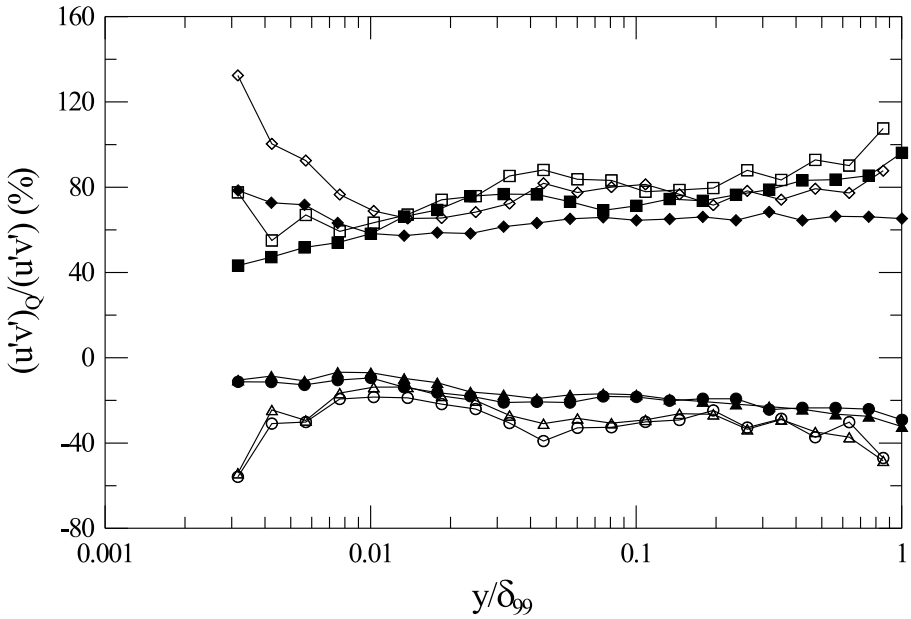

Figure 3.21: Quadrant analysis comparison $H = 2.5$ (closed symbols represent upstream reference location, open symbols represent the adverse pressure gradient location)($Q1\bullet, Q2\blacksquare, Q3\blacktriangle, Q4\blacklozenge$)

ejections and inward and outward interactions. The work of Lu and Willmarth (1973) developed the concept of the hyperbolic hole of size H, as described in Equations 1.33 and 1.34.

Quadrant analysis performed on the current data showed that for H = 0, or all events, the adverse pressure gradient increases the magnitude of the effects of all four components: sweeps, ejections, inward and outward interactions. The sweep and ejection (Q4, Q2) events are dominant for all locations in the flow over the outward and inward interaction (Q1, Q3) events. Figure 3.20 shows the four different quadrant results for both the flat plate location and an adverse pressure gradient location, 2/3 of the length down the ramp. The quadrant decomposition, shown as a percent, is plotted against the height above the wall scaled on the boundary layer thickness. When examining all locations, the sweeps (Q4) and ejections (Q2) are very similar in contribution throughout the boundary layer with sweeps contributing slightly less in the outer portion of the boundary layer and contributing slightly more in the inner portion. Figure 3.21 shows a comparison of the four different quadrant decomposition results for moderate and strong events (H = 2.5), for both the flat plate region of the flow and for the flow along the ramp, again 2/3 of the length down the ramp. The results at other locations in the adverse pressure gradient look similar, and the results are also similar for H = 4.0, strong events. The sweep (Q4) events for the adverse pressure gradient contribute a slightly smaller per cent of the total when compared to the flat plate case for the middle of the boundary layer, while being significantly less important in the very near wall region when compared with the flat plate case. In addition, for moderate and strong events the ejection (Q2) events are suppressed near the wall and dominated by the sweep (Q4) events, while in the outer part of the boundary layer the ejection (Q2) events are dominant, as seen by Krogstad and Skåre (1995). However, when the sum of the contributions of ejection and sweep (Q2, Q4) events for the adverse pressure gradient is comparable with the results for zero pressure gradient, the current data show no notable difference between the two cases.

3.7 Summary

The development of an adverse pressure gradient boundary layer at $Re_\theta = 3300$ is examined. The flow does not separate along the 4 degree ramp, although it is subjected to a prolonged adverse pressure gradient, before starting to redevelop along a flat plate. The pressure distribution shows that adverse pressure gradient without separation has been

developed for examination. Additionally, the flow is a non-equilibrium flow in the sense of Clauser due to the varying value of β.

The shape of the mean velocity profile continues to evolve along the entire length of the flow and has not recovered to that of a flat plate boundary layer at the farthest downstream measurement location. The mean flow follows the logarithmic law of the wall for all of the measurement locations, although the wake grows much larger in the adverse pressure gradient, causing the extent of the log region to shrink. No inflection point is noted in the mean flow profiles of the flow along the ramp, however an inflection point does appear in the mean flow at the start of the flat plate redevelopment.

The turbulent stresses all change in the adverse pressure gradient. The streamwise normal stress develops a secondary outer plateau which grows in the adverse pressure gradient and does not completely decay by the farthest downstream measurement location. The wall normal stress peak widens and moves away from the wall in the adverse pressure gradient. The inner layer appears to recover to that expected in the flat plate by the farthest downstream measurement location, but the outer layer is still affected. The Reynolds shear stress in the inner layer does not change much from that of the flat plate boundary layer, however the outer region develops a secondary peak similar to that seen in the other stresses.

The turbulent kinetic energy production shows that the flow is in equilibrium for the adverse pressure gradient and flat plate regions, although it is not for either the mild favorable pressure gradient or the start of the flat plate redevelopment. No outer peak is observed in the production. The development of q^2 is similar to that of the stresses, with the growth of an outer peak in the adverse pressure gradient and then the slow decay in the redevelopment flat plate.

Various structural parameters were examined for this flow. These parameters showed that the structure of the flow is only slightly perturbed by the adverse pressure gradient and does appear to be redeveloping to that of a flat plate boundary layer in the redevelopment region. The structural parameter of Townsend, a_1, does show a consistent reduction in the adverse pressure gradient and a slower recovery near the wall than in the outer layer.

Quadrant analysis showed that only small changes occur in the importance of sweeps, ejections and inward and outward interactions. This is once again indicative of the small changes in the mean velocity profiles and the shear stress profiles.

Overall the flow examined here is only slightly modified from that of a flat plate boundary layer. However small changes in the overall flow have led to much larger changes in the

development of the stresses and they no longer collapse in the traditional flat plate coordinates, which collapse the flat plate data so well. In the next chapter, Reynolds number effects and scalings capable of collapsing the mean and turbulence data are examined.

Chapter 4

Reynolds Number Effects on the Mean Flow and Turbulence

This chapter examines the effects of Reynolds number on the adverse pressure gradient boundary layer described in Chapter 3. The study of the effects of Reynolds number on this adverse pressure gradient flow, which is not highly perturbed when compared with that of a flat plate boundary layer, allows for the examination of the changes caused to the mean flow and turbulence by the application of an adverse pressure gradient and how the scaling of the mean flow and turbulence is thus modified. This flow was measured at three momentum thickness Reynolds numbers, $Re_{\theta,ref} = 3300, 14,100$ and 20,600, as evaluated at the upstream reference location, $x' = -0.33$. Table 4.1 gives values for the atmospheric conditions inside the tank for each of these cases.

The overall effects of changing the Reynolds number are first discussed with respect to the development of the flow, followed by an examination of the mean flow and Reynolds stress changes due to Reynolds number, and finally the Reynolds number effects on the structure of the flow and quadrant analysis. In addition, scaling of the Reynolds stresses, both over the range of Reynolds numbers examined and over the changing pressure gradient along the ramp are presented.

$Re_{\theta,ref}$	$Temperature(K)$	$Pressure(Pa)$	ν x $10^6(m^2/s)$
3300	297	101,300	15.45
14,100	297	481,000	3.26
20,600	299	770,000	2.06

Table 4.1: Wind tunnel conditions

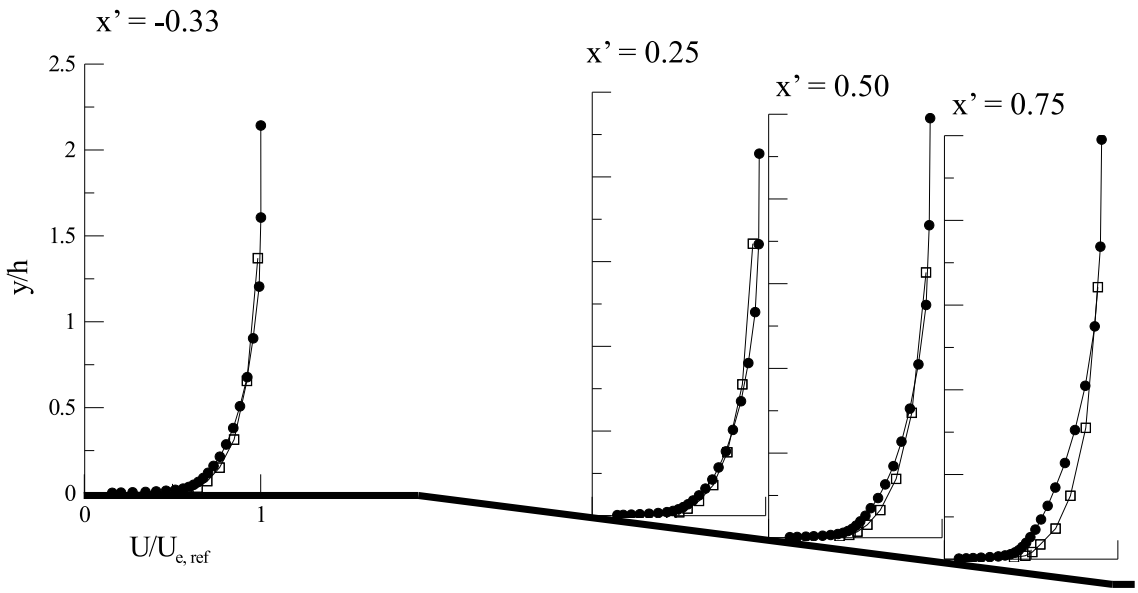

Figure 4.1: Mean flow development for the low and high Reynolds number cases normalized using the fixed quantity, U_e, measured at the reference location (closed symbols represent $Re_{\theta,ref} = 3300$, open symbols represent $Re_{\theta,ref} = 20,600$)

4.1 Overall Reynolds number effects on the flow development

The overall effects of the Reynolds number on the flow development for the streamwise mean velocity are shown in Figure 4.1 for the low and high Reynolds numbers, $Re_{\theta,ref} =$ 3300 and 20,600. In these figures showing the overall development of the flow, the closed circles represent the $Re_{\theta,ref} = 3300$ data and the open squares represent the $Re_{\theta,ref} = 20,600$ data. Unlike in Chapter 3, the redevelopment region is not shown in these figures and the profiles along the ramp are shown at three equally spaced locations, $x' = 0.25, 0.5$ and 0.75, or one quarter, one half and three quarters of the distance down the ramp. The upstream flat plate region and the ramp are shown with the profiles positioned along the ramp at the correct physical locations, with the mean velocity normalized using the freestream velocity at the reference location for each condition and the distance above the wall normalized using the ramp height. The large differences in Reynolds number do not produce large changes for the mean flow development, although some differences are noted as the flow travels further along the ramp. At the farthest location down the ramp, $x' = 0.75$, the mean velocity profile has a significantly different shape, with the higher Reynolds number case showing a much fuller velocity profile. This difference in profile

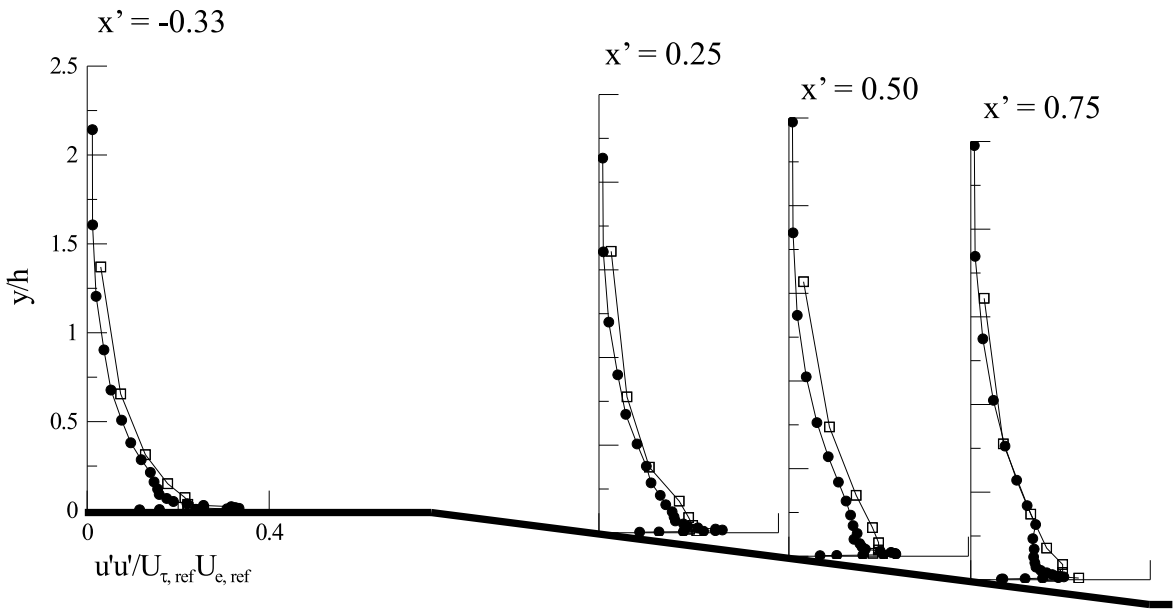

Figure 4.2: Streamwise normal stress development for the low and high Reynolds number cases normalized using the fixed quantity, $(U_e u_\tau)$, measured at the reference location (closed symbols for $Re_{\theta,ref} = 3300$, open symbols for $Re_{\theta,ref} = 20,600$)

shape is also noted at the middle Reynolds number at this location and may indicate that with a longer adverse pressure gradient the mean flow profiles would become less similar.

The Reynolds number effects on the development of the three Reynolds stress components are shown in Figure 4.2, 4.3 and 4.4. Only the ramp and upstream flat plate profiles are shown, with the stresses normalized using the flat plate boundary layer scaling, as described by DeGraaff and Eaton (2000), evaluated at the reference location. Changes are visible in the stress profiles and are observed to be larger than in the mean flow, but the overall Reynolds number effects on the stresses are observed to produce only moderate changes in the stress profiles as compared to flows in more rapidly changing pressure gradients, such as the separating and reattaching flow of Song (2002).

The overall flow parameters for the three Reynolds numbers examined are given in Tables 4.2, 4.3, and 4.4. Table 4.2 is a repeat of Table 3.1 to allow for easier comparison of the parameters between the three Reynolds number cases. Flow parameters are given for all locations where full profiles were measured. At the highest Reynolds number, data were measured at only four measurement locations due to the very low data rate, while for the other two Reynolds numbers a full set of profile data was measured. For the purpose of this

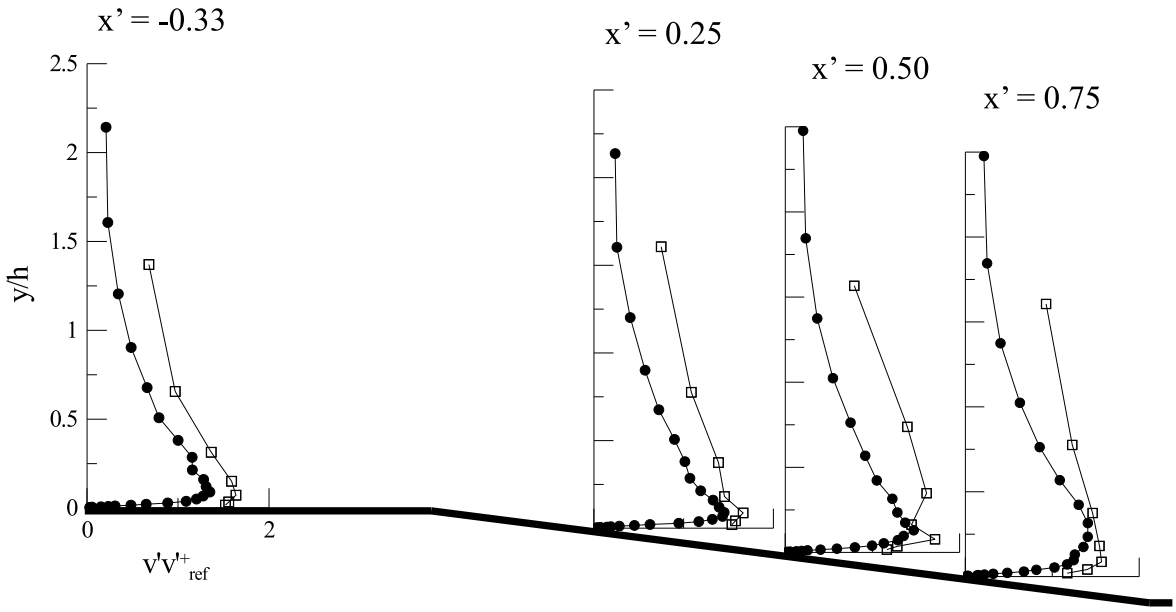

Figure 4.3: Wall normal stress development for the low and high Reynolds number cases normalized using the fixed quantity, (u_τ^2), measured at the reference location (closed symbols for $Re_{\theta,ref} = 3300$, open symbols for $Re_{\theta,ref} = 20,600$)

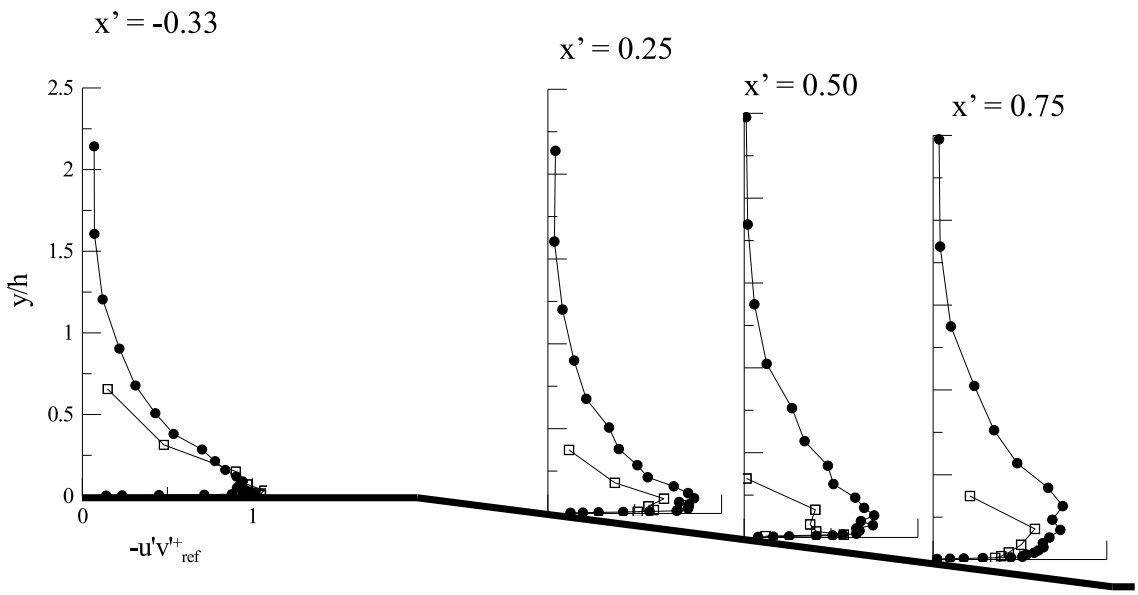

Figure 4.4: Reynolds shear stress development for low and high Reynolds number cases normalized using the fixed quantity, (u_τ^2), measured at the reference location (closed symbols for $Re_{\theta,ref} = 3300$, open symbols for $Re_{\theta,ref} = 20,600$)

x'	$U_e(m/s)$	$\delta_{99}(mm)$	$\theta(mm)$	H	Π	Re_θ	β	$U_\tau(m/s)$
-0.33	20.48	25.22	2.51	1.34	0.37	3330	-0.17	0.82
0	20.62	23.81	2.17	1.29	-0.04	2990	-0.07	0.89
0.25	19.87	29.18	3.10	1.39	0.72	3990	2.07	0.73
0.33	19.60	30.41	3.32	1.39	0.72	4210	1.74	0.72
0.5	19.20	33.77	3.78	1.42	0.87	4700	1.60	0.68
0.67	18.80	35.64	4.24	1.46	0.92	5160	2.31	0.66
0.75	18.71	37.53	4.60	1.48	1.29	5570	1.38	0.62
1	18.23	41.76	5.66	1.56	1.24	6680	-1.41	0.61
1.33	18.26	39.78	5.37	1.47	0.54	6340	-0.37	0.68
1.67	17.54	38.77	5.26	1.45	0.67	6320	-0.18	0.68

Table 4.2: Flow parameters at $Re_\theta = 3300$

x'	$U_e(m/s)$	$\delta_{99}(mm)$	$\theta(mm)$	H	Π	Re_θ	β	$U_\tau(m/s)$
-0.33	20.39	25.81	2.82	1.26	0.24	14080	-0.07	0.73
0	20.42	22.18	2.12	1.21	-0.18	10850	-0.53	0.79
0.25	19.65	31.17	3.76	1.31	0.65	17270	2.94	0.65
0.33	19.44	33.04	4.03	1.31	0.73	18190	2.38	0.63
0.5	18.99	34.57	4.48	1.33	0.91	19440	1.64	0.60
0.67	18.65	35.59	4.92	1.35	1.07	20810	2.74	0.58
0.75	18.50	35.35	5.16	1.38	1.19	21030	2.43	0.56
1	18.21	40.30	5.82	1.39	1.05	23290	-1.98	0.56
1.33	18.04	37.19	5.60	1.35	0.92	22860	-0.35	0.57
1.67	18.07	36.20	5.44	1.33	0.75	22540	-0.25	0.58

Table 4.3: Flow parameters at $Re_\theta = 14,100$

chapter, data from the locations examined at all three Reynolds numbers, $x' = 0.25, 0.5$ and 0.75, will be used.

The skin friction distribution along the bottom wall is shown in Figure 4.5. The overall effect of the increase in Reynolds number is a decrease in the skin friction coefficient, c_f,

x'	$U_e(m/s)$	$\delta_{99}(mm)$	$\theta(mm)$	H	Π	Re_θ	β	$U_\tau(m/s)$
-0.33	16.68	31.57	3.13	1.24	0.15	20560	-0.15	0.58
0.25	15.64	35.45	3.87	1.29	0.25	22940	3.42	0.53
0.5	15.60	38.87	5.04	1.30	0.81	29500	1.78	0.48
0.75	14.90	39.82	5.66	1.38	1.24	31650	2.75	0.44

Table 4.4: Flow parameters at $Re_\theta = 20,600$

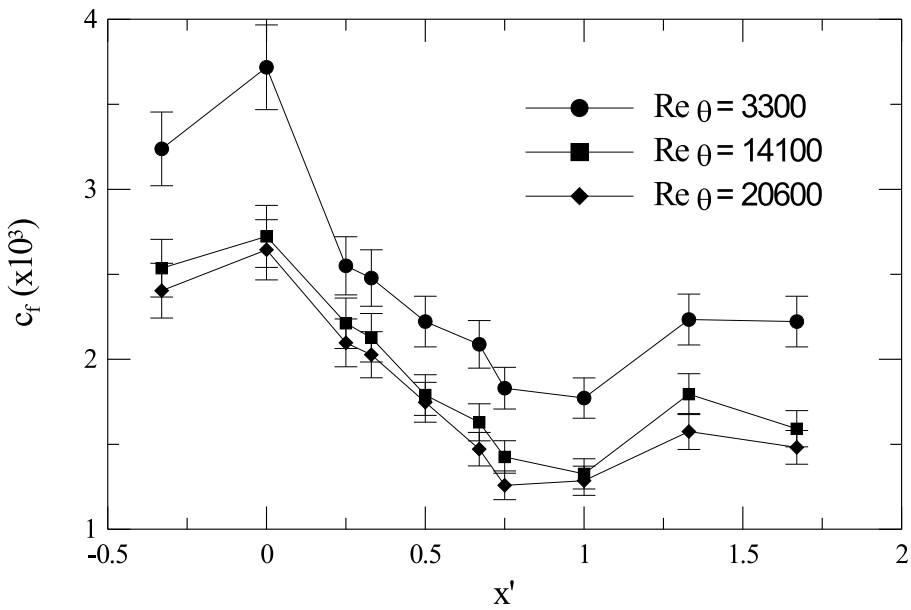

Figure 4.5: Skin friction distribution along bottom wall for all three Reynolds numbers

along the entire length of the flow examined. At the initial upstream flat plate location, the effect of the increasing Reynolds number is to decrease the local skin friction, which is used as the reference value for c_f along the ramp. Other than this decrease with Reynolds numbers, the trend in the skin friction coefficient appears similar for the three Reynolds number cases, with a drop of approximately 50% in the value of the skin friction coefficient along the length of the ramp. The upstream flat plate value of the skin friction was determined through the standard log law fitting of the mean velocity profile. For the one and four atmosphere cases, the velocity at which the wind tunnel was run for the velocity measurements and for the oil flow interferometry measurements were nominally the same and therefore the

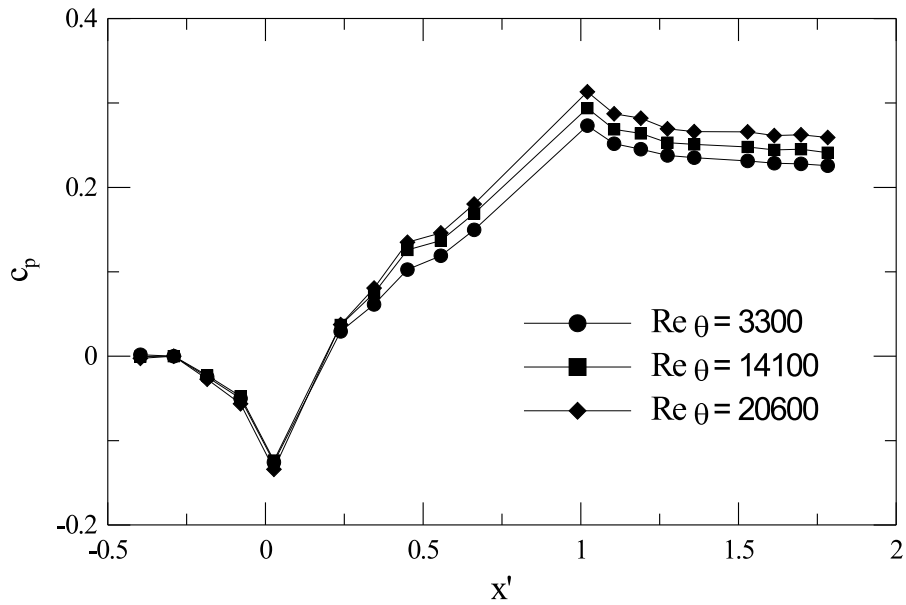

Figure 4.6: Wall static pressure distribution on bottom wall for all three Reynolds numbers

friction velocity was easily extracted from the skin friction coefficient computed using the oil flow technique. For the eight atmosphere case, the oil flow measurements were made at a higher velocity than the subsequent velocity profile measurements. The trends in the skin friction coefficient distribution are similar for all three Reynolds numbers, therefore a similar technique was used to determine the friction velocity for this case. At the reference location, the standard log law fit was used to determine the friction velocity, which was then used to calculate the skin friction coefficient at the reference location. The ratio of the skin friction coefficient at the ramp location and the reference location was determined using the oil flow technique, as described in Chapter 2. This allowed for the calculation of the skin friction coefficient at the ramp location. The value of the friction velocity was then backed out of the skin friction coefficient using the locally measured value of the freestream velocity from the mean profile. This value of the friction velocity was then used when analyzing the data.

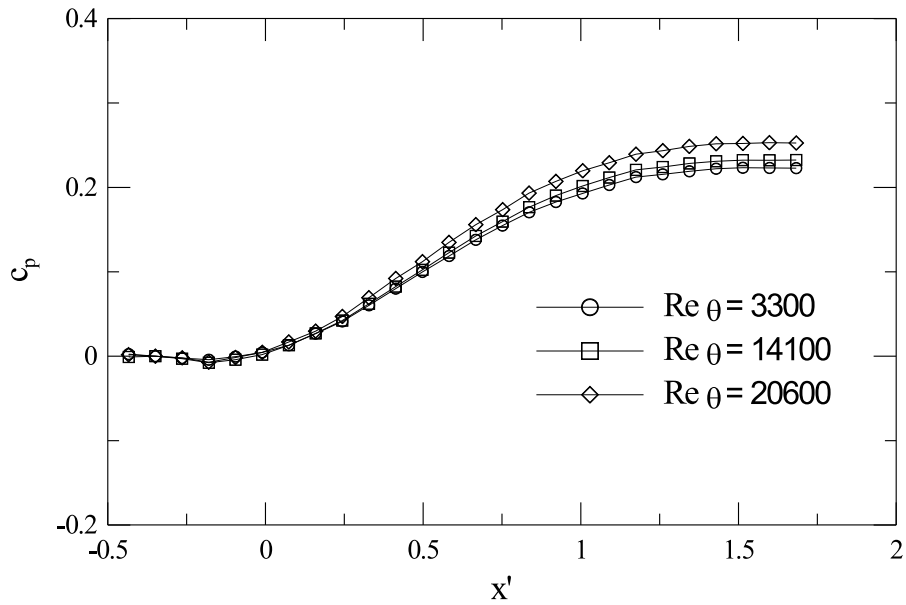

Figure 4.7: Wall static pressure distribution on top wall for all three Reynolds numbers

4.2 Wall Static Pressure Distribution

The wall static pressure distribution was measured at all three Reynolds numbers along both the top and bottom walls of the wind tunnel. Figure 4.6 shows the pressure distribution, C_p, along the bottom wall of the wind tunnel. The pressure distribution shows no Reynolds number effects until approximately half way down the ramp at which point the value of C_p increases with increasing Reynolds number along the remainder of the ramp. In the downstream redevelopment region, the Reynolds number dependence remains, but the shift between profiles remains constant indicating that the Reynolds number effects are most pronounced in the region of adverse pressure gradient and do not disappear when the pressure gradient is removed. The pressure distribution along the top wall of the tunnel is shown in Figure 4.7 and similar Reynolds number effects are observed.

The Clauser pressure gradient parameter, β, was calculated for each of the Reynolds numbers examined in the flow. Figure 4.8 shows that small Reynolds number effects on the value of β are present. The development of β as described in Chapter 3, is also observed at the higher Reynolds numbers, with the peak value of β increasing slightly with increasing Reynolds number. The peak value of β at the highest Reynolds number is still significantly smaller than values typical of flows near separation.

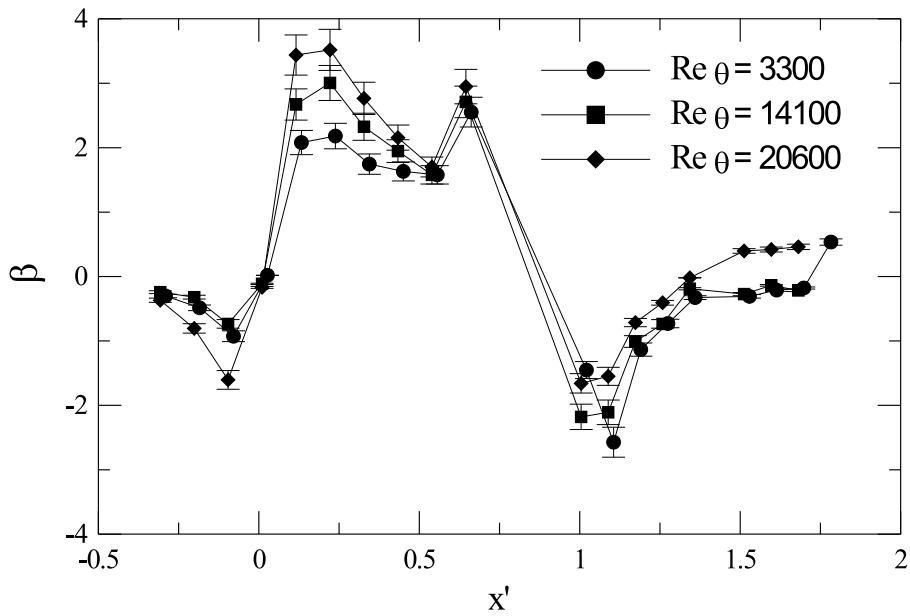

Figure 4.8: β distribution along bottom wall for all three Reynolds numbers

4.3 Mean Flow

As shown previously, the mean flow is not affected greatly by Reynolds number and remains attached along the entire length of the adverse pressure gradient ramp. A few of the typical mean velocity scalings are examined for the range of Reynolds numbers examined in this experiment and for various locations along the adverse pressure gradient ramp.

4.3.1 Law of the wall

The "law of the wall" plot at the upstream flat plate reference location is shown in Figure 4.9. At this location, the reference value of the skin friction is calculated using the standard log law fitting, as previously described. As the Reynolds number increases the logarithmic layer length in y^+ increases. In addition, the value of the wake parameter, Π, decreases with increasing Reynolds number. This can also be observed in the tables of flow parameters. As noted in Chapter 3, the mean flow follows the logarithmic law along the entire length of the ramp; therefore the "law of the wall" plot at $x' = 0.50$, half way down the ramp, is shown in Figure 4.10 as indicative of the "law of the wall" plot at other locations along the ramp. The extent of the logarithmic layer moves to larger values of y^+ at higher Reynolds numbers, as seen for the flat plate boundary layer. The wake region

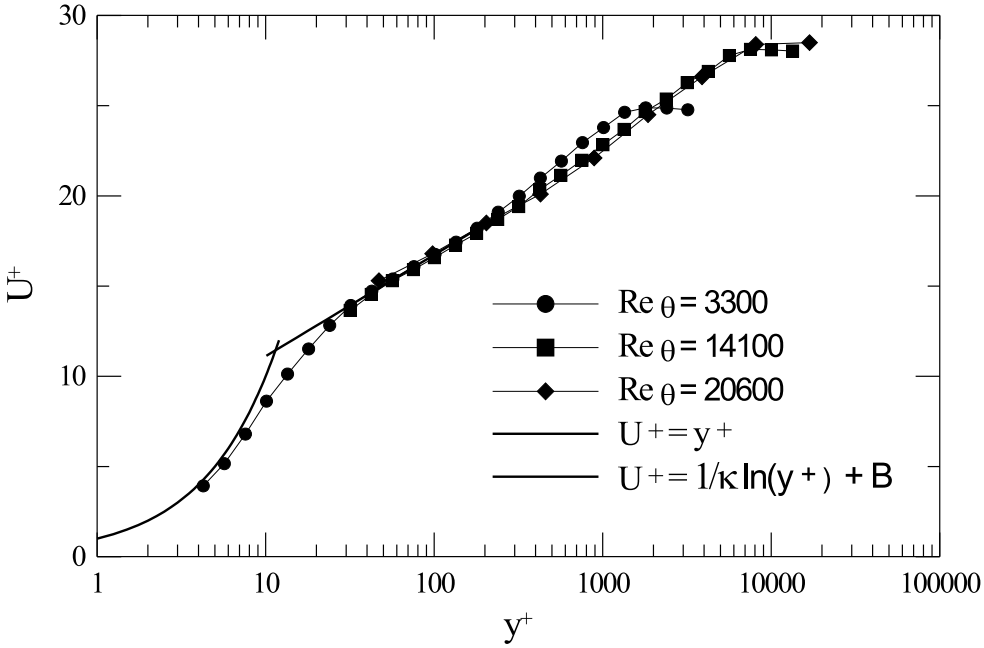

Figure 4.9: Law of the wall plot at x' = -0.33 for all three Reynolds numbers (κ = 0.41, B = 5.5)

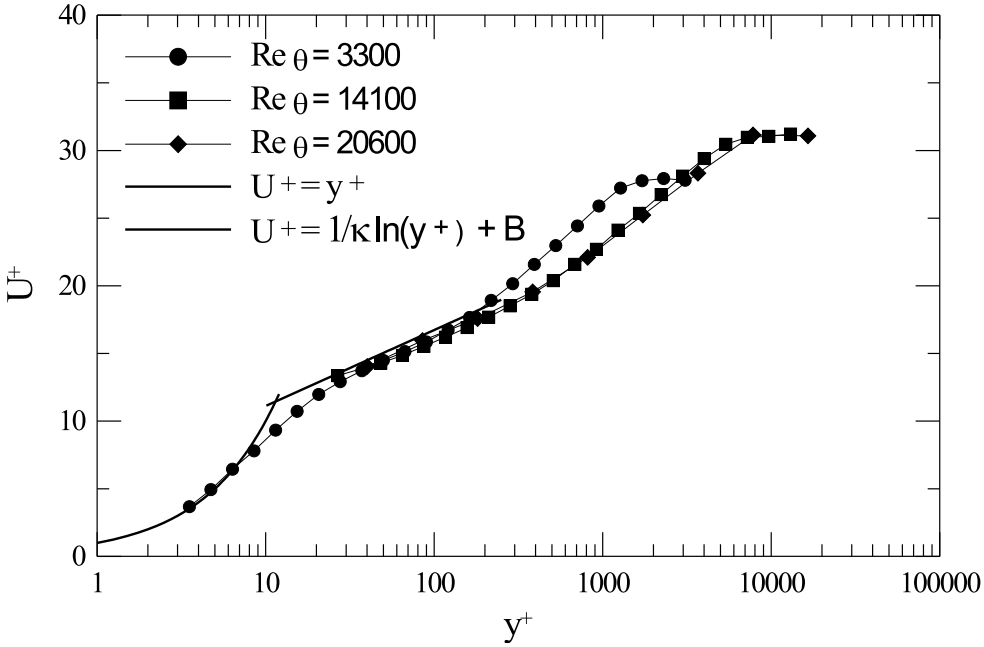

Figure 4.10: Law of the wall plot at x' = 0.50 for all three Reynolds numbers (κ = 0.41, B = 5.5)

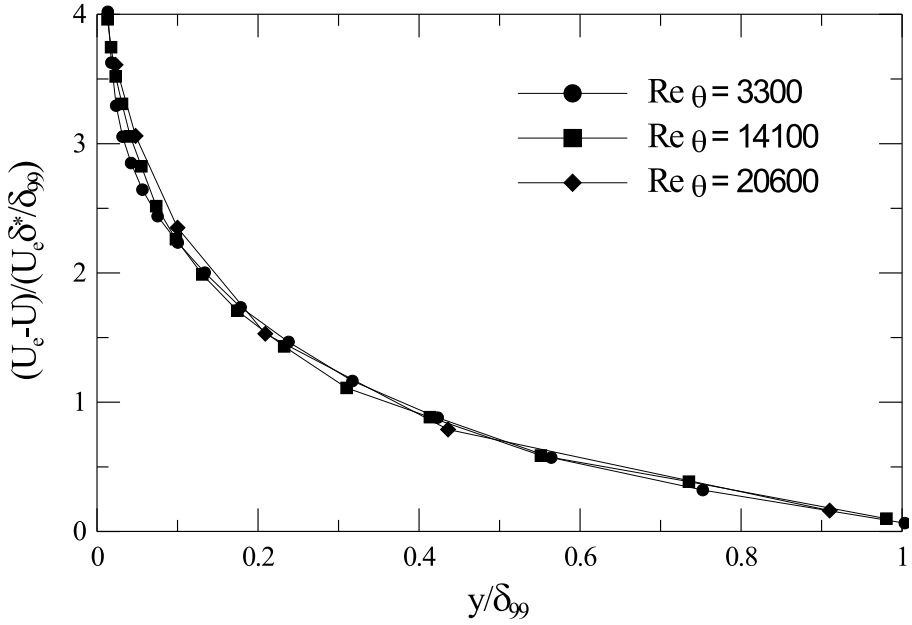

Figure 4.11: Velocity deficit scaling at x' = -0.33 for all three Reynolds numbers

of the flow has increased as the flow travels down the adverse pressure gradient ramp and therefore the wake region for all three Reynolds numbers covers a larger region of y^+ than for the flat plate boundary layer. Additionally, as for the flat plate boundary layer, the value of the wake parameter, Π, decreases with increasing Reynolds number as seen in previous experiments.

4.3.2 Velocity Deficit Scaling

The velocity deficit profile at the upstream flat plate reference location is shown in Figure 4.11 for all three Reynolds numbers using the Zagarola and Smits (1998) scaling of $(U_e - U)/(U_e\delta^*/\delta_{99})$. The profiles collapse very well for $y/\delta_{99} > 0.1$. Figure 4.12 shows the velocity deficit profiles for the flat plate profile as well as the profiles for locations along the ramp for the low Reynolds number, $Re_{\theta,ref} = 3300$, condition. The differences in the velocity deficit profiles are most notable for $y/\delta_{99} < 0.4$, where the value of the velocity deficit can be observed to increase with distance down the ramp for any given value of y/δ_{99}. This is in disagreement with the similarity analysis of Castillo and George (2001) who predict a single curve for an adverse pressure gradient flow. The lack of collapse of these profiles is due to the changing mean velocity profile shape, as observed in Figure

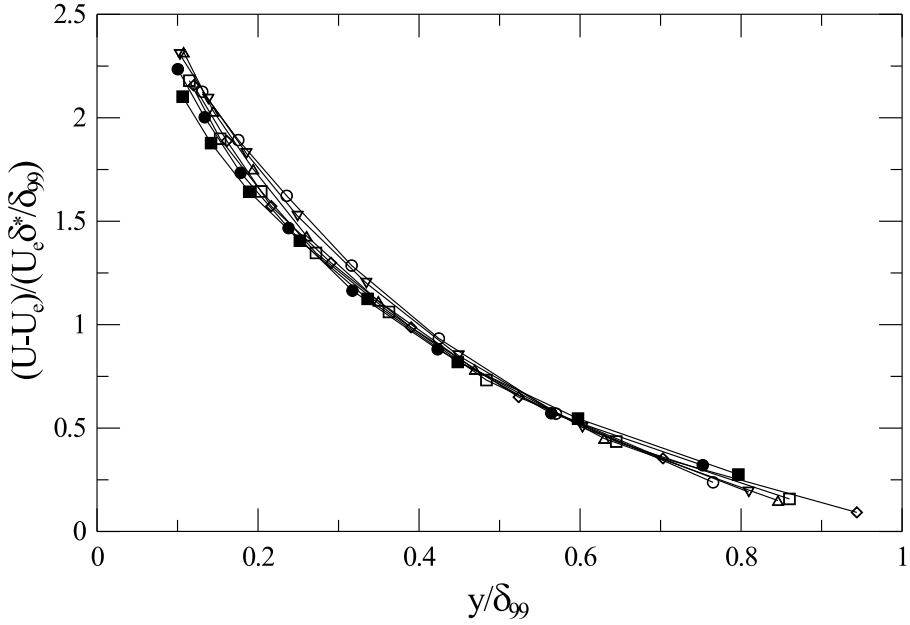

Figure 4.12: Velocity deficit scaling along ramp at $Re_\theta = 3300$ (symbols as in Chapter 3: x' = -0.33 •, x' = 0.0 ■, x' = 0.25 ⊡, x' = 0.33 ◊, x' = 0.5 △, x' = 0.67 ▽, x' = 0.75 ○)

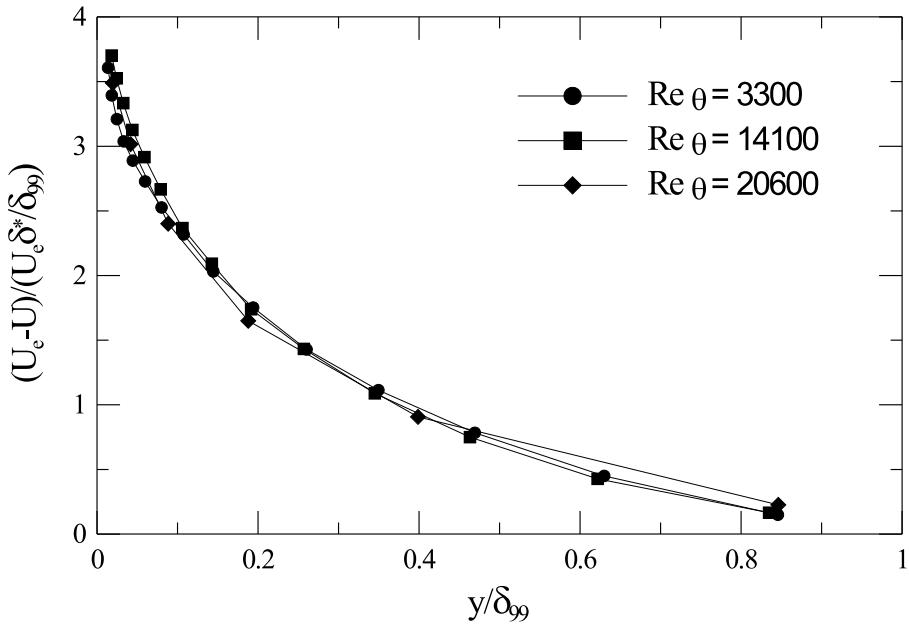

Figure 4.13: Velocity deficit scaling at x' = 0.50 for all three Reynolds numbers

3.6 and indicated by the changing value of the shape function, H, along the ramp. The velocity deficit profile for half way down the ramp, $x' = 0.50$, is shown in Figure 4.13, which shows reasonable collapse over the same range as the flat plate profile, $y/\delta_{99} > 0.1$. Similar collapse is seen at other measurement locations along the ramp and is due to the flow at each measurement location having the same pressure history and similar profile shapes and values of the shape factor. While this scaling collapses the mean velocity profiles at each specific location for the range of Reynolds numbers examined, it does not account for the changing shape of the mean profile due to the adverse pressure gradient and is not generally applicable for collapsing the mean velocity profile in any arbitrary adverse pressure gradient flow.

4.4 Turbulence

The turbulent stresses, as seen in Chapter 3, change greatly in the outer layer as the flow travels along the adverse pressure gradient ramp when plotted in traditional flat plate coordinates. However, the effects due to varying Reynolds number appear to be much less than those due to the changing flow field due to the adverse pressure gradient as seen in the plots of the stress development shown previously. The collapse of the stress data is shown in traditional scalings as well as newly proposed scalings, which collapse the changing stress profiles for this adverse pressure gradient flow.

4.4.1 Flat Plate Reference Location

At the upstream reference flat plate boundary layer, the DeGraaff and Eaton (2000) scaling, $\overline{u'u'}/u_\tau U_e$, $\overline{v'v'}/u_\tau^2$ and $-\overline{u'v'}/u_\tau^2$, collapses the three Reynolds numbers examined, as seen in Figures 4.14, 4.15, and 4.16. The outer layer for the Reynolds shear stress is less well collapsed than for the data of DeGraaff and Eaton (2000). Because this collapse is not very good due to the difficulties involved in measuring the shear stress, the shear stress collapse with Reynolds number will not be examined further along the adverse pressure gradient boundary layer.

4.4.2 Adverse Pressure Gradient Ramp

The streamwise normal stress, $\overline{u'u'}$ is shown scaled on the DeGraaff and Eaton (2000) scaling for all three Reynolds numbers at x' locations of 0.25, 0.5 and 0.75, in Figures 4.17,

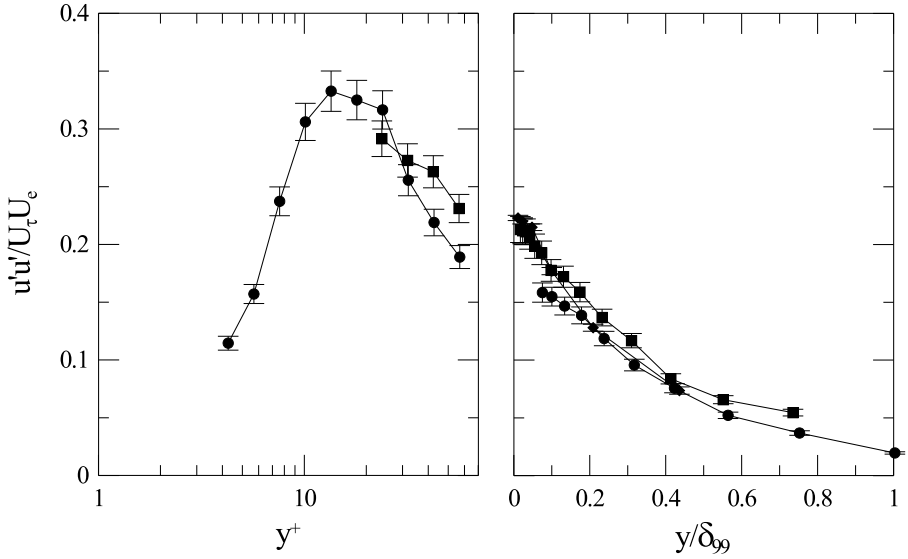

Figure 4.14: Reynolds number scaling for $\overline{u'u'}$ at x' = -0.33 (Re_θ = 3300 •, $Re_\theta = 14,100$ ■, $Re_\theta = 20,600$ ♦)

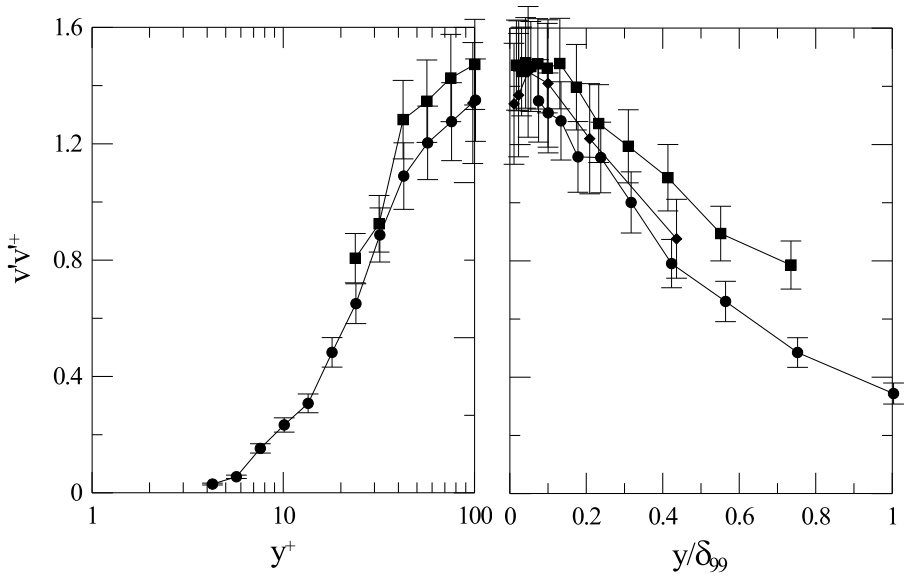

Figure 4.15: Reynolds number scaling for $\overline{v'v'}$ at x' = -0.33 (Re_θ = 3300 •, $Re_\theta = 14,100$ ■, $Re_\theta = 20,600$ ♦)

4.18, and 4.19. Each figure shows the three upstream flat plate profiles as well as the profiles for all three Reynolds numbers at the given x' location. As seen in Figure 3.11, the peak value for the streamwise normal stress along the ramp does not collapse in the DeGraaff

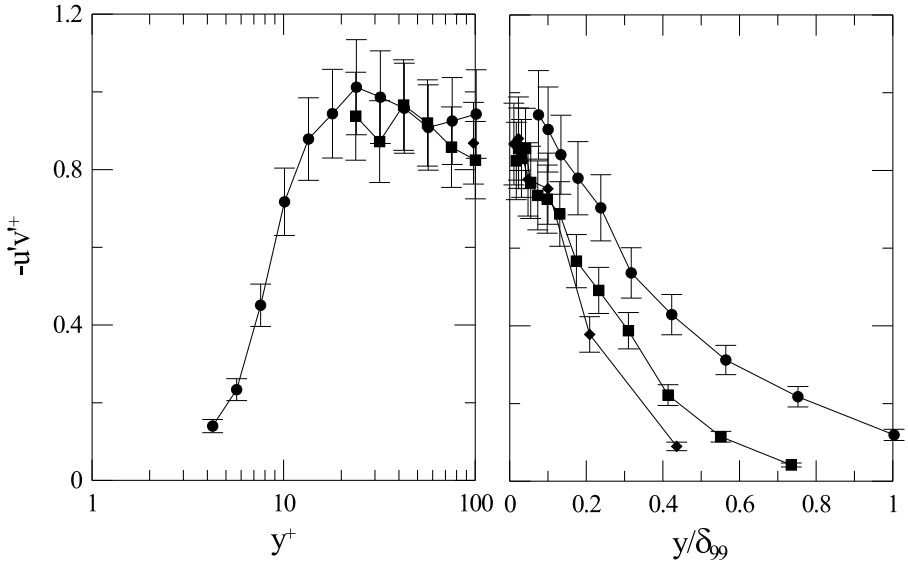

Figure 4.16: Reynolds number scaling for $-\overline{u'v'}$ at x' = -0.33 (Re_θ = 3300 •, $Re_\theta = 14,100$ ■, $Re_\theta = 20,600$ ♦)

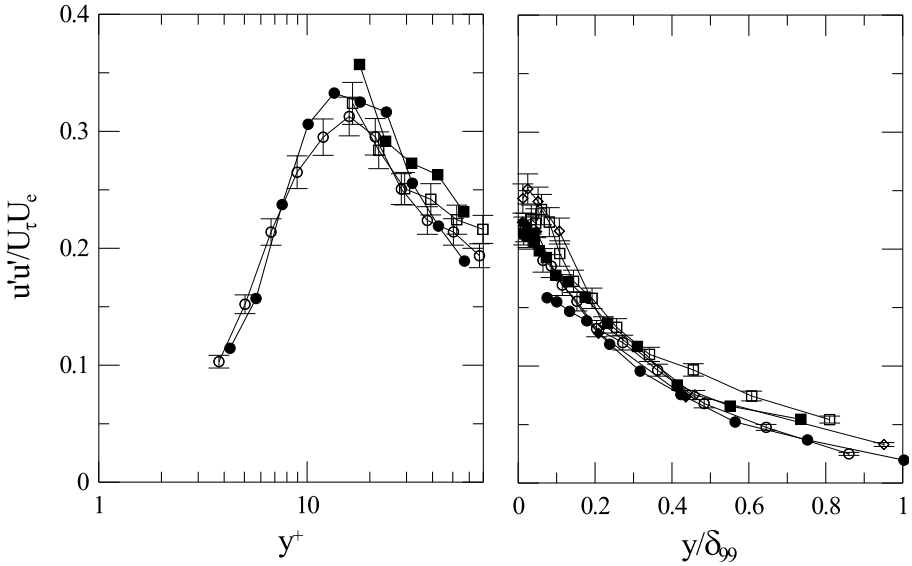

Figure 4.17: DeGraaff & Eaton flat plate scaling for $\overline{u'u'}$ at x' = 0.25 (filled symbols represent x' = -0.33 and open symbols represent x' = 0.25, Re_θ = 3300 •, $Re_\theta = 14,100$ ■, $Re_\theta = 20,600$ ♦), uncertainty bars indicative of uncertainty in all profiles

and Eaton (2000) coordinates onto the flat plate peak, although all the ramp profiles do collapse on each other at a slightly lower peak value as seen in Figure 3.11. The DeGraaff

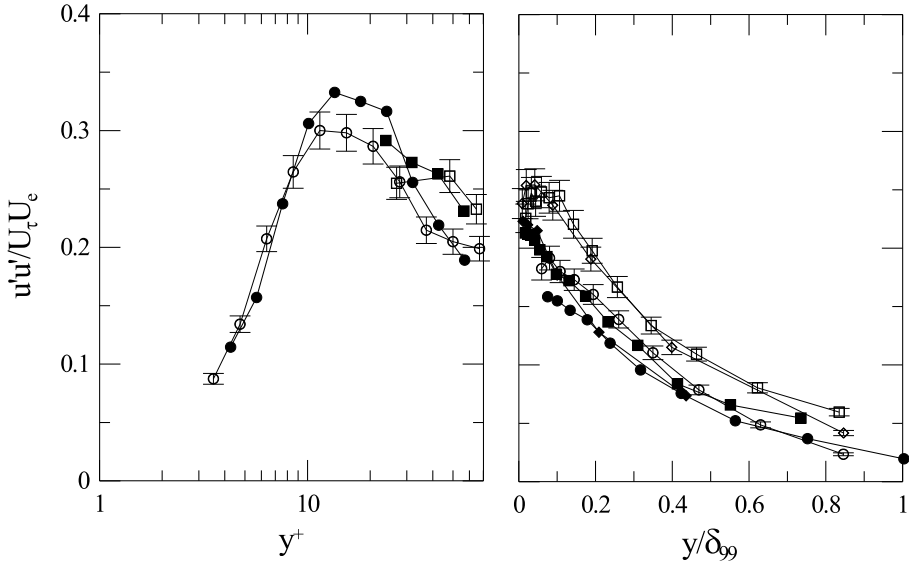

Figure 4.18: DeGraaff & Eaton flat plate scaling for $\overline{u'u'}$ at x' = 0.50 (filled symbols represent x' = -0.33 and open symbols represent x' = 0.5, $Re_\theta = 3300$ •, $Re_\theta = 14,100$ ■, $Re_\theta = 20,600$ ♦), uncertainty bars indicative of uncertainty in all profiles

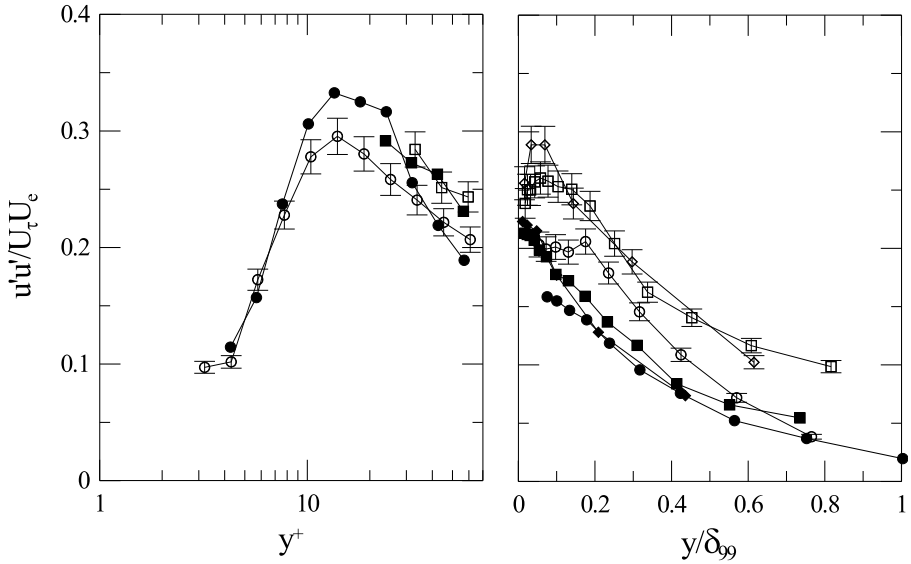

Figure 4.19: DeGraaff & Eaton flat plate scaling for $\overline{u'u'}$ at x' = 0.75 (filled symbols represent x' = -0.33 and open symbols represent x' = 0.75, $Re_\theta = 3300$ •, $Re_\theta = 14,100$ ■, $Re_\theta = 20,600$ ♦), uncertainty bars indicative of uncertainty in all profiles

and Eaton (2000) scaling in the outer layer of the boundary layer appears to not collapse the range of Reynolds number data available for this flow, particularly as the flow progresses

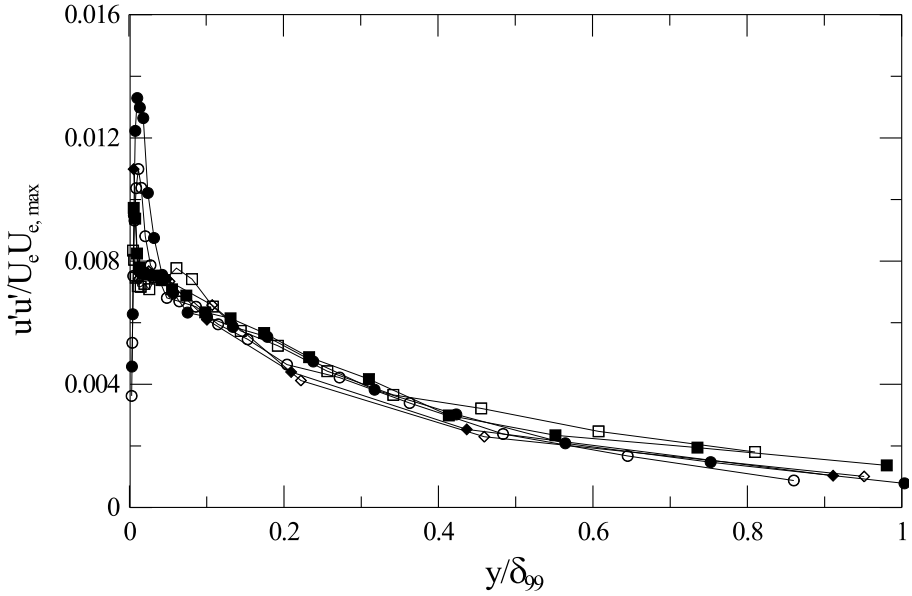

Figure 4.20: Outer layer scaling for $\overline{u'u'}$ at x' = 0.25 (filled symbols represent x' = -0.33 and open symbols represent x' = 0.25, $Re_\theta = 3300$ •, $Re_\theta = 14,100$ ■, $Re_\theta = 20,600$ ♦)

down the ramp. This is due to the outer peak, which develops as the flow advances down the ramp. Overall, the DeGraaff and Eaton (2000) scaling does not appear to collapse the flat plate and adverse pressure gradient profiles for this particular flow.

Since the outer peak in the streamwise normal stress does not collapse in the flat plate scaling proposed by DeGraaff and Eaton (2000), other outer layer scalings were tested. The outer scaling proposed by Elsberry et al. (2000), $U_eU_{e,max}$ is shown in Figures 4.20, 4.21, and 4.22. In this scaling, U_e is the local freestream velocity and $U_{e,max}$ is the maximum freestream velocity, which for these profiles is the freestream velocity at the start of the ramp, $x' = 0.0$. This value was measured for the highest Reynolds number case as a single data point to allow for the application of this scaling for all three Reynolds numbers. As in the previous figures, the upstream flat plate profiles are included at each location and the stresses are plotted for $x' = 0.25, 0.5$ and 0.75. The collapse of the streamwise normal stress in these coordinates is better than in the DeGraaff and Eaton (2000) scaling for the outer region of the flow, particularly for the outer layer stress peak. Again as the flow travels down the ramp, the scaling has more difficulties in collapsing the stress peak, which develops in the flow along the ramp and overall the scaling appears less acceptable as the flow travels further down the ramp.

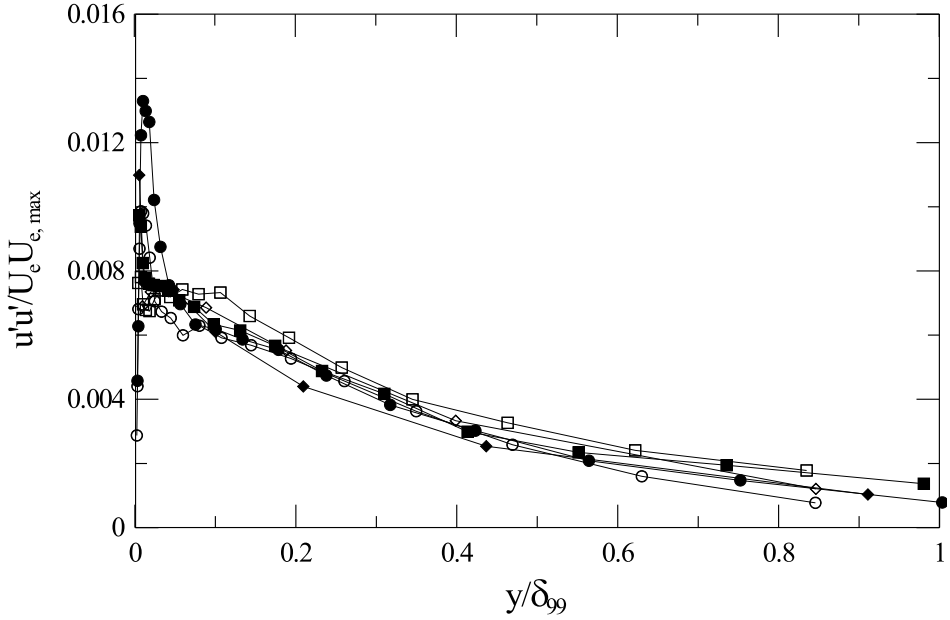

Figure 4.21: Outer layer scaling for $\overline{u'u'}$ at x' = 0.50 (filled symbols represent x' = -0.33 and open symbols represent x' = 0.5, $Re_\theta = 3300$ •, $Re_\theta = 14,100$ ■, $Re_\theta = 20,600$ ♦)

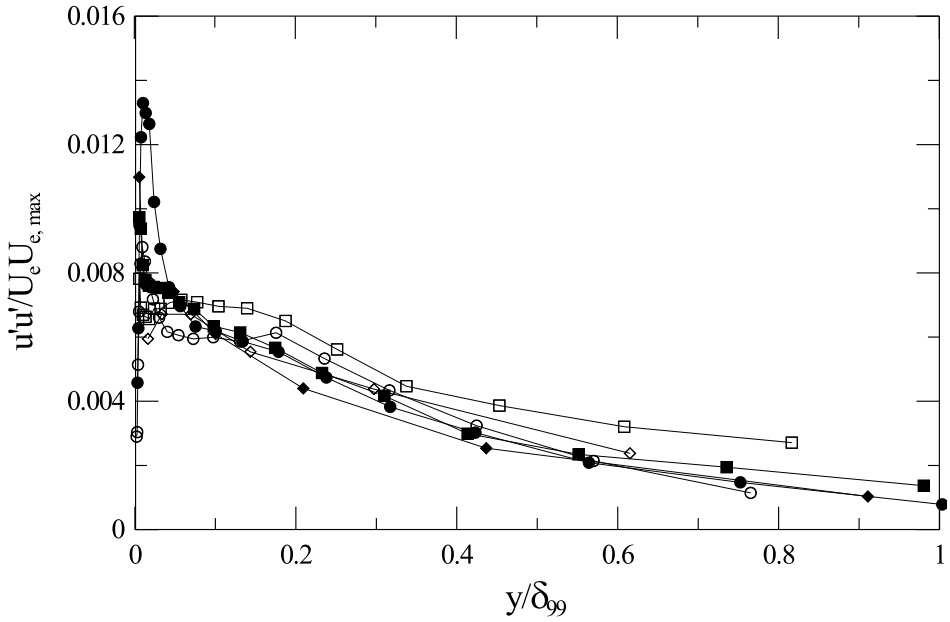

Figure 4.22: Outer layer scaling for $\overline{u'u'}$ at x' = 0.75 (filled symbols represent x' = -0.33 and open symbols represent x' = 0.75, $Re_\theta = 3300$ •, $Re_\theta = 14,100$ ■, $Re_\theta = 20,600$ ♦)

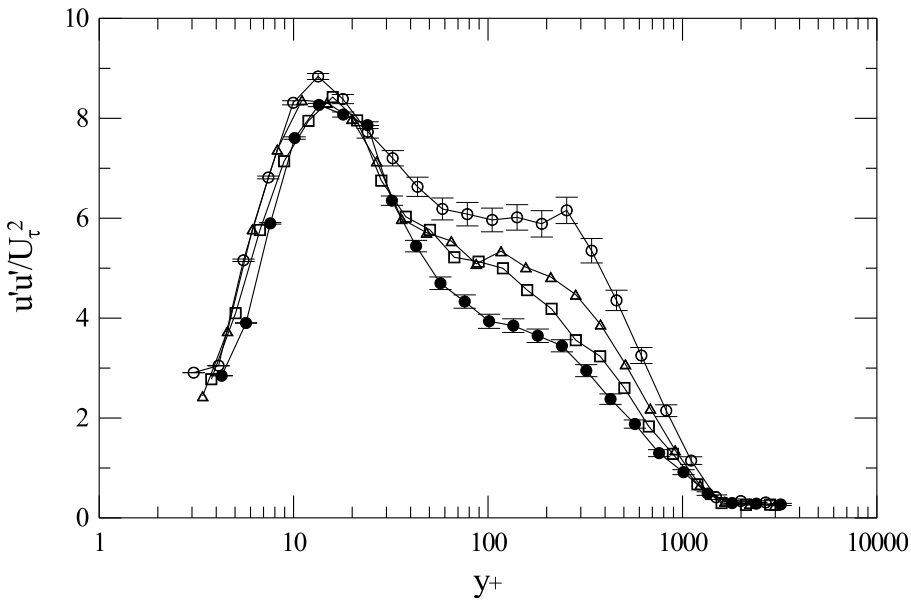

Figure 4.23: Traditional scaling for $\overline{u'u'}$ at $Re_\theta = 3300$ (x' = -0.33 •, x' = 0.25 ⊡, x' = 0.5 △, x' = 0.75 ○), uncertainty bars indicative of uncertainty in all profiles

For the inner region of the streamwise normal stress, the $Re_{\theta,ref} = 3300$ data along the ramp was examined with the goal of collapsing the peak between the adverse pressure gradient profiles and the flat plate data at one Reynolds number. In the DeGraaff and Eaton (2000) scaling, the peaks for the adverse pressure gradient locations collapse on each other, but not on the flat plate profile. The traditional streamwise normal stress scaling, $\overline{u'u'}/u_\tau^2$, was found to collapse the peak for the flat plate and the adverse pressure gradient profile for this one Reynolds number, as seen in Figure 4.23. This scaling also does not appear to collapse the outer peak in the profiles along the ramp. Since this scaling was already shown by DeGraaff and Eaton (2000) to not collapse the flat plate streamwise normal stress profiles over a wide Reynolds number range, a modification of this scaling was examined to collapse the adverse pressure gradient profiles along with the flat plate profiles over the Reynolds number range examined.

Starting from the traditional streamwise normal stress scaling, $\overline{u'u'}/u_\tau^2$, which was observed to collapse the adverse pressure gradient and flat plate profiles for the inner layer at one Reynolds number, a modification to this scaling to account for Reynolds number effects was found using the data gathered in this study, the data of DeGraaff (1999) and that of Österlund (1999). The new scaling for the streamwise normal stress to collapse the adverse

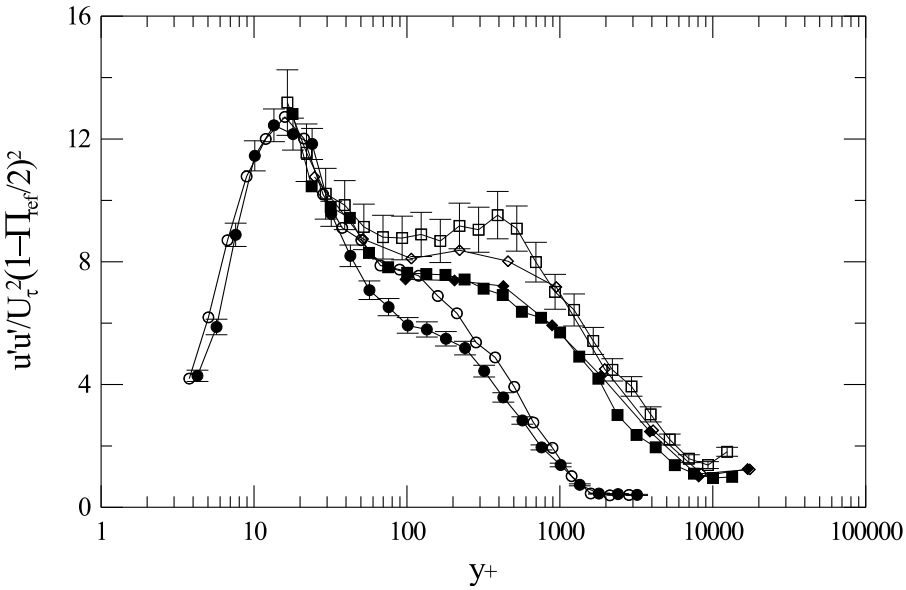

Figure 4.24: New proposed inner scaling for $\overline{u'u'}$ at x' = 0.25 (filled symbols represent x' = -0.33 and open symbols represent x' = 0.25, $Re_\theta = 3300$ •, $Re_\theta = 14,100$ ■, $Re_\theta = 20,600$ ♦), uncertainty bars indicative of uncertainty in all profiles

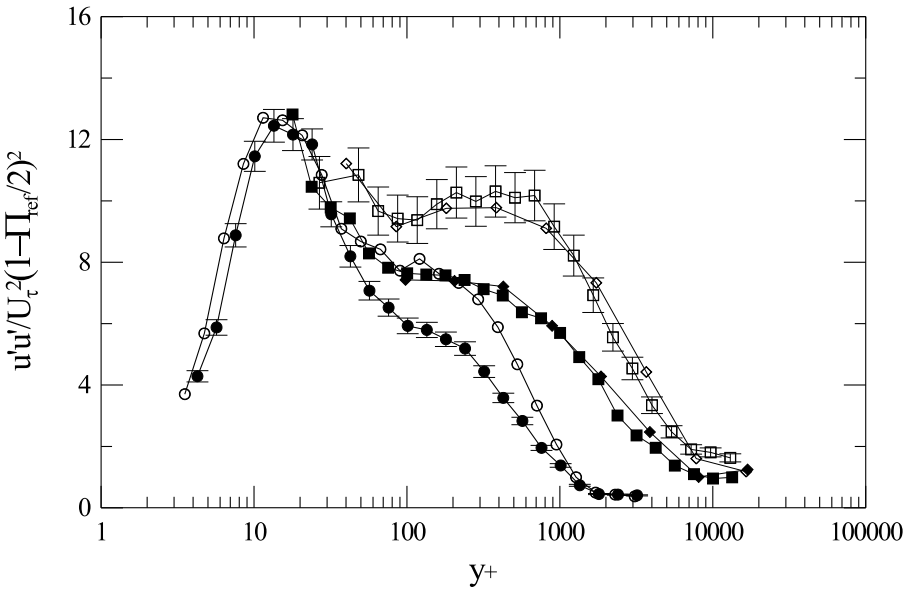

Figure 4.25: New proposed inner scaling for $\overline{u'u'}$ at x' = 0.50 (filled symbols represent x' = -0.33 and open symbols represent x' = 0.5, $Re_\theta = 3300$ •, $Re_\theta = 14,100$ ■, $Re_\theta = 20,600$ ♦), uncertainty bars indicative of uncertainty in all profiles

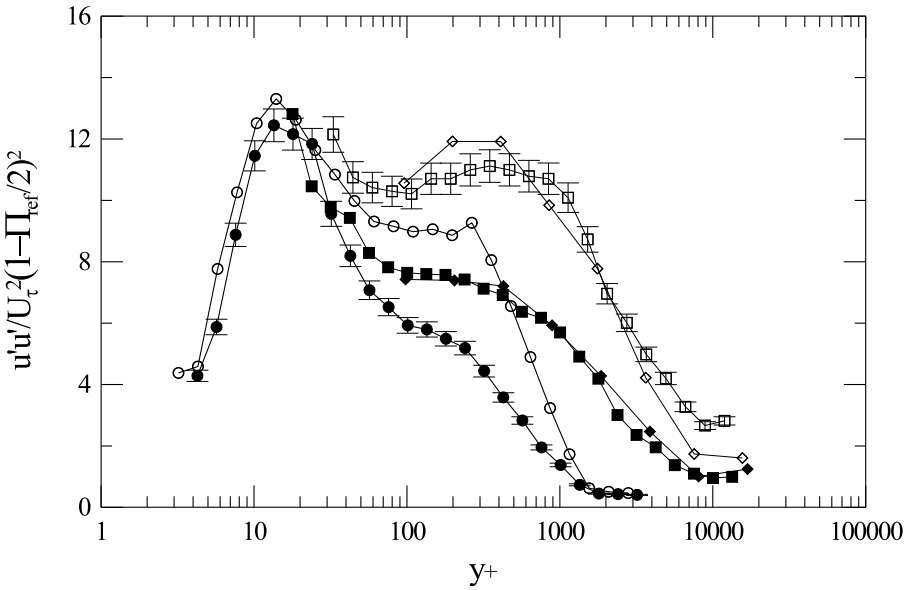

Figure 4.26: New proposed inner scaling for $\overline{u'u'}$ at x' = 0.75 (filled symbols represent x' = -0.33 and open symbols represent x' = 0.75, $Re_\theta = 3300$ •, $Re_\theta = 14,100$ ■, $Re_\theta = 20,600$ ♦), uncertainty bars indicative of uncertainty in all profiles

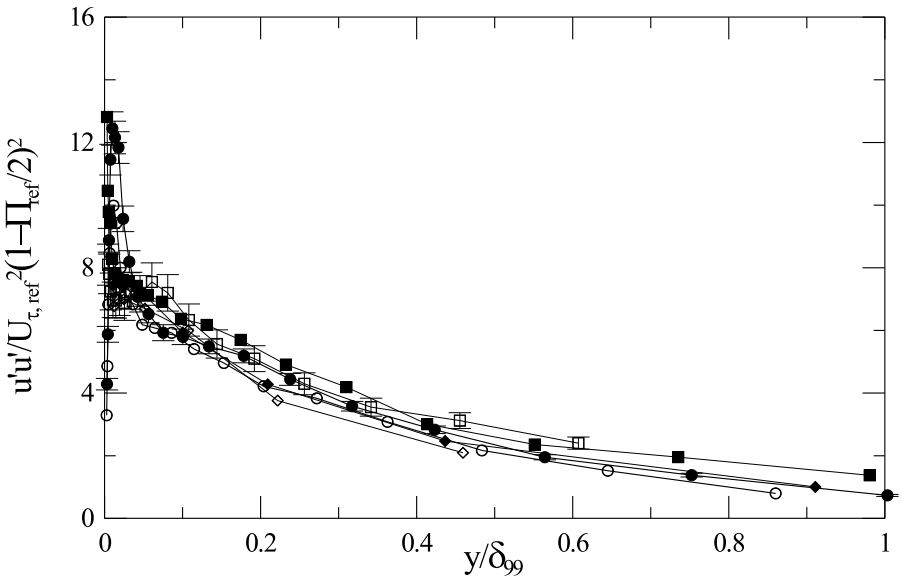

Figure 4.27: New proposed outer scaling for $\overline{u'u'}$ at x' = 0.25 (filled symbols represent x' = -0.33 and open symbols represent x' = 0.25, $Re_\theta = 3300$ •, $Re_\theta = 14,100$ ■, $Re_\theta = 20,600$ ♦), uncertainty bars indicative of uncertainty in all profiles

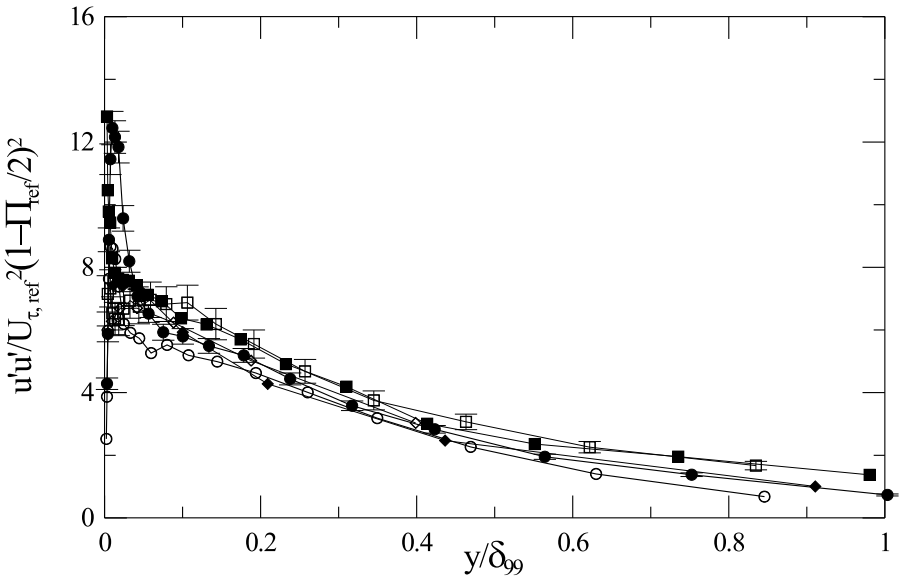

Figure 4.28: New proposed outer scaling for $\overline{u'u'}$ at x' = 0.50 (filled symbols represent x' = -0.33 and open symbols represent x' = 0.5, $Re_\theta = 3300$ •, $Re_\theta = 14,100$ ■, $Re_\theta = 20,600$ ♦), uncertainty bars indicative of uncertainty in all profiles

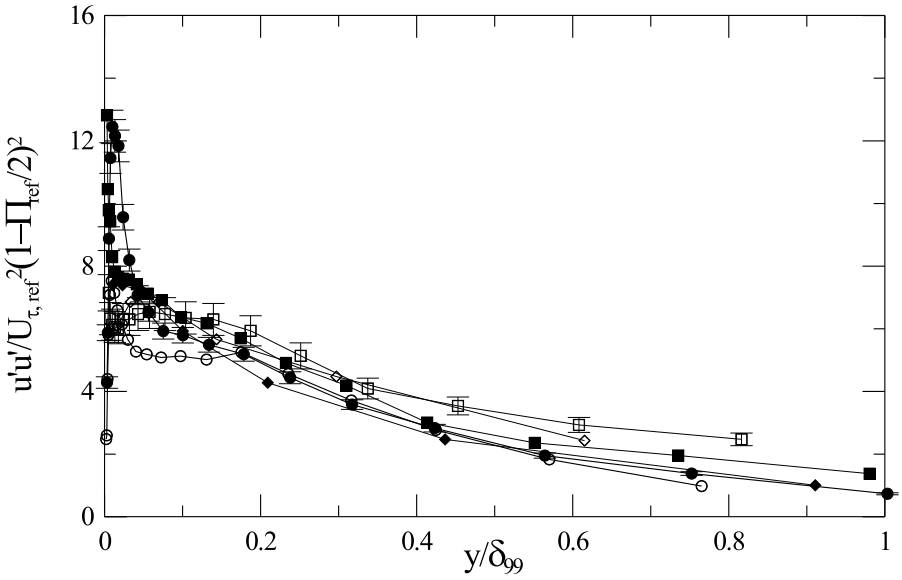

Figure 4.29: New proposed outer scaling for $\overline{u'u'}$ at x' = 0.75 (filled symbols represent x' = -0.33 and open symbols represent x' = 0.75, $Re_\theta = 3300$ •, $Re_\theta = 14,100$ ■, $Re_\theta = 20,600$ ♦), uncertainty bars indicative of uncertainty in all profiles

pressure gradient data for the inner layer, as well as the flat plate data, over the Reynolds number range in which experimental data were available is:

$$\frac{\overline{u'u'}}{(u_\tau^2(1-0.5\Pi_{ref})^2)} \tag{4.1}$$

The value of 0.5 in front of Π_{ref} was found by fitting the flat plate data of DeGraaff and Eaton (2000) and Österlund (1999). The collapse of the inner layer portion of the data from the current experiments are shown in Figure 4.24, 4.25, and 4.26. This scaling has both a local component involving the local value of u_τ, and an upstream history or non-local reference component, $1-0.5\Pi_{ref}$. The history component for this flow is based on the value of the wake function, Π, on the upstream flat plate. For the flat plate data used to test this new scaling, the value of Π was computed from the given mean velocity profiles or from tabulated results. The value of Π decreases with increasing Reynolds number, meaning that the history component becomes closer to one for higher Reynolds number. While this scaling collapses the inner peak in the streamwise normal stress, the outer layer does not collapse, and the peak which is observed to develop along the adverse pressure gradient is evident in these figures. Some justification for the new inner layer scaling is needed. Dimensionally, the near wall peak in the streamwise normal stress decays as the flow travels down the adverse pressure gradient ramp at a rate similar to the change in the friction velocity squared. The coefficient $(1-0.5\Pi_{ref})^2$ was determined to collapse the range of Reynolds number data for flat plate onto a single profile using traditional scaling. Elsberry et al. (2000) note that the wake parameter, Π, has been shown to be proportional to the inverse of the square root of the skin friction coefficient, c_f. This proportionality comes from:

$$\frac{U}{u_\tau} = \frac{1}{\kappa} ln\left(\frac{yu_\tau}{\nu}\right) + B + \frac{\Pi}{\kappa} w\left(\frac{y}{\delta_{99}}\right) \tag{4.2}$$

where the wake parameter, Π, can be solved for at the edge of the boundary layer, giving:

$$\Pi = \frac{\kappa}{2}\left[\frac{2}{\sqrt{c_f}} - B - \frac{1}{\kappa} ln\left(\frac{\delta_{99}u_\tau}{\nu}\right)\right] \tag{4.3}$$

In order to examine how this relationship can be used to help understand this new scaling, the scaling must be expanded using an arbitrary constant of proportionality, C, between the skin friction coefficient and the wake parameter:

$$\frac{\overline{u'u'}}{\left(u_\tau^2\left(1-\frac{CU_{e,ref}}{\sqrt{2}u_{\tau,ref}}+\frac{C^2U_{e,ref}^2}{8u_{\tau,ref}^2}\right)\right)} \tag{4.4}$$

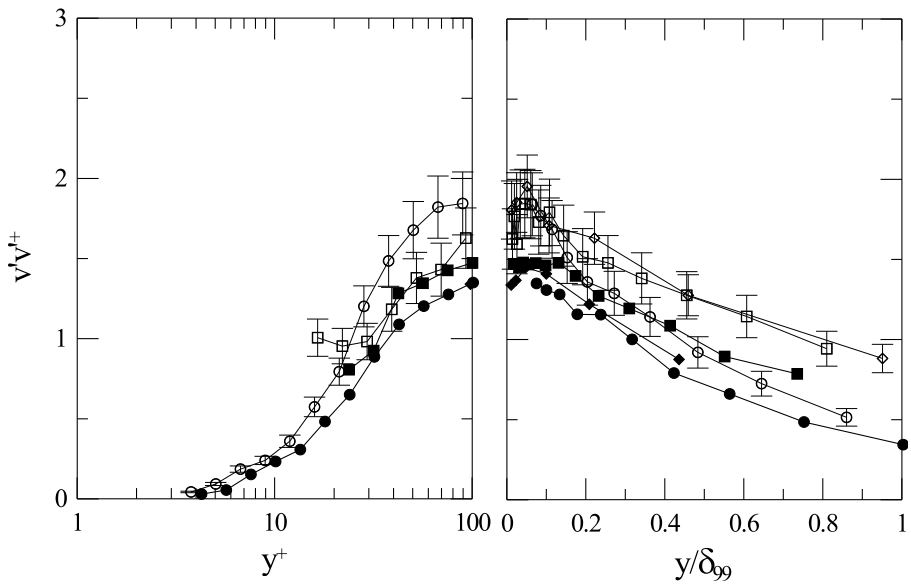

Figure 4.30: Scaling for $\overline{v'v'}$ using local values of u_τ at x' = 0.25 (filled symbols represent x' = -0.33 and open symbols represent x' = 0.25, $Re_\theta = 3300$ •, $Re_\theta = 14,100$ ■, $Re_\theta = 20,600$ ♦), uncertainty bars indicative of uncertainty in all profiles

This scaling can then be examined for the flat plate boundary layer, where the reference and local values are the same.

$$\frac{\overline{u'u'}}{\left(u_\tau^2 - \frac{CU_e u_\tau}{\sqrt{2}} + \frac{C^2 U_e^2}{8}\right)} \tag{4.5}$$

This scaling is a mix of inner and outer scalings to collapse the inner streamwise normal stress peak. Equation 4.5 can be thought of as an alternative to the DeGraaff and Eaton (2000) mixing scaling. In order to determine the value of C, a large amount of data would be necessary, however the value must be less than 1 and could be easily calculated if enough good data were available over a range of Reynolds numbers for the value of the peak streamwise normal stress and the necessary velocities for a flat plate.

A separate scaling is needed for the outer flow since the turbulence in the log and wake layers is out of equilibrium with the mean flow. The new scaling:

$$\frac{\overline{u'u'}}{\left(u_{\tau,ref}^2 \left(1 - 0.5\Pi_{ref}\right)^2\right)} \tag{4.6}$$

where no local information is used, collapses the streamwise normal stress for the outer layer. The lack of local information is necessary since the dimensional outer plateau in the

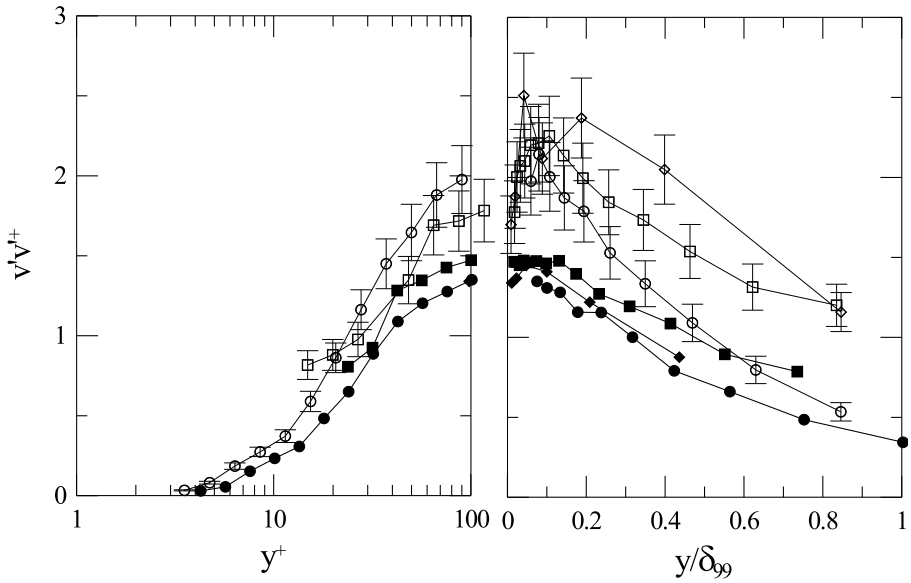

Figure 4.31: Scaling for $\overline{v'v'}$ using local values of u_τ at x' = 0.50 (filled symbols represent x' = -0.33 and open symbols represent x' = 0.5, $Re_\theta = 3300$ •, $Re_\theta = 14,100$ ■, $Re_\theta = 20,600$ ♦), uncertainty bars indicative of uncertainty in all profiles

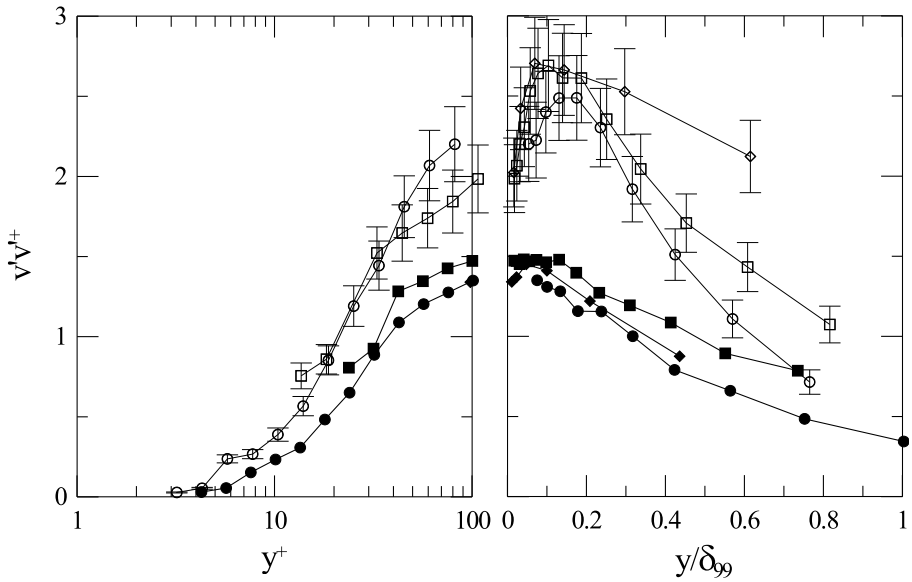

Figure 4.32: Scaling for $\overline{v'v'}$ using local values of u_τ at x' = 0.75 (filled symbols represent x' = -0.33 and open symbols represent x' = 0.75, $Re_\theta = 3300$ •, $Re_\theta = 14,100$ ■, $Re_\theta = 20,600$ ♦), uncertainty bars indicative of uncertainty in all profiles

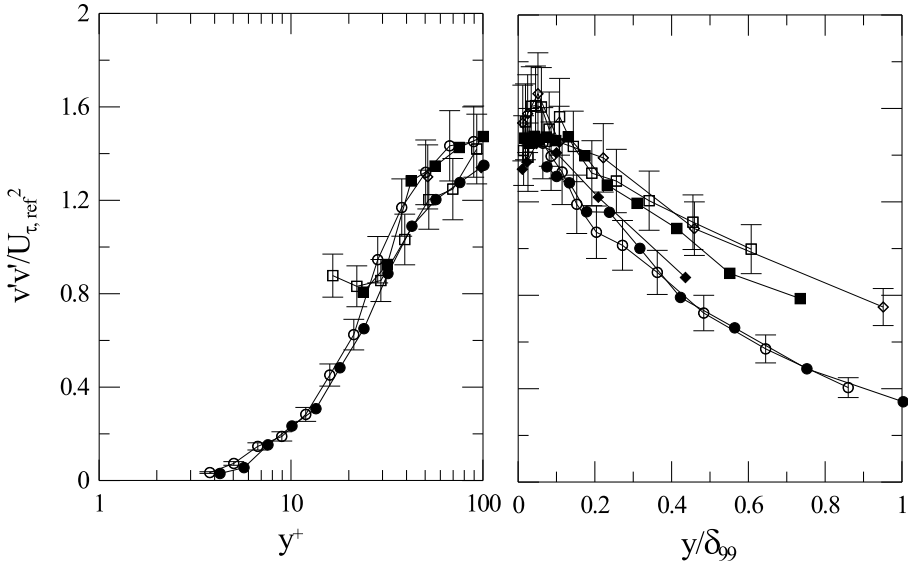

Figure 4.33: Scaling for $\overline{v'v'}$ using reference values of u_τ at x' = 0.25 (filled symbols represent x' = -0.33 and open symbols represent x' = 0.25, $Re_\theta = 3300$ •, $Re_\theta = 14,100$ ■, $Re_\theta = 20,600$ ♦), uncertainty bars indicative of uncertainty in all profiles

streamwise normal stress does not change as the flow travels down the ramp. The use of the additional element in the scaling accounts for the change in the flow due to the changing Reynolds number, as discussed above for the inner layer peak. The results of this scaling are seen in Figures 4.27, 4.28, and 4.29 plotted in outer layer coordinates. While the collapse is not perfect, there is no clear trend to the variations around a mean line. This is a clear indication that the outer layer normal stress is out of equilibrium with the mean flow and is primarily determined by upstream conditions over the length of the ramp.

The wall normal stress scaled using the traditional scaling, u_τ^2, is shown in Figures 4.30, 4.31, and 4.32 for the three Reynolds numbers at one quarter, one half and three quarters of the way down the adverse pressure gradient ramp respectively. Neither the inner nor outer layer profiles collapse in these coordinates. The outer layer in particular shows stress variations in these coordinates indicating a weak connection at most between the outer layer normal stress and the local friction velocity. The wall normal stress scaled on $u_{\tau,ref}^2$ is shown in Figures 4.33, 4.34, and 4.35 for the three adverse pressure gradient profiles at all Reynolds numbers. This scaling is observed to collapse the inner region of the wall normal stress very well. This degree of collapse for the inner layer at all locations along the ramp indicates that the inner layer is determined by the upstream condition and the

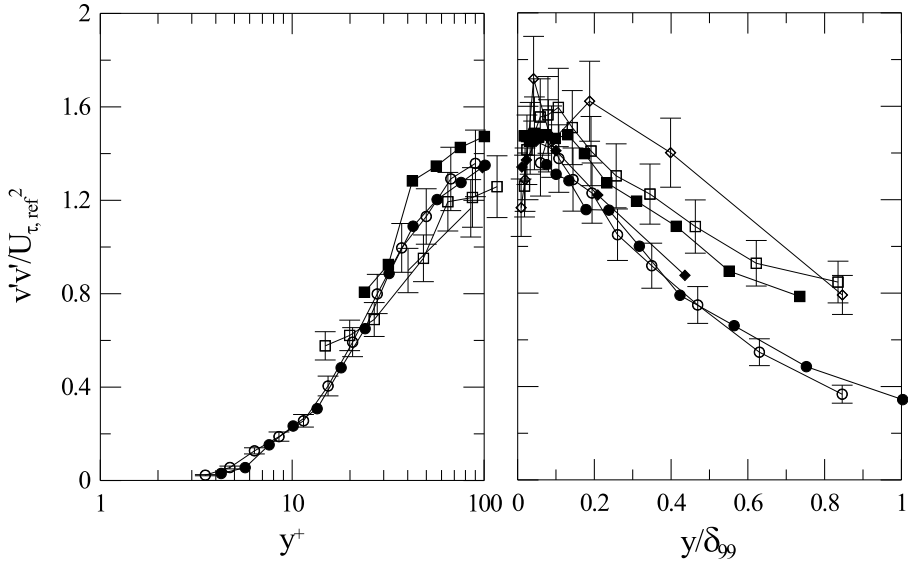

Figure 4.34: Scaling for $\overline{v'v'}$ using reference values of u_τ at x' = 0.50 (filled symbols represent x' = -0.33 and open symbols represent x' = 0.5, $Re_\theta = 3300$ •, $Re_\theta = 14,100$ ■, $Re_\theta = 20,600$ ♦), uncertainty bars indicative of uncertainty in all profiles

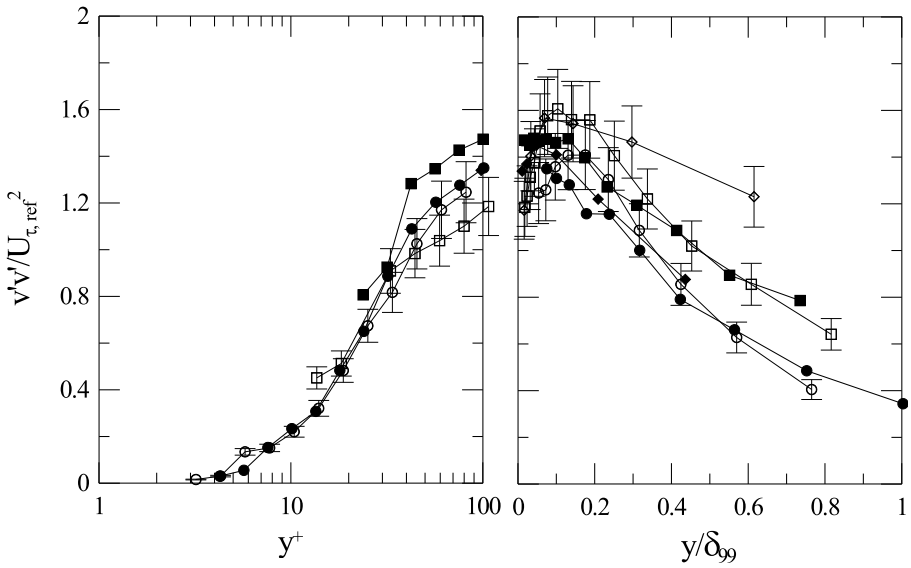

Figure 4.35: Scaling for $\overline{v'v'}$ using reference values of u_τ at x' = 0.75 (filled symbols represent x' = -0.33 and open symbols represent x' = 0.75, $Re_\theta = 3300$ •, $Re_\theta = 14,100$ ■, $Re_\theta = 20,600$ ♦), uncertainty bars indicative of uncertainty in all profiles

locally changing parameters, such as skin friction, play no part in determining the stress for this flow. In addition, the outer peak collapses in this scaling and the outer layer collapse

for the data along the adverse pressure gradient ramp and the flat plate is as good as the collapse for the flat plate data shown previously using the traditional scaling. This scaling, due only to upstream reference values of the friction velocity, implies that the dimensional values of the wall normal stress remain constant, independent of the changing mean velocity profiles. As the boundary layer thickens and the value of the friction velocity decreases, the outer layer peak grows in traditional scaling due entirely to the change in the skin friction. The wall normal stress over the entire flow field reaches a constant peak value, which moves further from the wall as the boundary layer thickens.

To test the ability of the new stress scalings to collapse data from other adverse pressure gradient experiments, the data from the increasingly adverse pressure gradient experiment of Samuel and Joubert (1974) were examined. For this flow, flat plate data was not available as the first measurement location was already located in the adverse pressure gradient region of the flow, therefore the reference location was taken to be the first location at which data were presented. The experimental data from this experiment could only be used to examine the outer layer scalings, since the inner layer behavior of the turbulence was not captured near the wall in this experiment. The scaling of the streamwise normal stress is shown in Figure 4.36, and for the wall normal stress in Figure 4.37. The collapse of the data for the streamwise normal stress is poor, although this is likely due to the lack of a flat plate reference location from which to gather the values of the wake function and the friction velocity. The value of the wake function at the first location in the experiment of Samuel and Joubert (1974) is comparable to the value measured one third of the distance down the ramp in the present experiment under similar Reynolds number conditions. For the wall normal stress, the collapse is adequate, note that the near wall data were taken using a hotwire and the values in this region are subject to relatively large uncertainties. The profile shapes of both stresses are much different from the shapes measured in this work, particularly as the flow travels farther along the pressure gradient and this difference is likely due to the differing flow conditions and the rapidly changing pressure gradient. However, this comparison shows that the collapse of the wall normal stress data is quite robust.

The general conclusion here is that for the present case of mild adverse pressure gradient with falling skin friction and no observable inflection point in the mean profile, the normal stresses are controlled almost entirely by their upstream levels. Overall the wall normal stress is unaffected by the pressure gradient caused by the ramp when plotted using the rotated coordinate system and collapses well using a constant scaling. The streamwise

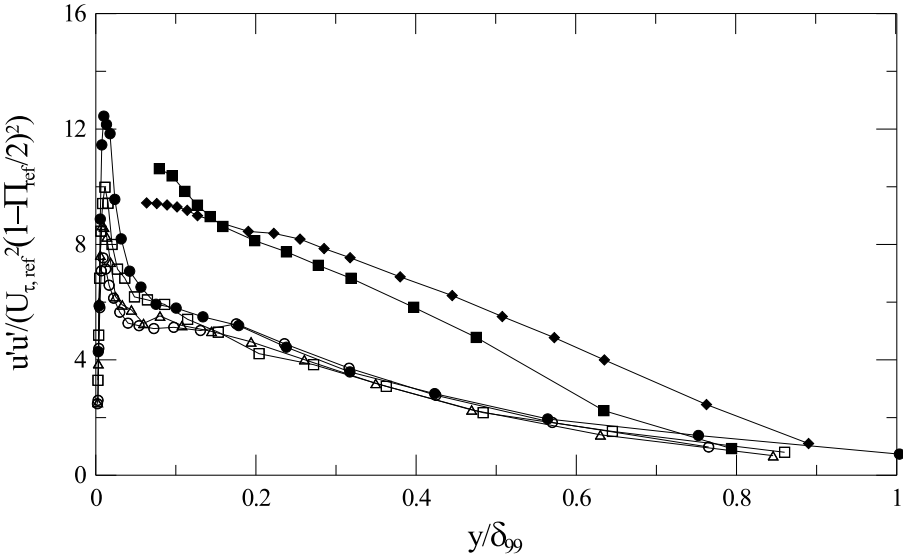

Figure 4.36: Test of new scaling for $\overline{u'u'}$ with data of Samuel & Joubert (1974) (x = 1.04 m ■, x = 1.79 m ♦) and experimental data at $Re_\theta = 3300$ (x' = -0.33 •, x' = 0.25 ⊡, x' = 0.5 △, x' = 0.75 ○)

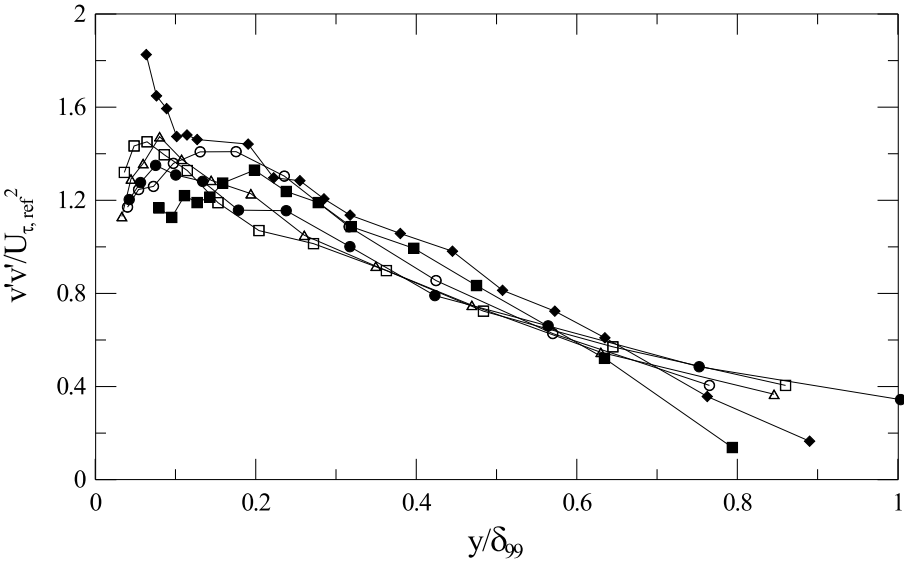

Figure 4.37: Test of new scaling for $\overline{v'v'}$ with data of Samuel & Joubert (1974) (x = 1.04 m ■, x = 1.79 m ♦) and experimental data at $Re_\theta = 3300$ (x' = -0.33 •, x' = 0.25 ⊡, x' = 0.5 △, x' = 0.75 ○)

normal stress in the outer layer is also unaffected by the pressure gradient. When plotted in the rotated coordinates, it collapses using a constant scaling. The inner layer of the streamwise normal stress collapses in a new scaling which collapses the adverse pressure

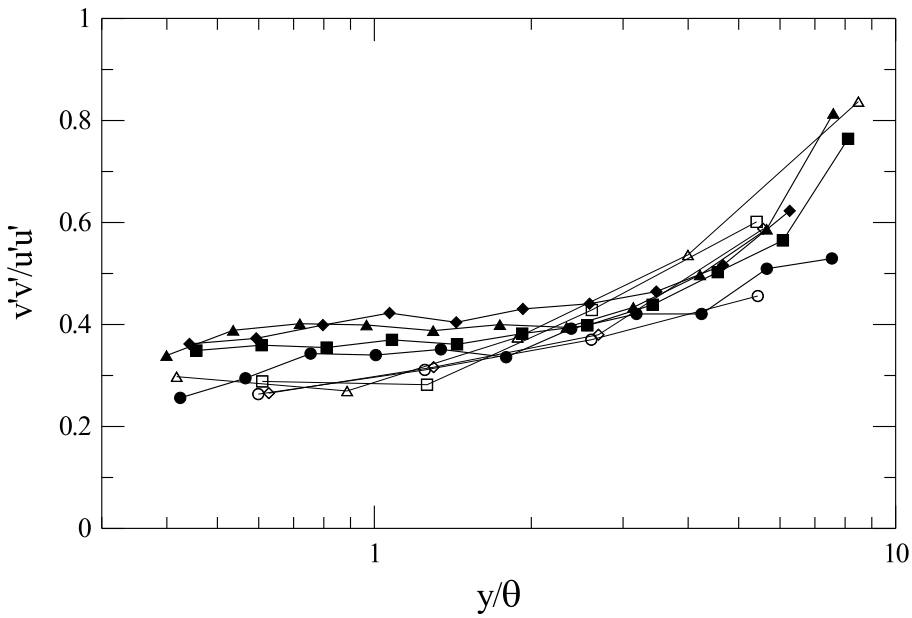

Figure 4.38: Anisotropy parameter for $Re_\theta = 3300$ and 20,600 (closed symbols for $Re_\theta = 3300$ and open symbols for $Re_\theta = 20,600$, x' = -0.33 ●, x' = 0.25 ■, x' = 0.5 ▲, x' = 0.75 ♦)

gradient data onto the flat plate data for the range of Reynolds numbers examined. This new scaling is a mix of inner and outer layer scalings from the local and the reference locations, taking into account both the upstream history of the flow and the local conditions.

4.5 Structural and Quadrant Analysis

A number of structural parameters were examined in Chapter 3. Here, the Reynolds number effects on one of those parameters will be examined. The anisotropy parameter is shown in Figure 4.38 for both $Re_\theta = 3300$ and 20,600 with solid symbols used for the low Reynolds number values and open symbols used for the high Reynolds numbers. The actual symbols for the three ramp locations and reference flat plate location are the same as in Chapter 3. The value for the anisotropy parameter in the flat plate reference location is between 0.3 and 0.4 for both Reynolds numbers, although the value for the higher Reynolds number is consistently lower than that of the lower Reynolds number. In the outer portion of the boundary layer, the anisotropy parameter is observed to increase moving downstream in a similar manner for both Reynolds numbers for the locations along the ramp. In the inner region, the parameter appears to approach a constant value for the higher Reynolds

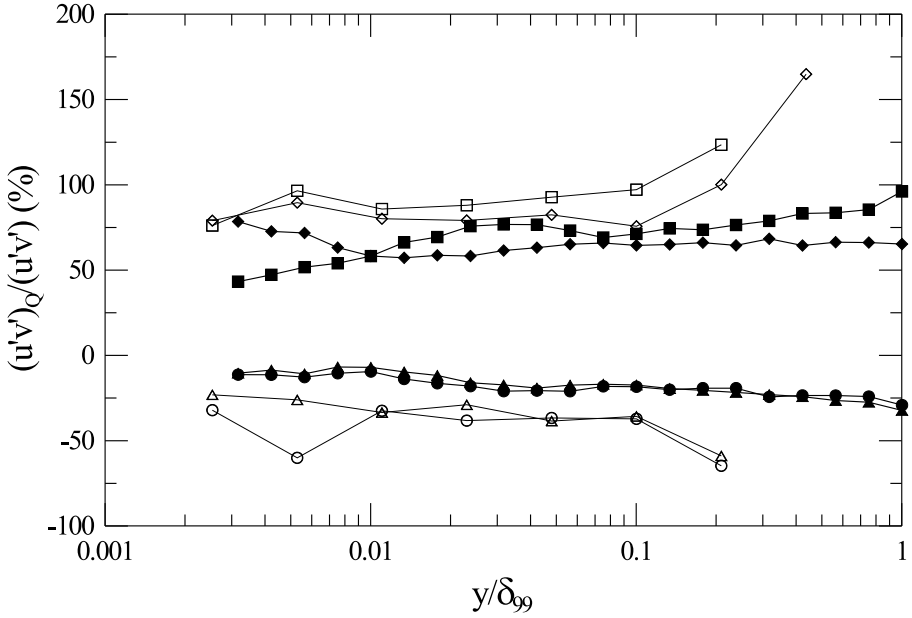

Figure 4.39: Quadrant analysis (H = 0.0) for flat plate at Re_θ = 3300 and 20,600 (closed symbols for Re_θ = 3300 and open for Re_θ = 20,600) (Q1 •, Q2 ■, Q3 ▲ Q4 ♦)

number, unlike the lower Reynolds number case where the parameter increases as the flow is subjected to the adverse pressure gradient. Overall, the anisotropy parameter values and the trends observed for the adverse pressure gradient appear to be similar between the two Reynolds numbers, indicating that the structure of the flow is not changed significantly by the increasing Reynolds number.

The effect of Reynolds number on quadrant analysis was examined by Priyadarshana and Klewicki (2004), who noted that the contributions from all quadrants increased with increasing Reynolds number. The present data show the same trends as seen in Figure 4.39, where all events are compared at Re_θ = 3300 and 20,600 for the flat plate reference location. They noted that close to the wall, contributions from ejections are larger for lower Reynolds numbers, while at high Reynolds numbers sweeps remain large at a larger distance from the wall than for lower Reynolds numbers. For all events, ejections in the near wall region appear to be comparable to the contributions due to sweeps for the higher Reynolds number, while for the lower Reynolds number sweeps appear to dominate ejections in the near wall region, consistent with their observations. For the outer region of the flow, the contributions due to sweeps appear to be much larger for the higher Reynolds number as compared to the lower case. The contributions from the sweep events do not flatten out

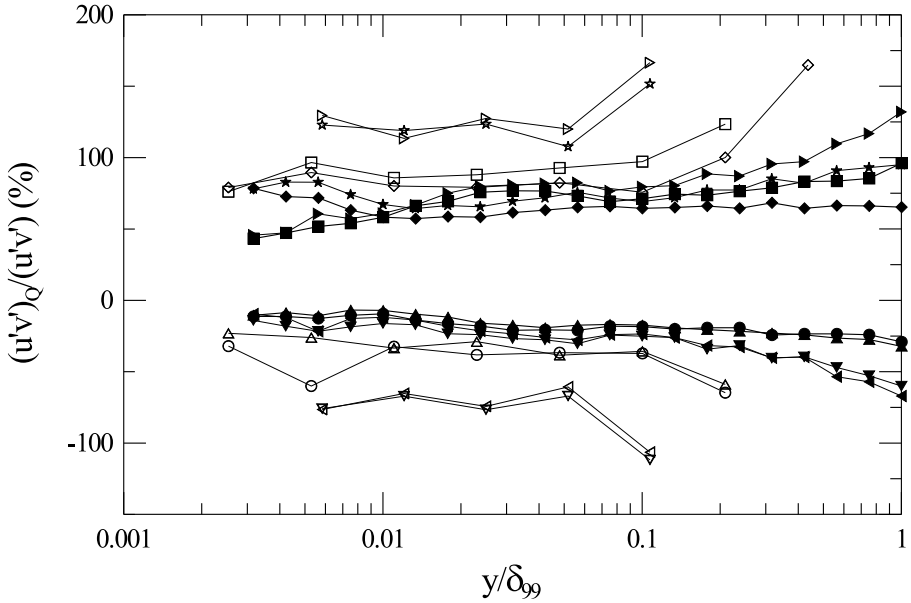

Figure 4.40: Quadrant analysis (H = 0.0) for ramp ($x' = 0.25$), along with flat plate ($x' = -0.33$) at $Re_\theta = 3300$ and 20,600 (symbols same as above with addition of ramp data using Q1 ▼, Q2 ►, Q3 ◄, Q4 ★)

for the higher Reynolds number as they did for the lower Reynolds number case, appearing instead to increase with distance from the wall. The difference between this case and the one examined by Priyadarshana and Klewicki (2004) may be affected by the wall roughness of their high Reynolds number cases, but the overall trends observed in their work are also seen in this data, although they are less pronounced as the Reynolds number range examined here is smaller than the range they examined.

Figure 4.40 shows the contributions from the four quadrants for both Reynolds numbers at the flat plate reference location and one quarter of the way along the ramp for all events. The effects of the increasing Reynolds number are as seen for the flat plate with the increasing Reynolds number increasing the contribution of all quadrants. Along the ramp, the increase in the contribution of each quadrant is larger for the higher Reynolds number as seen for the flat plate region. The contributions along the ramp and on the flat plate for both inward and outward interactions are approximately equal, this is observed for both Reynolds numbers. Also for all locations, ejections are dominant over sweeps even far from the wall. Overall, the trends in the contributions of the various quadrants appear to be similar for the two Reynolds numbers, with the main difference being that for larger

Reynolds number, the contributions are larger for all components.

4.6 Summary

The Reynolds number effects on an adverse pressure gradient flow were examined at $Re_{\theta,ref} = 3300, 14, 100$, and 20,600. Overall, the adverse pressure gradient only mildly impacted the mean flow and the Reynolds number effects on the mean flow were similar to those on a flat plate boundary layer with the law of the wall remaining valid for the range of Reynolds numbers examined at all locations along the adverse pressure gradient ramp. The value of the wake function, Π, decreases with increasing Reynolds number at both the flat plate location and locations along the ramp. The velocity deficit scaling originally proposed by Zagarola and Smits (1998) is observed to hold for individual locations along the adverse pressure gradient as well as along the flat plate location; however this scaling does not collapse the various adverse pressure gradient profiles onto each other as predicted by Castillo and George (2001). This is due to the changing shape of the mean velocity profile as the flow is subjected to the adverse pressure gradient.

The wall pressure distribution, C_p, for both the top and bottom walls was found to display Reynolds number effects once the flow has traveled down approximately half of the ramp. These Reynolds number differences are also observed in the distribution of the pressure gradient parameter, β, although the differences in the value of this parameter are small and the flow is far from separation even at the highest Reynolds number.

The skin friction coefficient, c_f, shows Reynolds number effects along the entire length of the flow. The upstream reference flat plate skin friction value is observed to decrease with increasing Reynolds number and this trend is then observed to persist through the rest of the flow field. The decrease in skin friction over the length of the adverse pressure gradient ramp is observed to remain at approximately 50% for the range of Reynolds numbers examined.

The Reynolds stresses are observed to collapse in the coordinates of DeGraaff and Eaton (2000) for the flat plate boundary layer over the range of Reynolds numbers. However, as the flow travels down the adverse pressure gradient ramp, the streamwise normal stress is shown to not collapse the adverse pressure gradient stress data onto that of the flat plate boundary layer using this scaling, while the traditional streamwise normal stress scaling, u_τ^2 is observed to collapse the inner peak for one Reynolds number. For the range of Reynolds numbers examined, the streamwise normal stresses are observed to collapse using $(u_\tau^2(1 - 0.5\Pi_{ref})^2)$

for the inner layer and $(u^2_{\tau,ref}(1 - 0.5\Pi_{ref})^2)$ for the outer layer peak. This scale is a mix of a local and a non-local scaling. The outer region of the streamwise normal stress also collapses using the outer layer scaling $U_e U_{e,max}$ proposed by Elsberry et al. (2000), although the effectiveness of this collapse appears to decrease as the flow travels further down the ramp. Choosing between these two scales for the streamwise normal stress is not possible without more data from similar flows, as each collapses the flow reasonably well.

For the wall normal stress, the constant scaling of $u^2_{\tau,ref}$ collapses the range of Reynolds number for the flat plate and adverse pressure gradient ramp. Overall, the normal stresses in the outer layer do not change as the flow is exposed to the adverse pressure gradient. Because of this lack of change, the use of local values of the friction velocity will produce the development of the outer peak observed in Chapter 3 due to the large decrease in the skin friction along the length of the ramp; therefore reference values are most appropriate for the outer layer scales of these stresses.

The proposed scalings collapse the data of Samuel and Joubert (1974) in the wall normal direction, but not in the streamwise normal direction. This is due to the lack of information about the flow before the start of the pressure gradient, where reference parameters were determined for this flow. The measurement location from their experiment used for the calculation of reference parameters was located in the adverse pressure gradient, leading to a value of the wake parameter comparable to that measured in the experiment one third of the distance down the ramp in the current experiment.

An attempt was made to use a commercial CFD package, Fluent, to model the flow with the hope that the stress scalings tested in this chapter could be reproduced computationally. The goal was to use CFD as an additional tool for changing the Reynolds number and to be able to test the Reynolds number stress scalings proposed here on a larger range of Reynolds numbers. The stress models available in Fluent were unable to capture the necessary stress changes and the results can be seen in Appendix C.

Finally, the structure of the flow is only changed mildly with Reynolds number. Quadrant analysis shows that the contributions from all quadrants increase with increasing Reynolds number as observed by Priyadarshana and Klewicki (2004). Overall the contributions from each quadrant have similar overall contributions relative to each other over the range of Reynolds numbers examined.

Chapter 5

Conclusions and Future Work

5.1 Conclusions

An adverse pressure gradient flow far from separation along a 4° ramp was examined at three separate momentum thickness Reynolds numbers, $Re_\theta = 3300, 14, 100$, and 20,600, as measured at the reference flat plate location. Reynolds number scaling of the mean velocity and Reynolds stress profiles was examined. In addition, basic structural parameters for the flow were examined to evaluate how far out of equilibrium the flow becomes in the adverse pressure gradient. The measurements of the mean velocity and Reynolds stress profiles were made using a custom 2-component high resolution LDA system as described in Chapter 2. The flow development for the entire flow field was examined in depth in Chapter 3 for $Re_{\theta,ref} = 3300$. The Reynolds number scaling of the mean velocity and turbulent stresses was examined in Chapter 4. Appendix C describes the computational modeling done of this flow using Fluent and the differences between the experimental mean and turbulence profiles and those from the computation.

The flow examined starts as a flat plate boundary layer, which is then subjected to an adverse pressure gradient along a 4° ramp before a short redevelopment flat plate region allows for some examination of the redevelopment of the flow. The redevelopment region for this flow was too short to show signs of the stress equilibrium layer observed by Song (2002). This adverse pressure gradient flow is only mildly perturbed from that of the flat plate, as observed through the examination of various structural parameters.

The mean velocity profiles along the adverse pressure gradient do not develop inflection points and the logarithmic law of the wall remains valid for all measurement locations, although the wake grows substantially in the pressure gradient. Over the range of Reynolds numbers examined, the changes in the mean velocity profile are small. However by the end of the adverse pressure gradient ramp, the mean velocity profile does have a notably different shape for the three different Reynolds number cases. The velocity deficit scaling of Zagarola and Smits (1998) is observed to collapse the mean velocity profile at any particular location along the ramp for the range of Reynolds numbers, but is not generally valid for

collapsing the profiles from different locations along the pressure gradient. This is due to the changing shape of the mean velocity profile and contradicts the similarity analysis of Castillo and George (2001).

Reynolds number effects are observed in the stress profiles, although the larger changes in these profiles are due to the changing pressure gradient and the large decreases observed in the skin friction along the length of the ramp. Using the DeGraaff and Eaton (2000) coordinates for the flat plate boundary layer to scale the stresses, the normal stresses are observed to develop a large outer layer peak or plateau as the flow travels along the adverse pressure gradient for all three Reynolds numbers examined. For the wall normal stress, the entire stress profile, including both the inner and outer layers, is observed to scale using the value of the friction velocity at the upstream flat plate reference location. This scaling is also observed to collapse the data of Samuel and Joubert (1974), as well as being the wall normal stress scaling at the separation point in the flow of Song (2002). A new scaling for the streamwise normal stress, which accounts for both the local and upstream history effects on the flow, was determined to collapse the inner layer peak for the adverse pressure gradient and flat plate profiles. This new scaling $U_\tau^2(1-\Pi_{ref}/2)^2$ applies for the inner layer of the profile, while for the outer layer the local value of the friction velocity is replaced with the flat plate reference value. This scaling does not collapse the data of Samuel and Joubert (1974), although no flat plate reference values are given for this flow, accounting for the lack of collapse. The outer layers for both the wall normal and streamwise normal stress profiles along the ramp are observed to collapse using the value of the friction velocity from the upstream flat plate reference location. These scalings show that the normal stresses are determined almost entirely by the upstream flat plate values, and the turn that the flow experiences over the 4° ramp only weakly affects the normal stresses.

Finally, modeling of the entire flow domain using Fluent and its standard Reynolds stress transport model was performed to determine how commercial CFD codes perform in modeling basic flows, particularly for the turbulent stresses. Fluent did a reasonable job of predicting the wall pressure distribution over the entire domain. Fluent also captured the trends in the stresses and mean flow, but the actual values predicted using Fluent were sufficiently different from those measured experimentally to prevent the use of Fluent for testing the proposed scalings for various Reynolds numbers with confidence. Additionally, for the redevelopment region the mean velocity profiles differed substantially between the Fluent predictions and the experimental measurements, particularly in the profile shapes.

5.2 Future Work

Even for this mild adverse pressure gradient flow, the empirically derived scalings for collapsing the turbulent stresses over a range of Reynolds number are difficult to explain physically. Although these scalings collapse the stresses measured in this experiment, the applicability of these scalings to other adverse pressure gradient flows without separation for different geometries is questionable. The Reynolds number scalings proposed in this work, the work of Song (2002) and the work of DeGraaff (1999) are all empirically determined and other scalings may collapse the stresses in a similar manner, making it difficult to determine the correct empirical scaling. The use of commercially available codes, such as Fluent, do not provide accurate enough predictions of the turbulent stresses to test the Reynolds number scalings proposed for the variety of geometries already examined experimentally. Flows similar to those examined in this facility over the years should be examined using more state of the art turbulence models, which have been developed to predict the flow based on moderate and not low Reynolds number experimental data. The ability of these models to predict the results observed over the range of Reynolds number examined experimentally should be tested using the now available experimental data in order to examine whether these empirically derived scalings are useful for the modeling of the turbulence, or whether these trends in the turbulent stresses with Reynolds number are already predicted by the turbulence models currently being implemented. Once this is possible, CFD may be useful for determining the correct scaling for these stresses in a variety of basic flows. The data for the flow examined in this thesis, as well as the other flows examined in this facility, provide highly resolved data with which to test and calibrate new models using a range of Reynolds number data previously not available. The use of this data to develop new models, or to modify existing models, is an obvious extension of this work.

The examination of the flow field for a massively separated flow is one for which current CFD modeling is unable to capture the physics of the flow or accurately predict the overall flow field, including the mean and turbulent stress profiles. The use of the current facility to measure this flow over a range of Reynolds number, particularly using PIV to examine the entire flow field, would produce more high resolution data with which to more accurately compare the current computational models. This data would also be useful for the development of new models by providing the necessary data to calibrate the values of various constants for this massively separated flow.

Appendix A

Vibration Isolator Redesign

The vibration isolator used to maintain the LDA optical rail at a constant height was redesigned. The vibration isolator system consists of three air feet (Technical Manufacturing Corp Model 64-301) supporting the corners of the optics mount as shown in Figure 2.7. These vibration isolators do not hold a steady vertical position so an additional custom control system is required to maintain each foot at the desired position. The control system uses four solenoid valves to fill and drain each air foot. The position of each foot is indicated by an infrared detector and a custom logic circuit controls the valves. During the course of the present experiments a number of system components failed. The original logic circuit developed by DeGraaff and Eaton (2000) was repaired. During the course of the vibration isolator redesign, numerous components in the electronic circuit were replaced. In addition, the valves used for controlling the air flow into the air feet were replaced and the entire air supply system was redesigned.

Each air foot is controlled by four solenoid valves (Clippard Minimatics, Model ET-2-24VDC), coarse and fine fill valves and coarse and fine drain valves. The flow rate through each valve is controlled by a needle valve (IDEAL, Model 52-1-11). The coarse valves are used to rapidly fill or drain the air foot if it is far below or above the desired position. In principle, these could be active at any time, but in practice they only operate during startup or shutdown. The fine valves are used to supply or discharge very small flowrates from the air foot for precise positioning. The needle valves for the coarse supply are set for a flowrate of 5 scfh, while the for the fine they are set for 2.5 scfh. A schematic of the air supply system is shown in Figure A.1 and a photograph of the box containing the valves and the control electronics is shown in Figure A.2. This box is mounted inside the tank near the LDA system. Figure A.1 shows the valves for a single air foot.

The air at the inlet is supplied from a cylinder of breathable air located outside of the tank. The location of tees and crosses in the diagram corresponds to those found in the physical box. In this diagram a circle indicates a valve and the letter inside indicates whether it is a solenoid valve (S) or a needle valve (N). The first letter in any letter combination indicates whether the set of valves are for coarse (C) or fine adjustment (F), while the

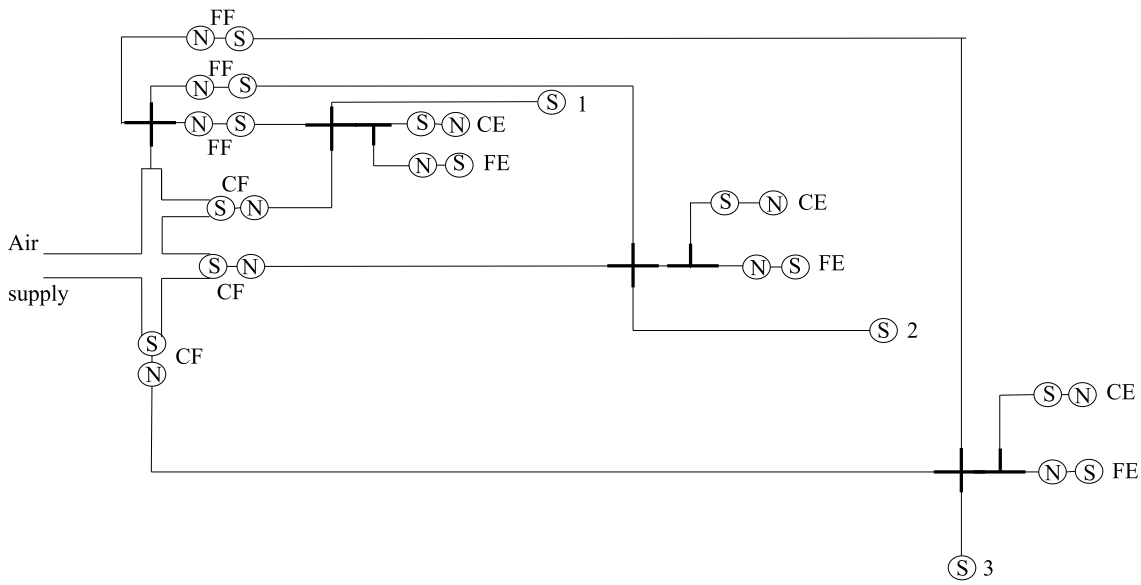

Figure A.1: Vibration isolator circuit for one channel

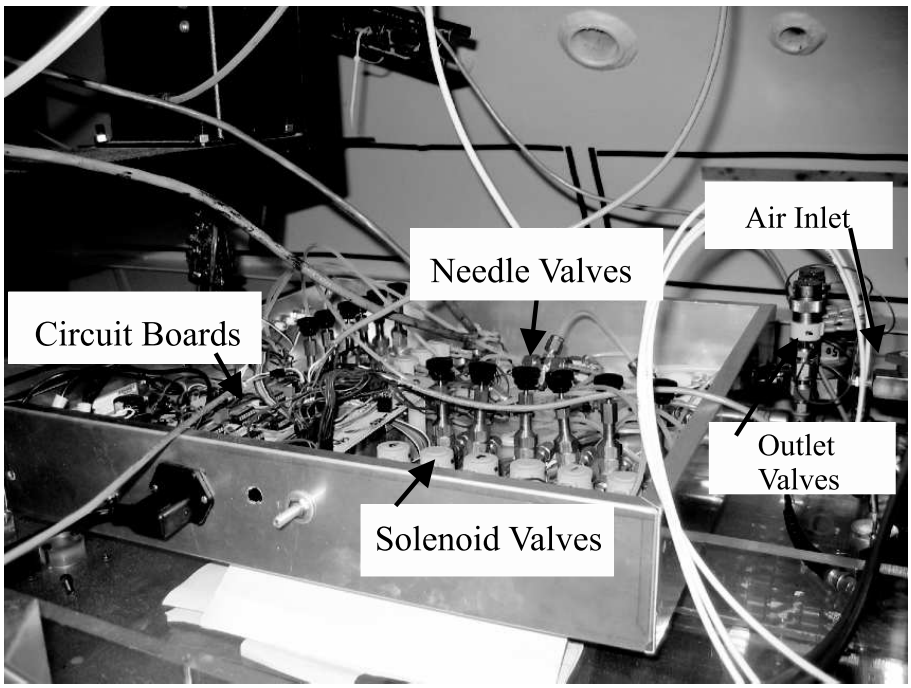

Figure A.2: Vibration isolator electronics box

second letter refers to whether the valves are for filling (F) or emptying (E). A final set of three valves are labeled with a number. These valves are three way valves which are always

open between the air supply system and the feet while the system is running. When the system is turned off, these valves close to allow the system to drain most effectively through their outlet. The numbers indicate which foot they correspond to, but since the three feet are all treated identically, this is just to show that there are three separate systems.

The infrared detectors (Model H21B1) control the signals sent by the electronics box to the various valves, in turn controlling the air supply to the feet. These detectors are mounted near the air feet and send a signal to the electronics box indicating whether the air feet are underfilled or overfilled. The signal has four possible voltage ranges, two for underfilled and two for overfilled. The difference between the two voltage signal ranges for each condition indicates whether the system needs to perform both a coarse and fine adjustment or only a fine adjustment. A coarse and fine fill is performed if the voltage is less than 0.28 V and only a fine fill is performed if the voltage is between 0.28 V and 2.36 V. A coarse and fine empty is performed if the voltage is greater that 4.72 V and only a fine empty is performed if the signal is between 2.64 V and 4.72 V. Technically if the signal is between 2.36 V and 2.64 V the foot neither fills nor empties but this is only infrequently observed. Typically the voltage signals take on values of 0.05 V, 5.0 V, 0.3 V or 4.6 V corresponding to the various states of filling and emptying. These detectors receive their power from the 5 volt supply inside the vibration isolator.

The electronic control circuit for one foot is shown in Figure A.3. The other feet have identical circuits. Each foot operates entirely independently from the others, so while one foot many require only a fine adjustment, the others may require both a coarse and fine adjustment. The infrared detector signal can be found as an input into the circuit in this diagram. While the signal from the infrared detector indicates that a coarse alignment is necessary, the coarse fill or empty valves run continuously. Only when the infrared detector signal indicates that the system has reached a state where only a fine adjustment is necessary do the coarse alignment valves stop operating.

The fine alignment for each foot operates at all times, but uses a timing signal to determine which foot is operating at any given time. The timing signal was designed by DeGraaff and Eaton (2000) and is shown in Figure A.4, and can also be found as an input into the circuit in Figure A.3. This was not changed in the redesign and the choice of ordering of the signals was previously decided. The timing signal comes from a few logic chips used to produce a signal with four distinct beats, a counter and a clock chip. The clock chip was attached to a variable potentiometer, which could be adjusted to allow the signals

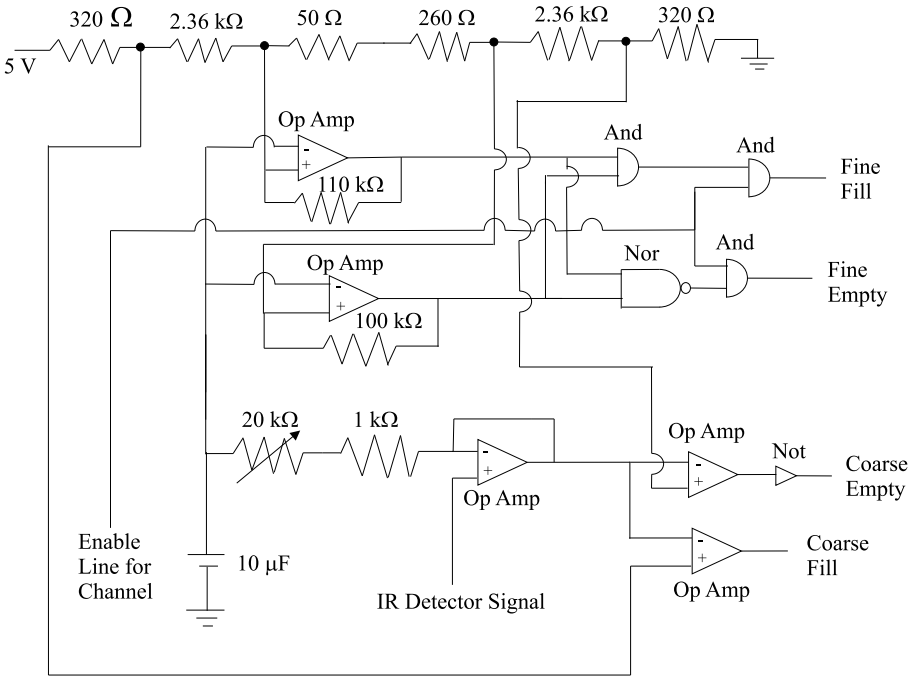

Figure A.3: Vibration isolator circuit for one channel

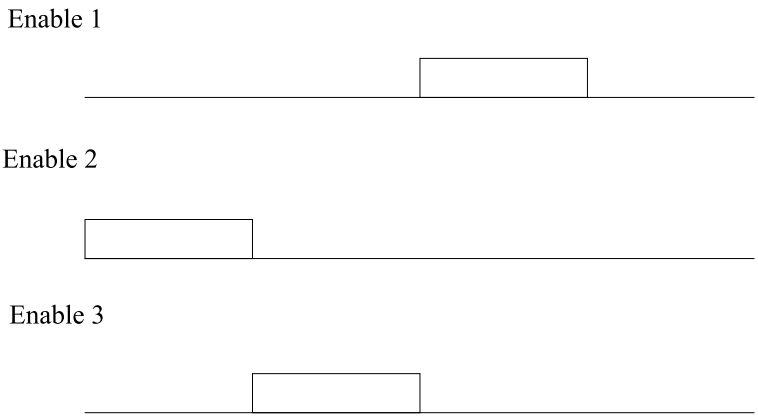

Figure A.4: Enable signal for control of vibration isolator

to change at a rate of approximately 1 Hz. This allowed the timing signal to change at the same rate, thus changing which foot was able to perform fine adjustment every second. There are four counts in this signal. Each foot has one count and there is also a rest count during which time none of the feet do anything.

As compared to the original system, the redesigned vibration isolator fills relatively

rapidly. At one atmosphere of ambient pressure the system takes approximately 5 minutes to lift off, while at eight atmospheres it takes approximately 15 minutes.

Appendix B

Flat Plate Boundary Layer Produced in Two Different Ways

A brief study was performed to examine whether producing the same Reynolds number in two different ways produced the same mean velocity and turbulent stresses, or whether the different methods led to different stress profiles.

The same momentum thickness Reynolds number $Re_\theta \approx 7000$, was produced at both 2 atmospheres and 4 atmospheres of ambient pressure. The freestream velocity at 2 atmospheres was 20.3 m/s, producing a momentum thickness Reynolds number at the measurement location of $Re_\theta = 7480$. For the 4 atmosphere case, the freestream velocity was 11 m/s, producing a Reynolds number of $Re_\theta = 7040$. An additional 2 atmospheres case with a Reynolds number of 6730 is also shown. For all three cases, the mean velocity when plotted inner normalized is shown in Figure B.1. The mean velocity profiles all collapse very well on each other for all three cases.

Next the turbulent stresses were examined. The streamwise normal stress is shown in Figure B.2. Here the stress is normalized using the DeGraaff and Eaton (2001) scaling of $u_\tau U_e$, using local values. The stress profiles collapse very well for all three of the Reynolds numbers. The streamwise normal stress profiles show no discernable difference.

The wall normal stress is shown in Figure B.3. Here the stress is normalized using the scaling of u_τ^2. The stress profiles collapse very well for all three of the Reynolds numbers over the entire boundary layer.

The Reynolds shear stress is shown in Figure B.4. Here the stress is normalized using the scaling of u_τ^2. The stress profiles collapse very well for all three of the Reynolds numbers.

The method of producing a flow with a particular Reynolds number does not appear to affect the mean and turbulent quantities. In fact the mean and turbulence produced by these two methods are identical when scaled using inner coordinates.

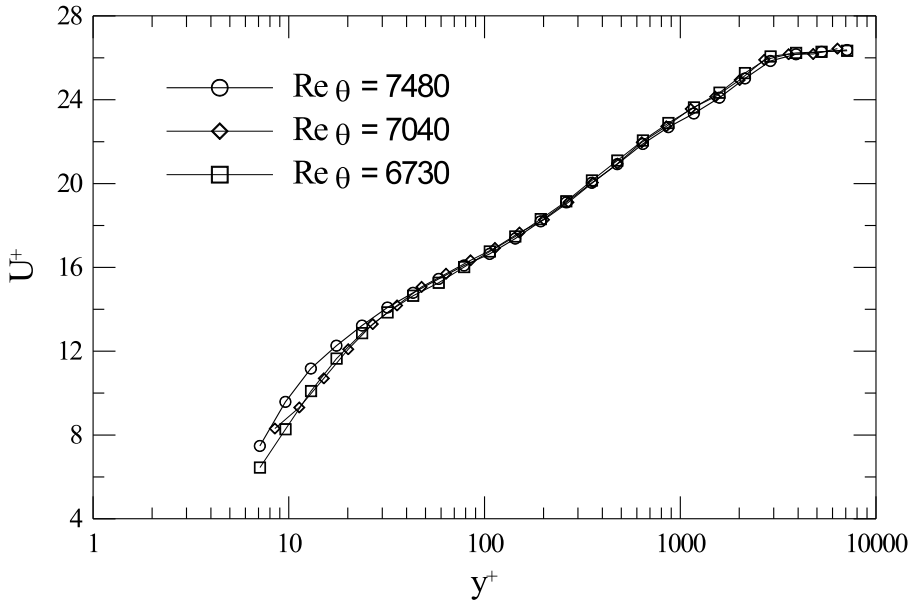

Figure B.1: Law of the wall plot for three Reynolds number cases

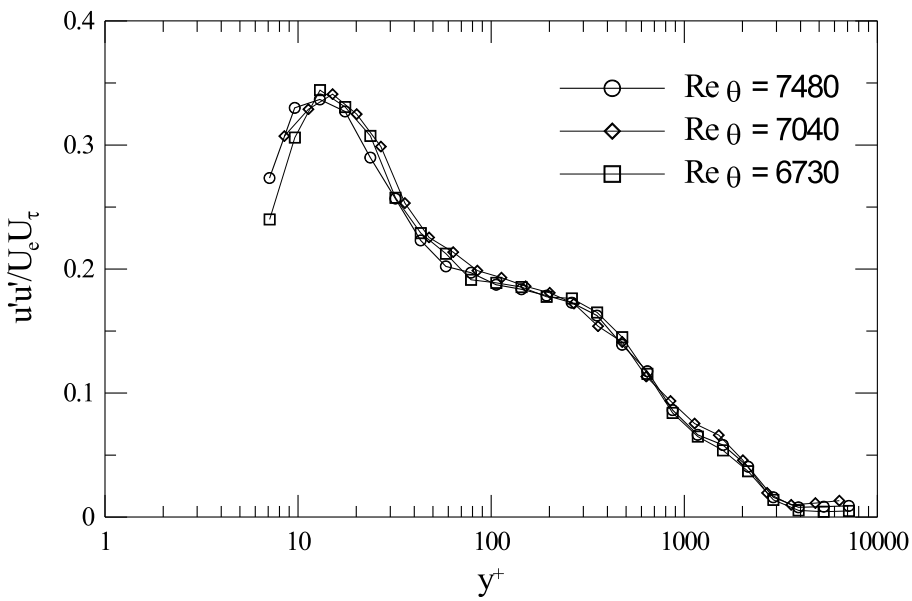

Figure B.2: Streamwise normal stress profiles in DeGraaff & Eaton coordinates for three Reynolds number cases

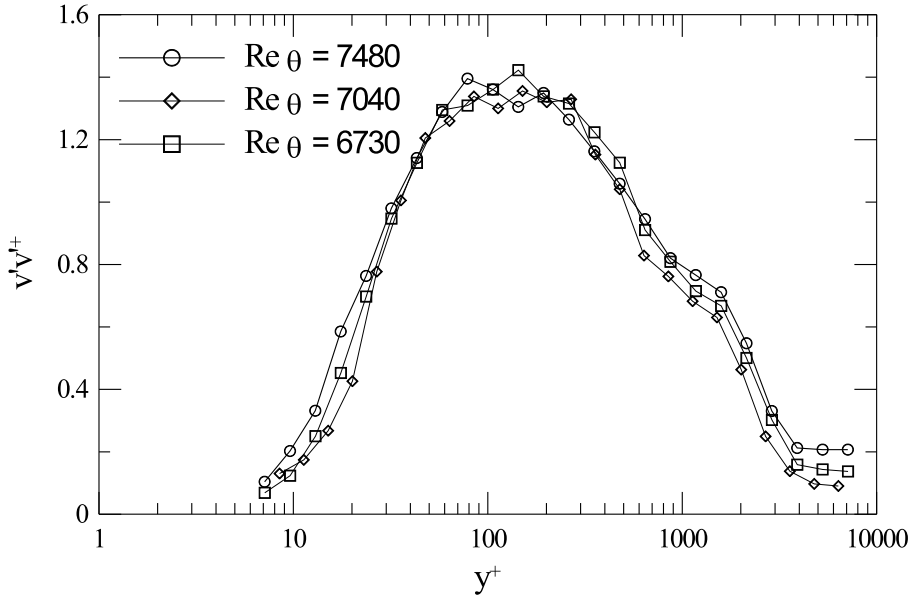

Figure B.3: Wall normal stress profiles in traditional coordinates for three Reynolds number cases

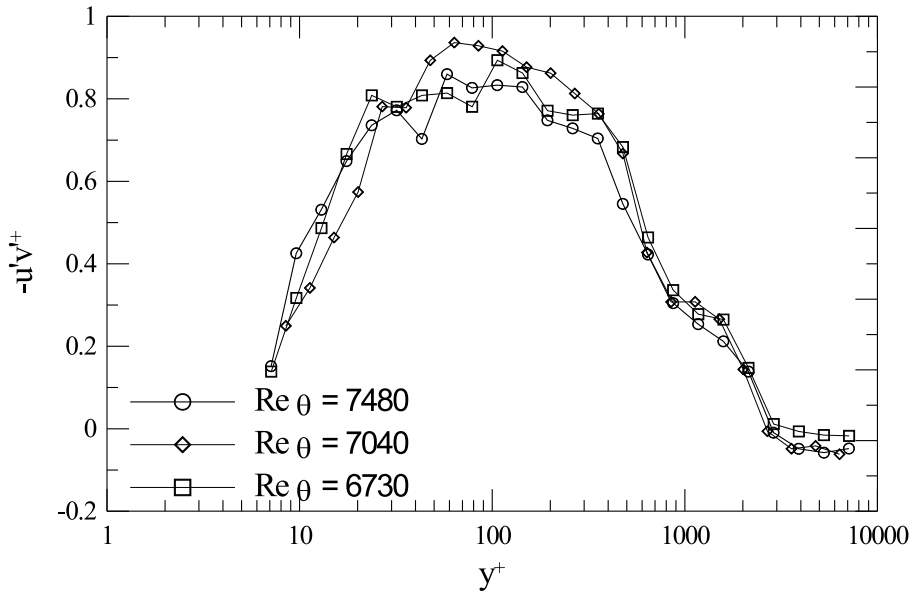

Figure B.4: Reynolds shear stress profiles in traditional coordinates for three Reynolds number cases

Appendix C

Computational Modeling of Adverse Pressure Gradient Flow

Computational modeling was performed using the commercial CFD package Fluent with the goal of using the modeled stress data over the boundary layer to further examine the Reynolds number scaling of the turbulent stresses. The experimental work was done with the goal of producing Reynolds number scalings for the turbulent stresses as a way to enhance computational modeling. The idea of this final part of the project was to examine whether typical commercially available turbulent stress models already followed the scaling laws found experimentally. If so, the computations would corroborate the experimental work and lead to another method for examining the Reynolds stress scalings and determining parameters from the flow which are important in predicting the changes in the turbulent stress profiles. As this was a side project to the overall experimental work on this adverse pressure gradient flow, only the Reynolds stress model available in Fluent was examined. Since the typical use of a CFD package such as Fluent is to accurately predict the mean flow and produce results for more complex flows, the turbulent stress model in Fluent was found to not adequately represent the experiment results, making it difficult to test many of the proposed scalings, which were of particular interest. The overall ability of Fluent to match the trends of the flow was very good, although matching various flow parameters was found to be less acceptable than originally expected.

C.1 Model Specifications

The Reynolds stress transport model was used in Fluent to model the flow, including the turbulent stresses. Before the Reynolds stress transport model was implemented, the $k - \epsilon$ model was used to converge the mean velocity and the values of k and ϵ for the entire flow field. Then the Reynolds stress transport model was switched on and allowed to converge as well. The closure modeling techniques employed by Fluent can be found in the Fluent users manual. The models used in this computation are not the most advanced available,

they are however general models typical of those available in commercial packages, including Fluent. Other models may have produced better results for the stresses or mean flow or skin friction coefficient, however the idea here was to test what a commercially available package was capable of.

The Reynolds stress model was run using a 2D steady coupled implicit solver with second order upwind discrimination. The use of this solver, the compressible solver, was found to give better results for the mean flow field and the turbulent stresses than the incompressible solver.

The grid used to model this flow was set up to have the same physical dimensions as the actual wind tunnel flow from the upstream flat plate measurement location to the final downstream location. The grid was generated in Gambit. In the streamwise direction, cells were located every millimeter along the length of the flow field. In the wall normal direction, the grid was double sided with a clustering of points located in the near wall region on both the top and bottom walls. For this direction, 200 elements were used. The overall grid has approximately 120,000 quadrilateral cells.

The inlet boundary conditions were set from the experimental data measured on the flat plate. The values for k, $\overline{w'w'}$ and ϵ were estimated from the experimental values of the other stresses and the mean velocity profile using standard approximations. Since the experimental data were measured only for the bottom half of the boundary layer, the profile was reflected over the centerline of the inlet. The no-slip condition was used as the boundary condition for the top and bottom wall. The outlet boundary condition was set to the outflow condition, which sets the gradients to zero at the exit.

C.2 Comparison of Experimental Data and Fluent Results at $\mathrm{Re}_\theta = 3300$

The Fluent results were compared with the experimental data along the adverse pressure gradient ramp for $Re_\theta = 3300$. To allow for easier comparison, two locations along the adverse pressure gradient ramp were selected for these comparisons. The locations chosen were $x' = 0.25$ and 0.75 or one quarter and three quarters of the distance down the ramp. This allowed for an examination of how the flow compares near the start of the adverse pressure gradient as well as a good distance down the ramp.

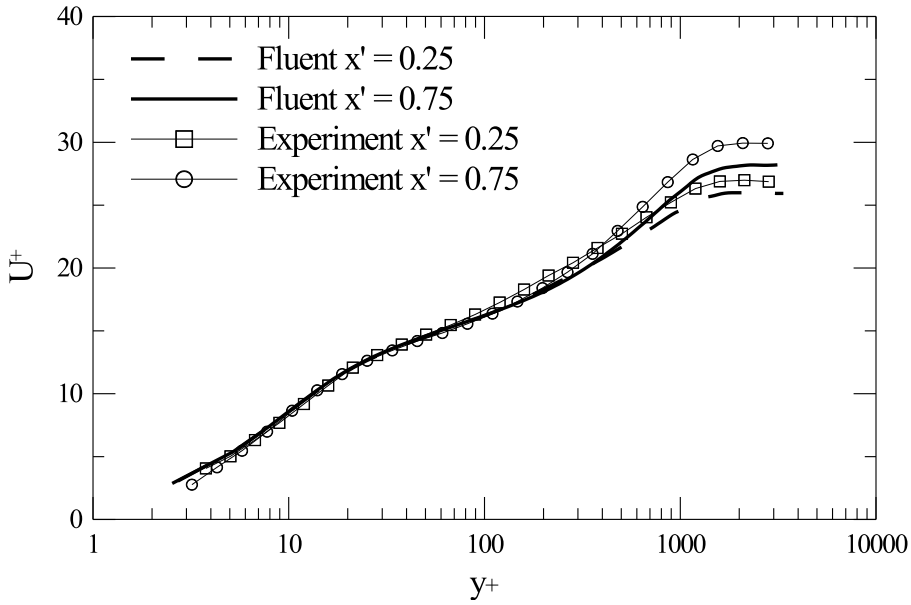

Figure C.1: Law of the wall at two locations along the ramp at $Re_\theta = 3300$ for both experiments and Fluent

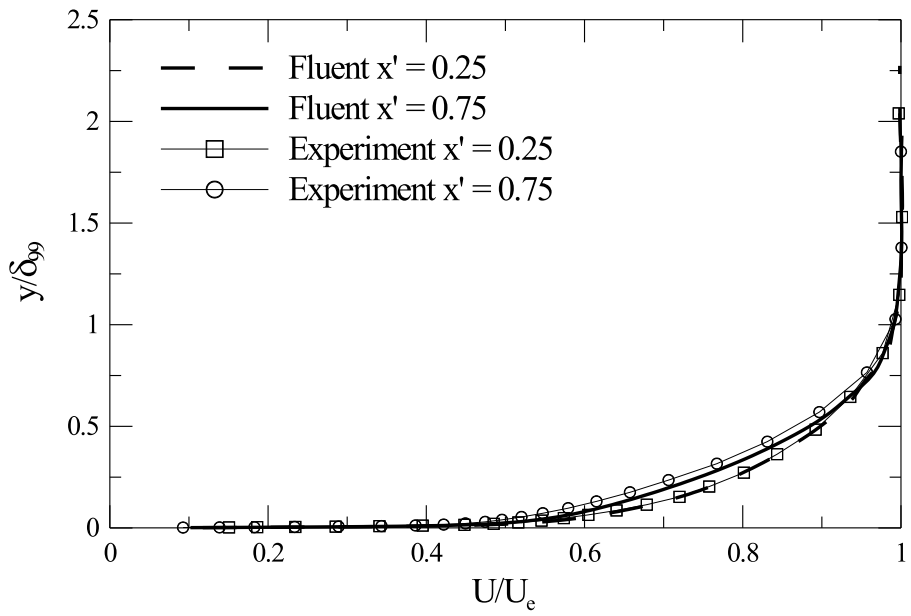

Figure C.2: Mean velocity profiles in outer layer scaling at $Re_\theta = 3300$ for both experiments and Fluent

First the mean velocity profiles were compared at the two locations between the experimental data and the Fluent results. Figure C.1 shows the traditional logarithmic law

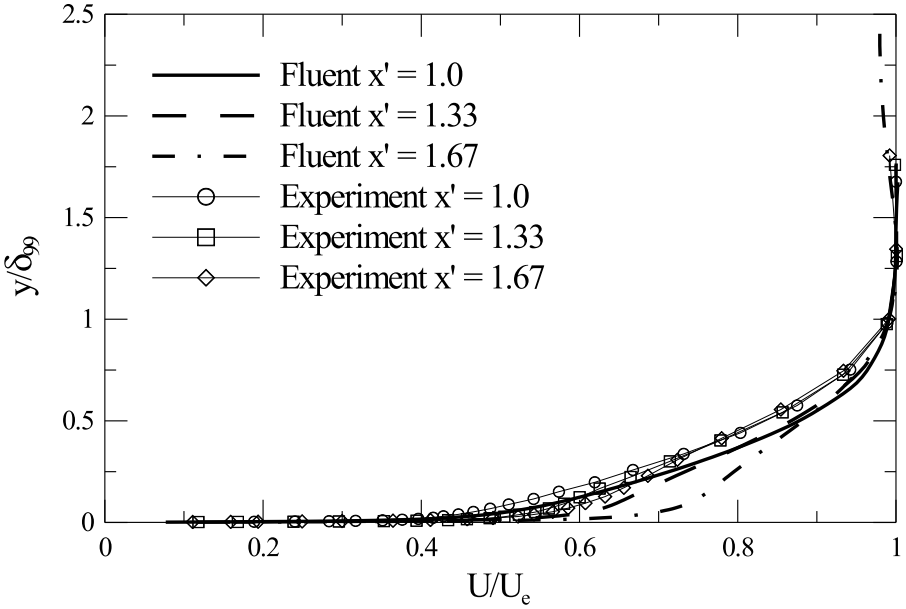

Figure C.3: Mean velocity profiles in outer layer scaling at $Re_\theta = 3300$ for both experiments and Fluent in the redevelopment region

of the wall coordinates for the two locations. At $x' = 0.25$, the profiles from Fluent and the experiment are very similar, however as the flow travels along the ramp, the profiles at $x' = 0.75$ show that Fluent underpredicts the wake. Fluent does predict an increase in the wake portion of the mean velocity profile, however the actual values are lower than those observed experimentally. The mean velocity profile at the same two locations are shown in outer layer scaling in Figure C.2. Again, the profiles from the experiment and Fluent at $x' = 0.25$ are very similar, but as the flow travels farther down the ramp, the differences in the profile shapes between the experiments and Fluent are observed to become more significant. Finally, the ability of Fluent to accurately predict the mean velocity profile downstream of the ramp in the redevelopment region is examined. These mean velocity profiles for both the experiments and Fluent at all three locations starting at the end of the ramp and progressing into the redevelopment region are shown in Figure C.3. The development of an inflection point in the mean flow profile is observed in the Fluent results similar to that described in Chapter 3 for the experiments, however the mean velocity profiles from the Fluent predictions have a different overall profile shape than those measured experimentally. The modeled results appear to respond much more quickly to the change in pressure gradient.

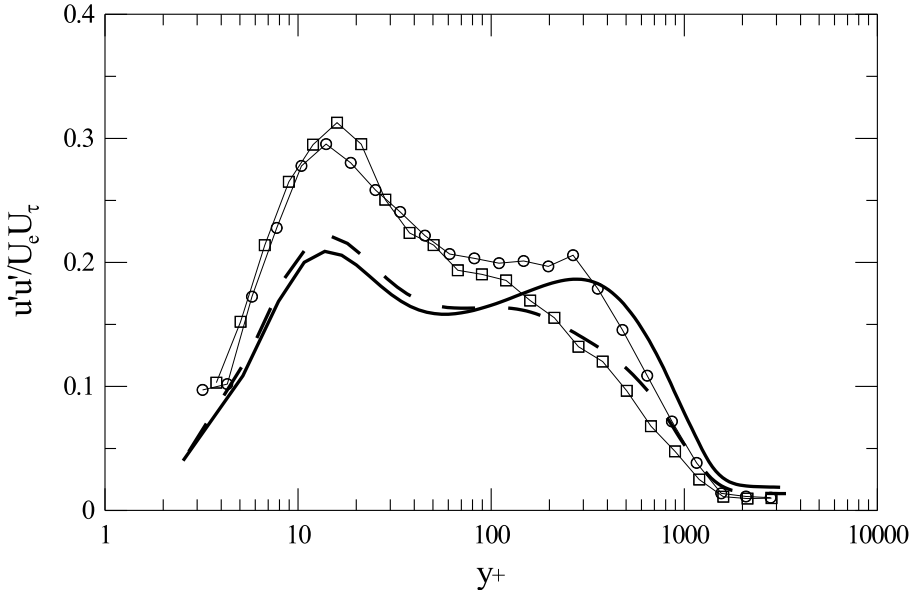

Figure C.4: Streamwise normal stress in DeGraaff & Eaton scaling for two locations along the ramp at $Re_\theta = 3300$ for experiments and Fluent (experiment x' = 0.25 ⊡, experiment x' = 0.75 ∘, Fluent x' = 0.25 dashed line, Fluent x' = 0.75 solid line)

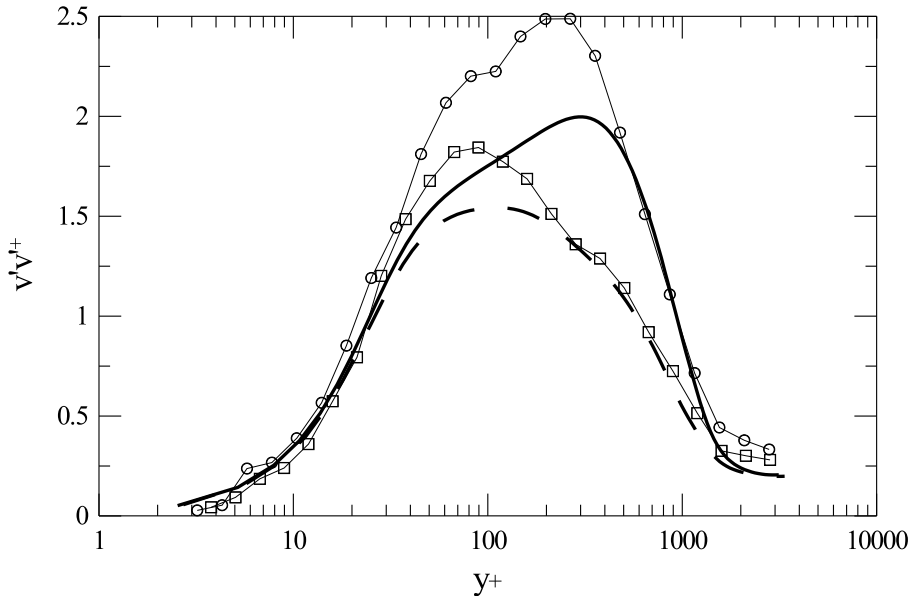

Figure C.5: Wall normal stress in traditional scaling for two locations along ramp for experiments and Fluent (experiment x' = 0.25 ⊡, experiment x' = 0.75 ∘, Fluent x' = 0.25 dashed line, Fluent x' = 0.75 solid line)

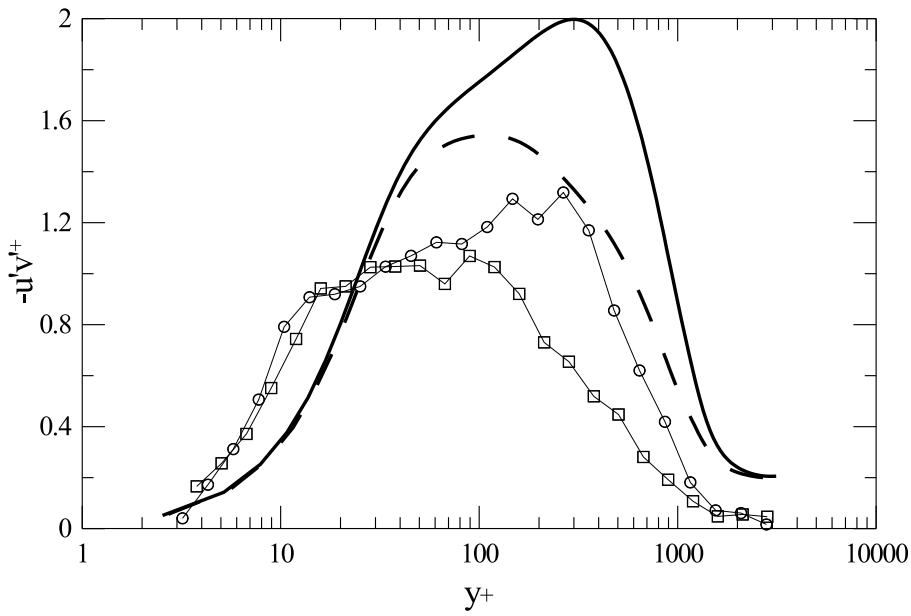

Figure C.6: Reynolds shear stress in traditional scaling at two locations along ramp for experiments and Fluent (experiment x' = 0.25 ⊡, experiment x' = 0.75 ∘, Fluent x' = 0.25 dashed line, Fluent x' = 0.75 solid line)

The stresses were then examined at the same two locations as the mean velocity profiles. The streamwise normal stress is shown in Figure C.4 in the DeGraaff and Eaton (2000) scaling. The inner layer peak is observed to be far underpredicted by Fluent for both locations. This is likely due to modeling of the k equation used to compute the boundary conditions and how the stresses in the near wall region are calculated based on these values. Overall, the inner peak in the streamwise normal stress is depressed compared to the experimentally measured value regardless of the initialization of this stress profile, because of the wall boundary conditions on the value of the kinetic energy. The development of the outer layer plateau along the adverse pressure gradient ramp is observed, although the Fluent profiles are not the same as those measured experimentally.

The comparison of the experiment and the Fluent results for the wall normal stress is shown in Figure C.5. The development of the outer layer peak is observed in the Fluent results, although the peak values are observed to be slightly lower than those from the experiments. The inner layer from the Fluent results collapses well with the experimental results and the outer layer also collapses reasonably for distances beyond the location of the stress peak. Overall, the wall normal stress is better represented by Fluent than the

streamwise normal stress, but there are still large differences between the experiments and the Fluent profiles.

Finally, the Reynolds shear stress comparison is shown in Figure C.6. Unlike for the normal stresses, the shear stress peak is overpredicted by Fluent compared with the experimental results. The inner layer for the shear stress is significantly different between the experiments and Fluent results and the differences do not disappear over the entire boundary layer. In addition, the trends observed in the Fluent results for the shear stress are different than those observed experimentally, with the stress profiles diverging over more of the profile than in the experimental results. Since the Reynolds shear stress profiles were difficult to measure experimentally and were not discussed in depth for the Reynolds number scaling, the results from Fluent for higher Reynolds numbers will not be discussed in this chapter either.

Based on this comparison, Fluent does a reasonable job at accurately representing the trends in the turbulent stresses and the mean flow. Unfortunately, the stresses in particular are not well enough predicted to test the turbulent stress scalings as originally intended. This is likely due to the choice of model used in this work and better results may be observed using other more recent models.

C.3 Fluent Trends with Reynolds Number

Next the Reynolds number trends of the Fluent results were examined at the same three Reynolds numbers examined experimentally to see how the Reynolds number trends were captured by Fluent.

The wall pressure distribution along the ramp for the three Reynolds numbers is shown for both the experimental data and the Fluent predictions in Figure C.7. The Reynolds number effects are not observed to start until approximately half way down the ramp for the experimental data, however for the Fluent data, the Reynolds number effects start earlier along the ramp. Overall, the pressure coefficient at the start of the ramp is underestimated, but the entire pressure distribution is reasonably well predicted using Fluent for all three Reynolds numbers.

The skin friction coefficient distribution for all three Reynolds numbers is shown in Figure C.8 with both the experimental and Fluent data. The trends in the skin friction coefficient along the ramp are similar between the experiments and the Fluent results;

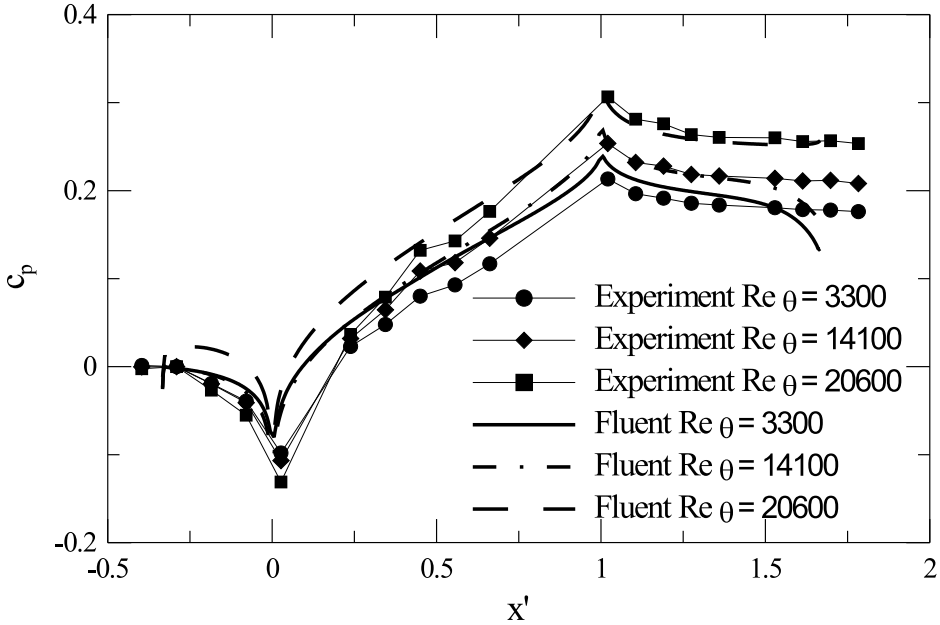

Figure C.7: Wall static pressure distribution on bottom wall at three Reynolds numbers for experiments and Fluent

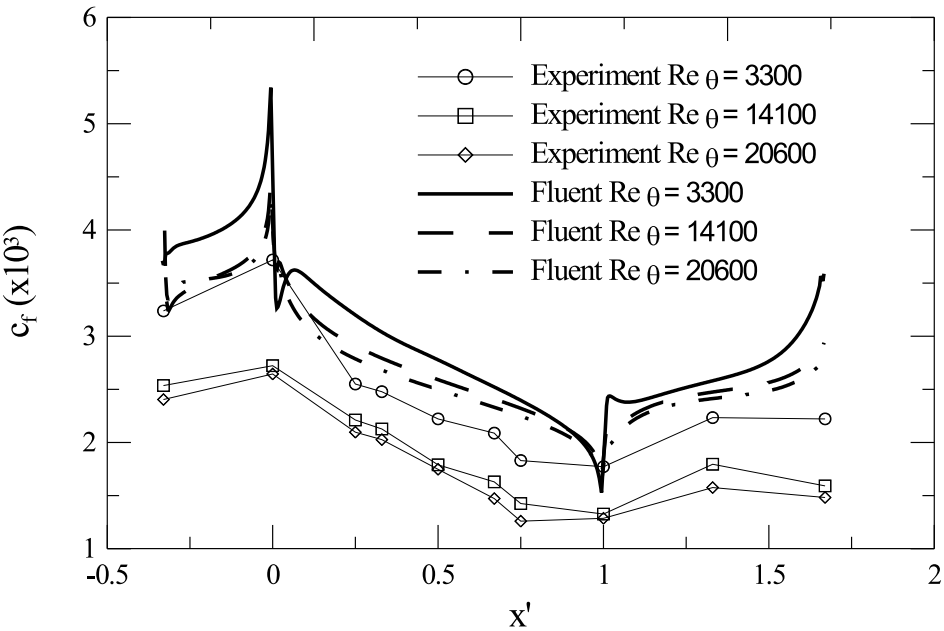

Figure C.8: Skin friction coefficient distribution at three Reynolds numbers for experiments and Fluent

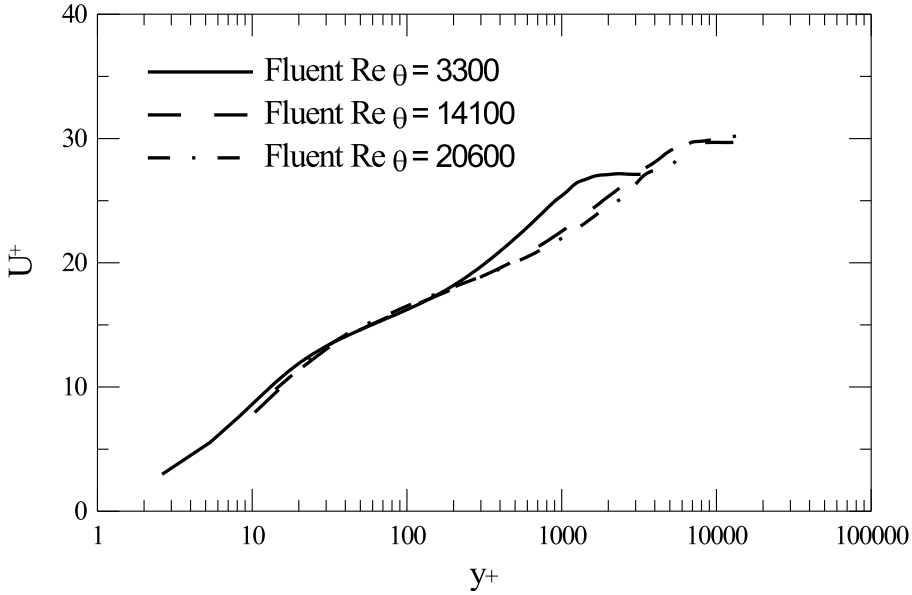

Figure C.9: Law of the wall at x' = 0.5 for all three Reynolds numbers from Fluent

however the actual values in the skin friction coefficient are substantially different, with Fluent overestimating the skin friction coefficient along the entire length of the ramp. In addition, at the start and end of the ramp, the changes in the skin friction coefficient observed in the Fluent results are very different than those measured experimentally. This again is due to the choice of model and may be improved with the use of a more advanced model or a model designed to work particularly for adverse pressure gradient flows.

No experimental results are shown here to make the Reynolds number trends easier to identify. These results are all shown at $x' = 0.5$ or half way down the adverse pressure gradient ramp. At each Reynolds number, similar results to those shown previously for $Re_{\theta,ref} = 3300$ were observed between the experimental results and those computed using Fluent.

The mean velocity profile is shown in Figure C.9 for the three Reynolds numbers. As seen in the previous section, the amount that the wake grows is underpredicted using Fluent, but the overall trend in the growth of the wake as the flow travels along the adverse pressure gradient ramp is observed. For the range of Reynolds numbers examined, the mean velocity profile change with Reynolds number is similar to the changes observed in the experimental results.

The Reynolds number changes for the stresses were also examined. Again, similar results

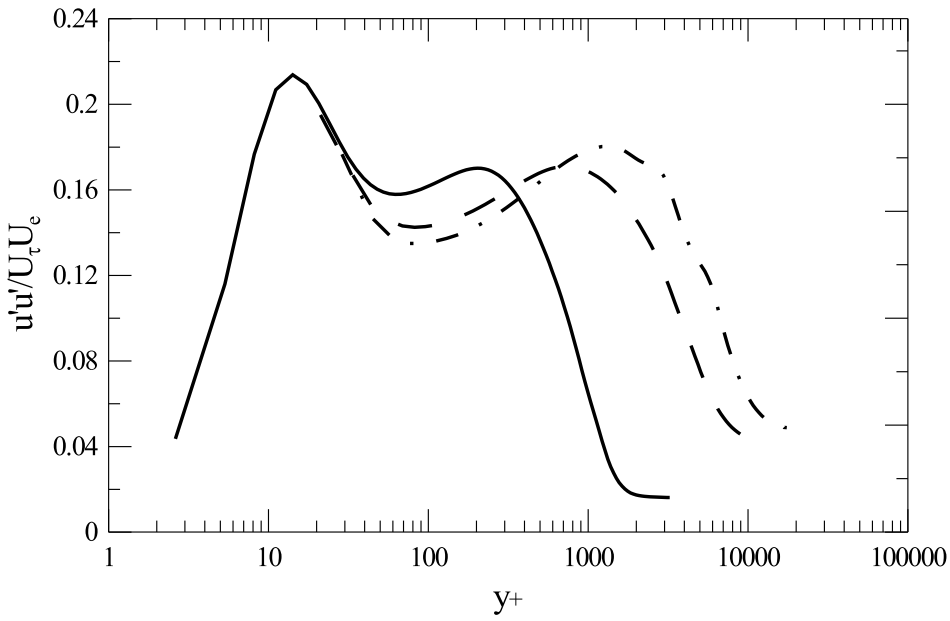

Figure C.10: Streamwise normal stress for inner layer in DeGraaff & Eaton at x' = 0.5 for all three Reynolds numbers from Fluent ($Re_\theta = 3300$ solid line, $Re_\theta = 14,100$ dashed line, $Re_\theta = 20,600$ dash dot line)

were observed when comparing the experimental results with those from Fluent as discussed before. The streamwise normal stress in the DeGraaff and Eaton (2000) scaling is shown in inner coordinates in Figure C.10 and in outer coordinates in Figure C.11. The inner peak has already been shown to not match well with the experimental data and therefore the collapse of the inner layer observed can not be used to validate any scaling. However, the outer layer peak value is observed to increase and shift out in the boundary layer with the scaling used. This is similar to the trends observed in the experimental data except that the values of the scaled stress are lower than those from the experimental data. The outer layer scaling shows that this outer peak for the Fluent data is located farther from the wall than for the experimental data as well. The wall normal stress is shown in the traditional scaling in both inner, Figure C.12, and outer, Figure C.13, coordinates. The inner layer collapse seen in the Fluent data is also observed in the experimental data. The shift in the peak with Reynolds number as observed in the inner coordinates is similar to that observed in the experimental data as well. The outer layer plot of the wall normal stress shows that the peak value remains approximately the same normalized value for the three cases and is located in a similar location for the three cases as well, which is similar to the results

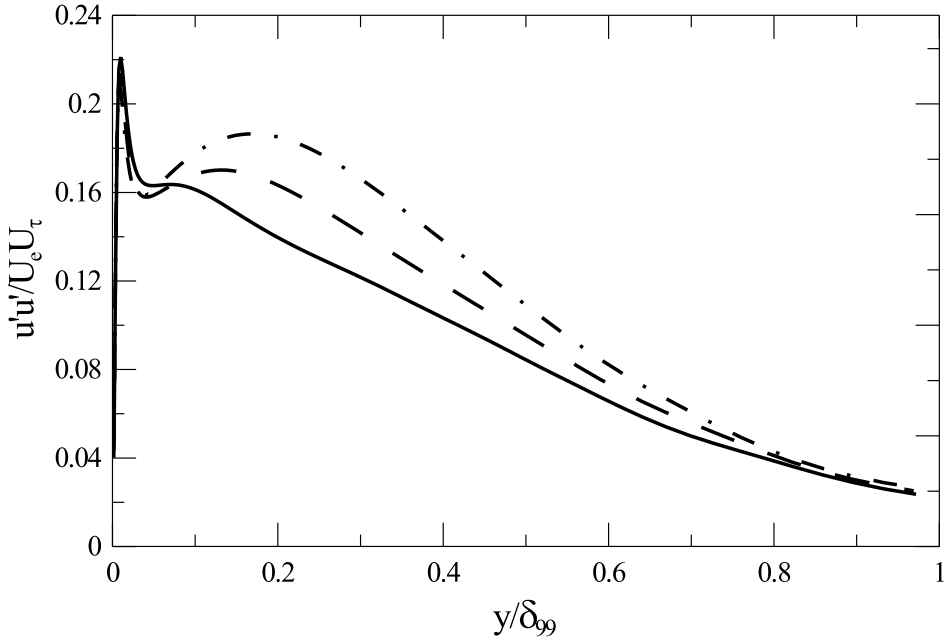

Figure C.11: Streamwise normal stress in DeGraaff & Eaton outer layer scaling for all three Reynolds numbers at x' = 0.5 from Fluent ($Re_\theta = 3300$ solid line, $Re_\theta = 14,100$ dashed line, $Re_\theta = 20,600$ dash dot line)

found experimentally. However, the changing shape of the outer layer of the profile is not observed in the experimental results.

C.4 Reynolds Number Scaling for Outer Layer for Fluent Data

The Reynolds number normal stress scalings determined in Chapter 4 to hold for the adverse pressure gradient ramp data, particularly in the outer layer, were tested with the Fluent data to determine if even with the differences in results between the experiments and Fluent, the resulting profiles still follow the same scaling laws as determined from the experiments.

For the streamwise normal stress, Figure C.14 shows the fixed outer scaling, $u^2_{\tau,ref}$, with the stress plotted in outer layer coordinates. Both experimental and Fluent data are shown for $Re_\theta = 3300$ at three locations along the ramp. The collapse of the Fluent data for the outer layer is very reasonable, although the collapse between the experimental and

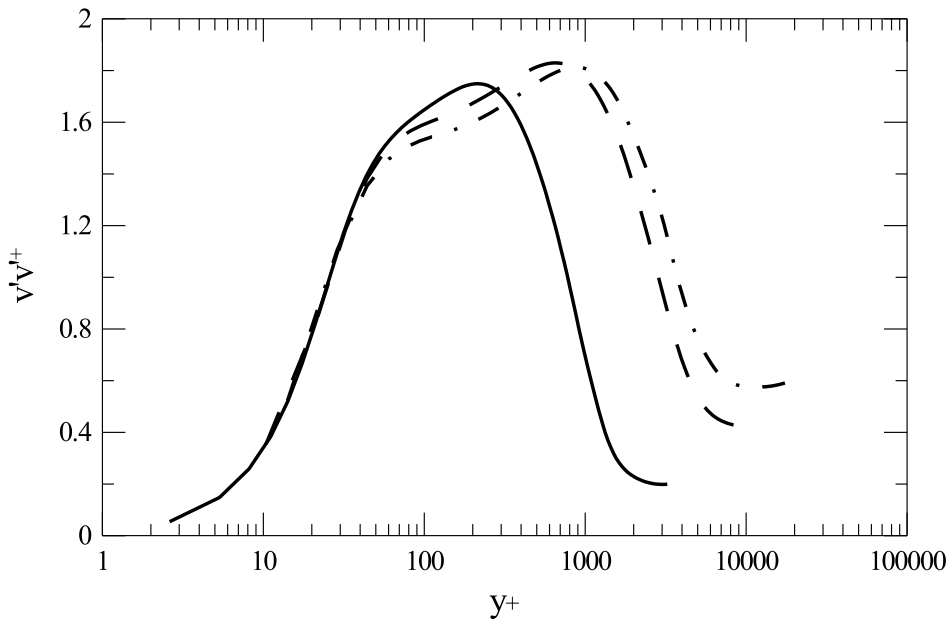

Figure C.12: Wall normal stress at x' = 0.5 for three Reynolds numbers in traditional scaling from Fluent ($Re_\theta = 3300$ solid line, $Re_\theta = 14,100$ dashed line, $Re_\theta = 20,600$ dash dot line)

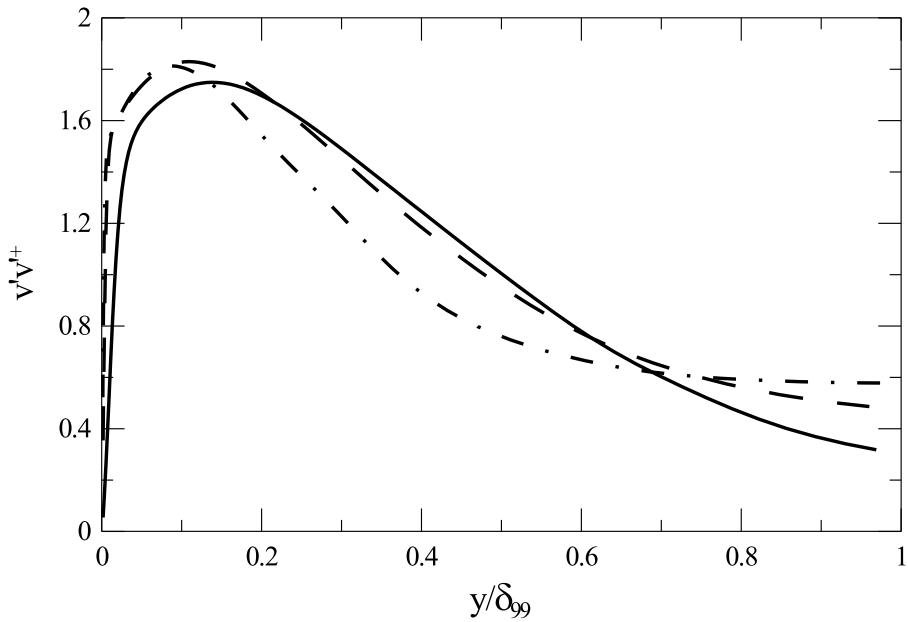

Figure C.13: Wall normal stress in traditional scaling for outer layer at x' = 0.5 for three Reynolds numbers from Fluent ($Re_\theta = 3300$ solid line, $Re_\theta = 14,100$ dashed line, $Re_\theta = 20,600$ dash dot line)

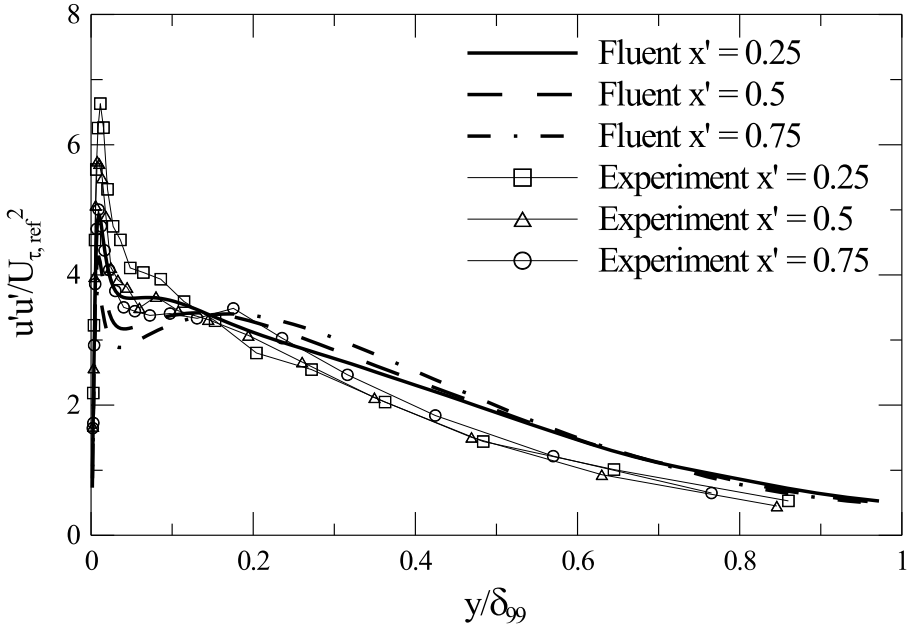

Figure C.14: Streamwise normal stress in a fixed outer layer scaling at $Re_\theta = 3300$ for experiments and Fluent along the ramp

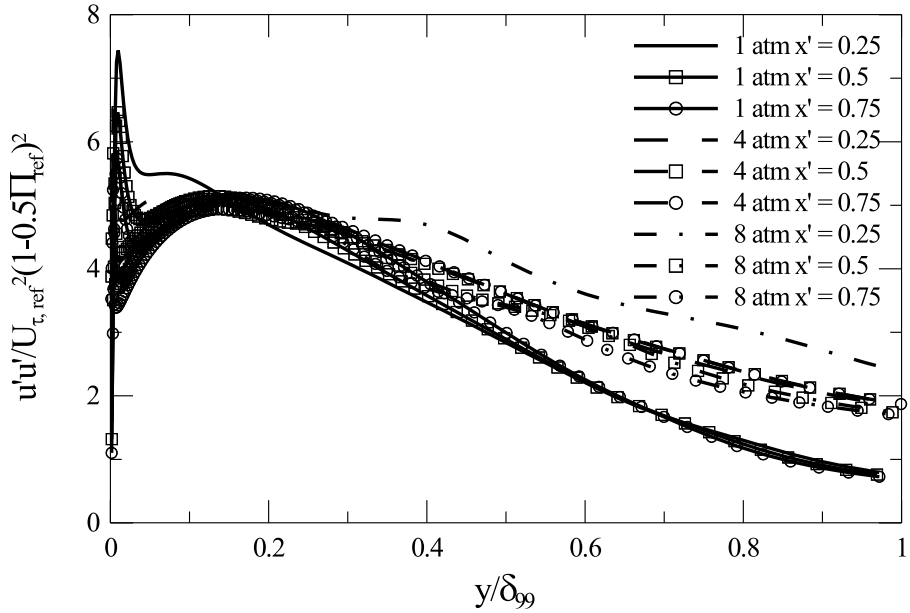

Figure C.15: Streamwise normal stress in new outer layer scaling along ramp for three Reynolds numbers using Fluent

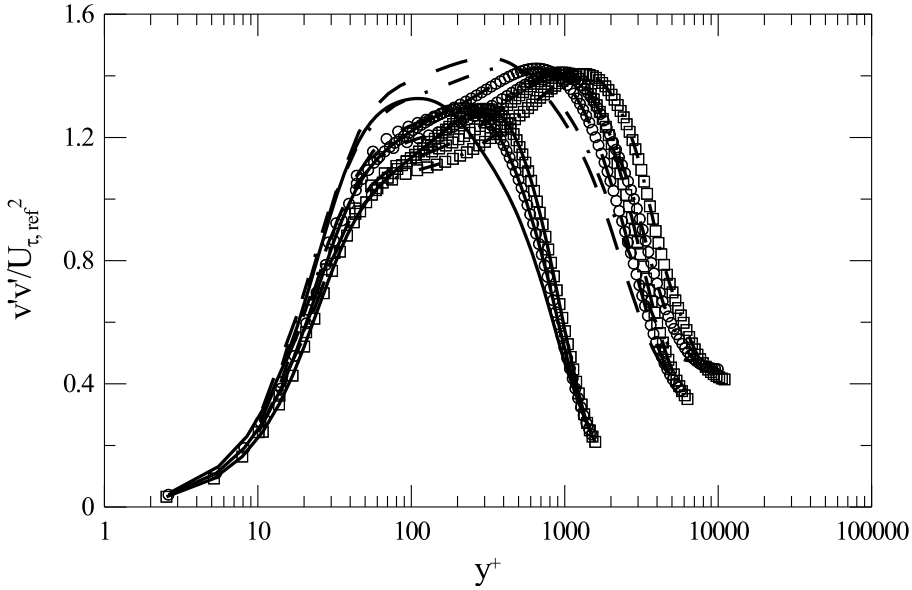

Figure C.16: Wall normal stress for inner layer in new scaling at three locations along the ramp for three Reynolds numbers (profiles as defined in C.15 and C.17)

Fluent data is not perfect, as expected based on the previous discussion. As discussed in Chapter 4, this scaling was used as the starting point to collapse the Reynolds number range for the streamwise normal stress between the flat plate and the adverse pressure gradient ramp. The outer layer scaling determined in Chapter 4 is shown in Figure C.15 for all three Reynolds numbers at three locations along the ramp, no experimental data is shown in this figure. The collapse of the Fluent data in this scaling is not as good as the collapse observed for the experimental data. The data appear to collapse reasonably well for each Reynolds number in this scaling, but profiles for each Reynolds number do not collapse on each other in this scaling for the Fluent data. The profiles also appear to become less well collapsed in this scaling with increasing Reynolds number.

The wall normal stress is shown in Figure C.16 using the scaling $u^2_{\tau,ref}$, which was shown to collapse the wall normal stress over the adverse pressure gradient ramp and Reynolds number range examined in Chapter 4 for the inner layer. The inner layer scaling is shown here since the wall normal stress profiles from Fluent were similar to those measured experimentally. The collapse seen in the inner layer for the Fluent data appears to collapse the wall normal stress at a particular location along the ramp at all Reynolds numbers, as with the streamwise normal stress. The inner layer does not collapse in this scaling for

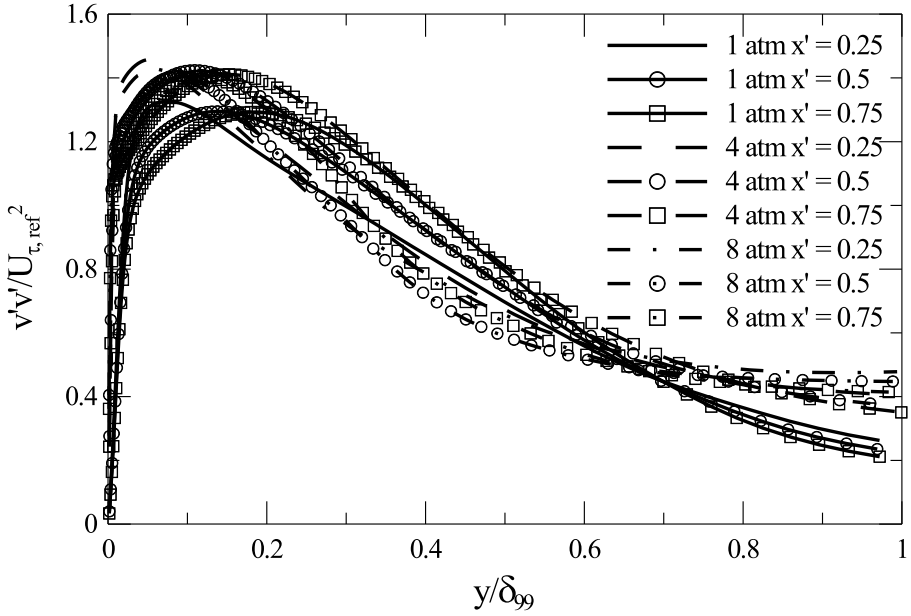

Figure C.17: Wall normal stress for outer layer in new scaling at three locations along ramp for three Reynolds numbers

all locations and Reynolds numbers. The ability of this scaling to collapse the outer layer can be examined in Figure C.17. The collapse of the peak value is not as reasonable as that observed in the experimental data. This is due to the increase in the peak value with Reynolds number observed in the Fluent data and not in the experiments. The overall collapse using this scaling is not as good as for the experimental results and again the collapse appears to be reasonable at a given Reynolds number but not acceptable for collapsing the range of Reynolds number data available onto a particular profile.

Overall, the scalings observed to collapse the experimental data do not appear to collapse the Fluent data the same way. This is not surprising since the Fluent stress profiles do not match the experimental stress profiles. Additionally, while the Fluent stress profiles have similar trends the changes in the locations and values of the stress peaks occur at different rates than in the experiments. Since commercial CFD packages typically are used to predict the mean flow, the collapse of the turbulent stresses observed is quite reasonable. However, it is evident that this code can not be used to test the scaling over a larger Reynolds number range or to test the accuracy of these empirical scalings.

C.5 Conclusions

The use of commercial packages such as Fluent to test the scaling of the turbulent stresses is not currently possible due to the modeling used for the stresses in these packages. Overall Fluent is capable of accurately predicting the wall pressure distribution and showing trends in both the mean velocity and turbulent stress profiles. Again, the model used for the turbulence was that available in Fluent and other models which are more modern or tuned specifically for adverse pressure gradient flows may have produced better results for the various parameters examined. The stress profiles were tested using newly determined scalings, while the scalings worked reasonably well for a particular Reynolds number along the entire length, they were not capable of collapsing the Reynolds number range examined as originally intended. In addition, the inability of Fluent to accurately predict the turbulent stress profiles makes the testing of these scalings suspect and any collapse or lack of collapse is not entirely indicative of an acceptable or unacceptable scaling. Since the goal of this modeling was to test the scalings determined for the adverse pressure gradient ramp and for the flat plate boundary layer, the modeling was not successful. However, the profiles shown demonstrate that the use of Fluent as an experimental tool for testing turbulent stress scalings will require the use of more accurate models, particularly in the near wall region.

Appendix D

LDA Data Archive

The adverse pressure gradient LDA data presented here are corrected for the LDA-biases described in Chapter 2 for all cases, Re_θ = 3300, 14,100 and 20,600. In addition, the data along the ramp are rotated by the 4° angle of the ramp. The data given here are all dimensional.

y(mm)	U(m/s)	V(m/s)	uu (m^2/s^2)	vv (m^2/s^2)	uv (m^2/s^2)
8.000E-02	3.235E+00	-1.183E-01	1.933E+00	2.050E-02	-9.499E-02
1.067E-01	4.250E+00	-1.428E-01	2.650E+00	3.749E-02	-1.587E-01
1.423E-01	5.601E+00	-1.896E-01	4.004E+00	1.037E-01	-3.061E-01
1.897E-01	7.105E+00	-2.670E-01	5.164E+00	1.585E-01	-4.869E-01
2.530E-01	8.343E+00	-3.282E-01	5.613E+00	2.089E-01	-5.966E-01
3.374E-01	9.489E+00	-3.779E-01	5.483E+00	3.279E-01	-6.410E-01
4.499E-01	1.057E+01	-4.201E-01	5.339E+00	4.416E-01	-6.872E-01
5.999E-01	1.147E+01	-4.859E-01	4.313E+00	6.019E-01	-6.698E-01
8.000E-01	1.213E+01	-5.414E-01	3.695E+00	7.394E-01	-6.505E-01
1.067E+00	1.269E+01	-5.646E-01	3.190E+00	8.169E-01	-6.169E-01
1.423E+00	1.325E+01	-6.027E-01	2.941E+00	8.665E-01	-6.281E-01
1.897E+00	1.381E+01	-6.466E-01	2.673E+00	9.167E-01	-6.403E-01
2.530E+00	1.437E+01	-6.584E-01	2.614E+00	8.887E-01	-6.148E-01
3.374E+00	1.500E+01	-7.013E-01	2.477E+00	8.700E-01	-5.706E-01
4.499E+00	1.574E+01	-7.594E-01	2.340E+00	7.859E-01	-5.296E-01
6.000E+00	1.647E+01	-7.681E-01	2.002E+00	7.845E-01	-4.779E-01
8.001E+00	1.729E+01	-8.239E-01	1.615E+00	6.796E-01	-3.641E-01
1.067E+01	1.807E+01	-8.443E-01	1.276E+00	5.369E-01	-2.912E-01
1.423E+01	1.891E+01	-8.769E-01	8.805E-01	4.485E-01	-2.119E-01
1.897E+01	1.960E+01	-9.405E-01	6.220E-01	3.294E-01	-1.477E-01
2.530E+01	2.030E+01	-1.014E+00	3.310E-01	2.335E-01	-8.101E-02
3.374E+01	2.050E+01	-9.750E-01	2.021E-01	1.554E-01	-4.809E-02
4.499E+01	2.049E+01	-9.931E-01	1.941E-01	1.419E-01	-4.702E-02
6.000E+01	2.041E+01	-9.145E-01	1.834E-01	1.371E-01	-4.610E-02

(a) $x' = -0.33$.

y(mm)	U(m/s)	V(m/s)	uu (m^2/s^2)	vv (m^2/s^2)	uv (m^2/s^2)
8.000E-02	4.104E+00	-1.871E-01	1.755E+00	2.002E-02	-1.154E-01
1.200E-01	5.907E+00	-2.830E-01	3.181E+00	5.293E-02	-2.777E-01
1.423E-01	6.736E+00	-2.835E-01	4.077E+00	1.097E-01	-3.565E-01
1.897E-01	8.370E+00	-3.751E-01	5.283E+00	1.524E-01	-5.190E-01
2.530E-01	9.957E+00	-4.556E-01	5.469E+00	2.251E-01	-6.156E-01
3.374E-01	1.112E+01	-5.429E-01	5.259E+00	3.265E-01	-6.683E-01
4.499E-01	1.201E+01	-6.186E-01	4.718E+00	4.283E-01	-6.340E-01
5.999E-01	1.279E+01	-6.849E-01	3.912E+00	5.757E-01	-6.361E-01
8.000E-01	1.354E+01	-7.698E-01	3.291E+00	7.140E-01	-6.503E-01
1.067E+00	1.403E+01	-8.306E-01	2.937E+00	8.079E-01	-6.208E-01
1.423E+00	1.454E+01	-8.586E-01	2.706E+00	8.553E-01	-5.631E-01
1.897E+00	1.501E+01	-9.491E-01	2.588E+00	8.856E-01	-5.914E-01
2.530E+00	1.552E+01	-1.020E+00	2.476E+00	8.732E-01	-6.040E-01
3.374E+00	1.607E+01	-1.105E+00	2.363E+00	8.818E-01	-5.750E-01
4.499E+00	1.664E+01	-1.159E+00	2.089E+00	8.731E-01	-5.399E-01
6.000E+00	1.721E+01	-1.226E+00	1.925E+00	7.548E-01	-4.829E-01
8.001E+00	1.789E+01	-1.311E+00	1.637E+00	6.778E-01	-4.009E-01
1.067E+01	1.863E+01	-1.406E+00	1.271E+00	5.673E-01	-2.959E-01
1.423E+01	1.930E+01	-1.433E+00	8.457E-01	4.571E-01	-2.021E-01
1.897E+01	1.995E+01	-1.470E+00	5.789E-01	3.674E-01	-1.496E-01
2.530E+01	2.053E+01	-1.494E+00	3.058E-01	2.536E-01	-6.796E-02
3.374E+01	2.065E+01	-1.518E+00	1.855E-01	1.825E-01	-4.782E-02
4.499E+01	2.056E+01	-1.507E+00	1.833E-01	1.645E-01	-4.872E-02
6.000E+01	2.036E+01	-1.428E+00	1.737E-01	1.436E-01	-3.919E-02

(b) $x' = 0.00$.

Table D.1 Data for $Re_\theta = 3300$

y(mm)	U(m/s)	V(m/s)	uu (m^2/s^2)	vv (m^2/s^2)	uv (m^2/s^2)
7.981E-02	2.968E+00	-9.056E-02	1.484E+00	2.317E-02	-8.860E-02
1.064E-01	3.671E+00	-1.066E-01	2.191E+00	4.971E-02	-1.368E-01
1.419E-01	4.618E+00	-1.470E-01	3.080E+00	9.935E-02	-1.985E-01
1.893E-01	5.621E+00	-1.758E-01	3.816E+00	1.283E-01	-2.945E-01
2.524E-01	6.712E+00	-2.108E-01	4.248E+00	1.922E-01	-3.976E-01
3.365E-01	7.788E+00	-2.579E-01	4.502E+00	3.067E-01	-5.034E-01
4.488E-01	8.828E+00	-3.180E-01	4.252E+00	4.243E-01	-5.077E-01
5.985E-01	9.556E+00	-3.583E-01	3.609E+00	6.422E-01	-5.479E-01
7.981E-01	1.017E+01	-3.563E-01	3.222E+00	7.938E-01	-5.494E-01
1.064E+00	1.075E+01	-4.095E-01	3.081E+00	8.962E-01	-5.514E-01
1.419E+00	1.130E+01	-4.390E-01	2.788E+00	9.732E-01	-5.130E-01
1.893E+00	1.192E+01	-4.480E-01	2.742E+00	9.854E-01	-5.716E-01
2.524E+00	1.262E+01	-4.930E-01	2.671E+00	9.475E-01	-5.481E-01
3.366E+00	1.337E+01	-5.069E-01	2.437E+00	9.017E-01	-4.920E-01
4.488E+00	1.418E+01	-5.204E-01	2.237E+00	8.078E-01	-3.903E-01
5.985E+00	1.492E+01	-5.270E-01	1.901E+00	7.265E-01	-3.499E-01
7.981E+00	1.579E+01	-5.300E-01	1.729E+00	6.884E-01	-2.773E-01
1.064E+01	1.662E+01	-5.377E-01	1.390E+00	6.097E-01	-2.392E-01
1.419E+01	1.757E+01	-5.345E-01	9.780E-01	4.915E-01	-1.502E-01
1.893E+01	1.844E+01	-4.925E-01	6.857E-01	3.873E-01	-1.025E-01
2.524E+01	1.924E+01	-4.815E-01	3.596E-01	2.748E-01	-5.729E-02
3.366E+01	1.966E+01	-4.277E-01	1.596E-01	1.741E-01	-2.559E-02
4.488E+01	1.973E+01	-3.512E-01	1.385E-01	1.609E-01	-2.970E-02
5.985E+01	1.964E+01	-1.847E-01	1.429E-01	1.500E-01	-2.500E-02

(c) $x' = 0.25$.

y(mm)	U(m/s)	V(m/s)	uu (m^2/s^2)	vv (m^2/s^2)	uv (m^2/s^2)
7.981E-02	3.014E+00	-9.779E-02	1.600E+00	3.053E-02	-1.004E-01
1.071E-01	3.762E+00	-1.399E-01	2.136E+00	4.314E-02	-1.588E-01
1.438E-01	4.582E+00	-1.621E-01	2.878E+00	8.953E-02	-2.131E-01
1.931E-01	5.862E+00	-1.909E-01	3.945E+00	1.447E-01	-3.346E-01
2.592E-01	7.084E+00	-2.288E-01	4.361E+00	2.237E-01	-4.280E-01
3.480E-01	8.040E+00	-2.327E-01	4.171E+00	3.381E-01	-4.787E-01
4.672E-01	8.760E+00	-2.727E-01	3.887E+00	4.781E-01	-5.029E-01
6.272E-01	9.490E+00	-3.127E-01	3.456E+00	5.977E-01	-4.925E-01
8.421E-01	1.003E+01	-3.277E-01	3.083E+00	8.063E-01	-5.102E-01
1.130E+00	1.051E+01	-3.522E-01	2.879E+00	8.410E-01	-5.101E-01
1.518E+00	1.103E+01	-3.876E-01	2.610E+00	9.288E-01	-5.126E-01
2.037E+00	1.165E+01	-3.923E-01	2.605E+00	9.542E-01	-5.085E-01
2.735E+00	1.231E+01	-4.106E-01	2.564E+00	9.580E-01	-4.859E-01
3.672E+00	1.307E+01	-4.252E-01	2.375E+00	9.183E-01	-4.530E-01
4.930E+00	1.386E+01	-4.265E-01	2.250E+00	8.691E-01	-4.206E-01
6.618E+00	1.479E+01	-4.888E-01	1.810E+00	7.316E-01	-2.881E-01
8.885E+00	1.560E+01	-4.701E-01	1.586E+00	6.631E-01	-2.493E-01
1.193E+01	1.652E+01	-4.227E-01	1.342E+00	5.882E-01	-2.233E-01
1.601E+01	1.752E+01	-4.087E-01	9.225E-01	4.567E-01	-1.435E-01
2.150E+01	1.839E+01	-4.420E-01	5.593E-01	3.402E-01	-8.311E-02
2.886E+01	1.916E+01	-4.427E-01	2.572E-01	2.290E-01	-3.276E-02
3.874E+01	1.942E+01	-3.697E-01	1.446E-01	1.485E-01	-2.112E-02
5.201E+01	1.945E+01	-3.197E-01	1.209E-01	1.414E-01	-1.387E-02
6.983E+01	1.943E+01	-1.095E-01	1.080E-01	1.436E-01	-1.843E-02

(d) $x' = 0.33$.

Table D.1 Data for $Re_\theta = 3300$

y(mm)	U(m/s)	V(m/s)	uu (m^2/s^2)	vv (m^2/s^2)	uv (m^2/s^2)
7.981E-02	2.510E+00	-7.761E-02	1.137E+00	1.555E-02	-5.445E-02
1.071E-01	3.373E+00	-8.451E-02	1.745E+00	3.786E-02	-1.137E-01
1.438E-01	4.402E+00	-1.272E-01	2.696E+00	8.630E-02	-1.755E-01
1.931E-01	5.329E+00	-1.473E-01	3.441E+00	1.277E-01	-2.812E-01
2.592E-01	6.374E+00	-1.792E-01	3.903E+00	1.737E-01	-3.455E-01
3.480E-01	7.325E+00	-1.615E-01	3.878E+00	2.749E-01	-3.855E-01
4.672E-01	8.176E+00	-2.108E-01	3.727E+00	4.023E-01	-4.386E-01
6.272E-01	8.821E+00	-2.722E-01	3.331E+00	5.425E-01	-4.397E-01
8.421E-01	9.374E+00	-3.637E-01	2.792E+00	6.764E-01	-4.509E-01
1.130E+00	9.892E+00	-3.734E-01	2.665E+00	7.677E-01	-4.382E-01
1.518E+00	1.034E+01	-3.968E-01	2.586E+00	8.770E-01	-5.030E-01
2.037E+00	1.083E+01	-4.143E-01	2.373E+00	9.221E-01	-4.562E-01
2.735E+00	1.143E+01	-4.159E-01	2.491E+00	1.000E+00	-5.080E-01
3.672E+00	1.206E+01	-4.372E-01	2.342E+00	9.345E-01	-4.686E-01
4.930E+00	1.292E+01	-4.770E-01	2.251E+00	8.733E-01	-4.338E-01
6.618E+00	1.376E+01	-4.688E-01	2.086E+00	8.341E-01	-3.487E-01
8.885E+00	1.474E+01	-4.641E-01	1.808E+00	7.130E-01	-3.271E-01
1.193E+01	1.569E+01	-4.746E-01	1.436E+00	6.228E-01	-2.361E-01
1.601E+01	1.668E+01	-4.528E-01	1.023E+00	5.087E-01	-1.869E-01
2.150E+01	1.769E+01	-4.680E-01	6.331E-01	3.715E-01	-8.803E-02
2.886E+01	1.859E+01	-4.107E-01	3.062E-01	2.492E-01	-4.002E-02
3.874E+01	1.896E+01	-3.812E-01	1.521E-01	1.595E-01	-1.375E-02
5.201E+01	1.908E+01	-2.127E-01	1.318E-01	1.393E-01	-7.862E-03
6.983E+01	1.899E+01	-1.264E-01	1.144E-01	1.296E-01	-9.203E-03

(e) $x' = 0.50$.

y(mm)	U(m/s)	V(m/s)	uu (m^2/s^2)	vv (m^2/s^2)	uv (m^2/s^2)
7.981E-02	2.426E+00	-1.627E-02	9.781E-01	1.752E-02	-2.503E-02
1.071E-01	2.987E+00	-2.953E-02	1.413E+00	2.654E-02	-5.861E-02
1.438E-01	3.779E+00	-8.211E-02	2.171E+00	8.231E-02	-1.250E-01
1.931E-01	4.694E+00	-1.365E-01	2.824E+00	1.120E-01	-2.244E-01
2.592E-01	5.621E+00	-1.685E-01	3.461E+00	1.544E-01	-3.034E-01
3.480E-01	6.557E+00	-2.045E-01	3.652E+00	2.318E-01	-3.851E-01
4.672E-01	7.341E+00	-2.350E-01	3.463E+00	3.424E-01	-4.194E-01
6.272E-01	8.090E+00	-2.864E-01	3.207E+00	4.859E-01	-4.553E-01
8.421E-01	8.617E+00	-3.060E-01	2.784E+00	6.141E-01	-4.198E-01
1.130E+00	9.078E+00	-3.274E-01	2.619E+00	7.250E-01	-3.903E-01
1.518E+00	9.582E+00	-3.477E-01	2.490E+00	8.216E-01	-4.382E-01
2.037E+00	1.007E+01	-3.402E-01	2.329E+00	8.817E-01	-4.315E-01
2.735E+00	1.059E+01	-3.754E-01	2.429E+00	9.388E-01	-4.661E-01
3.672E+00	1.118E+01	-3.552E-01	2.333E+00	9.629E-01	-4.875E-01
4.930E+00	1.187E+01	-4.225E-01	2.250E+00	9.833E-01	-5.059E-01
6.618E+00	1.273E+01	-4.268E-01	2.189E+00	9.106E-01	-4.111E-01
8.885E+00	1.371E+01	-4.184E-01	1.950E+00	8.206E-01	-4.035E-01
1.193E+01	1.476E+01	-4.095E-01	1.565E+00	6.782E-01	-2.802E-01
1.601E+01	1.589E+01	-3.850E-01	1.140E+00	5.490E-01	-2.278E-01
2.150E+01	1.701E+01	-4.056E-01	7.346E-01	4.010E-01	-1.232E-01
2.886E+01	1.802E+01	-4.008E-01	3.960E-01	2.631E-01	-4.956E-02
3.874E+01	1.857E+01	-3.937E-01	1.446E-01	1.550E-01	-2.005E-02
5.201E+01	1.867E+01	-3.979E-01	1.213E-01	1.504E-01	-2.781E-02
6.983E+01	1.860E+01	-1.973E-01	1.282E-01	1.258E-01	-2.350E-02

(f) $x' = 0.67$.

Table D.1 Data for $Re_\theta = 3300$

y(mm)	U(m/s)	V(m/s)	uu (m^2/s^2)	vv (m^2/s^2)	uv (m^2/s^2)
7.981E-02	1.716E+00	-9.385E-02	1.118E+00	1.072E-02	-1.556E-02
1.071E-01	2.571E+00	-7.974E-02	1.172E+00	2.068E-02	-6.624E-02
1.438E-01	3.389E+00	-1.163E-01	1.983E+00	9.121E-02	-1.199E-01
1.931E-01	4.331E+00	-1.511E-01	2.620E+00	1.027E-01	-1.946E-01
2.592E-01	5.363E+00	-1.905E-01	3.195E+00	1.495E-01	-3.043E-01
3.480E-01	6.370E+00	-1.936E-01	3.397E+00	2.177E-01	-3.489E-01
4.672E-01	7.167E+00	-1.992E-01	3.224E+00	3.277E-01	-3.535E-01
6.272E-01	7.827E+00	-2.329E-01	2.971E+00	4.578E-01	-3.652E-01
8.421E-01	8.337E+00	-2.680E-01	2.768E+00	5.549E-01	-3.949E-01
1.130E+00	8.799E+00	-3.258E-01	2.549E+00	6.962E-01	-4.113E-01
1.518E+00	9.195E+00	-3.899E-01	2.378E+00	7.950E-01	-4.316E-01
2.037E+00	9.651E+00	-4.087E-01	2.338E+00	8.462E-01	-4.291E-01
2.735E+00	1.015E+01	-4.303E-01	2.293E+00	8.552E-01	-4.547E-01
3.672E+00	1.075E+01	-4.480E-01	2.313E+00	9.225E-01	-4.973E-01
4.930E+00	1.141E+01	-4.595E-01	2.263E+00	9.562E-01	-4.662E-01
6.618E+00	1.219E+01	-4.451E-01	2.367E+00	9.566E-01	-5.068E-01
8.885E+00	1.310E+01	-4.400E-01	2.057E+00	8.853E-01	-4.497E-01
1.193E+01	1.423E+01	-4.478E-01	1.674E+00	7.376E-01	-3.289E-01
1.601E+01	1.542E+01	-4.406E-01	1.250E+00	5.806E-01	-2.384E-01
2.150E+01	1.664E+01	-4.408E-01	8.255E-01	4.262E-01	-1.611E-01
2.886E+01	1.775E+01	-4.311E-01	4.413E-01	2.748E-01	-6.969E-02
3.874E+01	1.842E+01	-4.735E-01	1.589E-01	1.702E-01	-2.751E-02
5.201E+01	1.856E+01	-3.897E-01	1.296E-01	1.455E-01	-2.341E-02
6.983E+01	1.855E+01	-1.199E-01	1.188E-01	1.279E-01	-6.265E-03

(g) $x' = 0.75$.

y(mm)	U(m/s)	V(m/s)	uu (m^2/s^2)	vv (m^2/s^2)	uv (m^2/s^2)
1.500E-01	3.441E+00	-2.144E-01	1.810E+00	5.411E-02	-1.834E-01
1.959E-01	4.380E+00	-2.687E-01	2.525E+00	1.292E-01	-2.603E-01
2.560E-01	5.167E+00	-2.986E-01	2.744E+00	1.613E-01	-3.183E-01
3.344E-01	5.779E+00	-3.153E-01	2.823E+00	2.170E-01	-3.542E-01
4.368E-01	6.400E+00	-3.169E-01	2.581E+00	3.080E-01	-3.394E-01
5.706E-01	6.853E+00	-3.537E-01	2.544E+00	4.286E-01	-4.014E-01
7.453E-01	7.224E+00	-3.509E-01	2.323E+00	4.824E-01	-3.589E-01
9.736E-01	7.567E+00	-3.667E-01	2.184E+00	6.381E-01	-3.795E-01
1.272E+00	7.803E+00	-3.307E-01	2.125E+00	7.166E-01	-4.071E-01
1.661E+00	8.148E+00	-3.468E-01	2.097E+00	7.649E-01	-4.215E-01
2.170E+00	8.493E+00	-3.238E-01	2.173E+00	8.000E-01	-4.542E-01
2.835E+00	8.880E+00	-3.164E-01	2.233E+00	8.612E-01	-4.939E-01
3.704E+00	9.307E+00	-3.080E-01	2.281E+00	9.208E-01	-5.447E-01
4.838E+00	9.881E+00	-3.151E-01	2.275E+00	9.636E-01	-5.555E-01
6.320E+00	1.046E+01	-3.185E-01	2.300E+00	1.037E+00	-5.840E-01
8.256E+00	1.129E+01	-3.062E-01	2.290E+00	9.901E-01	-5.897E-01
1.078E+01	1.217E+01	-3.402E-01	2.116E+00	9.424E-01	-5.140E-01
1.409E+01	1.334E+01	-3.742E-01	2.001E+00	8.782E-01	-4.803E-01
1.840E+01	1.465E+01	-4.492E-01	1.455E+00	7.033E-01	-3.486E-01
2.404E+01	1.595E+01	-5.044E-01	9.505E-01	5.127E-01	-2.192E-01
3.140E+01	1.718E+01	-5.859E-01	5.331E-01	3.660E-01	-1.377E-01
4.102E+01	1.803E+01	-6.647E-01	1.975E-01	2.717E-01	-6.398E-02
5.359E+01	1.824E+01	-6.889E-01	1.460E-01	2.065E-01	-5.396E-02
7.000E+01	1.823E+01	-4.991E-01	1.546E-01	1.784E-01	-4.499E-02

(h) $x' = 1.00$.

Table D.1 Data for $Re_\theta = 3300$

y(mm)	U(m/s)	V(m/s)	uu (m^2/s^2)	vv (m^2/s^2)	uv (m^2/s^2)
8.000E-02	2.160E+00	-1.501E-03	8.206E-01	9.054E-03	-1.986E-02
1.074E-01	3.069E+00	-9.301E-04	1.369E+00	1.754E-02	-4.912E-02
1.442E-01	4.354E+00	-2.430E-03	2.407E+00	6.311E-02	-1.183E-01
1.936E-01	5.401E+00	-1.794E-03	3.095E+00	8.996E-02	-1.836E-01
2.599E-01	6.438E+00	-1.993E-03	3.262E+00	1.468E-01	-2.218E-01
3.489E-01	7.195E+00	-5.744E-04	3.177E+00	1.995E-01	-2.591E-01
4.683E-01	7.922E+00	-1.844E-02	2.978E+00	2.918E-01	-3.001E-01
6.288E-01	8.358E+00	1.792E-02	2.733E+00	3.519E-01	-2.798E-01
8.441E-01	8.882E+00	-3.474E-03	2.385E+00	4.432E-01	-3.291E-01
1.133E+00	9.222E+00	5.071E-03	2.205E+00	5.306E-01	-3.086E-01
1.521E+00	9.556E+00	-3.423E-03	1.975E+00	5.824E-01	-3.155E-01
2.042E+00	9.937E+00	3.297E-02	1.928E+00	6.674E-01	-3.332E-01
2.742E+00	1.025E+01	5.178E-02	1.819E+00	7.065E-01	-3.231E-01
3.681E+00	1.060E+01	2.823E-02	1.882E+00	7.676E-01	-3.600E-01
4.942E+00	1.096E+01	5.898E-02	1.958E+00	8.807E-01	-4.277E-01
6.634E+00	1.142E+01	8.438E-02	2.106E+00	9.245E-01	-4.851E-01
8.906E+00	1.213E+01	7.119E-02	2.159E+00	1.002E+00	-5.286E-01
1.196E+01	1.304E+01	6.780E-02	2.147E+00	9.523E-01	-5.166E-01
1.605E+01	1.421E+01	7.893E-03	1.835E+00	8.341E-01	-4.401E-01
2.155E+01	1.564E+01	-3.505E-02	1.306E+00	6.455E-01	-3.170E-01
2.893E+01	1.704E+01	-1.581E-01	6.604E-01	4.188E-01	-1.732E-01
3.884E+01	1.805E+01	-2.424E-01	2.294E-01	2.157E-01	-5.295E-02
5.214E+01	1.828E+01	-2.566E-01	1.429E-01	1.511E-01	-3.048E-02
7.000E+01	1.824E+01	-2.621E-01	1.407E-01	1.598E-01	-3.646E-02

(i) $x' = 1.33$.

y(mm)	U(m/s)	V(m/s)	uu (m^2/s^2)	vv (m^2/s^2)	uv (m^2/s^2)
8.000E-02	2.058E+00	-1.447E-02	8.923E-01	9.687E-03	-1.545E-02
1.074E-01	2.950E+00	1.272E-02	1.313E+00	1.282E-02	-1.952E-02
1.442E-01	3.591E+00	2.045E-02	1.933E+00	4.510E-02	-5.896E-02
1.936E-01	4.625E+00	5.385E-03	2.789E+00	5.810E-02	-1.213E-01
2.599E-01	5.564E+00	-8.248E-04	3.299E+00	8.471E-02	-1.868E-01
3.489E-01	6.753E+00	-5.112E-03	3.784E+00	1.410E-01	-2.512E-01
4.683E-01	7.631E+00	-1.585E-02	3.678E+00	1.990E-01	-2.800E-01
6.288E-01	8.496E+00	-3.730E-02	3.240E+00	3.143E-01	-3.163E-01
8.441E-01	9.099E+00	-4.268E-02	2.839E+00	4.295E-01	-3.381E-01
1.133E+00	9.685E+00	3.355E-02	2.598E+00	4.813E-01	-3.265E-01
1.521E+00	1.006E+01	5.781E-02	2.367E+00	5.553E-01	-3.249E-01
2.042E+00	1.050E+01	2.192E-02	2.059E+00	5.868E-01	-3.226E-01
2.742E+00	1.086E+01	2.836E-02	2.115E+00	6.387E-01	-3.625E-01
3.681E+00	1.126E+01	6.525E-02	2.090E+00	6.816E-01	-3.635E-01
4.942E+00	1.172E+01	6.897E-02	1.989E+00	7.347E-01	-3.572E-01
6.634E+00	1.217E+01	1.184E-01	1.970E+00	8.431E-01	-3.863E-01
8.906E+00	1.273E+01	1.181E-01	2.042E+00	8.508E-01	-4.467E-01
1.196E+01	1.342E+01	9.868E-02	2.049E+00	9.210E-01	-4.588E-01
1.605E+01	1.446E+01	7.188E-02	1.955E+00	8.508E-01	-4.166E-01
2.155E+01	1.584E+01	7.720E-02	1.536E+00	7.157E-01	-3.530E-01
2.893E+01	1.731E+01	-1.963E-02	7.827E-01	4.619E-01	-1.785E-01
3.884E+01	1.838E+01	-1.088E-01	2.496E-01	2.583E-01	-4.888E-02
5.214E+01	1.855E+01	-1.990E-01	1.381E-01	1.783E-01	-3.052E-02
7.000E+01	1.840E+01	-1.821E-01	1.397E-01	1.660E-01	-2.542E-02

(j) $x' = 1.67$.

Table D.1: Data for $Re_\theta = 3300$

y(mm)	U(m/s)	V(m/s)	uu (m^2/s^2)	vv (m^2/s^2)	uv (m^2/s^2)
8.000E-02	9.021E+00	-5.662E-02	5.288E+00	3.935E-01	-4.703E-01
1.067E-01	9.518E+00	-8.254E-02	4.316E+00	4.252E-01	-4.941E-01
1.423E-01	9.911E+00	-9.224E-02	4.037E+00	4.877E-01	-4.597E-01
1.897E-01	1.056E+01	-1.244E-01	3.892E+00	6.763E-01	-5.093E-01
2.530E-01	1.111E+01	-1.191E-01	3.421E+00	7.097E-01	-4.849E-01
3.374E-01	1.155E+01	-8.147E-02	3.228E+00	7.517E-01	-4.521E-01
4.499E-01	1.204E+01	-1.020E-01	3.153E+00	7.763E-01	-4.345E-01
5.999E-01	1.254E+01	-1.179E-01	3.137E+00	7.751E-01	-4.519E-01
8.000E-01	1.301E+01	-1.624E-01	3.125E+00	7.648E-01	-4.380E-01
1.067E+00	1.357E+01	-1.372E-01	3.063E+00	7.804E-01	-4.515E-01
1.423E+00	1.409E+01	-1.521E-01	2.939E+00	7.739E-01	-4.054E-01
1.897E+00	1.478E+01	-1.783E-01	2.854E+00	7.787E-01	-3.878E-01
2.530E+00	1.535E+01	-1.440E-01	2.629E+00	7.709E-01	-3.828E-01
3.374E+00	1.595E+01	-1.046E-01	2.549E+00	7.792E-01	-3.626E-01
4.499E+00	1.658E+01	-5.730E-02	2.351E+00	7.364E-01	-2.987E-01
6.000E+00	1.720E+01	-5.078E-02	2.026E+00	6.705E-01	-2.589E-01
8.001E+00	1.791E+01	-8.962E-02	1.729E+00	6.293E-01	-2.042E-01
1.067E+01	1.842E+01	-3.799E-03	1.240E+00	5.724E-01	-1.169E-01
1.423E+01	1.908E+01	-4.961E-02	9.729E-01	4.712E-01	-6.046E-02
1.897E+01	1.953E+01	-7.781E-02	8.074E-01	4.142E-01	-2.205E-02
2.530E+01	2.017E+01	-4.477E-02	5.681E-01	3.247E-01	3.261E-02
3.374E+01	2.042E+01	-6.740E-02	4.526E-01	2.423E-01	7.146E-02
4.499E+01	2.040E+01	-2.177E-02	3.939E-01	2.417E-01	6.207E-02
6.000E+01	2.035E+01	-6.814E-03	4.093E-01	2.368E-01	6.487E-02

(a) $x' = -0.33$.

y(mm)	U(m/s)	V(m/s)	uu (m^2/s^2)	vv (m^2/s^2)	uv (m^2/s^2)
8.000E-02	9.914E+00	-4.664E-01	5.946E+00	5.481E-01	-7.849E-01
1.067E-01	1.061E+01	-6.749E-01	5.458E+00	4.295E-01	-7.674E-01
1.423E-01	1.137E+01	-7.369E-01	4.305E+00	4.773E-01	-6.505E-01
1.897E-01	1.216E+01	-7.936E-01	3.952E+00	6.172E-01	-5.035E-01
2.530E-01	1.271E+01	-7.922E-01	3.492E+00	7.116E-01	-5.224E-01
3.374E-01	1.316E+01	-7.858E-01	3.221E+00	7.582E-01	-4.890E-01
4.499E-01	1.366E+01	-7.803E-01	3.036E+00	7.440E-01	-4.129E-01
5.999E-01	1.414E+01	-7.461E-01	3.165E+00	7.762E-01	-4.825E-01
8.000E-01	1.458E+01	-7.635E-01	2.893E+00	7.872E-01	-4.429E-01
1.067E+00	1.499E+01	-7.844E-01	2.866E+00	8.210E-01	-4.592E-01
1.423E+00	1.543E+01	-8.292E-01	2.891E+00	7.812E-01	-4.303E-01
1.897E+00	1.593E+01	-7.824E-01	2.810E+00	8.126E-01	-3.838E-01
2.530E+00	1.646E+01	-7.601E-01	2.796E+00	7.849E-01	-3.560E-01
3.374E+00	1.688E+01	-6.863E-01	2.645E+00	8.622E-01	-3.238E-01
4.499E+00	1.744E+01	-7.017E-01	2.583E+00	8.020E-01	-2.649E-01
6.000E+00	1.779E+01	-6.579E-01	2.129E+00	7.970E-01	-2.110E-01
8.001E+00	1.840E+01	-6.899E-01	2.018E+00	7.212E-01	-1.671E-01
1.067E+01	1.881E+01	-6.763E-01	1.725E+00	6.830E-01	-5.814E-02
1.423E+01	1.932E+01	-6.559E-01	1.360E+00	6.129E-01	2.667E-02
1.897E+01	1.992E+01	-5.682E-01	1.118E+00	5.250E-01	4.353E-02
2.530E+01	2.029E+01	-5.371E-01	1.059E+00	5.110E-01	1.474E-01
3.374E+01	2.038E+01	-4.598E-01	5.954E-01	4.841E-01	1.355E-01
4.499E+01	2.030E+01	-4.518E-01	5.259E-01	4.586E-01	1.169E-01
6.000E+01	2.024E+01	-4.038E-01	5.340E-01	4.292E-01	1.181E-01

(b) $x' = 0.00$.

Table D.2 Data for $Re_\theta = 14,100$

y(mm)	U(m/s)	V(m/s)	uu (m^2/s^2)	vv (m^2/s^2)	uv (m^2/s^2)
7.981E-02	7.787E+00	-3.183E-02	4.315E+00	4.625E-01	-3.620E-01
1.064E-01	8.197E+00	-5.942E-02	3.780E+00	4.384E-01	-3.742E-01
1.419E-01	8.587E+00	-9.455E-02	3.343E+00	4.514E-01	-3.235E-01
1.893E-01	9.078E+00	-8.820E-02	3.222E+00	5.440E-01	-2.736E-01
2.524E-01	9.418E+00	-8.483E-02	2.990E+00	6.340E-01	-2.838E-01
3.365E-01	9.850E+00	-1.106E-01	2.879E+00	6.578E-01	-2.520E-01
4.488E-01	1.024E+01	-8.058E-02	2.871E+00	7.482E-01	-2.859E-01
5.985E-01	1.066E+01	-1.186E-01	2.909E+00	8.132E-01	-3.218E-01
7.981E-01	1.108E+01	-1.023E-01	2.839E+00	7.333E-01	-2.912E-01
1.064E+00	1.163E+01	-9.202E-02	2.999E+00	8.482E-01	-2.882E-01
1.419E+00	1.219E+01	-9.465E-02	2.959E+00	8.497E-01	-3.338E-01
1.893E+00	1.286E+01	-6.124E-02	3.114E+00	8.467E-01	-3.359E-01
2.524E+00	1.357E+01	-6.950E-02	2.971E+00	7.966E-01	-2.770E-01
3.366E+00	1.424E+01	4.037E-03	2.614E+00	8.246E-01	-2.527E-01
4.488E+00	1.499E+01	-1.261E-03	2.297E+00	7.577E-01	-1.485E-01
5.985E+00	1.570E+01	2.105E-02	2.104E+00	6.973E-01	-1.349E-01
7.981E+00	1.634E+01	2.939E-02	1.774E+00	6.796E-01	-9.283E-02
1.064E+01	1.711E+01	9.932E-02	1.465E+00	6.352E-01	-3.497E-02
1.419E+01	1.778E+01	1.838E-01	1.289E+00	5.866E-01	3.476E-02
1.893E+01	1.853E+01	2.270E-01	9.912E-01	5.259E-01	8.107E-02
2.524E+01	1.915E+01	2.774E-01	7.229E-01	4.334E-01	1.071E-01
3.366E+01	1.955E+01	3.565E-01	5.191E-01	3.679E-01	1.155E-01
4.488E+01	1.965E+01	4.662E-01	4.506E-01	3.342E-01	1.300E-01
5.985E+01	1.967E+01	6.144E-01	5.919E-01	3.328E-01	1.402E-01

(c) $x' = 0.25$.

y(mm)	U(m/s)	V(m/s)	uu (m^2/s^2)	vv (m^2/s^2)	uv (m^2/s^2)
7.981E-02	7.971E+00	2.176E-01	4.812E+00	7.979E-01	-1.642E-02
1.071E-01	8.176E+00	-2.277E-02	3.442E+00	4.530E-01	-3.531E-01
1.438E-01	8.325E+00	-7.198E-02	3.306E+00	4.370E-01	-3.012E-01
1.931E-01	8.853E+00	-1.315E-01	3.121E+00	5.297E-01	-2.726E-01
2.592E-01	9.364E+00	-1.113E-01	2.899E+00	5.943E-01	-2.848E-01
3.480E-01	9.688E+00	-9.926E-02	2.683E+00	6.809E-01	-2.672E-01
4.672E-01	1.005E+01	-7.959E-02	2.852E+00	7.281E-01	-2.681E-01
6.272E-01	1.053E+01	-1.105E-01	2.770E+00	7.617E-01	-2.519E-01
8.421E-01	1.093E+01	-1.295E-01	2.864E+00	7.811E-01	-2.947E-01
1.130E+00	1.143E+01	-1.085E-01	2.910E+00	7.932E-01	-3.130E-01
1.518E+00	1.192E+01	-1.095E-01	2.953E+00	8.231E-01	-2.932E-01
2.037E+00	1.259E+01	-1.232E-01	2.898E+00	8.454E-01	-3.212E-01
2.735E+00	1.332E+01	-1.315E-01	2.814E+00	8.083E-01	-2.940E-01
3.672E+00	1.394E+01	-7.375E-02	2.614E+00	7.775E-01	-2.442E-01
4.930E+00	1.478E+01	-8.482E-02	2.389E+00	7.309E-01	-2.030E-01
6.618E+00	1.553E+01	-8.046E-02	2.002E+00	6.951E-01	-1.519E-01
8.885E+00	1.621E+01	-4.285E-02	1.812E+00	6.276E-01	-7.287E-02
1.193E+01	1.702E+01	-1.633E-02	1.519E+00	5.532E-01	-2.696E-02
1.601E+01	1.781E+01	5.404E-02	1.137E+00	4.915E-01	2.748E-02
2.150E+01	1.851E+01	9.960E-02	9.585E-01	4.418E-01	7.694E-02
2.886E+01	1.910E+01	1.676E-01	6.936E-01	3.335E-01	9.476E-02
3.874E+01	1.936E+01	2.714E-01	5.313E-01	2.875E-01	1.275E-01
5.201E+01	1.942E+01	3.657E-01	5.270E-01	2.878E-01	1.168E-01
6.983E+01	1.949E+01	5.965E-01	6.545E-01	3.195E-01	1.355E-01

(d) $x' = 0.33$.

Table D.2 Data for $Re_\theta = 14,100$

y(mm)	U(m/s)	V(m/s)	uu (m^2/s^2)	vv (m^2/s^2)	uv (m^2/s^2)
7.981E-02	8.021E+00	-1.438E-01	2.786E+00	3.039E-01	-8.381E-02
1.071E-01	8.134E+00	-1.731E-01	2.950E+00	3.276E-01	-1.592E-01
1.438E-01	8.153E+00	-1.394E-01	2.952E+00	3.635E-01	-2.238E-01
2.592E-01	8.714E+00	-1.075E-01	3.024E+00	5.016E-01	-1.596E-01
3.480E-01	9.064E+00	-9.535E-02	2.695E+00	6.293E-01	-2.665E-01
4.672E-01	9.479E+00	-1.110E-01	2.627E+00	6.389E-01	-2.518E-01
6.272E-01	9.885E+00	-9.138E-02	2.613E+00	6.633E-01	-2.454E-01
8.421E-01	1.032E+01	-1.097E-01	2.757E+00	7.452E-01	-3.135E-01
1.130E+00	1.079E+01	-9.181E-02	2.863E+00	7.711E-01	-2.699E-01
1.518E+00	1.130E+01	-1.091E-01	2.783E+00	7.823E-01	-2.537E-01
2.037E+00	1.182E+01	-1.150E-01	2.874E+00	8.191E-01	-2.793E-01
2.735E+00	1.243E+01	-1.259E-01	2.817E+00	8.239E-01	-2.812E-01
3.672E+00	1.317E+01	-1.273E-01	2.836E+00	8.407E-01	-2.903E-01
4.930E+00	1.385E+01	-9.044E-02	2.554E+00	7.952E-01	-2.101E-01
6.618E+00	1.471E+01	-7.769E-02	2.291E+00	7.424E-01	-1.505E-01
8.885E+00	1.547E+01	-1.934E-02	1.931E+00	6.864E-01	-8.984E-02
1.193E+01	1.631E+01	8.032E-03	1.549E+00	6.453E-01	-4.858E-02
1.601E+01	1.715E+01	6.754E-02	1.265E+00	5.719E-01	1.439E-02
2.150E+01	1.794E+01	8.657E-02	9.320E-01	4.890E-01	8.000E-02
2.886E+01	1.858E+01	1.592E-01	6.902E-01	4.467E-01	1.077E-01
3.874E+01	1.890E+01	2.298E-01	5.303E-01	3.526E-01	1.238E-01
5.201E+01	1.894E+01	3.174E-01	5.036E-01	3.538E-01	1.352E-01
6.983E+01	1.904E+01	4.800E-01	4.542E-01	3.646E-01	1.217E-01

(e) $x' = 0.50$.

y(mm)	U(m/s)	V(m/s)	uu (m^2/s^2)	vv (m^2/s^2)	uv (m^2/s^2)
7.981E-02	7.529E+00	3.911E-01	5.770E+00	1.020E+00	4.835E-01
1.071E-01	7.717E+00	1.523E-02	3.039E+00	4.821E-01	-2.678E-01
1.438E-01	7.808E+00	-6.917E-02	3.010E+00	4.541E-01	-2.677E-01
1.931E-01	8.069E+00	-5.464E-02	2.845E+00	5.731E-01	-2.443E-01
2.592E-01	8.592E+00	-8.620E-02	2.512E+00	5.370E-01	-2.229E-01
3.480E-01	8.864E+00	-7.038E-02	2.466E+00	6.117E-01	-2.383E-01
4.672E-01	9.273E+00	-5.547E-02	2.463E+00	6.209E-01	-2.238E-01
6.272E-01	9.592E+00	-7.560E-02	2.571E+00	6.472E-01	-2.259E-01
8.421E-01	9.965E+00	-7.186E-02	2.562E+00	6.824E-01	-2.371E-01
1.130E+00	1.039E+01	-5.841E-02	2.514E+00	7.436E-01	-2.226E-01
1.518E+00	1.080E+01	-7.604E-02	2.820E+00	7.546E-01	-2.647E-01
2.037E+00	1.130E+01	-8.780E-02	2.603E+00	7.935E-01	-2.663E-01
2.735E+00	1.184E+01	-3.515E-02	2.695E+00	8.548E-01	-3.167E-01
3.672E+00	1.245E+01	-5.839E-02	2.653E+00	8.463E-01	-2.734E-01
4.930E+00	1.317E+01	-5.450E-02	2.603E+00	8.686E-01	-2.565E-01
6.618E+00	1.402E+01	-9.112E-02	2.377E+00	8.481E-01	-1.932E-01
8.885E+00	1.486E+01	-3.162E-02	2.056E+00	7.571E-01	-1.462E-01
1.193E+01	1.573E+01	-2.814E-02	1.649E+00	6.312E-01	-6.224E-02
1.601E+01	1.660E+01	1.316E-02	1.263E+00	5.645E-01	-1.140E-02
2.150E+01	1.740E+01	8.713E-02	8.893E-01	4.956E-01	4.532E-02
2.886E+01	1.813E+01	1.731E-01	6.450E-01	4.339E-01	8.992E-02
3.874E+01	1.856E+01	2.916E-01	4.078E-01	3.881E-01	1.011E-01
5.201E+01	1.865E+01	4.005E-01	3.572E-01	3.436E-01	1.107E-01
6.983E+01	1.867E+01	4.815E-01	3.801E-01	3.503E-01	1.124E-01

(f) $x' = 0.67$.

Table D.2 Data for $Re_\theta = 14,100$

y(mm)	U(m/s)	V(m/s)	uu (m^2/s^2)	vv (m^2/s^2)	uv (m^2/s^2)
1.071E-01	7.788E+00	-2.186E-01	4.925E-01	2.703E-01	-7.748E-02
1.931E-01	8.003E+00	-1.772E-01	2.949E+00	4.791E-01	-1.200E-01
2.592E-01	8.279E+00	-1.658E-01	2.609E+00	5.183E-01	-2.623E-01
3.480E-01	8.607E+00	-1.448E-01	2.526E+00	5.475E-01	-2.215E-01
4.672E-01	8.938E+00	-1.494E-01	2.503E+00	5.801E-01	-2.137E-01
6.272E-01	9.266E+00	-1.355E-01	2.476E+00	6.246E-01	-2.311E-01
8.421E-01	9.647E+00	-1.624E-01	2.598E+00	6.500E-01	-2.281E-01
1.130E+00	1.004E+01	-1.530E-01	2.596E+00	6.924E-01	-2.707E-01
1.518E+00	1.056E+01	-1.664E-01	2.667E+00	7.256E-01	-2.515E-01
2.037E+00	1.101E+01	-1.647E-01	2.702E+00	7.968E-01	-2.986E-01
2.735E+00	1.152E+01	-1.396E-01	2.674E+00	8.313E-01	-3.034E-01
3.672E+00	1.212E+01	-1.474E-01	2.625E+00	8.468E-01	-2.471E-01
4.930E+00	1.277E+01	-1.174E-01	2.602E+00	8.224E-01	-2.914E-01
6.618E+00	1.359E+01	-1.103E-01	2.453E+00	8.219E-01	-2.545E-01
8.885E+00	1.446E+01	-6.260E-02	2.118E+00	7.412E-01	-1.797E-01
1.193E+01	1.539E+01	-5.790E-02	1.685E+00	6.434E-01	-8.948E-02
1.601E+01	1.629E+01	1.492E-02	1.458E+00	5.372E-01	-2.933E-02
2.150E+01	1.724E+01	-3.186E-02	1.210E+00	4.509E-01	6.631E-02
2.886E+01	1.802E+01	7.323E-02	1.022E+00	3.380E-01	1.087E-01
3.874E+01	1.841E+01	1.779E-01	7.947E-01	3.020E-01	1.224E-01
5.201E+01	1.843E+01	2.691E-01	6.469E-01	2.567E-01	8.907E-02
6.983E+01	1.855E+01	3.613E-01	6.835E-01	2.967E-01	1.308E-01

(g) $x' = 0.75$.

y(mm)	U(m/s)	V(m/s)	uu (m^2/s^2)	vv (m^2/s^2)	uv (m^2/s^2)
4.368E-01	9.355E+00	-5.962E-01	3.530E+00	6.328E-01	-4.543E-01
5.706E-01	9.745E+00	-6.384E-01	2.365E+00	5.878E-01	-3.141E-01
7.453E-01	1.009E+01	-6.445E-01	2.401E+00	6.555E-01	-3.421E-01
9.736E-01	1.032E+01	-6.545E-01	2.290E+00	6.899E-01	-3.315E-01
1.272E+00	1.059E+01	-6.820E-01	2.414E+00	7.714E-01	-3.761E-01
1.661E+00	1.083E+01	-6.711E-01	2.530E+00	8.021E-01	-4.139E-01
2.170E+00	1.116E+01	-6.841E-01	2.750E+00	8.460E-01	-4.641E-01
2.835E+00	1.145E+01	-7.033E-01	2.650E+00	8.895E-01	-4.595E-01
3.704E+00	1.190E+01	-7.083E-01	2.762E+00	9.175E-01	-4.969E-01
4.838E+00	1.233E+01	-7.004E-01	2.578E+00	9.467E-01	-4.965E-01
6.320E+00	1.294E+01	-6.896E-01	2.683E+00	9.707E-01	-5.194E-01
8.256E+00	1.360E+01	-6.775E-01	2.396E+00	8.963E-01	-4.271E-01
1.078E+01	1.440E+01	-6.729E-01	2.050E+00	8.107E-01	-3.463E-01
1.409E+01	1.526E+01	-6.374E-01	1.628E+00	7.200E-01	-2.569E-01
1.840E+01	1.617E+01	-6.311E-01	1.153E+00	5.984E-01	-1.267E-01
2.404E+01	1.694E+01	-6.637E-01	8.329E-01	4.832E-01	-4.747E-02
3.140E+01	1.764E+01	-6.721E-01	5.890E-01	4.175E-01	4.121E-02
4.102E+01	1.806E+01	-6.520E-01	3.485E-01	3.481E-01	5.050E-02
5.359E+01	1.819E+01	-5.925E-01	2.980E-01	3.349E-01	6.122E-02
7.000E+01	1.825E+01	-5.396E-01	3.085E-01	3.227E-01	5.812E-02

(h) $x' = 1.00$.

Table D.2 Data for $Re_\theta = 14,100$

y(mm)	U(m/s)	V(m/s)	uu (m^2/s^2)	vv (m^2/s^2)	uv (m^2/s^2)
1.442E-01	7.613E+00	-1.704E-01	3.427E+00	2.544E-01	-3.071E-01
1.936E-01	8.161E+00	-1.957E-01	3.052E+00	3.624E-01	-3.042E-01
2.599E-01	8.587E+00	-1.967E-01	2.763E+00	4.180E-01	-3.023E-01
3.489E-01	8.915E+00	-2.196E-01	2.534E+00	4.483E-01	-3.031E-01
4.683E-01	9.405E+00	-2.407E-01	2.402E+00	4.755E-01	-2.879E-01
6.288E-01	9.784E+00	-2.366E-01	2.408E+00	4.914E-01	-3.170E-01
8.441E-01	1.016E+01	-2.070E-01	2.336E+00	5.221E-01	-3.133E-01
1.133E+00	1.054E+01	-2.191E-01	2.275E+00	5.949E-01	-3.241E-01
1.521E+00	1.088E+01	-2.425E-01	2.257E+00	6.113E-01	-3.225E-01
2.042E+00	1.127E+01	-2.576E-01	2.224E+00	6.911E-01	-3.406E-01
2.742E+00	1.160E+01	-2.722E-01	2.276E+00	7.371E-01	-3.793E-01
3.681E+00	1.201E+01	-2.763E-01	2.252E+00	8.254E-01	-4.099E-01
4.942E+00	1.244E+01	-2.805E-01	2.346E+00	8.616E-01	-4.314E-01
6.634E+00	1.284E+01	-2.369E-01	2.294E+00	8.784E-01	-4.609E-01
8.906E+00	1.358E+01	-2.580E-01	2.309E+00	9.404E-01	-5.094E-01
1.196E+01	1.450E+01	-3.237E-01	2.055E+00	7.726E-01	-3.918E-01
1.605E+01	1.555E+01	-3.386E-01	1.501E+00	6.727E-01	-2.652E-01
2.155E+01	1.652E+01	-3.134E-01	1.055E+00	4.948E-01	-1.399E-01
2.893E+01	1.735E+01	-3.584E-01	6.383E-01	3.511E-01	-3.217E-02
3.884E+01	1.793E+01	-4.073E-01	4.778E-01	2.685E-01	4.375E-02
5.214E+01	1.803E+01	-4.113E-01	3.946E-01	2.104E-01	4.857E-02
7.000E+01	1.808E+01	-3.399E-01	3.387E-01	2.335E-01	6.305E-02

(i) $x' = 1.33$.

y(mm)	U(m/s)	V(m/s)	uu (m^2/s^2)	vv (m^2/s^2)	uv (m^2/s^2)
8.000E-02	6.537E+00	-1.365E-01	3.726E+00	1.459E-01	-2.610E-01
1.074E-01	7.197E+00	-1.417E-01	3.386E+00	2.012E-01	-2.882E-01
1.442E-01	7.806E+00	-1.538E-01	3.057E+00	2.639E-01	-2.944E-01
1.936E-01	8.411E+00	-1.477E-01	2.796E+00	4.167E-01	-2.954E-01
2.599E-01	8.830E+00	-1.619E-01	2.576E+00	4.705E-01	-2.836E-01
3.489E-01	9.165E+00	-1.410E-01	2.451E+00	5.230E-01	-2.678E-01
4.683E-01	9.572E+00	-1.511E-01	2.313E+00	5.556E-01	-2.690E-01
6.288E-01	9.991E+00	-1.559E-01	2.247E+00	5.383E-01	-2.634E-01
8.441E-01	1.045E+01	-1.986E-01	2.262E+00	5.469E-01	-2.788E-01
1.133E+00	1.080E+01	-2.038E-01	2.306E+00	5.830E-01	-3.054E-01
1.521E+00	1.120E+01	-1.880E-01	2.282E+00	6.052E-01	-2.970E-01
2.042E+00	1.166E+01	-2.254E-01	2.246E+00	6.154E-01	-3.056E-01
2.742E+00	1.204E+01	-2.479E-01	2.160E+00	6.526E-01	-2.941E-01
3.681E+00	1.242E+01	-2.497E-01	2.202E+00	7.345E-01	-3.437E-01
4.942E+00	1.277E+01	-2.440E-01	2.085E+00	7.748E-01	-3.567E-01
6.634E+00	1.323E+01	-2.332E-01	1.964E+00	8.549E-01	-3.958E-01
8.906E+00	1.375E+01	-2.241E-01	2.032E+00	8.368E-01	-3.962E-01
1.196E+01	1.450E+01	-2.591E-01	1.973E+00	8.294E-01	-3.688E-01
1.605E+01	1.545E+01	-2.485E-01	1.665E+00	7.372E-01	-2.982E-01
2.155E+01	1.652E+01	-2.462E-01	1.089E+00	5.394E-01	-1.127E-01
2.893E+01	1.743E+01	-2.393E-01	6.433E-01	3.557E-01	-2.297E-02
3.884E+01	1.801E+01	-2.360E-01	3.825E-01	2.495E-01	3.237E-02
5.214E+01	1.809E+01	-2.409E-01	2.443E-01	2.417E-01	3.687E-02
7.000E+01	1.805E+01	-2.828E-01	2.341E-01	2.659E-01	4.458E-02

(j) $x' = 1.67$.

Table D.2: Data for $Re_\theta = 14,100$

y(mm)	U(m/s)	V(m/s)	uu (m^2/s^2)	vv (m^2/s^2)	uv (m^2/s^2)
1.669E-01	8.819E+00	-1.606E-01	3.048E+00	4.287E-01	-2.734E-01
3.483E-01	9.702E+00	-4.441E-01	2.146E+00	4.935E-01	-2.899E-01
7.268E-01	1.070E+01	-4.334E-01	2.124E+00	5.033E-01	-2.946E-01
1.517E+00	1.162E+01	-5.657E-01	2.075E+00	5.335E-01	-2.596E-01
3.165E+00	1.279E+01	-6.041E-01	1.710E+00	5.196E-01	-2.516E-01
6.604E+00	1.415E+01	-5.943E-01	1.230E+00	4.493E-01	-1.262E-01
1.378E+01	1.537E+01	-6.141E-01	7.099E-01	3.219E-01	-2.996E-02
2.875E+01	1.641E+01	-5.578E-01	2.890E-01	2.317E-01	8.312E-02
6.000E+01	1.645E+01	-6.849E-01	3.541E-01	1.869E-01	8.998E-02

(a) x′ = -0.33.

y(mm)	U(m/s)	V(m/s)	uu (m^2/s^2)	vv (m^2/s^2)	uv (m^2/s^2)
9.976E-02	7.246E+00	-4.716E-01	2.588E+00	7.944E-01	3.969E-01
2.066E-01	7.612E+00	-4.753E-01	2.101E+00	4.344E-01	-1.729E-01
4.277E-01	8.379E+00	-5.415E-01	1.948E+00	5.137E-01	-2.039E-01
8.857E-01	9.171E+00	-5.566E-01	2.013E+00	5.271E-01	-1.935E-01
1.834E+00	1.027E+01	-7.047E-01	1.927E+00	5.556E-01	-2.234E-01
3.798E+00	1.164E+01	-7.380E-01	1.725E+00	4.864E-01	-1.289E-01
7.865E+00	1.300E+01	-8.883E-01	1.082E+00	4.638E-01	-4.085E-02
1.629E+01	1.444E+01	-8.096E-01	6.030E-01	3.626E-01	5.940E-02
3.372E+01	1.545E+01	-7.765E-01	2.641E-01	2.505E-01	1.045E-01
6.983E+01	1.547E+01	-6.662E-01	2.966E-01	2.477E-01	1.343E-01

(b) x′ = 0.25.

Table D.3 Data for $Re_\theta = 20,600$

y(mm)	U(m/s)	V(m/s)	uu (m^2/s^2)	vv (m^2/s^2)	uv (m^2/s^2)
1.694E-01	6.823E+00	-4.159E-01	2.211E+00	3.005E-01	-4.092E-02
3.596E-01	7.754E+00	-3.242E-01	1.806E+00	3.894E-01	-1.916E-01
7.633E-01	8.543E+00	-3.612E-01	1.923E+00	4.295E-01	-1.386E-01
1.620E+00	9.502E+00	-4.107E-01	1.927E+00	5.739E-01	-1.268E-01
3.439E+00	1.074E+01	-5.026E-01	1.795E+00	4.839E-01	-1.369E-01
7.301E+00	1.226E+01	-5.833E-01	1.445E+00	5.418E-01	-4.427E-03
1.550E+01	1.377E+01	-6.486E-01	8.725E-01	4.682E-01	6.656E-02
3.290E+01	1.514E+01	-7.454E-01	3.160E-01	2.646E-01	1.082E-01
6.983E+01	1.511E+01	-6.398E-01	2.323E-01	2.185E-01	1.095E-01

(c) $x' = 0.50$.

y(mm)	U(m/s)	V(m/s)	uu (m^2/s^2)	vv (m^2/s^2)	uv (m^2/s^2)
2.066E-01	6.706E+00	-1.098E+00	2.324E+00	6.829E-01	-3.858E-01
4.277E-01	7.786E+00	-1.480E+00	1.762E+00	4.394E-01	-3.326E-01
8.857E-01	8.461E+00	-1.631E+00	1.975E+00	5.209E-01	-3.753E-01
1.834E+00	9.218E+00	-1.765E+00	1.999E+00	5.821E-01	-3.915E-01
3.798E+00	1.070E+01	-2.042E+00	1.629E+00	5.684E-01	-3.966E-01
7.865E+00	1.212E+01	-2.210E+00	1.295E+00	5.118E-01	-2.094E-01
1.629E+01	1.360E+01	-2.499E+00	7.000E-01	4.128E-01	-4.285E-02
3.372E+01	1.476E+01	-2.667E+00	2.883E-01	2.893E-01	9.633E-02
6.983E+01	1.493E+01	-2.440E+00	2.698E-01	2.777E-01	9.023E-02

(d) $x' = 0.75$.

Table D.3: Data for $Re_\theta = 20,600$

References

Afzal, N. (1983). Analysis of a turbulent boundary layer subjected to a strong adverse pressure gradient. *International Journal of Engineering Science 21*(6), 563–576.

Alving, A. and H. Fernholz (1996). Turbulence measurements around a mild separation bubble and downstream of reattachment. *Journal of Fluid Mechanics 322*, 297–328.

Andreopoulos, J., F. Durst, Z. Zaric, and J. Jovanovic (1984). Influence of Reynolds number on characteristics of turbulent wall boundary layers. *Experiments in Fluids 2*, 7–16.

Ashjaee, J. (1980). *Subsonic Turbulent Flow in Plane-Wall Diffusers: Peak Pressure Recovery and Transitory Stall.* Ph. D. thesis, Stanford University.

Azad, R. (1996). Turbulent flow in a conical diffuser: a review. *Experimental Thermal and Fluid Science 13*, 318–337.

Balakrishnan, M. and C. Dancey (1998). Laser Doppler velocimetry velocity bias in turbulent open channel flow. *AIAA Journal 8*, 1544–1546.

Barenblatt, G. (1993a). Scaling laws for fully developed turbulent shear flows Part 1. Basic hypotheses and analysis. *Journal of Fluid Mechanics 248*, 513–520.

Barenblatt, G. (1993b). Scaling laws for fully developed turbulent shear flows Part 2. Processing of experimental data. *Journal of Fluid Mechanics 248*, 521–529.

Barenblatt, G., A. Chorin, and V. Prostokishin (2000). Self-similar intermediate structures in turbulent boundary layers at large Reynolds numbers. *Journal of Fluid Mechanics 410*, 263–283.

Barlow, R. and J. Johnston (1988). Structure of a turbulent boundary layer on a concave surface. *Journal of Fluid Mechanics 191*, 137–176.

Bernard, A., J. Foucaut, P. Dupont, and M. Stanislas (2003). Decelerating boundary layer: a new scaling and mixing length model. *AIAA Journal 41*(2), 248–255.

Bradshaw, P. (1967a). The turbulence structure of equilibrium boundary layers. *Journal of Fluid Mechanics 29*, 625–645.

Bradshaw, P. (1967b). Turbulent boundary layers. *Journal of the Royal Aeronautical Society 71*(684), 451–459.

Bradshaw, P., D. Ferriss, and N. Atwell (1967). Calculation of boundary-layer development using the turbulent energy equation. *Journal of Fluid Mechanics 28*, 593–616.

Breuer, M., N. Jovičić, and K. Mazaev (2003). Comparison of DES, RANS and LES for the separated flow around a flat plate at high incidence. *International Journal for Numerical Methods in Fluids 41*, 357–388.

Brodkey, R., J. Wallace, and H. Eckelmann (1974). Some properties of truncated turbulence signals in bounded shear flows. *Journal of Fluid Mechnics 63*, 209–224.

Buschmann, M. and M. Gad-el Hak (2003). Debate concerning the mean-velocity profile of a turbulent boundary layer. *AIAA Journal 41*(4), 565–572.

Castillo, L. and W. George (2001). Similarity analysis for turbulent boundary layer with pressure gradient: outer flow. *AIAA Journal 39*(1), 41–47.

Cebeci, T. and A. Smith (1974). *Analysis of Turbulent Boundary Layers*. New York: Academic Press.

Chukkapalli, G. and O. Turan (1995). Structural parameters and prediction of adverse pressure gradient turbulent flows: an improved k-ϵ model. *Journal of Fluids Engineering 117*, 424–432.

Clauser, F. (1954). Turbulent boundary layers in adverse pressure gradients. *Journal of Aero Sci 21*(2), 91–108.

Coles, D. (1956). The law of the wake in the turbulent boundary layer. *Journal of Fluid Mechanics 1*, 191–226.

Coles, D. and E. Hirst (1969). *1969 Proceeding Computation of Turbulent Boundary Layers - 1968 AFOSR-IFP-Stanford Conference*, Volume 2.

Corino, E. and R. Brodkey (1969). A visual investigation of the wall region in turbulent flow. *Journal of Fluid Mechanics 37*, 1–30.

Cutler, A. and J. Johnston (1989). The relaxation of a turbulent boundary layer in an adverse pressure gradient. *Journal of Fluid Mechanics 200*, 367–387.

DeGraaff, D. (1999). *Reynolds Number Scaling of the Turbulent Boundary Layer on a Flat Plate and on Swept and Unswept Bumps*. Ph. D. thesis, Stanford University.

DeGraaff, D. and J. Eaton (2000). Reynolds number scaling of the flat plate turbulent boundary layer. *Journal of Fluid Mechanics 422*, 319–346.

DeGraaff, D. and J. Eaton (2001). A high resolution laser Doppler anemometer: design, qualification, and uncertainty. *Experiments in Fluids 20*, 522–530.

Dengel, P. and H. Fernholz (1990). An experimental investigation of an incompressible turbulent boundary layer in the vicinity of separation. *Journal of Fluid Mechanics 212*, 615–636.

Dianat, M. and I. Castro (1991). Turbulence in a separated boundary layer. *Journal of Fluid Mechanics 226*, 91–123.

Driver, D. (2003). Application of oil-film interferometry skin-friction measurement to large wind tunnels. *Experiments in Fluids 34*, 717–725.

Driver, D. (June 1991). Reynolds shear stress measurements in a separated boundary layer. *AIAA Paper 91-0216*.

Durbin, P. and B. Pettersson Reif (2001). *Statistical Theory and Modeling for Turbulent Flows*. John Wiley and Sons Inc.

Durst, F., J. Jovanovic, and J. Sender (1995). LDA measurements in the near-wall region of a turbulent pipe flow. *Journal of Fluid Mechanics 295*, 305–335.

Efron, B. (1979). Computers and the theory of statistics: thinking the unthinkable. *Society for Industrial and Applied Mathematics Review 21*(4), 460–469.

Efron, B. (1982). The jackknife, and bootstrap and other resampling plans. Technical Report CBMS-NSF Regional Conference Series in Applied Mathematics, Technical Report 38.

Elsberry, K., J. Loeffler, D. Zhou, and I. Wygnanski (2000). An experimental study of a boundary layer that is maintained on the verge of separation. *Journal of Fluid Mechanics 423*, 227–261.

Figliola, R. and D. Beasley (1995). *Theory and Design for Mechanical Measurements* (2 ed.). John Wiley and Sons.

Galbraith, R. and M. Head (1975). Eddy viscosity and mixing length from measured boundary layer developments. *Aeronautical Quarterly 26*, 133–154.

Gould, R. and K. Loseke (1993). A comparison of four velocity bias correction techniques in laser Doppler velocimetry. *Journal of Fluids Engineering 115*, 508–514.

Hammache, M., F. Browand, and R. Blackwelder (2002). Whole-field velocity measurements around an axisymmetric body with a Stratford-Smith pressure recovery. *Journal of Fluid Mechanics 461*, 1–24.

Hanjalic, K., I. Hadzic, and S. Jakirlic (1999). Modeling turbulent wall flows subjected to strong pressure variations. *Journal of Fluids Engineering 121*, 57–64.

Head, M. (1976). Equilibrium and near-equilibrium turbulent boundary layers. *Journal of Fluid Mechanics 73*, 1–8.

Henkes, R. (1998). Scaling of equilibrium boundary layers under adverse pressure gradient using turbulence models. *AIAA Journal 36*(3), 321–326.

Houra, T., T. Tsuji, and Y. Nagano (2000). Effects of adverse pressure gradient on quasi-coherent structures in turbulent boundary layer. *International Journal of Heat and Fluid Flow 21*, 304–311.

Huang, P. and P. Bradshaw (1995). Law of the wall for turbulent flows in pressure gradients. *AIAA Journal 33*(4), 624–632.

Huffman, G. and P. Bradshaw (1972). A note on von Karman's constant in low Reynolds number turbulent flows. *Journal of Fluid Mechanics 53*, 45–60.

Hytopoulos, E., J. Schetz, and R. Simpson (1997). Turbulence model for steady and unsteady boundary layers in strong pressure gradients. *Journal of Fluids Engineering 119*, 541–549.

Klewicki, J. and R. Falco (1990). On accurately measuring statistics associated with small-scale structure in turbulent boundary layers using hot-wire probes. *Journal of Fluid Mechanics 219*, 119–142.

Krogstad, P. and J. Kaspersen (2002). Structure inclination angle in turbulent adverse pressure gradient boundary layer. *Journal of Fluid Engineering 142*, 1025–1033.

Krogstad, P. and P. Skåre (1995). Influence of a strong adverse pressure gradient on the turbulent structure in a boundary layer. *Physics of Fluids 7*(8), 2014–2024.

Launder, B., G. Reece, and W. Rodi (1975). Progress in the development of a Reynolds-stress turbulence closure. *Journal of Fluid Mechanics 68*, 537–566.

Lu, S. and W. Willmarth (1973). Measurements of the structure of the Reynolds stress in a turbulent boundary layer. *Journal of Fluid Mechanics 60*, 481–511.

Marusic, I. and J. Kunkel (2003). Streamwise turbulence intensity formulation for flat-plate boundary layers. *Physics of Fluids 15*(8), 2461–2464.

Marusic, I. and A. Perry (1995). A wall-wake model for the turbulence structure of boundary layers. Part 2. Further experimental support. *Journal of Fluid Mechanics 298*, 389–407.

Marusic, I., A. Uddin, and A. Perry (1997). Similarity law for the streamwise turbulence intensity in zero-pressure-gradient turbulent boundary layers. *Physics of Fluids 9*(12), 3718–3726.

Marvin, J. (1995). Perspective on computational fluid dynamics validation. *AIAA Journal 33*(10), 1778–1787.

McDonald, H., J. Ross, D. Driver, and S. Smith (2004). Wind tunnels and flight. *Proceedings of the 10th International Symposium on Applications of Laser Techniques to Fluid Mechanics*, 1–19.

McLaughlin, D. and W. Tiederman (1973). Biasing correction for individual realization of laser anemometer measurements in turbulent flows. *Physics of Fluids*, 2082–2088.

Mellen, C., J. Frohlich, and W. Rodi (2003). Lessons from LESFOIL project on large-eddy simulation of flow around an airfoil. *AIAA Journal 41*(4), 573–581.

Mellor, G. (1966). The effects of pressure gradients on turbulent flow near a smooth wall. *Journal of Fluid Mechanics 24*, 255–274.

Mellor, G. and D. Gibson (1966). Equilibrium turbulent boundary layers. *Journal of Fluid Mechanics 24*, 225–253.

Menter, F. (1992). Performance of popular turbulence models for attached and separated adverse pressure gradient flows. *AIAA Journal 30*(8), 2066–2072.

Menter, F. (1994). Two-equation eddy-viscosity turbulence model for engineering applications. *AIAA Journal 32*(8), 1598–1605.

Metzger, M., J. Klewicki, K. Bradshaw, and R. Sadr (2001). Scaling the near-wall axial turbulent stress in the zero pressure gradient boundary layer. *Physics of Fluids 13*(6), 1819–1821.

Mochizuki, S. and F. Nieuwstadt (1996). Reynolds-number-dependence of the maximum in the streamwise velocity fluctuations in wall turbulence. *Experiments in Fluids 21*, 218–226.

Monson, D., G. Mateer, and F. Menter (1993). Boundary-layer transition and global skin friction measurement with an oil-fringe imaging technique. Technical Report 932550, SAE Tech Paper Series.

Nagano, Y., T. Tsuji, and T. Houra (1998). Structure of turbulent boundary layer subjected to adverse pressure gradient. *International Journal of Heat and Fluid Flow 19*, 563–572.

Nikitin, N., F. Nicoud, B. Wasistho, K. Squires, and P. Spalart (2000). An approach to wall modeling in large-eddy simultations. *Physics of Fluids 12*(7), 1629–1632.

Olcmen, M., R. Simpson, and J. George (2001). Some Reynolds number effects on two- and three-dimensional turbulent boundary layers. *Experiments in Fluids 31*, 219–228.

Österlund, J. (1999). *Experimental Studies of Zero Pressure-Gradient Turbulent Boundary Layer Flow.* Ph. D. thesis, Kungl Tekniska Högskolan.

Perry, A., J. Bell, and P. Joubert (1966). Velocity and temperature profiles in adverse pressure gradient turbulent boundary layers. *Journal of Fluid Mechanics 25*, 299–320.

Perry, A. and I. Marusic (1995). A wall-wake model for the turbulence structure of boundary layers. Part 1. Extension of the attached eddy hypothesis. *Journal of Fluid Mechanics 298*, 361–388.

Perry, A., I. Marusic, and M. Jones (2002). On the streamwise evolution of turbulent boundary layers in arbitrary pressure gradients. *Journal of Fluid Mechanics 461*, 61–91.

Perry, A. and W. Schofield (1973). Mean velocity and shear stress distributions in turbulent boundary layers. *Physics of Fluids 16*(12), 2068–2074.

Pompeo, L., M. Bettelini, and H. Thomann (1993). Laterally strained turbulent boundary layers near a plane of symmetry. *Journal of Fluid Mechanics 257*, 507–532.

Priyadarshana, P. and J. Klewicki (2004). Study of the motions contributing to the Reynolds stress in high and low Reynolds number turbulent boundary layers. *Physics of Fluids 16*(12), 4586–4600.

Rodi, W. and G. Scheuerer (1986). Scrutinizing the k-ϵ turbulence model under adverse pressure gradient conditions. *Journal of Fluids Engineering 108*, 174–179.

Samuel, A. and P. Joubert (1974). A boundary layer developing in an increasingly adverse pressure gradient. *Journal of Fluid Mechanics 66*, 481–505.

Schlichting, H. (1979). *Boundary Layer Theory* (7 ed.). McGraw-Hill.

Schofield, W. (1981). Equilibrium boundary layers in moderate to strong adverse pressure gradients. *Journal of Fluid Mechanics 113*, 91–122.

Schubauer, G. and P. Klebanoff (1950). Investigation of separation of the turbulent boundary layer. Technical Report 1030, NACA Technical Reports.

Simpson, R., Y. Chew, and B. Shivaprasad (1981). The structure of a separating turbulent boundary layer Part 1. Mean flow and Reynolds stresses. *Journal of Fluid Mechanics 113*, 23–51.

Simpson, R., J. Strickland, and P. Barr (1977). Features of a separating turbulent boundary layer in the vicinity of separation. *Journal of Fluid Mechanics 79*, 553–594.

Skåre, P. and P. Krogstad (1994). A turbulent equilibrium boundary layer near separation. *Journal of Fluid Mechanics 272*, 319–348.

Skote, M. and D. Henningson (2002). Direct numerical simulation of a separated turbulent boundary layer. *Journal of Fluid Mechanics 471*, 107–136.

Skote, M., D. Henningson, and R. Henkes (1998). Direct numerical simulation of self-similar turbulent boundary layers in adverse pressure gradients. *Flow, Turbulence and Combustion 60*, 47–85.

Smith, A. (1977). Stratford's turbulent separation criterion for axially-symmetric flows. *Z. Angew Math Phys 28*, 929–939.

Smits, A. and D. Wood (1985). The response of turbulent boundary layers to sudden perturbations. *Annual Review of Fluid Mechanics 17*, 321–358.

Song, S. (2002). *Reynolds Number Effects on a Turbulent Boundary Layer with Separation, Reattachment and Recovery.* Ph. D. thesis, Stanford University.

Song, S. and J. Eaton (2004). Reynolds number effects on a turbulent boundary layer with separation, reattachment and recovery. *Experiments in Fluids 36*, 246–258.

Spalart, P., W.-H. Jou, and S. Allmaras (August 1997). Comments on the feasibility of LES for wings, and on a hybrid RANS/LES approach. *First AFOSR International Conference on DNS/LES Ruston LA, in Advances in DNS/LES, Liu C, Liu Z (eds) Greyden Press*.

Spalart, P. and J. Watmuff (1993). Experimental and numerical study of a turbulent boundary layer with pressure gradients. *Journal of Fluid Mechanics 249*, 337–371.

Stevenson, W., H. Thompson, and T. Roesler (1982). Direct measurement of laser velocimetry bias erros in a turbulent flow. *AIAA Journal 20*(12), 1720–1723.

Townsend, A. (1961). Equilibrium layers and wall turbulence. *Journal of Fluid Mechanics 11*, 97–120.

Tsuji, Y. and Y. Morikawa (1976). Turbulent boundary layer with pressure gradient alternating in sign. *Aeronautical Quarterly 27*, 15–28.

Tulapurkara, E., A. Khoshnevis, and J. Narasimhan (2001). Wake-boundary layer interaction subject to convex and concave curvatures and adverse pressure gradient. *Experiments in Fluids 31*, 697–707.

von Karman, T. (1921). On laminar and turbulent friction. Technical Report 1092, NACA Report.

Wallace, J., H. Eckelmann, and R. Brodkey (1972). The wall region in turbulent shear flow. *Journal of Fluid Mechanics 54*, 39–48.

Webster, D., D. DeGraaff, and J. Eaton (1996a). Turbulence characteristics of a boundary layer over a two-dimensional bump. *Journal of Fluid Mechanics 320*, 53–69.

Webster, D., D. DeGraaff, and J. Eaton (1996b). Turbulence characteristics of a boundary layer over a swept bump. *Journal of Fluid Mechanics 323*, 1–22.

Wilcox, D. (1993). Comparison of two-equation turbulence models for boundary layers with pressure gradient. *AIAA Journal 31*(8), 1414–1421.

Yorke, C. and G. Coleman (2004). Assessment of common turbulence models for an idealised adverse pressure gradient flow. *European Journal of Mechanics B/Fluids 23*, 319–337.

Zagarola, M. and A. Smits (1998). Mean-flow scaling of turbulent pipe flow. *Journal of Fluid Mechanics 373*, 33–79.